N73 25047

NASA TECHNICAL NOTE

NASA TN D-7191

NASA TN D-7191

CASE FILE COPY

AERODYNAMIC CHARACTERISTICS OF A VECTORED-THRUST V/STOL FIGHTER IN THE TRANSITION-SPEED RANGE

by

Raymond E. Mineck

Langley Directorate, U.S. Army Air Mobility R&D Laboratory
Hampton, Va. 23365

and

Myles F. Schwendemann

Aircraft Division, Northrop Corporation
Hawthorne, Calif. 90250

NATIONAL AERONAUTICS AND SPACE ADMINISTRATION • WASHINGTON, D. C. • MAY 1973

1. Report No.	2. Government Accession No.	3. Recipient's Catalog No.
NASA TN D-7191		

4. Title and Subtitle	5. Report Date
AERODYNAMIC CHARACTERISTICS OF A VECTORED-THRUST V/STOL FIGHTER IN THE TRANSITION-SPEED RANGE	May 1973
	6. Performing Organization Code

7. Author(s)	8. Performing Organization Report No.
Raymond E. Mineck (Langley Directorate, U.S. Army Air Mobility R&D Laboratory) and Myles F. Schwendemann (Aircraft Division, Northrop Corporation)	L-8457
	10. Work Unit No. 136-63-02-08
9. Performing Organization Name and Address NASA Langley Research Center Hampton, Va. 23665	11. Contract or Grant No.
	13. Type of Report and Period Covered Technical Note
12. Sponsoring Agency Name and Address National Aeronautics and Space Administration Washington, D.C. 20546	14. Sponsoring Agency Code

15. Supplementary Notes

16. Abstract

A wind-tunnel investigation was conducted with a vectored-thrust V/STOL fighter configuration. The model was equipped with two nacelle-mounted vectored-thrust jet simulators and one lift-jet simulator. The vectored-thrust jet could be tested at two alternate longitudinal positions and three nozzle deflection angles. The vectored-thrust configuration with the rear nozzles showed an increase in lift and a decrease in pitching moment when compared with the forward nozzles. The rear nozzles also improve stall characteristics.

17. Key Words (Suggested by Author(s))	18. Distribution Statement
Vectored thrust V/STOL aircraft Aerodynamic characteristics	Unclassified – Unlimited

19. Security Classif. (of this report)	20. Security Classif. (of this page)	21. No. of Pages	22. Price*
Unclassified	Unclassified	180	$3.00

*For sale by the National Technical Information Service, Springfield, Virginia 22151

AERODYNAMIC CHARACTERISTICS OF A VECTORED-THRUST V/STOL FIGHTER IN THE TRANSITION-SPEED RANGE

By Raymond E. Mineck
Langley Directorate, U.S. Army Air Mobility R&D Laboratory

and

Myles F. Schwendemann
Aircraft Division, Northrop Corporation

SUMMARY

Predicting the aerodynamic characteristics of high-disk-loaded VTOL aircraft is difficult in the transition-flight regime, that is, at velocities between hover and wingborne flight. To cope with this problem, the Northrop Corporation, under a U.S. Air Force contract, has developed several prediction methods. A wind-tunnel investigation was conducted in the Langley V/STOL tunnel on a vectored-thrust V/STOL configuration to obtain data to verify these methods. The model was equipped with one lift-jet and two single-nozzle vectored-thrust engine simulators. The vectored-thrust engine simulators were tested with two alternate exit locations and up to three exit nozzle deflection angles. The model was tested through an angle-of-attack range from 0° to 20° and an angle-of-sideslip range from -12° to 12° at four effective velocity ratios.

The vectored-thrust configuration with the rear nozzles showed an increase in lift and a decrease in pitching moment when compared with the front nozzles. The rear nozzles also improved stall characteristics. When determining the effect of the jet thrust on the aircraft aerodynamics, it was found that the inlet configuration to be used for determining power-off data had a significant effect on the computed jet-induced interference effects.

INTRODUCTION

The transition regime of a VTOL aircraft covers the effective velocity range between hover (zero forward speed) to cruise (wingborne flight). For high-disk-loaded VTOL aircraft in the transition regime, the jet exhaust effects tend to dominate the free-stream aerodynamic characteristics. It is difficult to predict both the aerodynamic characteristics because of the free stream and the pressure and velocity fields induced by the jet exhaust.

Under a U.S. Air Force contract, the Northrop Corporation has developed some aerodynamic prediction methods for V/STOL aircraft. (See ref. 1.) The purpose of the present investigation was to obtain aerodynamic, flow-field, and pressure data to verify these new techniques.

This report presents the aerodynamic and flow-field data but does not include any comparisons with the prediction methods. The investigation conducted in reference 2 shows additional aerodynamic effects of a five-jet VTOL configuration. However, volume II of reference 1 does contain some comparisons of the results of the tests and the prediction methods. The model tested was a vectored-thrust V/STOL fighter configuration equipped with one lift-jet and two vectored-thrust engine simulators. The vectored-thrust engine simulators were tested with two alternate exit nozzle locations and up to three nozzle deflection angles.

The investigation was conducted in the Langley V/STOL tunnel. The model was tested through an angle-of-attack range from 0° to 20° and an angle-of-sideslip range from -12° to 12° at four effective velocity ratios. Also, measurements were taken through an effective velocity-ratio range at two angles of attack and sideslip. This report presents the effects of jet thrust on the longitudinal and lateral characteristics of the aircraft as well as the effects of jet thrust on the flow field near the horizontal tail.

SYMBOLS

The units used for the physical quantities defined in this paper are given in the International System of Units (SI) and parenthetically in the U.S. Customary Units. Conversion factors for the SI system are presented in reference 3. The longitudinal results are presented in the stability-axis system and the lateral results in the body-axis system (fig. 1).

A_j effective jet exit area, $\sum$ Exit areas of devices producing thrust, cm^2 (in^2) (see fig. 2(a) for exit areas)

b wing span, 102.24 cm (40.25 in.)

C_D drag coefficient, $D/q_\infty S$

C_L lift coefficient, $L/q_\infty S$

C_l rolling-moment coefficient, $M_X/q_\infty Sb$

C_{l_β}	effective dihedral parameter, $\partial C_l/\partial\beta$
C_m	pitching-moment coefficient about $0.25\bar{c}$, $M_Y/q_\infty S\bar{c}$
C_{m_α}	longitudinal-stability parameter, $\partial C_m/\partial\alpha$
C_n	yawing-moment coefficient, $M_Z/q_\infty Sb$
C_{n_β}	directional-stability parameter, $\partial C_n/\partial\beta$
C_T	thrust coefficient, $T/q_\infty S$
C_Y	side-force coefficient, $F_Y/q_\infty S$
$\bar{c}$	mean aerodynamic chord of wing, 21.21 cm (8.35 in.)
D	drag force, N (lbf)
D_e	effective jet-exit diameter, $\sqrt{4A_j/\pi}$
F_Y	side force, N (lbf)
h	height measured from center of lift-jet exit to tunnel floor, cm (in.)
i_t	horizontal-tail incidence, leading edge up is positive, deg
L	lift, N (lbf)
M_X	rolling moment about X-axis (body axis)
M_Y	pitching moment about Y-axis (body axis)
M_Z	yawing moment about Z-axis (body axis)
q_c	free-stream dynamic pressure corrected for wall effects, N/m^2 (lbf/ft^2)
q_∞	free-stream dynamic pressure, N/m^2 (lbf/ft^2)
S	wing area, 2090 cm^2 (2.25 ft^2)

T static thrust measured perpendicular to jet exit, N (lbf)

V_j effective jet velocity, m/sec (ft/sec)

V_∞ free-stream velocity, m/sec (ft/sec)

$\left(\frac{V_\infty}{V_j}\right)_e$ effective velocity ratio, $\sqrt{\frac{\rho_\infty V_\infty^2}{\rho_j V_j^2}}$

$\dot{w}$ inlet weight flow rate, N/sec (lbf/sec)

X, Y, Z body reference axes (see fig. 1)

z distance measured from wing chord plane, cm (in.)

α angle of attack, deg

β angle of sideslip, deg

$\Delta\alpha$ change in angle of attack due to wall effects, deg

δ_f flap deflection, deg

ϵ downwash angle, deg

ρ_j jet exhaust density, kg/m^3 (lbm/ft^3)

ρ_∞ free-stream density, kg/m^3 (lbm/ft^3)

Model configuration symbols:

B body

f flap, 45^o deflection when installed

H horizontal tail, 0^o incidence unless otherwise noted

J lift jet

N_1	nacelles with front vectored-thrust nozzle, used with appropriate nozzle deflection in degrees
N_2	nacelles with rear vectored-thrust nozzles, used with appropriate nozzle deflection in degrees
V	vertical tail
W	wing
0,45,90	nozzle deflection angle in degrees

MODEL AND APPARATUS

The model tested was the vectored-thrust V/STOL fighter configuration presented in figure 2. The wing, flaps, empennage, and nacelles were removable for investigation of the aerodynamic effects of these components. The flaps used for part of the tests had a chord equal to 25 percent of the local wing chord and extended from 12.4 percent semispan to 64.6 percent semispan.

Two vectored-thrust engine simulators were mounted in fuselage-supported nacelles and one lift-jet simulator was mounted within the fuselage (fig. 2). The vectored-thrust engine simulators were of the ejector type which induced inlet flow. The vectored-thrust jet exits could be set 2.67 cm (1.05 in.) forward of the model moment reference center or 18.62 cm (7.33 in.) aft of the model moment reference center. The model moment reference center was at the 25-percent chord position of the mean aerodynamic chord. The vectored-thrust exhaust nozzles had an exit diameter of 9.32 cm (3.67 in.) and could be deflected downward parallel to the XZ plane at angles of 0°, 45°, and 90° measured from the horizontal plane.

The lift-jet simulator was a simple convergent nozzle with no external air intake. The lift-jet exit, located in the plane of the bottom of the fuselage 7.67 cm (3.02 in.) forward of the model moment reference center, was 5.71 cm (2.25 in.) in diameter and was limited to exhausting 90° from the horizontal plane.

For calibration purposes, a bellmouth flowmeter with a 8.25-cm-diameter (3.25-in.) throat was used to measure the vectored-thrust engine simulator inlet mass flow. (See fig. 2(c).) In addition, there were two flat plugs and two elliptical plugs (fig. 2(b)) which could be placed in the engine inlets to prevent flow through the vectored-thrust engine simulators. The flat plug was mounted flush in the plane of the inlet lip when it was used.

The model was supported by a strain-gage balance mounted to a sting support. (See fig. 2(c).) The model plenum chamber, attached to the balance, was supplied cold, dry high-pressure air through an air line which formed a limber spring across the strain-gage balance. The air line was made of invar to minimize any expansion or compression due to temperature change and had a coiled section to minimize effects caused by pressure changes.

Corrections have been made to the data to account for the presence of the air line. Before the addition of the air line, the balance had an accuracy of 0.5 percent of the full-scale load. Although the air line degrades this accuracy, no attempt has been made to determine the resultant accuracy. However, the repeatability obtained is within 0.5 percent of the full-scale load.

For some of the tests, a rake (figs. 3 and 4) was fastened to the sting. The rake consisted of seven yaw-pitch probes calibrated to determine the flow magnitude and direction at each probe tip. The rake was offset from the fuselage in the vicinity of the horizontal-tail plane as shown in figure 3. The forces and moments were transmitted to the sting so there would be no direct effect on the forces and moments measured on the model. All rake data were taken with the horizontal and vertical tails removed.

TEST PROCEDURES

The test was conducted in the Langley V/STOL tunnel which has a test section of 4.42 m (14.50 ft) by 6.63 m (21.75 ft). Photographs of the model in the V/STOL tunnel are presented in figure 4. All testing was done out of ground effect. Table I describes the test conditions for most of the tests. Data were obtained at Mach numbers ranging up to 0.22 and Reynolds numbers based on mean aerodynamic chord ranging up to 1.07×10^6.

The vectored-thrust configuration was tested with the nozzle exits either forward or aft of the model moment center. At each position, up to three nozzle deflection angles were tested: 0°, 45°, and 90°. Tests were also made with the flaps, with the engine inlets closed, and with the vertical and horizontal tails installed.

The height of the model above the tunnel floor varied with angle of attack because of the design of the model support system. The height of the model was about 1 wing span at an angle of attack of 0°, 1.5 wing spans at an angle of attack of 4°, and 2 wing spans at angles of attack of 8° or more. At a height of 2 spans, the model was located in the center of the tunnel.

In an effort to investigate the effect of wind-tunnel wall proximity, the vectored-thrust configuration with the rear nozzles was tested with special large-diameter (11.43 cm (4.50 in.)) 90° exit nozzles at several heights. These large-diameter nozzles

were used only for this special test for wall effects and were not used elsewhere in this investigation. The results of this special test, presented in figure 5, show that for heights greater than 1 span above the floor, there is little change in the longitudinal forces and moments except at the effective velocity ratio of 0.1.

The interference of the tunnel boundaries and the jet exhaust induce a change in angle of attack and in free-stream dynamic pressure. The corrections to angle of attack and dynamic pressure due to wind-tunnel wall effects were computed by using the method described in references 4 and 5. The results of these calculations are presented in figure 6 for both the 11.43-cm-diameter (4.50-in.) rear vectored-thrust jets and the 9.32-cm-diameter (3.67-in.) jets. The smaller area jets induce smaller corrections to angle of attack and free-stream dynamic pressure. For the test conditions encountered during most of the test (table I), the corrections to free-stream dynamic pressure were found to be small and were neglected. The corrections to angle of attack are small except at the low effective velocity ratios. However, at the low effective velocity ratios near hover, angle-of-attack effects are small and can be neglected. At the free-stream dynamic pressures used during the investigation, the corrections to drag and pitching moment due to the base pressure were found to be less than the accuracy of the balance without the air line and, therefore, were neglected.

The thrust of each jet simulator configuration was calibrated as a function of a reference pressure. To minimize interference, the calibrations were performed on the bare model plenum without the fuselage. For the lift jet, the difference between the lift-jet exit total pressure and the free-stream static pressure was used as the reference, whereas the ejector plenum static pressure was used as the reference pressure for each vectored-thrust engine simulator. A description of the calibration method appears in reference 6. The forces due to thrust were measured in the body-axis system. These forces were used to determine the actual thrust direction in the XZ plane. The nominal and actual thrust directions are shown in table II measured from the horizontal plane.

To determine the inlet weight flow rates for the various configurations at forward speeds, a test was made with an 8.25-cm-diameter (3.25-in.) bellmouth flowmeter mounted on the right vectored-thrust engine simulator inlet. (See fig. 2.) At several thrust levels and at forward speeds, the weight flow rate through the bellmouth flowmeter, the inlet static pressure of the left-hand vectored-thrust engine simulator, and the free-stream static measure were measured. From this calibration, the inlet weight flow rate was determined without the bellmouth flowmeter for the various configurations tested.

The effective velocity ratio was determined by using an effective jet-exit area (A_j). This effective area was the sum of the exit areas of the thrust devices in use – the right and left vectored-thrust jets and/or the lift jet. The effective area for the lift jet was

25.68 cm^2 (3.98 in^2), for the vectored thrust alone 68.26 cm^2 (10.58 in^2), and for the combination lift jet and vectored-thrust jets 93.94 cm^2 (14.56 in^2). The effective jet diameter was the diameter of a circle with an area equal to the effective jet area. The effective jet diameter D_e and effective velocity ratio $\left(V_\infty/V_j\right)_e$ were determined as follows:

$$D_e = \sqrt{\frac{4A_j}{\pi}}$$

$$\left(\frac{V_\infty}{V_j}\right)_e = \sqrt{\frac{\rho_\infty V_\infty^2}{\rho_j V_j^2}} = \sqrt{\frac{q_\infty}{T/2A_j}}$$

From these equations, it can be seen that small changes in thrust or free-stream dynamic pressure will change the effective velocity ratio slightly. This condition causes a small amount of scatter in the data, especially at the lower effective velocity ratios.

The data are presented at several effective velocity ratios and through an effective velocity ratio range. From the definition of thrust coefficient and effective velocity ratio, the relationship of the two parameters may be determined as follows:

$$C_T = \frac{2A_j}{S} \frac{1}{\left(\frac{V_\infty}{V_j}\right)_e^2}$$

The lift-jet-alone, the vectored-thrust-alone, and the combination lift-jet and vectored-thrust-jet configurations all have different effective exit areas. The relationship of thrust coefficient to effective velocity ratio is plotted in figure 7 for the major jet configurations tested. For a given effective velocity ratio, the thrust coefficient takes on one of three possible values, depending on the jet configuration. Effective velocity ratio was chosen as the best parameter to present the data through the transition regime because it starts at zero for hover and increases toward a finite value at cruise.

To determine whether the level of thrust affected the results at a particular effective velocity ratio, the vectored-thrust configuration with the front nozzles deflected 90° was tested at a thrust level lower than that used during the remainder of the test. The results of this test are presented in figure 8. The results identified as "high thrust" were run at the thrust levels normally used throughout the test. (See table II.) It should be noted that for the high-thrust runs, the thrust had to be lowered to obtain effective velocity ratios greater than 0.3 because of the limit on tunnel free-stream dynamic pressure. For the "low-thrust" runs, the thrust was held constant through the effective

velocity ratio range. For the low-thrust runs, the thrust was greater than that used for the high-thrust runs for the effective velocity ratio of 0.5.

As shown in figure 8, the results are found to be in good agreement. There is no difference in lift between the high- and low-thrust results but there is a constant difference in drag and pitching moment which is independent of angle of attack and effective velocity ratio. At both the high- and low-thrust levels, the inlet weight flow is approximately constant so that the difference in drag cannot be explained by engine inlet flow. The investigation in reference 7, using the same test techniques, showed a small discrepancy in drag but none in pitching moment. This discrepancy has not been explained.

PRESENTATION OF DATA

The results of the wind-tunnel investigation are presented in two basic ways: in terms of the conventional aerodynamic coefficients and in terms of force-thrust ratios. The longitudinal data are presented in the stability-axis system and the lateral data in the body-axis system. The results are presented as follows:

	Figure
Longitudinal aerodynamics:	
Cruise nozzle deflection configuration aerodynamics	9 to 11
Effect of model components	12 to 20
Effect of inlet flow	21 to 29
Effect of thrust location	30 to 41
Effect of tail incidence	42 to 51
Effect of flaps	52 to 65
Effect of angle of attack on downwash	66 to 89
Lateral aerodynamics:	
Effect of model components	90 to 96
Effect of thrust configuration	97 to 101
Effect of inlet flow	102 to 105
Effect of angle of attack	106 to 107

DISCUSSION OF RESULTS

Longitudinal Aerodynamics

Cruise nozzle deflection configuration aerodynamics.- The vectored-thrust configuration with the front nozzles set at 0^{o} was tested with the inlets open and with the horizontal and vertical tails removed. The results are presented in figure 9. The addition

of power increased the lift-curve slope and decreased the pitching moment. Power had little effect on stability and made the stall less severe.

Figures 10 and 11 show the effect of flaps with the horizontal and vertical tails installed with the horizontal-tail incidence set at 0°. The addition of flaps slightly increases the lift-curve slope without power. As expected, the lift increment and drag increment with power due to the flaps are very large.

Effect of model components.- The fuselage was tested with various combinations of the following components to determine their effect on the longitudinal aerodynamic characteristics: the engine nacelles, wing, and vertical and horizontal tails. The horizontal tail was set at 0° incidence when used for these data. Figures 12 to 14 present the results for the buildup of the model with the lift jet and figures 15 to 20 present the results for the model buildup of the vectored-thrust configuration with the front nozzles deflected 90°. The vectored-thrust inlets and exits and the lift-jet exit (when installed) were open for these data.

For the lift-jet configuration, interference effects cause a lift loss. Figure 13 shows the loss at an angle of attack of 0° is smallest at the low forward speed and increases with increasing forward speed. There is no inlet drag and the total drag is smaller than it would be if there were an external inlet. The pitching moment increases with forward speed at an angle of attack of 0° and decreases with forward speed at an angle of attack of 10°.

For the vectored-thrust configuration with the front nozzles deflected 90° (fig. 15), the addition of the engine nacelles to the fuselage gives both an increment in lift and drag and an increase in $C_{m_{\alpha}}$. The increment in lift due to the addition of the nacelles increases with angle of attack. Part of the lift and drag increments can be explained by the nozzles turning the momentum from the inlet mass flow 90°.

At an angle of attack of 0°, the addition of the wing to the combination of the body and nacelles results in a lift loss and indicates an interference between the nacelles and the wing. The loss is greater with power than without power. Figures 13 and 19 demonstrate that the front vectored-thrust configuration does not exhibit the severe lift loss experienced by the lift-jet configuration.

Effect of inlet flow.- The inlet weight flow rates for the left vectored-thrust engine simulator are presented in figure 21. Except for the low thrust runs, all powered data were obtained at thrust levels of at least 132 N (30 lbf) for each engine simulator. At these thrust levels, the inlet weight flow rate is nearly independent of free-stream dynamic pressure and thrust level but dependent on the nozzle configuration. Without thrust, the inlet weight flow is dependent on the free-stream dynamic pressure and nozzle configura-

tion. All unpowered data were obtained at a free-stream dynamic pressure of 2870 N/m^2 (60.0 lbf/ft^2).

To determine the effect of inlet flow, the vectored-thrust configurations were tested with both inlets closed with flat or elliptical plugs. The results for the front nozzles deflected 90°, presented in figure 22, show that there is little difference in lift and drag for the flat and elliptical plugs. The elliptical plug had a different C_{m_α} than the flat plug or the open inlet. The flat plug was chosen to determine the effects of inlet flow.

By use of the inlet weight flow rate and the free-stream density, the increment in lift due to the inlet flow was calculated to be significantly less than the measured lift increment. A comparison of a very limited amount of wing pressure profile data without power for the inlets open and inlets closed for the front vectored-thrust configuration helps explain part of this difference. These data show that closing the inlets induced a downwash on the wing; the downwash results in a decrease in a local angle of attack varying between 1° and 2°.

For the forward 90° nozzle configuration, there appears to be a discrepancy between the powered and unpowered results. Without power, the increment in lift due to opening the inlets is greater than the increment in drag due to opening the inlets. (See fig. 22.) However, with power, the increment in lift due to opening the inlets is less than the increment in drag due to opening the inlets. (See figs. 23 and 24.) All these data show that there are more effects due to opening the inlets than just the effect of the inlet weight flow rate. Because of this complexity, it was difficult to identify precisely the effects of power.

Effect of thrust configuration.- The position of the thrust vector relative to the wing has a large effect on the flow field over the wing. The results for the various thrust configurations are presented at four particular effective velocity ratios with the inlets open and the horizontal and vertical tails removed. When interpreting these results, it should be noted that there are three basic configurations: lift jet, vectored-thrust jets, and combination lift-jet and vectored-thrust jets. Each of the three configurations has a different jet area; consequently, the different configurations operating at the same effective velocity ratio will have different thrust coefficients. (See fig. 7.) For example, for a constant lift coefficient at an effective velocity ratio, the following equation shows that the ratio of wing lift to jet lift varies with jet area:

$$\frac{L}{T} = \frac{1}{A_j/S}\frac{C_L}{2}\left(\frac{V_\infty}{V_j}\right)_e^2$$

This equation, presented graphically in figure 30(a), shows how the wing-lift to jet-lift ratio varies at a lift coefficient of 1.0 at three effective velocity ratios. To obtain the

same ratio of wing lift to jet lift at a constant lift coefficient, different effective velocity ratios are needed for configurations with different ratios of jet area to wing area. The effective velocity ratio for the different configurations needed to produce the same wing-lift to jet-lift ratio is presented (as a function of a reference effective velocity ratio) in figure 30(b). Care should be taken when comparing configurations with different area ratios $\left(A_j/S\right)$.

The thrust configurations exhausting 90° from the horizontal plane are presented in figures 31 to 36 and the thrust configurations exhausting 45° from the horizontal plane are presented in figures 37 to 41.

For the unpowered case (fig. 31) with the vectored-thrust nozzles deflected 90°, the rear-nozzle position shows no change in lift coefficient at an angle of attack of 0° but shows an increase in lift-curve slope when compared with the front-nozzle position. The rear position also displays a more gradual stall. In addition, the rear nozzles provide a negative increment in pitch.

With the addition of power (figs. 35 and 36) for both the front and rear 90° nozzles, there is a slight lift loss at an angle of attack of 0°. For a given angle of attack, the lift loss with the front nozzles is greater than that of the rear nozzles.

For the vectored-thrust configuration with the nozzles deflected 45°, results were nondimensionalized by the thrust normal to the jet exit, not by the component of thrust normal to the model. The thrust normal to the model is T sin 40° (0.643T). (See table II.) The results for the 45° nozzles are similar to those with the 90° nozzle deflection. When unpowered (fig. 37), the rear-nozzle configuration has a greater lift-curve slope and more gradual stall. The powered results show a more gradual stall than the unpowered results and the rear-nozzle configuration shows a more gradual stall than the front-nozzle configuration.

In the transition-speed regime, the interference lift loss is greater with the forward 45° nozzles than with the rear 45° nozzles (figs. 40 and 41). Also, the difference in lift between the front-position and rear-position nozzles increases with increasing velocity ratio.

Horizontal-tail effectiveness.- The effect of the horizontal tail is shown in figures 42 to 51 at five tail incidences for the front nozzles, deflected 90° without the flaps, and at one tail incidence for the rear nozzles deflected 90° with the flaps extended.

For the front-nozzle configuration at angles of attack below stall (fig. 42), the unpowered model is longitudinally stable for tail incidences up to approximately 10°.

The effect of power is destabilizing. (See figs. 43 and 44.) Although the model is longitudinally unstable with power, the tail is still providing a stable contribution. At an

angle of attack of 0° (fig. 45), only a tail incidence of 10° (when compared with the tail off) is providing positive lift and a trimming pitching moment through the effective velocity ratio range; whereas at an angle of attack of 10°, both the 5° and 10° tail incidences are providing a trimming pitching moment.

For the rear-nozzle configuration without power and with the flaps extended, the addition of the horizontal tail at 5° incidence makes the model neutrally stable for angles of attack below stall (fig. 47). Above stall, the tail does not have much effect. The effect of power is destabilizing. (See figs. 48 and 49.) The tail is not contributing to stability and the download of the tail is insufficient to trim the model. With the center of gravity in the position chosen, neither the front nor the rear vectored-thrust configurations are trimmed in pitch.

Effect of flaps.- The vectored-thrust configuration was tested with the flaps extended 45° and the flaps removed. The results for the vectored-thrust configuration with the 90° nozzles are presented in figures 52 to 61 and with the 45° nozzles in figures 62 to 65. The flow entrained by the jet thrust interacts with the flow over the flaps. The flaps contribute a positive increment in lift and drag and a negative increment in pitching moment.

For the vectored-thrust configuration, the increment in lift coefficient from extending the flaps at 0° angle of attack was about 0.3 for the front nozzles deflected 90°, about 0.4 to 0.6 for the front nozzles deflected 45°, and about 0.5 to 0.75 for the rear nozzles deflected 90°.

Effect of Angle of Attack on Downwash Angle

The seven-probe rake was mounted on the sting with the probe tips in a vertical plane so that the center probe was located 0.76 cm (0.3 in.) above the plane of the horizontal tail and at the quarter chord of the tail mean aerodynamic chord. (See fig. 3.) Data are presented for the bottom ($z/\bar{c} = 0.32$), center ($z/\bar{c} = -0.40$), and top ($z/\bar{c} = -1.12$) probes. The results of these three probes are typical when compared with the other four. Figures 66 to 89 present the downwash angle measured from the direction of the free stream as a function of angle of attack for the various thrust configurations at a given effective velocity ratio. The measurements were taken at one spanwise station. There is some scatter in the results arising from the rather turbulent flow resulting from the wake of the wing or from the interaction of the jet with the free stream. In general, the downwash angle increases with decreasing velocity ratio at a given angle of attack, and the downwash angle is greater with the rear nozzles than with the front nozzles.

The results displayed two basic trends for the lift-jet configuration and for the vectored-thrust jets. The trends for the vectored-thrust configuration are as follows:

At the top location (figs. 66 to 69 and 78 to 81) without power, $d\epsilon/d\alpha$ is about zero. With power, the value of $d\epsilon/d\alpha$ is small, generally below 0.20, up to the angle of stall. Above stall the value varies with the configuration, but generally $d\epsilon/d\alpha$ increases sharply above stall. At the center location (figs. 70 to 73 and 82 to 85), $d\epsilon/d\alpha$ with and without power is about 0.5 up to stall. Above stall, $d\epsilon/d\alpha$ becomes more positive and sometimes becomes greater than 1.0. At the bottom location (figs. 74 to 77 and 86 to 89) without power, $d\epsilon/d\alpha$ is small up to the angle of stall and then changes sharply. With power, $d\epsilon/d\alpha$ varies widely and has different values above and below the angle of stall. For lift-jet alone with power, all the locations show similar characteristics, but different from those of vectored thrust; $d\epsilon/d\alpha$ is positive up to stall and then becomes negative above stall. The top location shows the best position for the horizontal tail for aerodynamic control in the transition regime. Only in this position can the tail provide near its maximum contribution to stability.

Lateral Aerodynamics

Effect of model components.- The fuselage was tested with various combinations of the following components to determine their effect on the lateral aerodynamic characteristics: the engine nacelles, the wing, and the vertical and horizontal tails. The results are presented in figures 90 to 96 through an angle-of-sideslip range at an angle of attack of 0°. Two important parameters of lateral stability, the effective dihedral C_{l_β} and the directional-stability parameter C_{n_β}, can be examined.

For the vectored-thrust configuration with the front jets deflected 90°, the effective dihedral parameter between angles of sideslip of 12° and -12° is approximately the same for power-off and power-on except for an effective velocity ratio of 0.2 (figs. 91 to 94). The effective dihedral for the wing-body nacelles is about -0.0014 and becomes -0.0035 with the addition of the vertical and horizontal tails.

The directional-stability parameter is negative for all configurations without the vertical tail. The addition of the vertical tail makes this parameter much more positive. The value at the higher velocity ratios is about 0.0075 as compared with about 0.0050 for the unpowered case.

Effect of thrust location.- The three basic thrust configurations, the vectored-thrust configuration with the front and rear nozzles deflected 90°, and the lift jet, were tested without the horizontal and vertical tails through an angle-of-sideslip range at an angle of attack of 0°. Comparisons of these results are presented in figures 97 to 101. Without power, all three configurations show the same amount of effective dihedral but with power all show a negative increment in effective dihedral.

Although all configurations without the vertical tail are directionally unstable, the vectored-thrust configurations show more directional stability than the lift jet and the

front vectored-thrust configuration shows slightly more directional stability than the rear vectored-thrust configuration.

Effect of inlet flow.- To determine the effects of inlet flow on the lateral characteristics, the vectored-thrust configuration with the nozzles deflected 90° in both the front and rear positions was tested through an angle-of-sideslip range at an angle of attack of 0°. Figure 102 shows that for the rear-position nozzles without power, opening the inlet does not change the effective dihedral or the directional stability. For the front-position nozzles without power (fig. 103), opening the inlets made the effective dihedral more negative and the directional stability less negative. With the addition of power for front-position nozzles, opening the inlets made the effective dihedral and the directional stability more negative.

Effect of angle of attack.- The vectored-thrust configuration with the front nozzles deflected 90° was tested through an angle-of-sideslip range at angles of attack of 0° and 10° with and without power. Figures 106 and 107 show that the effective dihedral becomes more negative with the increase in angle of attack. The effect is less pronounced with power on than with power off. The directional stability shows little change with the change in angle of attack with or without power.

CONCLUDING REMARKS

The investigation of a vectored-thrust V/STOL aircraft configuration has been conducted in the Langley V/STOL tunnel. The rear-position vectored-thrust nozzle configuration provided an increment in lift-curve slope over the front-position nozzles as well as a negative pitching-moment increment. The rear-position nozzle configuration did show a more gradual stall but did not show as large a lift loss from interference as the front-nozzle configuration. The increment in lift at a given angle of attack due to extending the flaps is larger with the rear nozzles than with the front nozzles. Because of the complex phenomena involved with inlet flow, it was difficult to identify precisely the effects of power.

Langley Research Center,
National Aeronautics and Space Administration,
Hampton, Va., February 23, 1973.

REFERENCES

1. Wooler, P. T.; Kao, H. C.; Schwendemann, M. F.; Wasson, H. R.; and Ziegler, H.: V/STOL Aircraft Aerodynamic Prediction Methods. AFFDL-TR-72-26, Vol. I-IV, U.S. Air Force, Jan. 1972.
   Vol. I – Theoretical Developments of Prediction Methods.
   Vol. II – Application of Prediction Methods.
   Vol. III – Manual for Computer Programs.
   Vol. IV – Literature Survey.

2. Margason, Richard J.; and Gentry, Garl L., Jr.: Aerodynamic Characteristics of a Five-Jet VTOL Configuration in the Transition Speed Range. NASA TN D-4812, 1968.

3. Mechtly, E. A.: The International System of Units – Physical Constants and Conversion Factors (Revised). NASA SP-7012, 1969.

4. Heyson, Harry H.: Fortran Programs for Calculating Wind-Tunnel Boundary Interference. NASA TM X-1740, 1969.

5. Heyson, Harry H.: Use of Superposition in Digital Computers To Obtain Wind-Tunnel Interference Factors for Arbitrary Configurations, With Particular Reference to V/STOL Models. NASA TR R-302, 1969.

6. Margason, Richard J.; and Gentry, Garl L.: Static Calibration of an Ejector Unit for Simulation of Jet Engines in Small-Scale Wind-Tunnel Models. NASA TN D-3867, 1967.

7. Margason, Richard J.; Vogler, Raymond D.; and Winston, Matthew M.: Wind-Tunnel Investigation at Low Speeds of a Model of the Kestrel (XV-6A) Vectored-Thrust V/STOL Airplane. NASA TN D-6826, 1972.

TABLE I.- TEST CONDITIONS FOR THE VECTORED-THRUST CONFIGURATION (N_1 AND N_2)

α, deg	β, deg	$\left(\frac{V_\infty}{V_j}\right)_e$	q_∞		T		Remarks
			N/m^2	lb/ft^2	N	lb	
0 to 20	0	∞	2870	60.0	0	0	
		0.3	2050	42.9	623	140	
		.2	910	19.0	623	140	
		.1	227	4.76	623	140	
0	-12 to +12	∞	2870	60.0	0	0	
		.3	2050	42.9	623	140	
		.2	910	19.0	623	140	
		.1	227	4.76	623	140	
10	-12 to +12	∞	2870	60.0	0	0	
		.2	910	19.0	623	140	
0 or 10	0	0 to 0.3, 0.4, 0.5	0 to 2870, 2870, 2870	0 to 60.0, 60.0, 60.0	623, 489, 315	140, 110, 71	High thrust
0 or 10	0	0 to 0.5	0 to 3350	0 to 70.0	374	84	Low thrust
0	-8 or +8	0 to 0.3, 0.4, 0.5	0 to 2870, 2870, 2870	0 to 60.0, 60.0, 60.0	623	140	

TABLE II.- EXIT NOZZLE POSITION AND THRUST DIRECTION

Thrust device	Nominal direction, deg	Actual direction, deg	Exit center position			
			x station		Water line	
			cm	in.	cm	in.
Lift jet	90	90.1	50.93	20.05	-7.82	-3.08
Front vectored	0	-1.2	49.71	19.57	2.11	.83
	45	40.1	51.52	20.28	.30	.12
	90	85.2	55.93	22.02	-4.11	-1.62
Rear vectored	45	40.0	72.80	28.66	.30	.12
	90	85.0	77.22	30.40	-4.11	-1.62

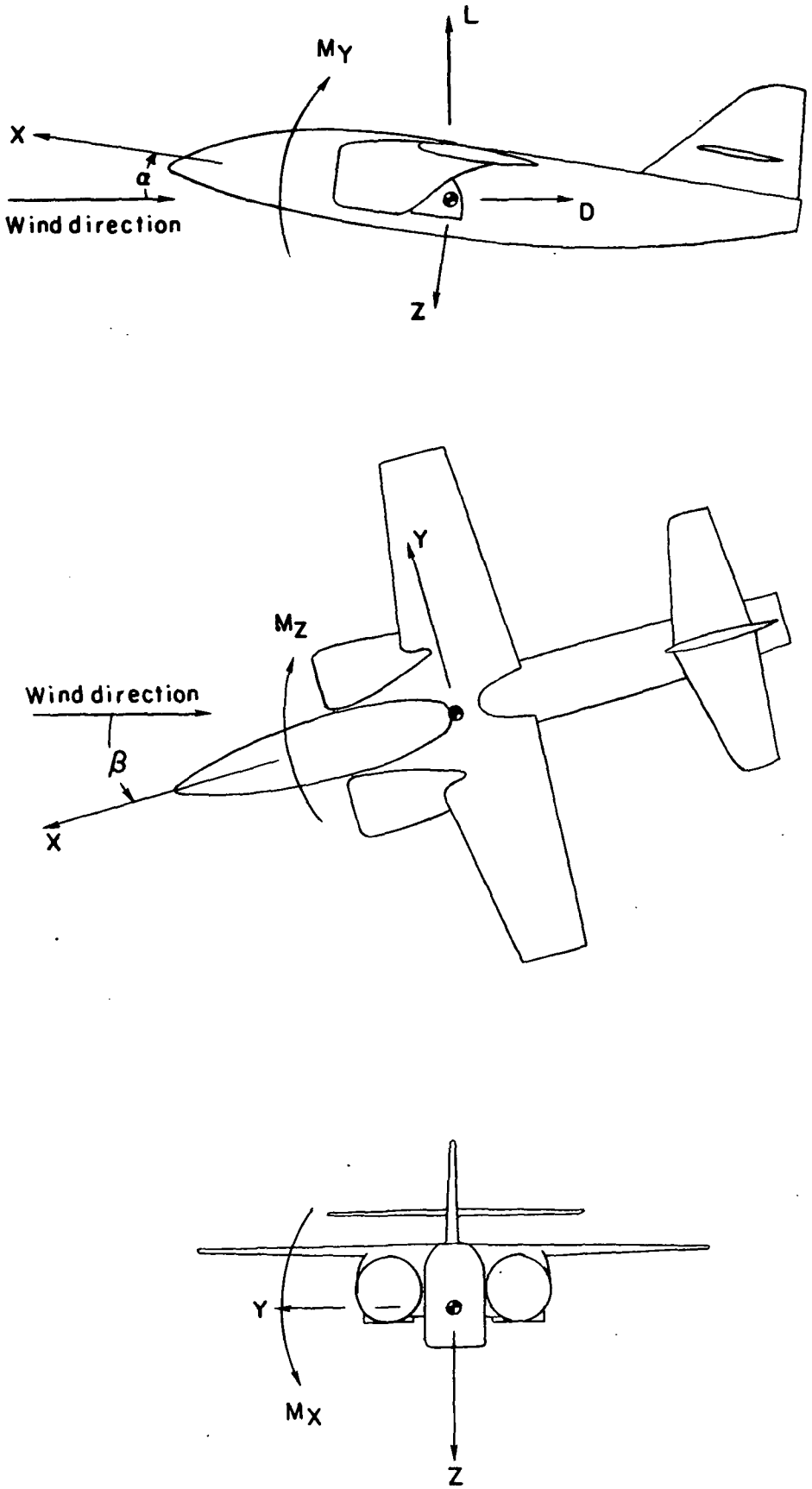
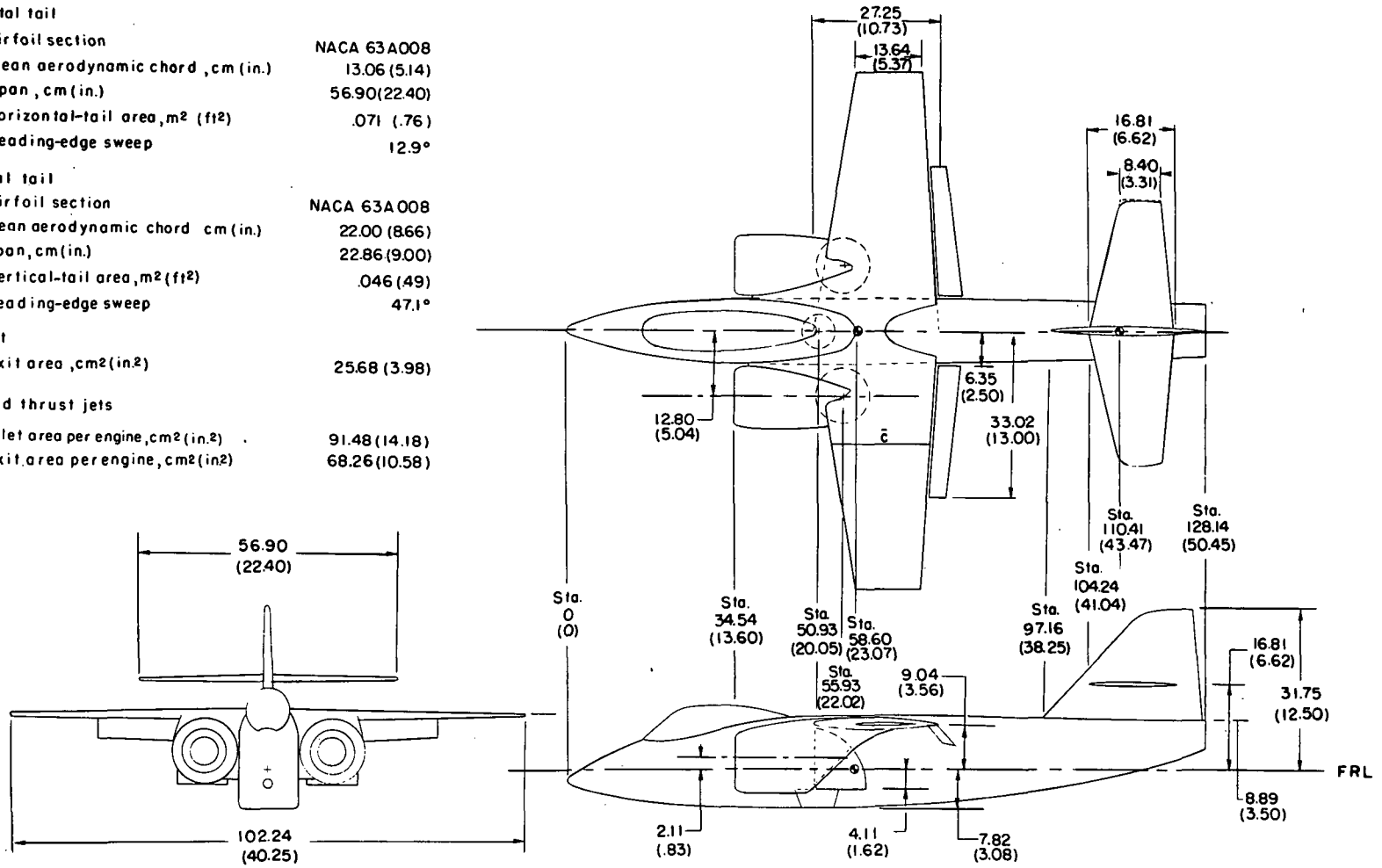


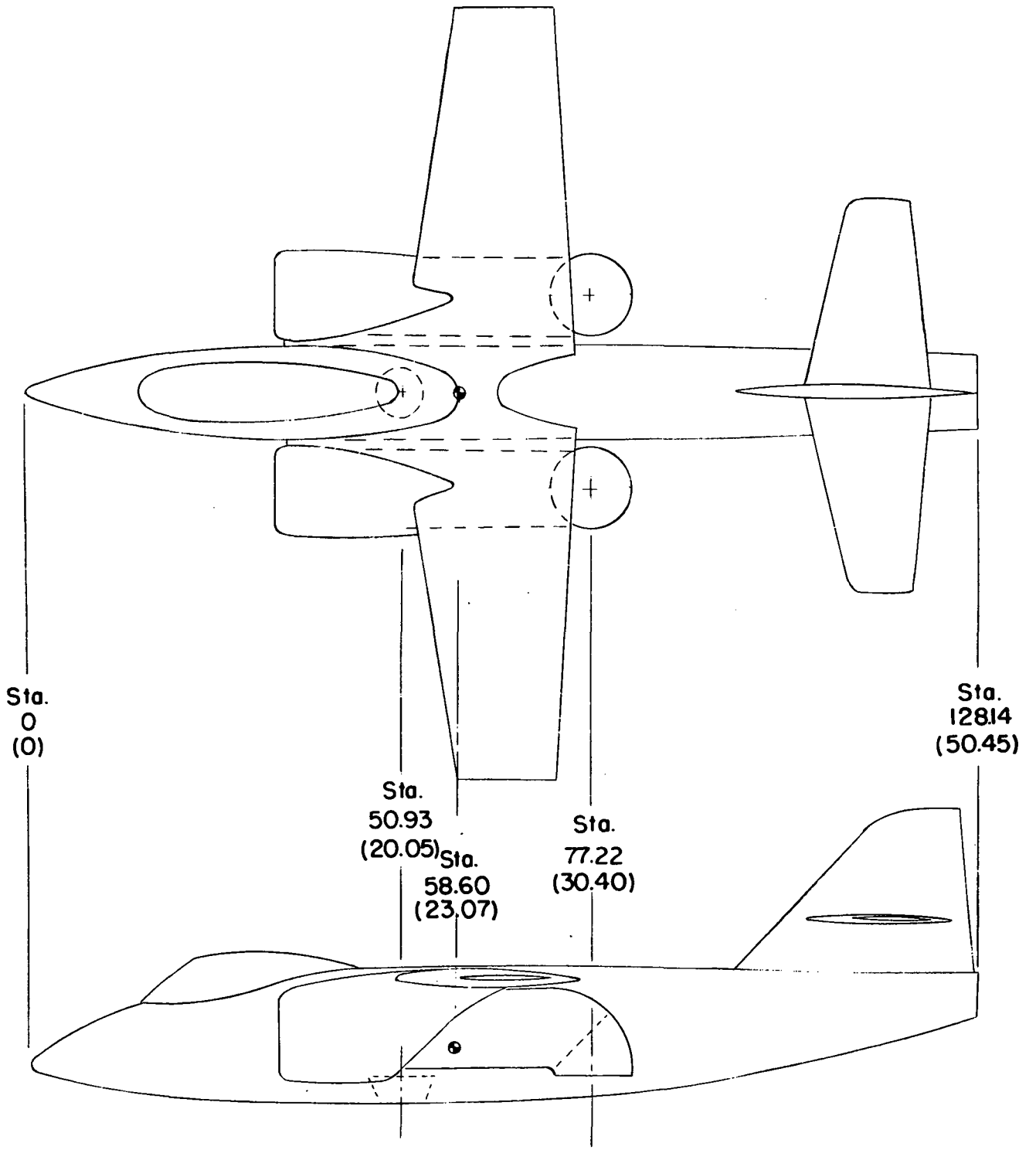
Figure 1.- System of axes. Positive directions of forces and moments and angles are indicated by arrows.

WING GEOMETRY	
Airfoil section	NACA 63A010
Mean aerodynamic chord, cm (in.)	21.21 (8.35)
Span, cm (in.)	102.24 (40.25)
Wing area, m^2 (ft^2)	.209 (2.25)
Aspect ratio	5.0
Taper ratio	0.5
Wing incidence	0°
Leading-edge sweep	9.8°
Horizontal tail	
Airfoil section	NACA 63A008
Mean aerodynamic chord, cm (in.)	13.06 (5.14)
Span, cm (in.)	56.90 (22.40)
Horizontal-tail area, m^2 (ft^2)	.071 (.76)
Leading-edge sweep	12.9°
Vertical tail	
Airfoil section	NACA 63A008
Mean aerodynamic chord cm (in.)	22.00 (8.66)
Span, cm (in.)	22.86 (9.00)
Vertical-tail area, m^2 (ft^2)	.046 (.49)
Leading-edge sweep	47.1°
Lift jet	
Exit area, cm^2 ($in.^2$)	25.68 (3.98)
Vectored thrust jets	
Inlet area per engine, cm^2 ($in.^2$)	91.48 (14.18)
Exit area per engine, cm^2 ($in.^2$)	68.26 (10.58)



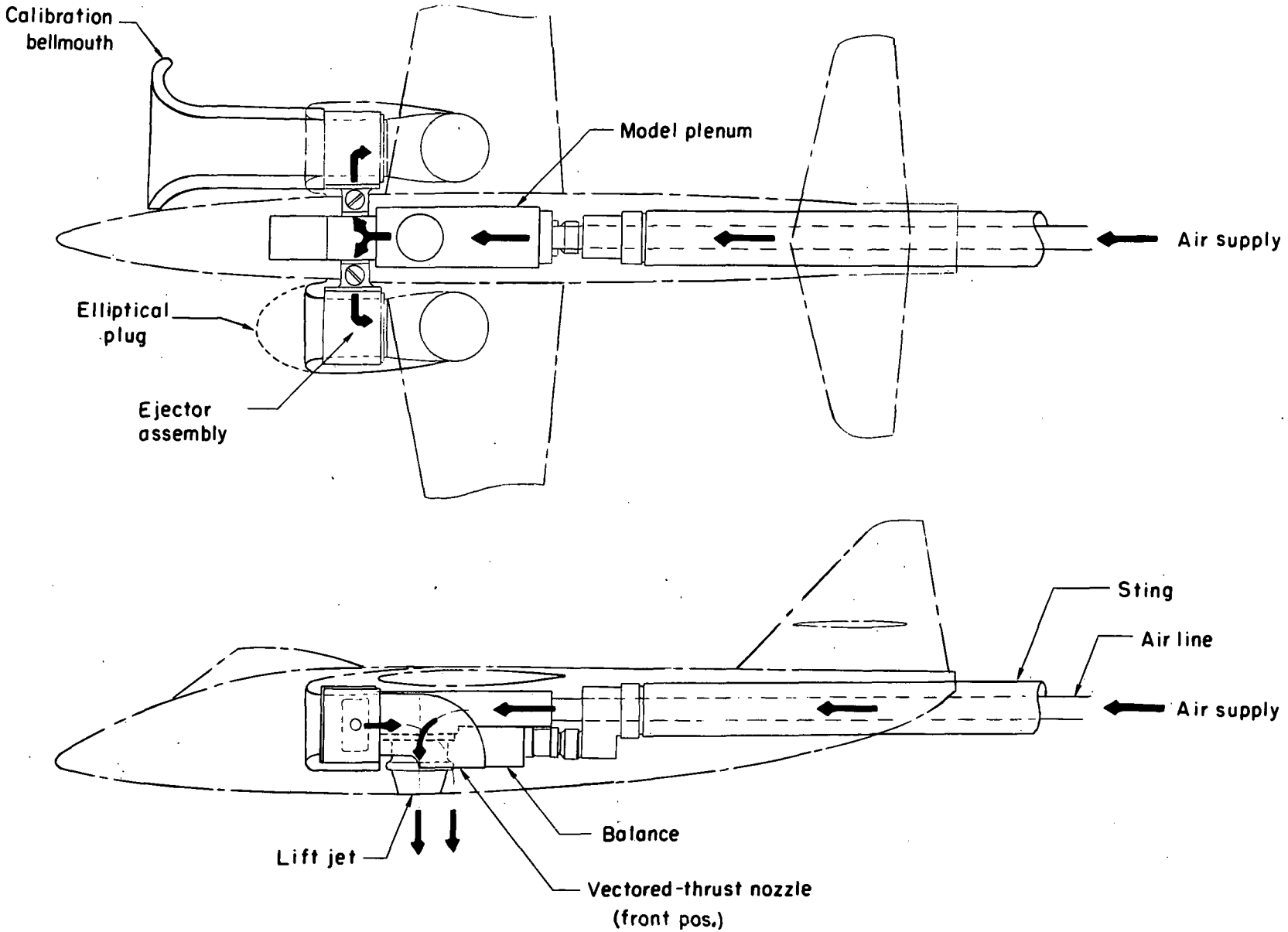
(a) Three-view drawing of front nozzle and lift-jet configuration with flaps.

Figure 2.- Details of model. All dimensions are in centimeters (inches) unless otherwise noted. FRL denotes fuselage reference line.



(b) Sketch of rear vectored-thrust configuration (N_2).

Figure 2.- Continued.



(c) Sketch of high-pressure air system used to simulate jet thrust.

Figure 2.- Concluded.

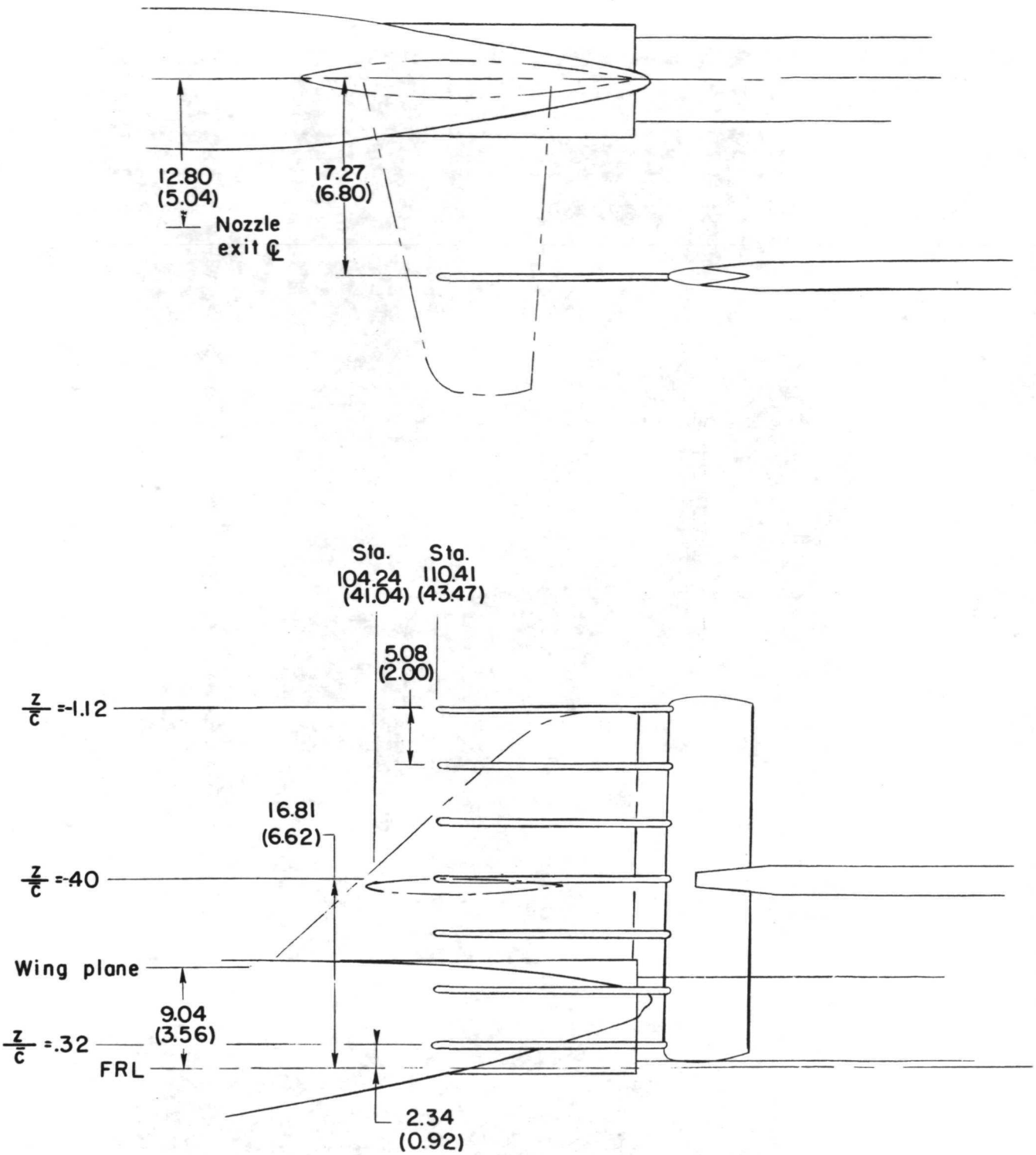
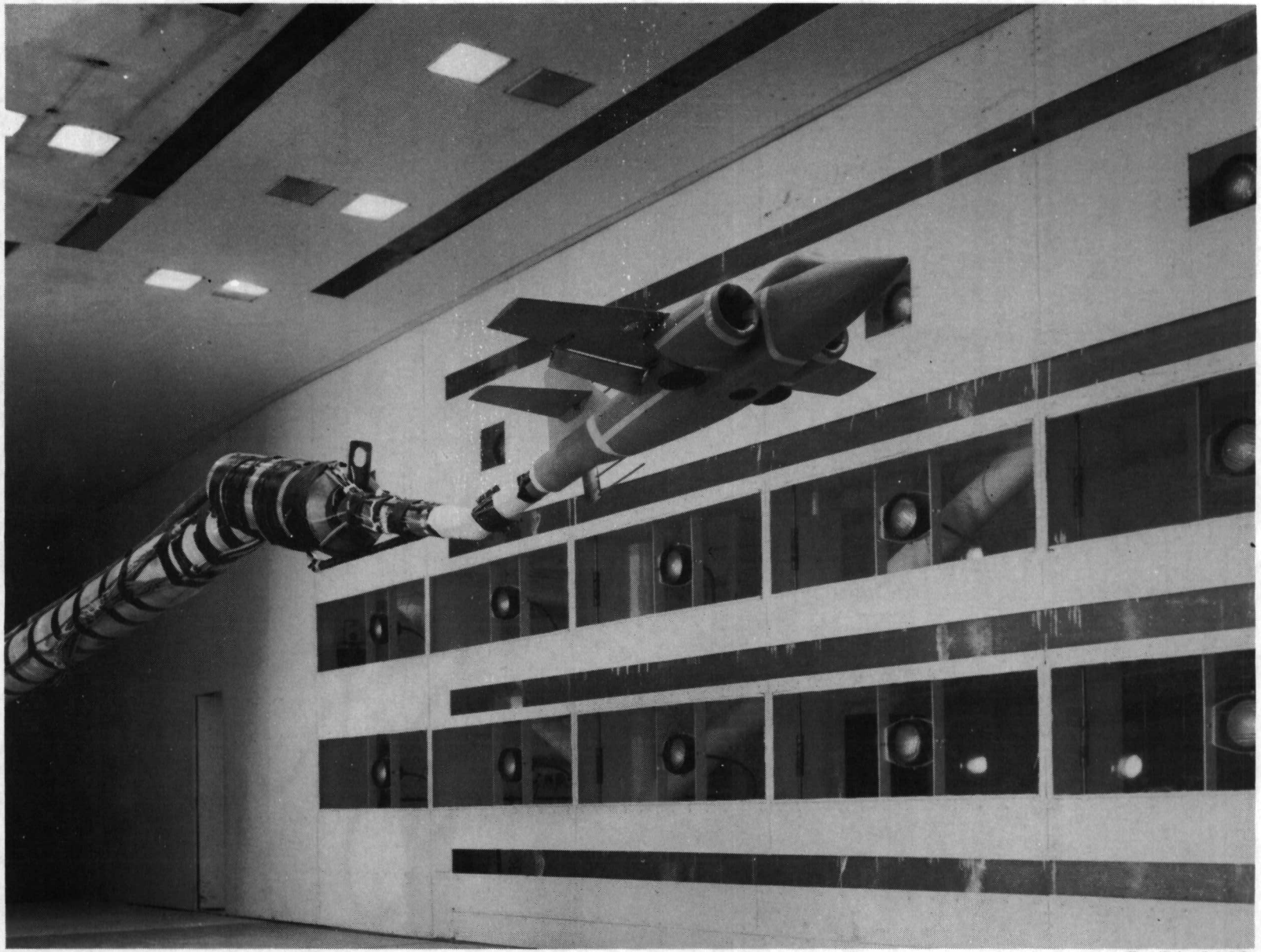


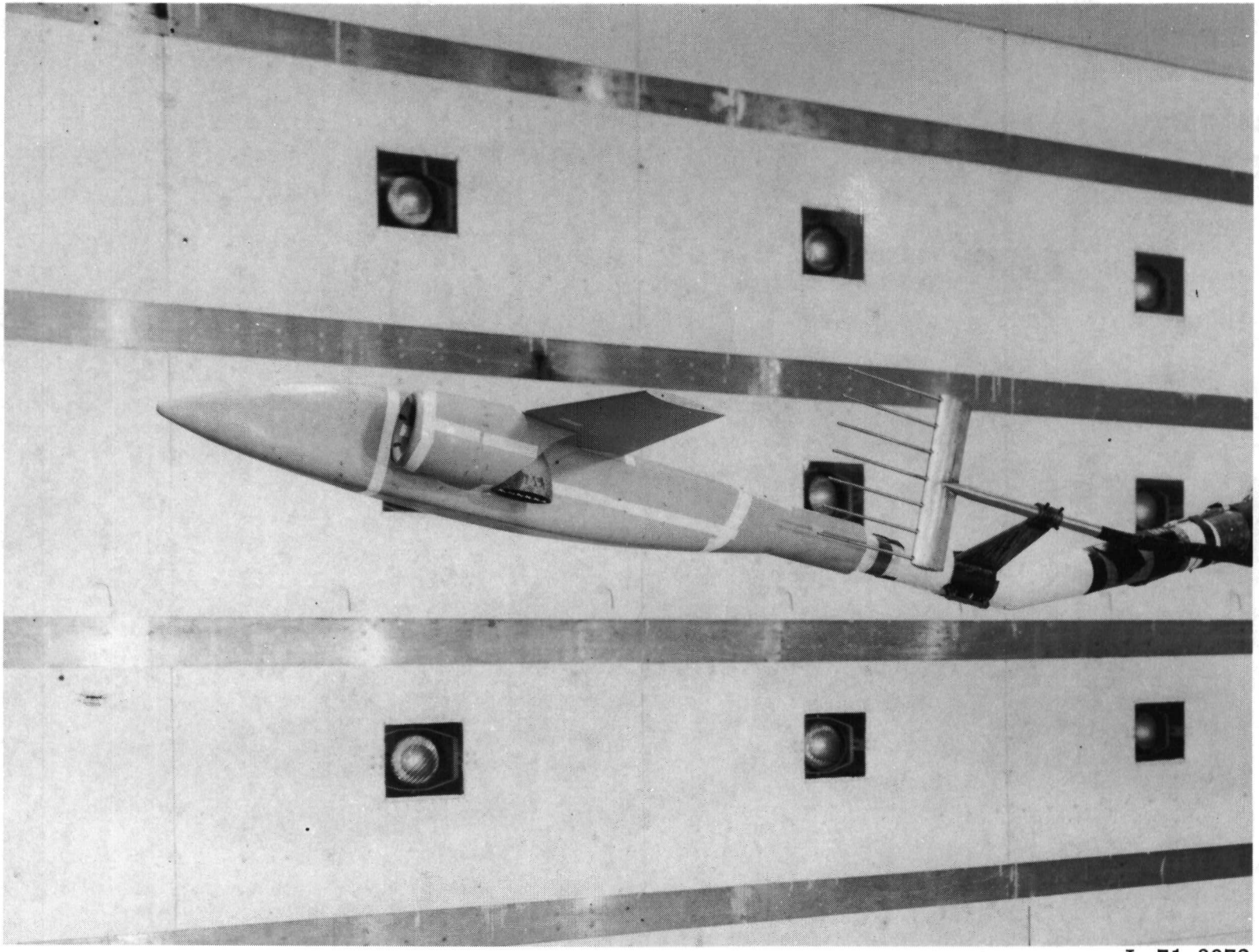
Figure 3.- Sketch of rake position relative to model. Dimensions are in centimeters (inches). FRL denotes fuselage reference line.



L-71-3069

(a) Model in Langley V/STOL tunnel.

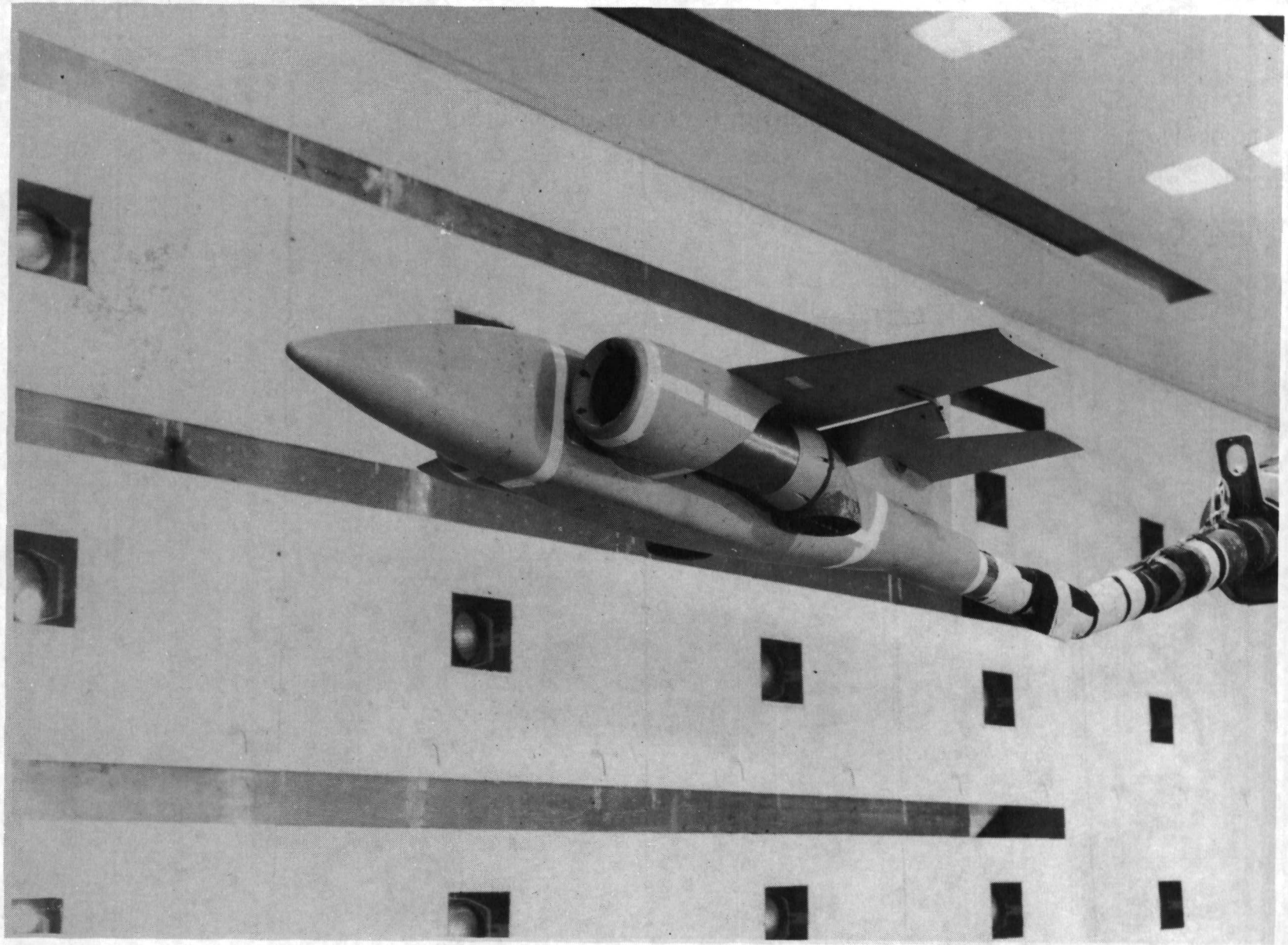
Figure 4.- Model photographs.



L-71-3072

(b) Front 90° nozzles with rake.

Figure 4.- Continued.



(c) Rear 90° nozzles with flaps. L-71-3212

Figure 4.- Concluded.

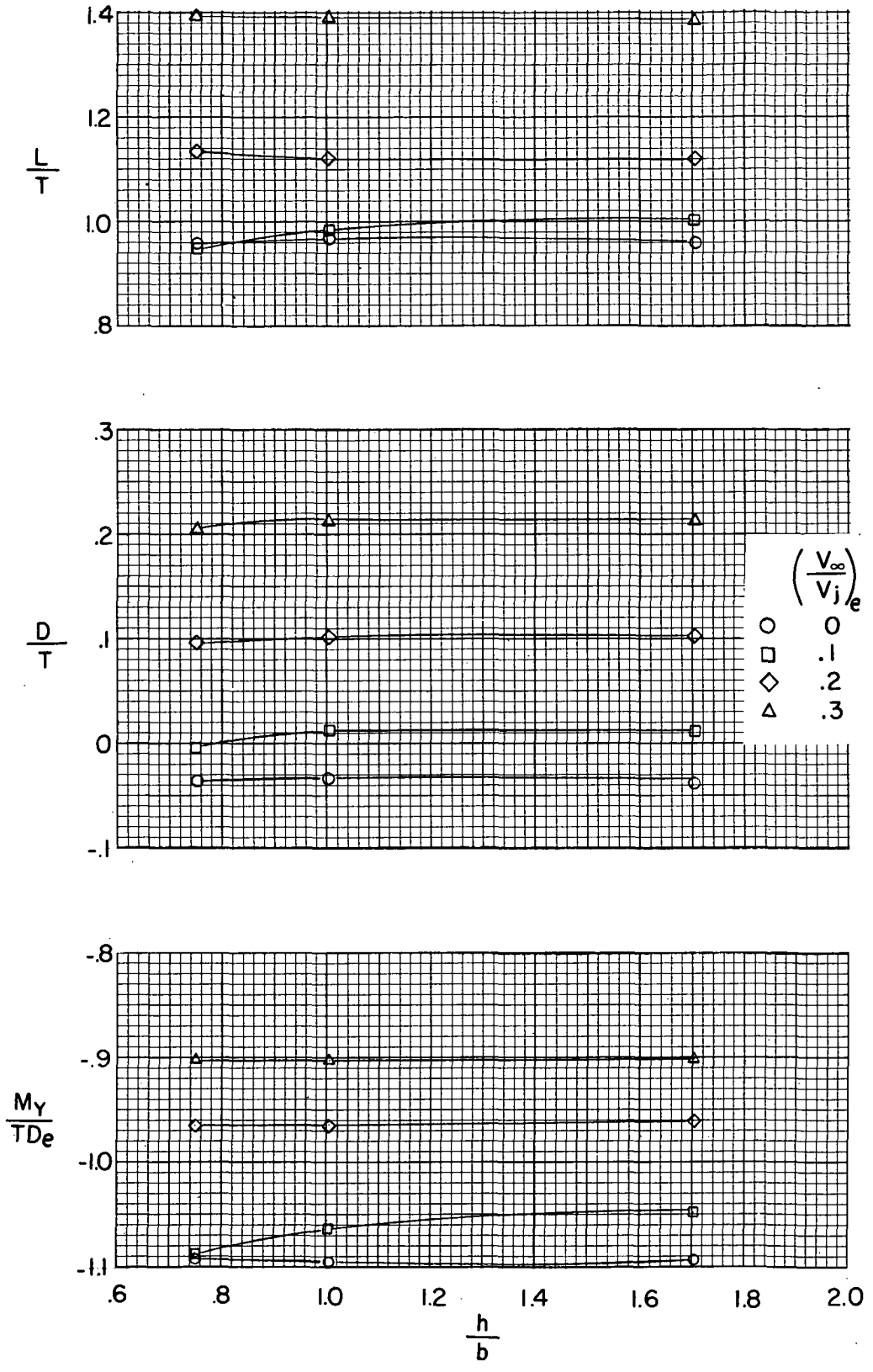


Figure 5.- Variation of longitudinal aerodynamic characteristics with height at an angle of attack of 6° for $BWN_1 90$ configuration with 11.43-cm-diameter (4.50-in.) exits.

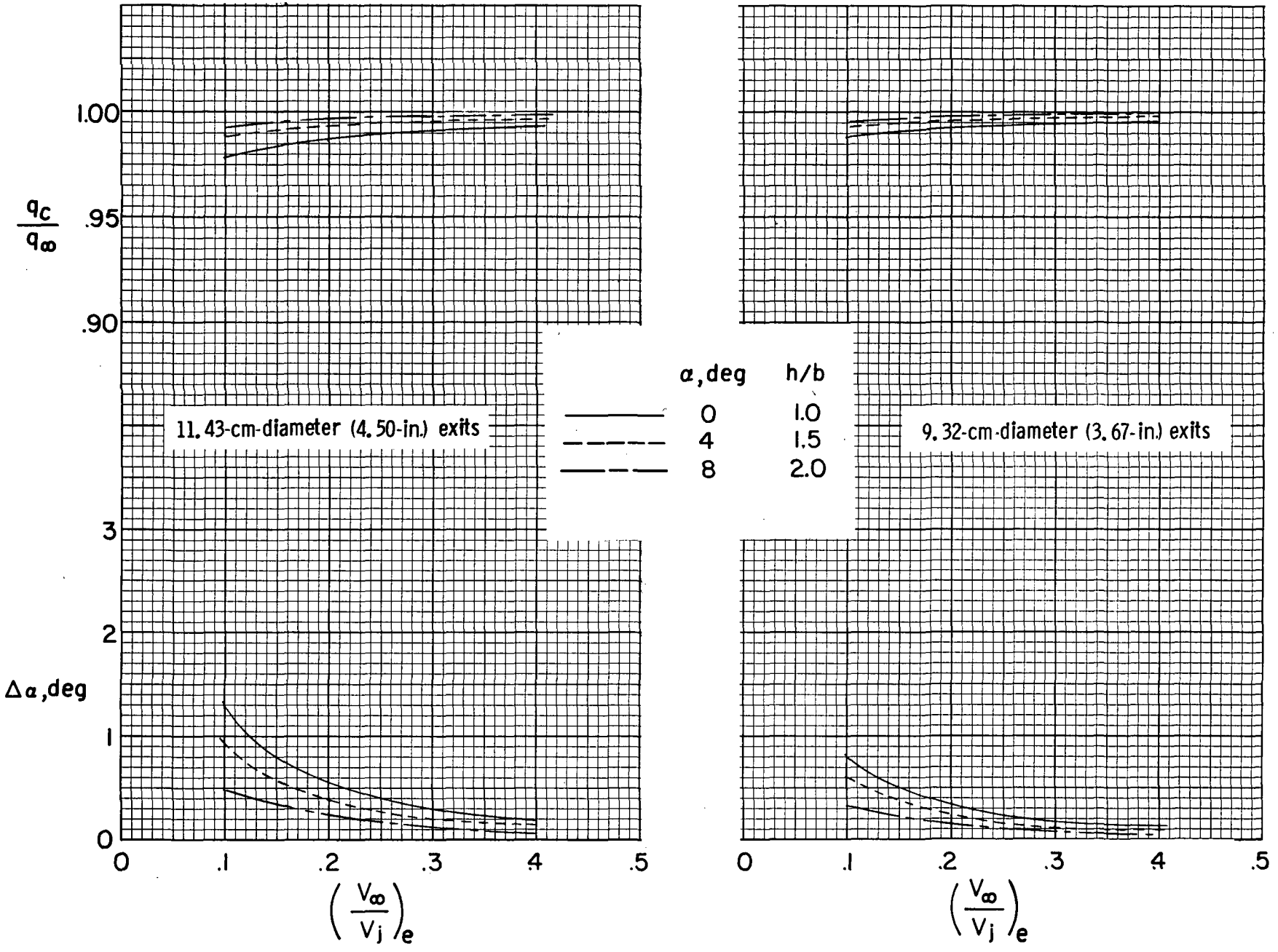


Figure 6.- Corrections to free-stream dynamic pressure and angle of attack for $BWN_2 90$ configuration.

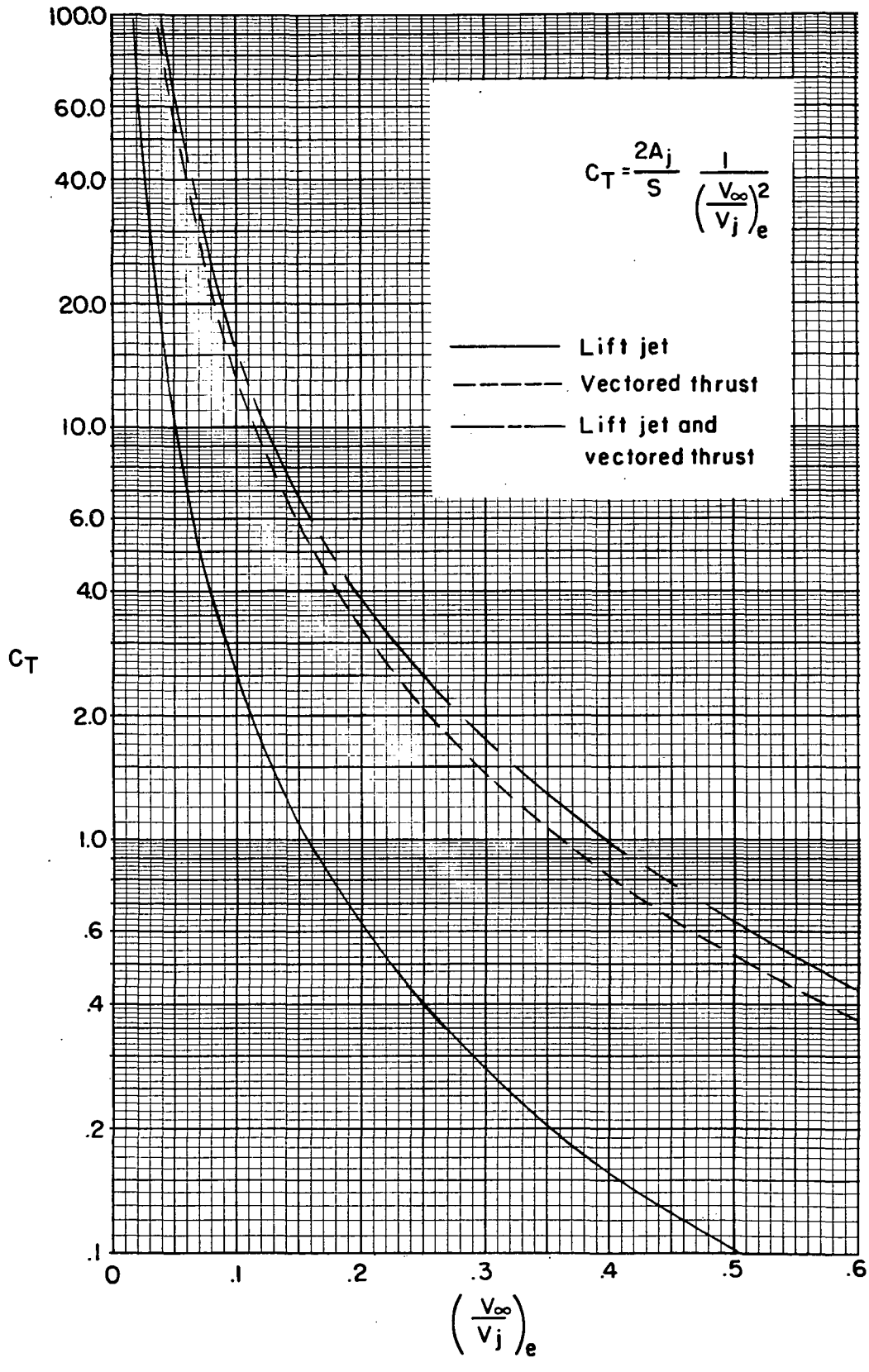
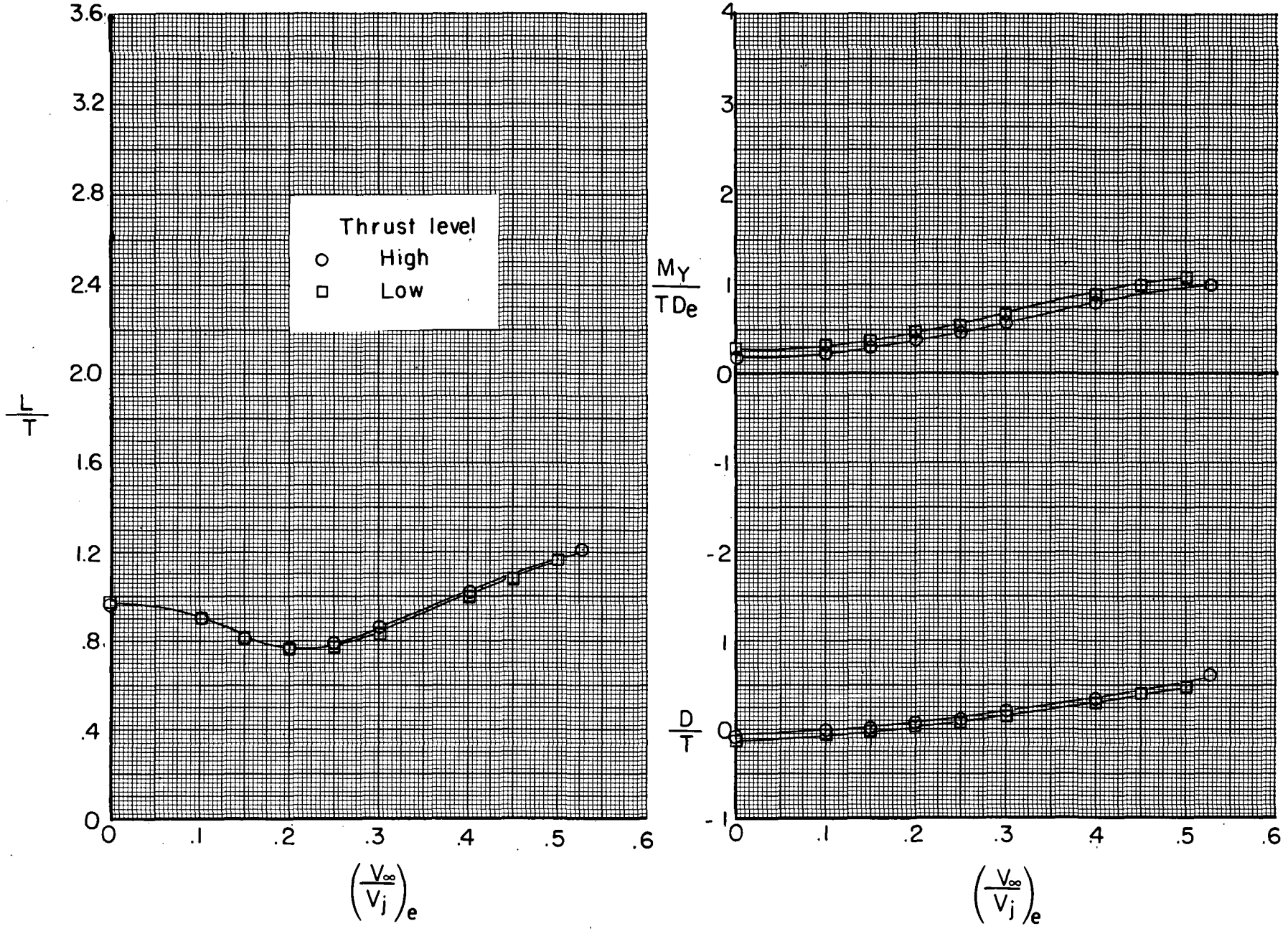
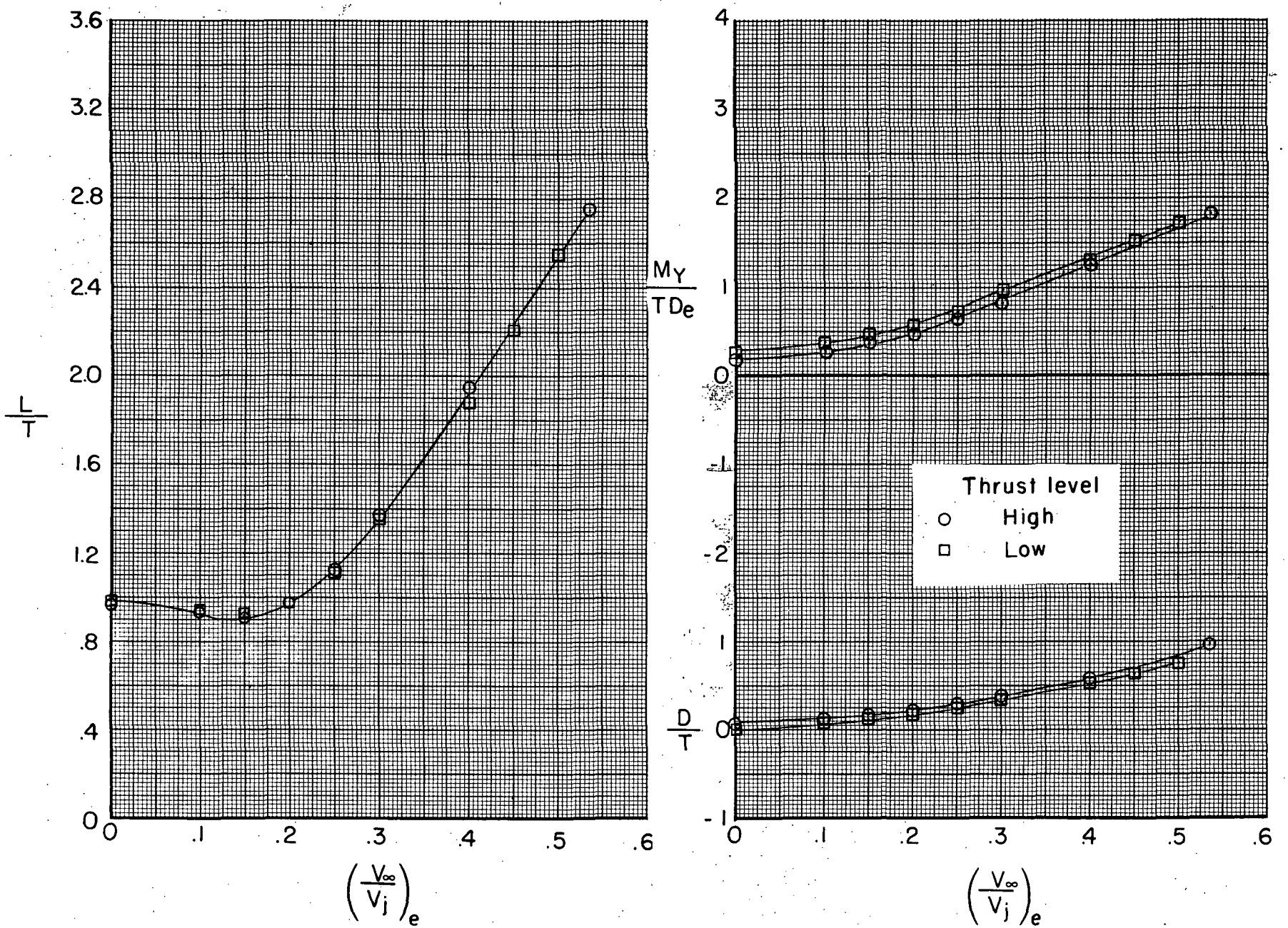


Figure 7.- Thrust coefficient as a function of effective velocity ratio.



(a) $\alpha \approx 0^o$.

Figure 8.- Effect of thrust level on longitudinal characteristics for BWN_190 configuration.



(b) $\alpha \approx 10^{\circ}$.

Figure 8.- Concluded.

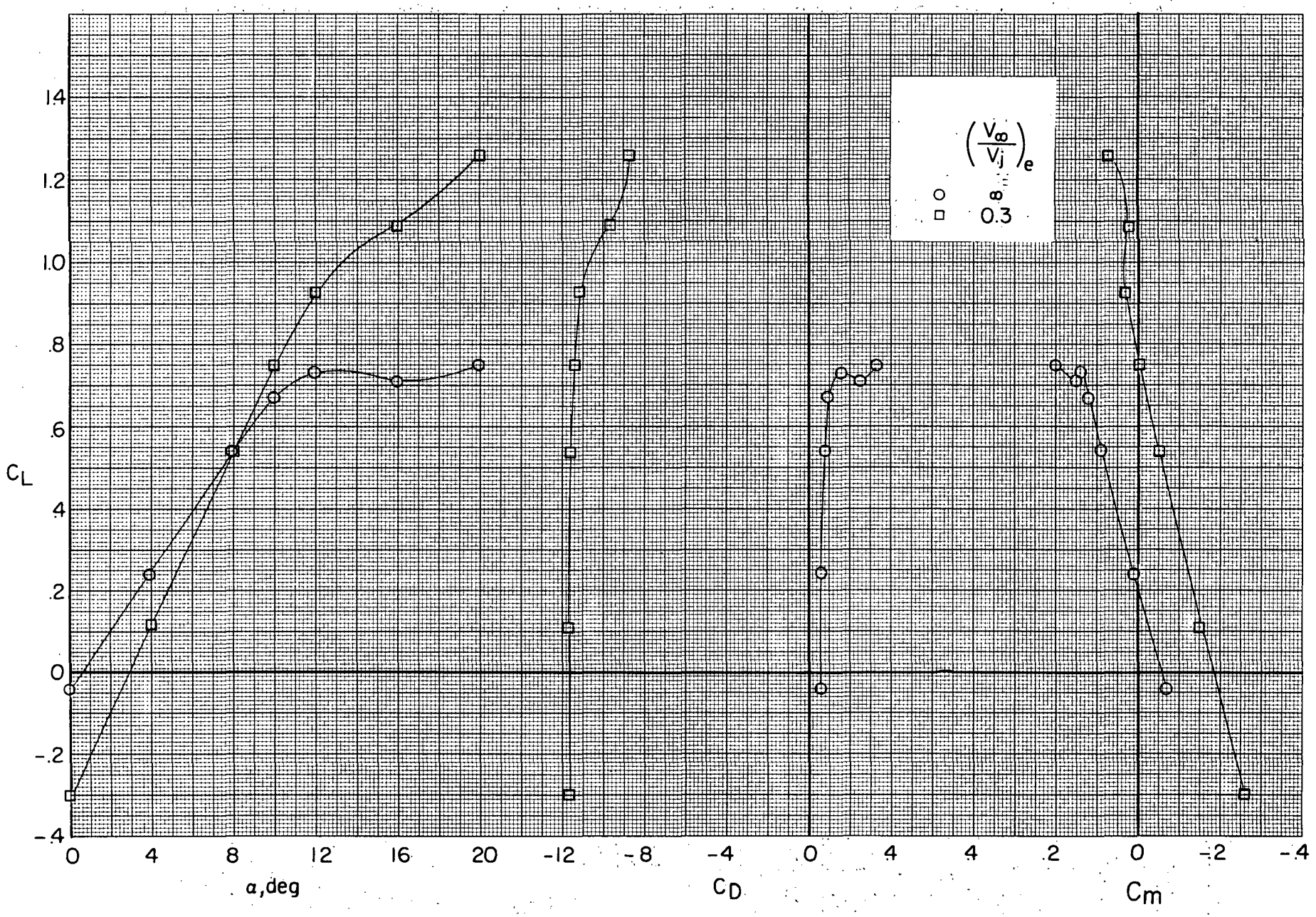


Figure 9.- Longitudinal aerodynamic characteristics for cruise $BWN_1 0$ configuration with and without power.

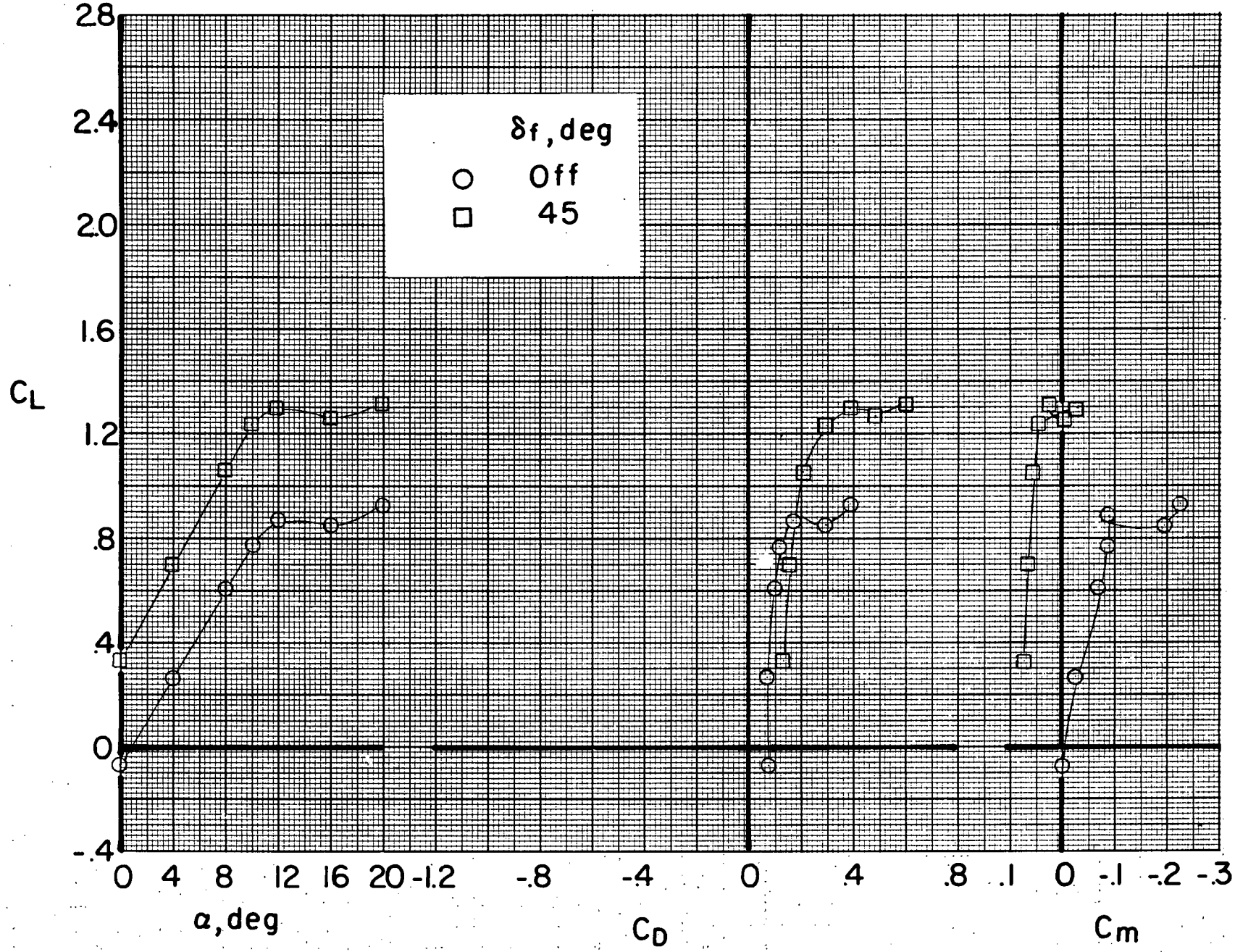


Figure 10.- Longitudinal aerodynamic characteristics of cruise configuration. $BWN_1 0VHf$; $\left(V_\infty/V_j\right)_e = \infty$.

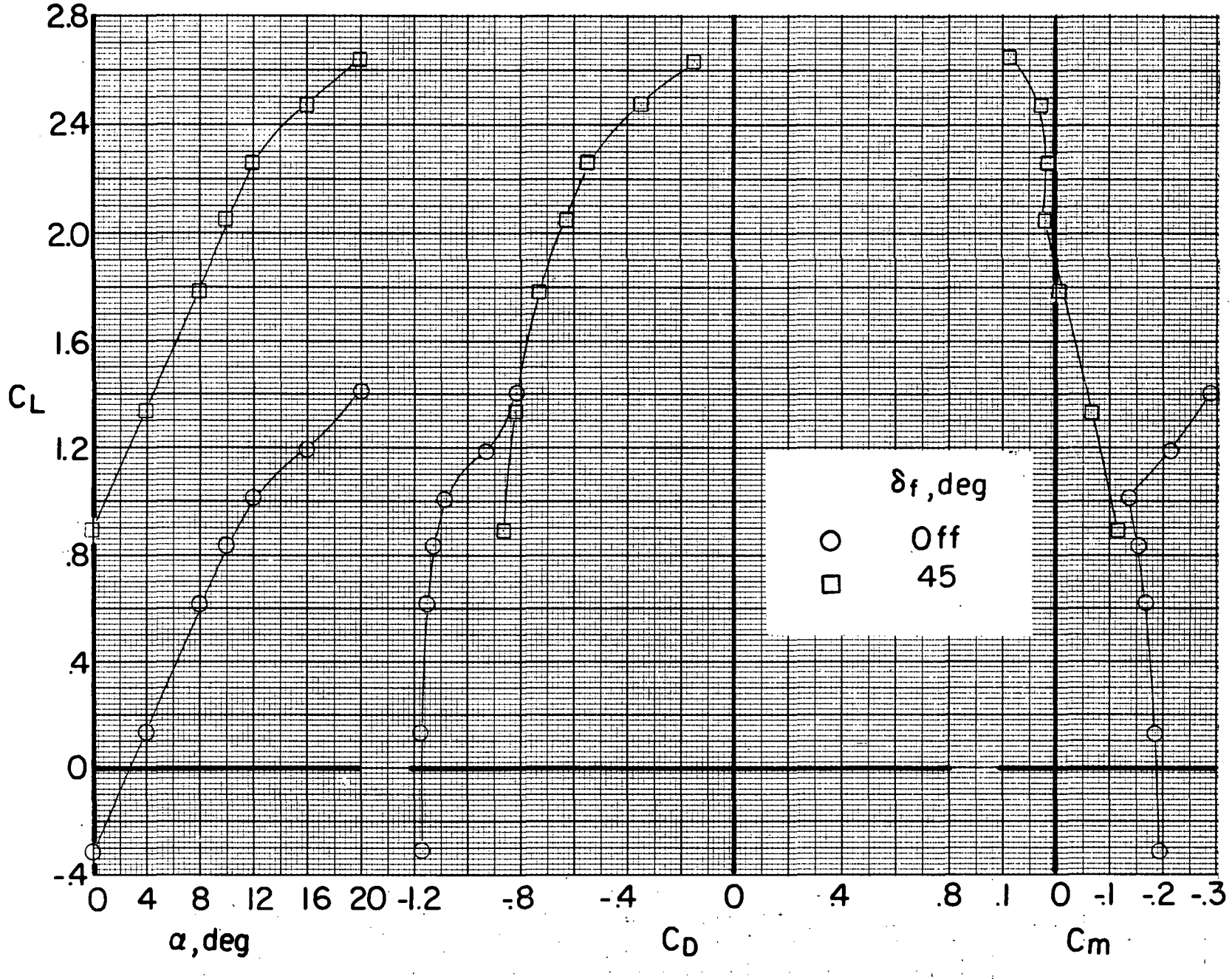
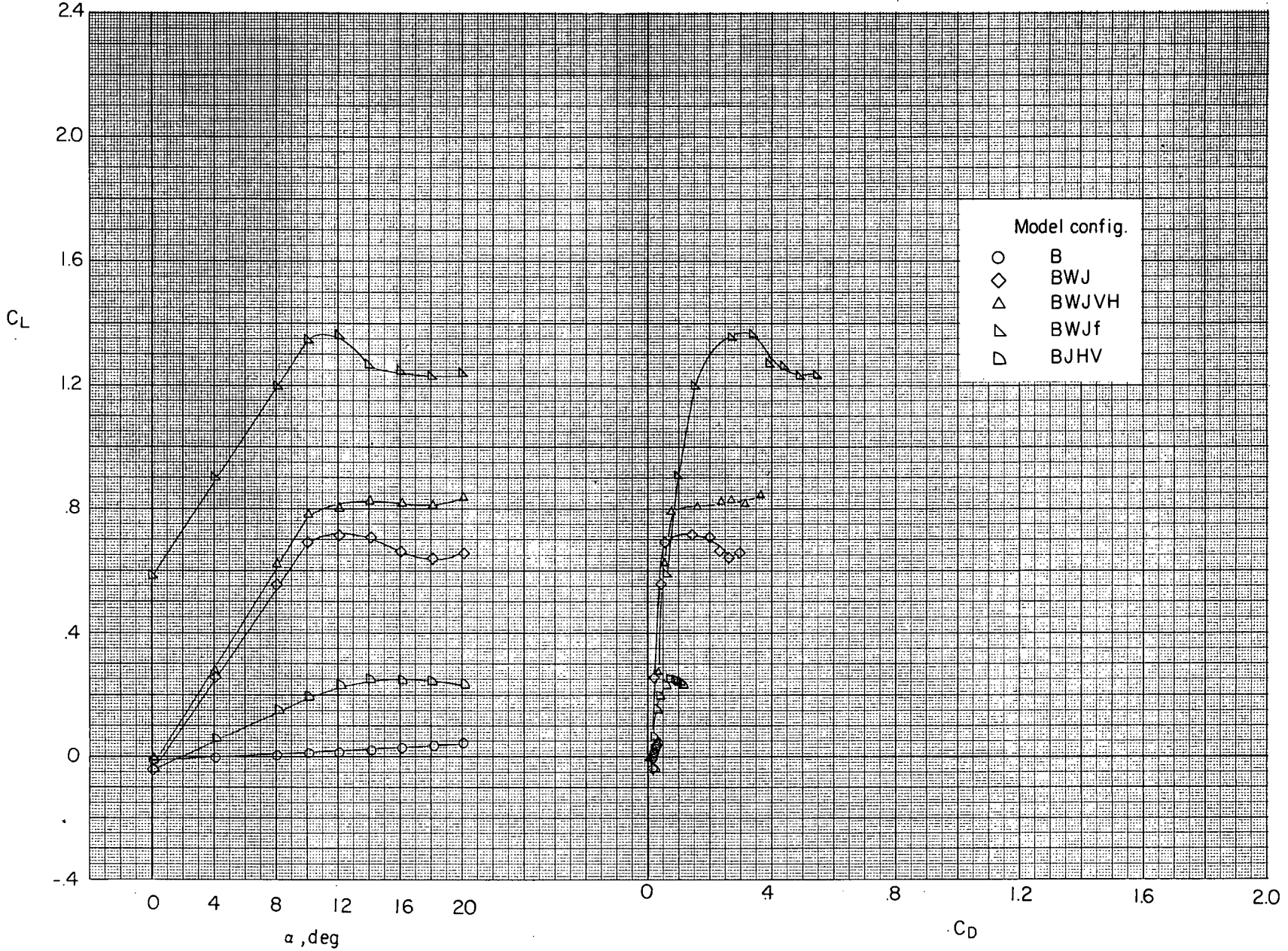
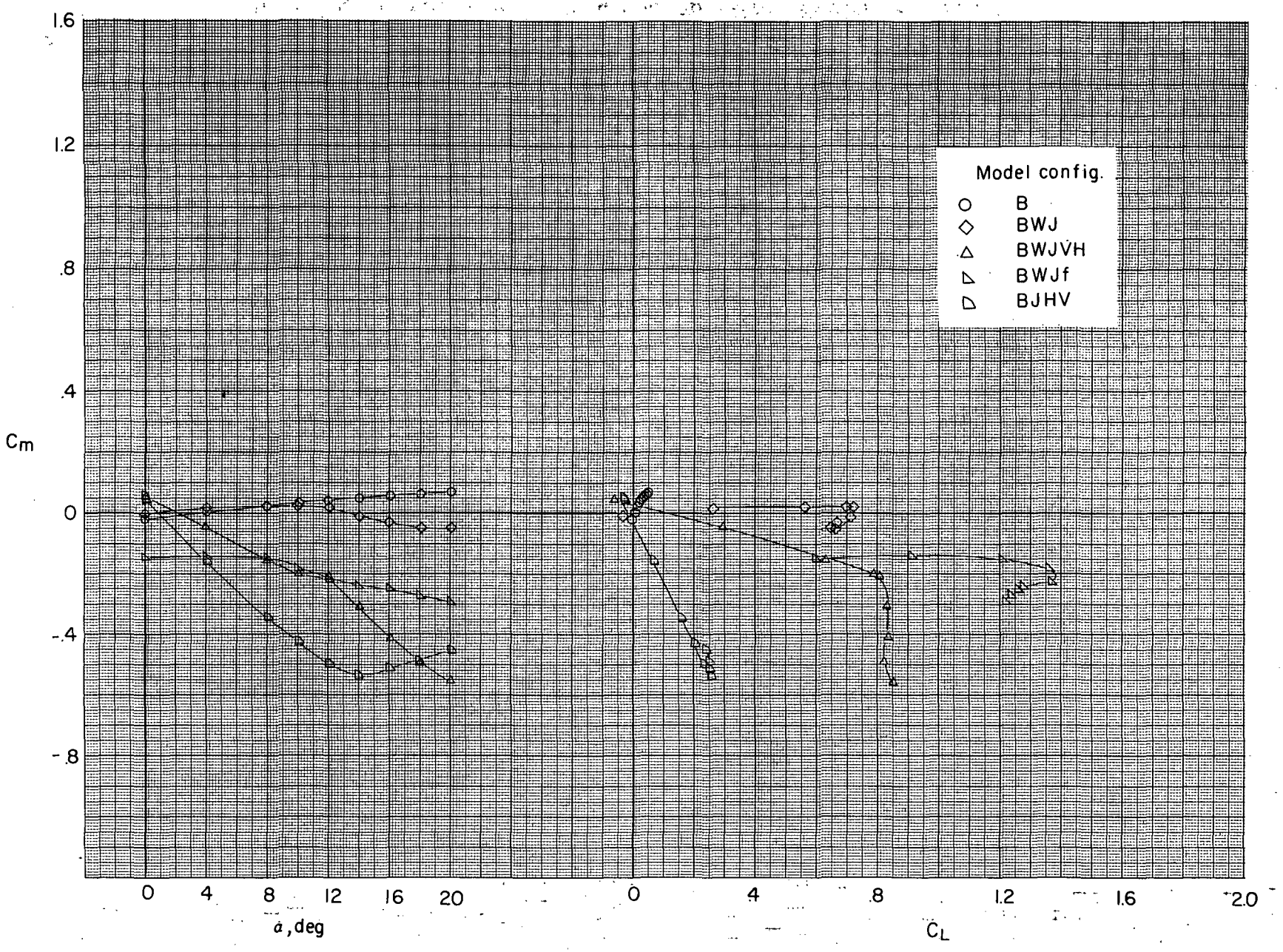


Figure 11.- Longitudinal aerodynamic characteristics of cruise configuration. $BWN_1 0VHf$; $\left(V_\infty/V_j\right)_e = 0.3$.



(a) Variation of C_L with α and C_D.

Figure 12.- Effect of model components on longitudinal aerodynamic characteristics of lift-jet configuration without power. $\left(V_\infty/V_j\right)_e = \infty$.



(b) Variation of C_m with α and C_L.

Figure 12.- Concluded.

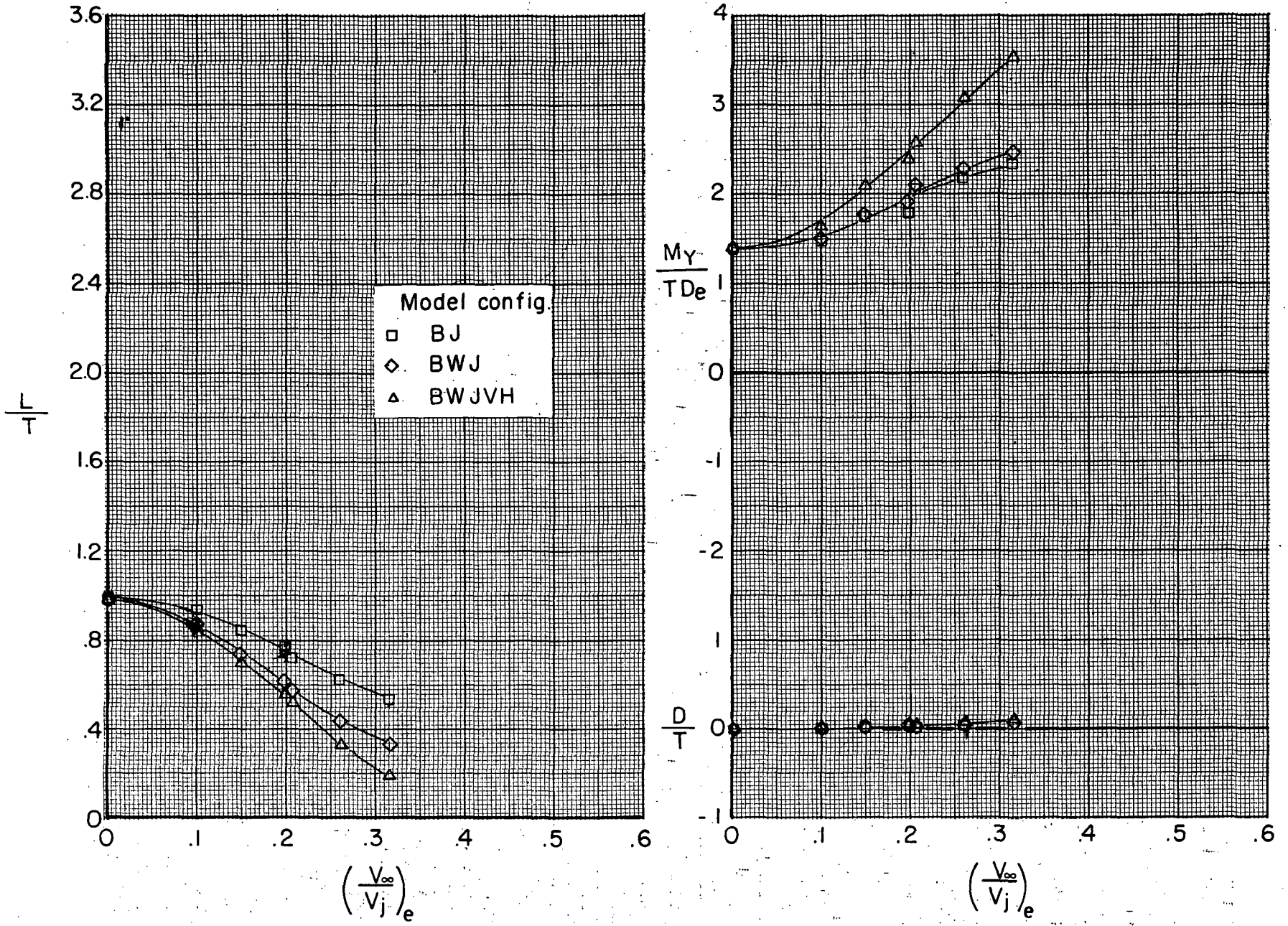


Figure 13.- Effect of model components on longitudinal aerodynamic characteristics of lift-jet configuration at an angle of attack of 0^{o} through an effective velocity ratio range.

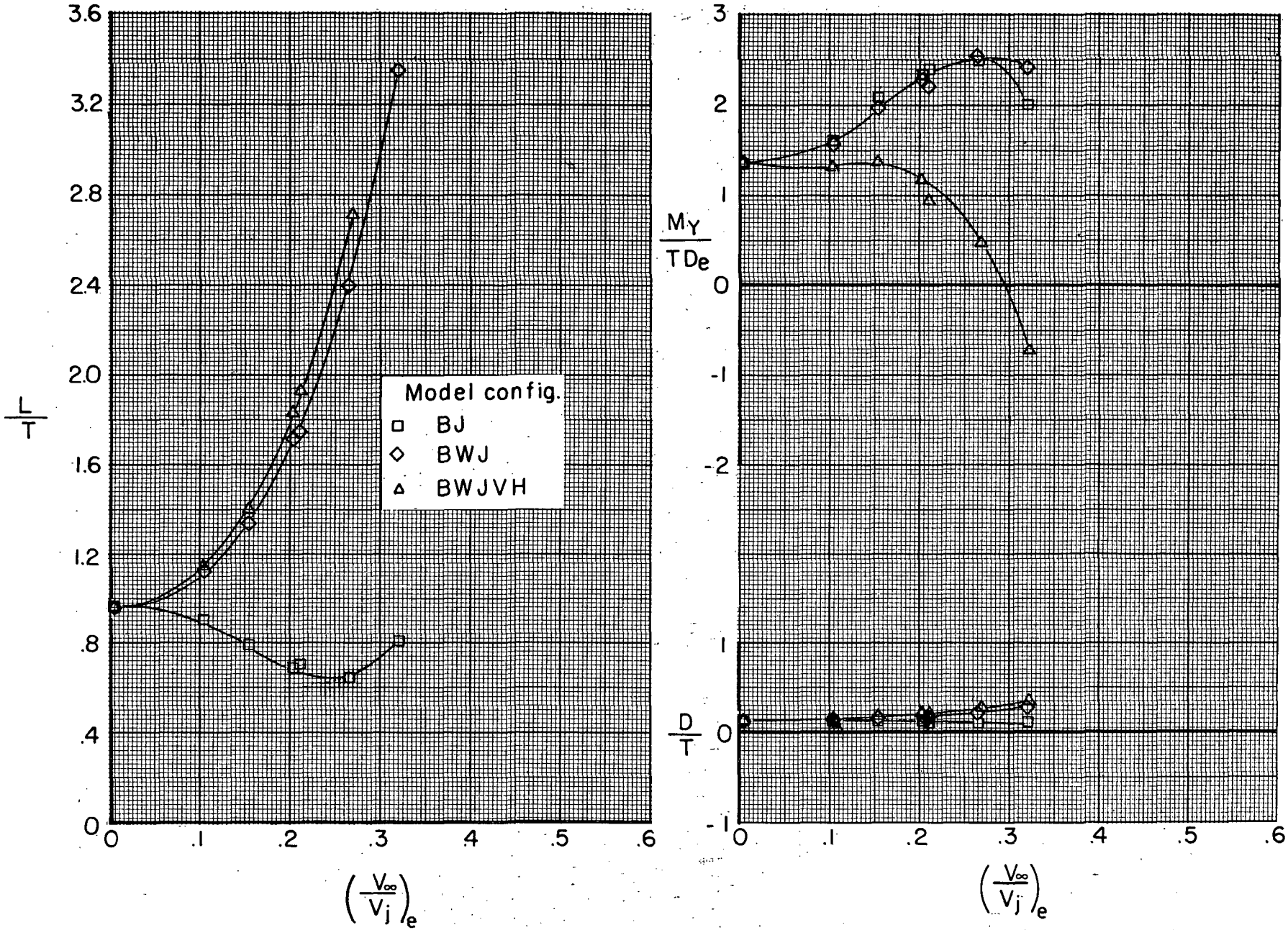
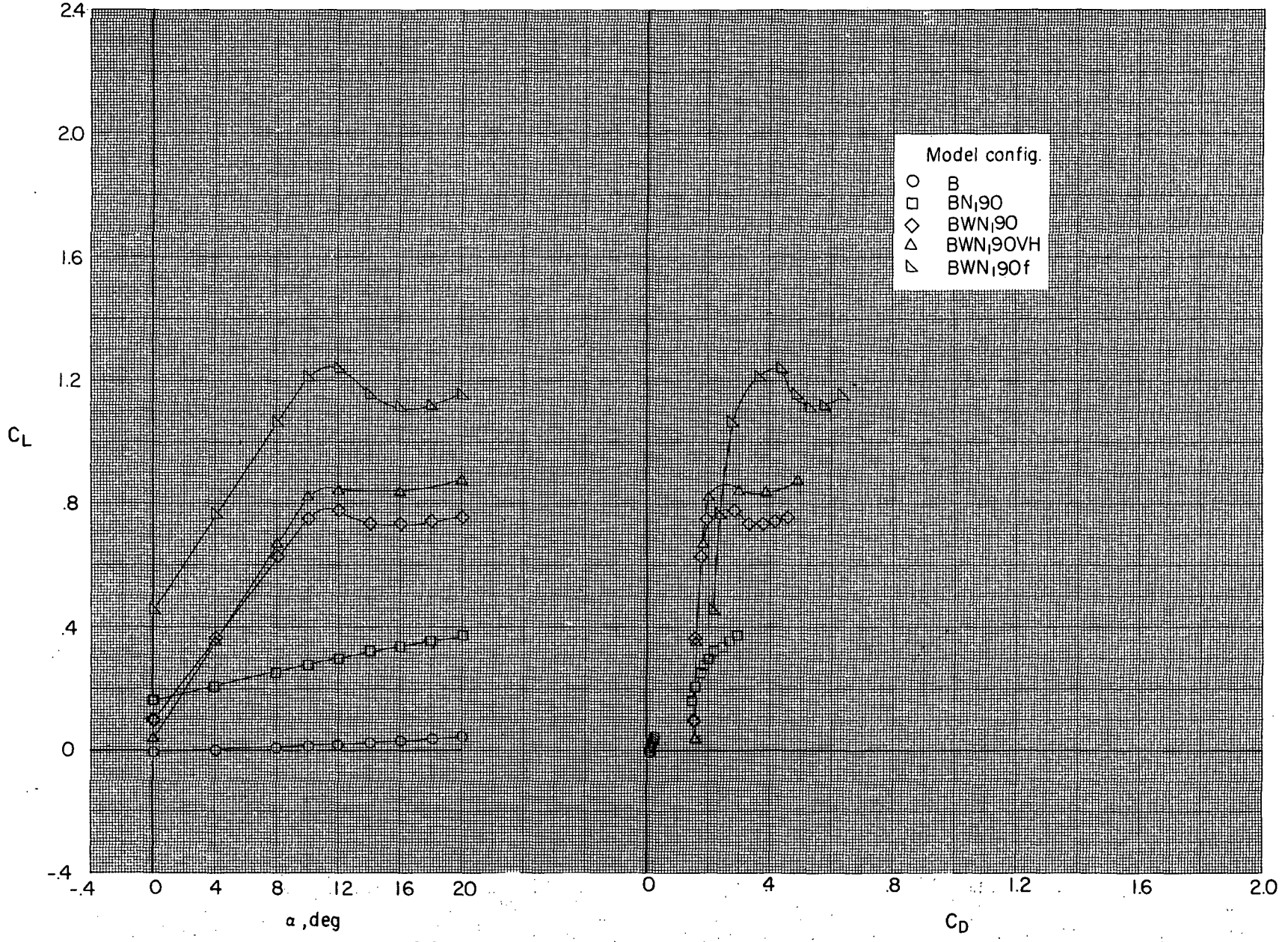
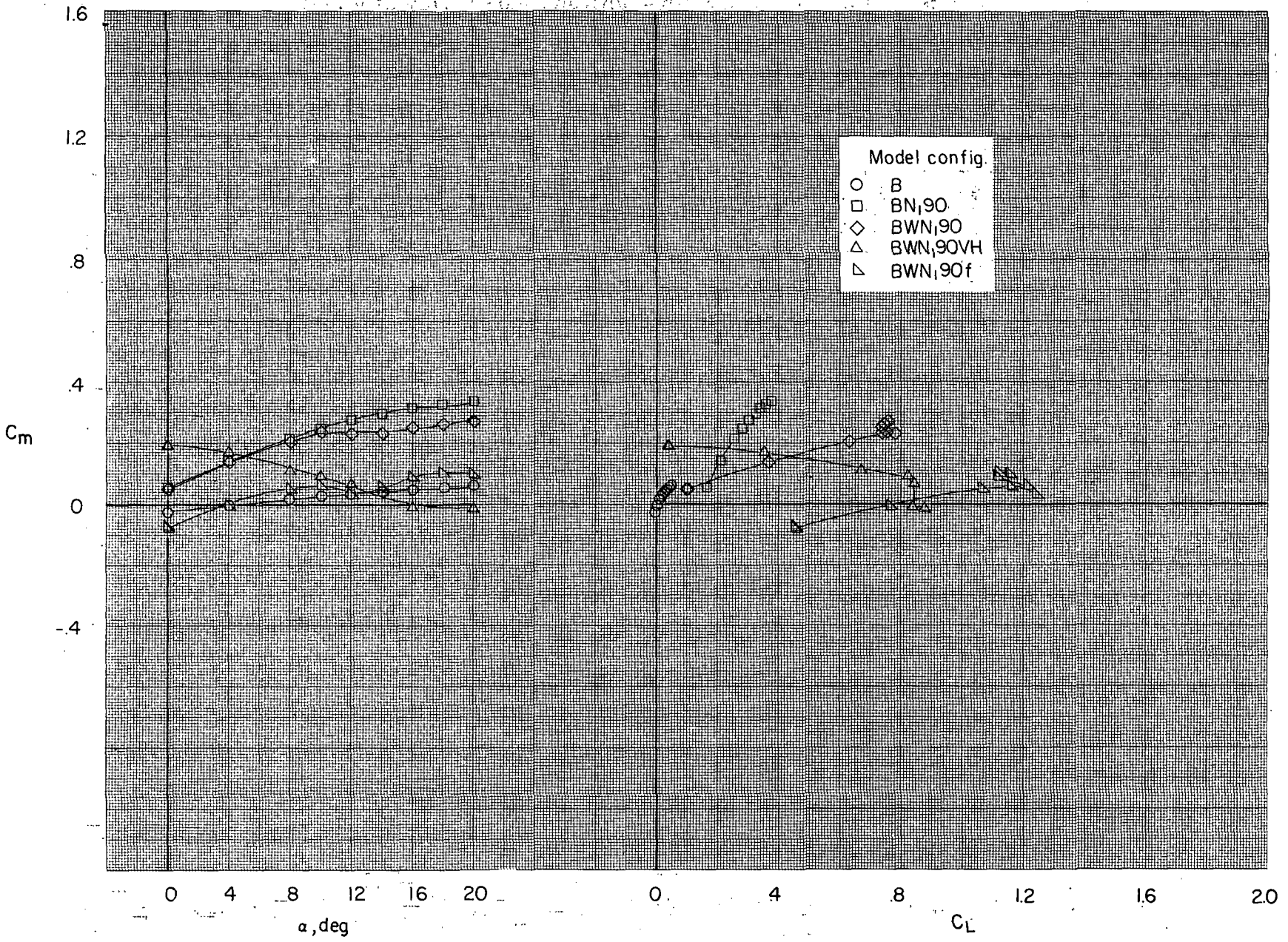


Figure 14.- Effect of model components on longitudinal aerodynamic characteristics of lift-jet configuration at an angle of attack of 10^{o} through an effective velocity ratio range.



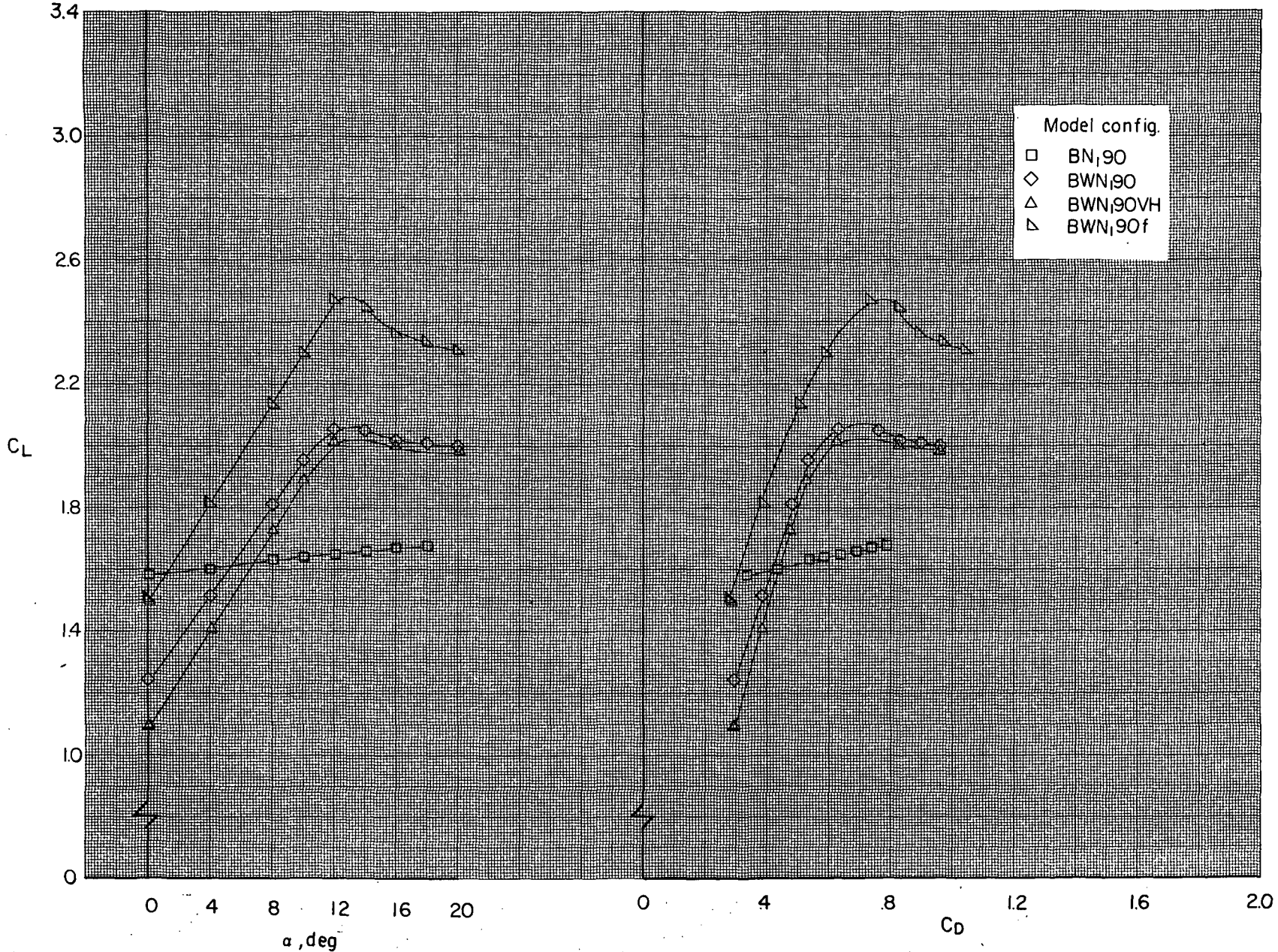
(a) Variation of C_L with α and C_D.

Figure 15.- Effect of model components on longitudinal aerodynamic characteristics of front vectored-thrust configuration without power. $\left(V_\infty/V_j\right)_e = \infty$.



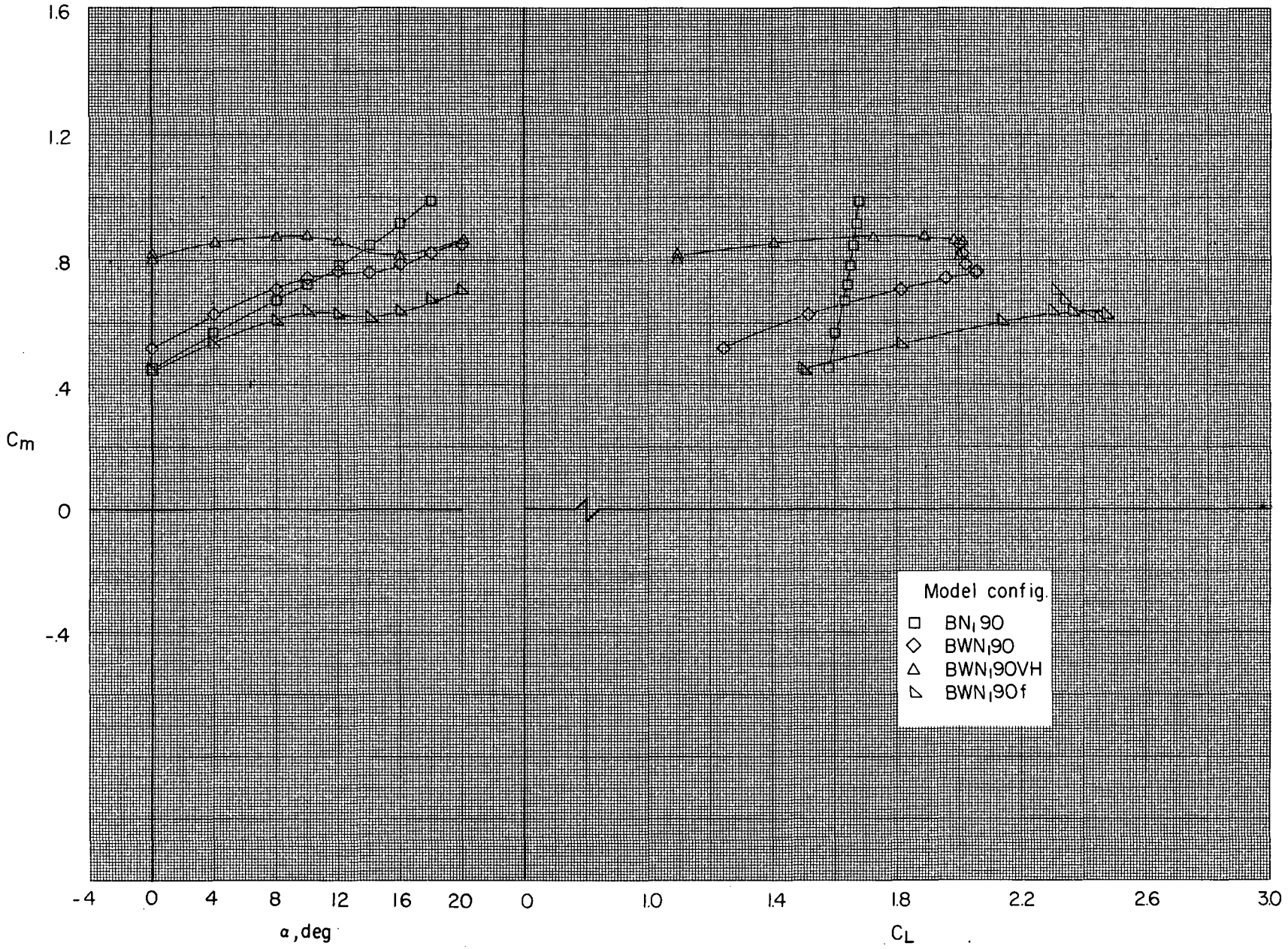
(b) Variation of C_m with α and C_L.

Figure 15.- Concluded.



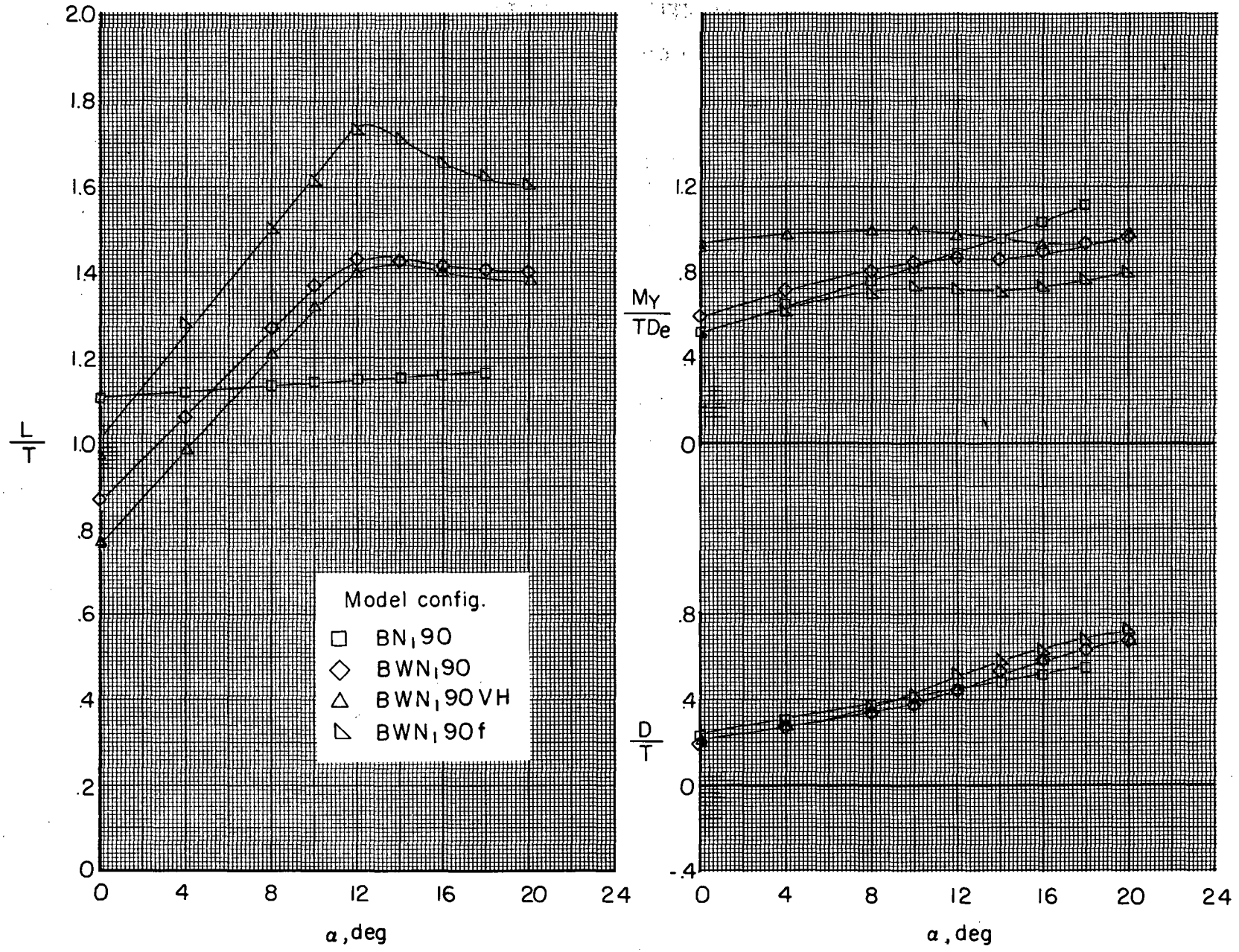
(a) Variation of C_L with α and C_D.

Figure 16.- Effect of model components on longitudinal aerodynamic characteristics of front vectored-thrust configuration with power. $\left(V_\infty/V_j\right)_e = 0.3$.



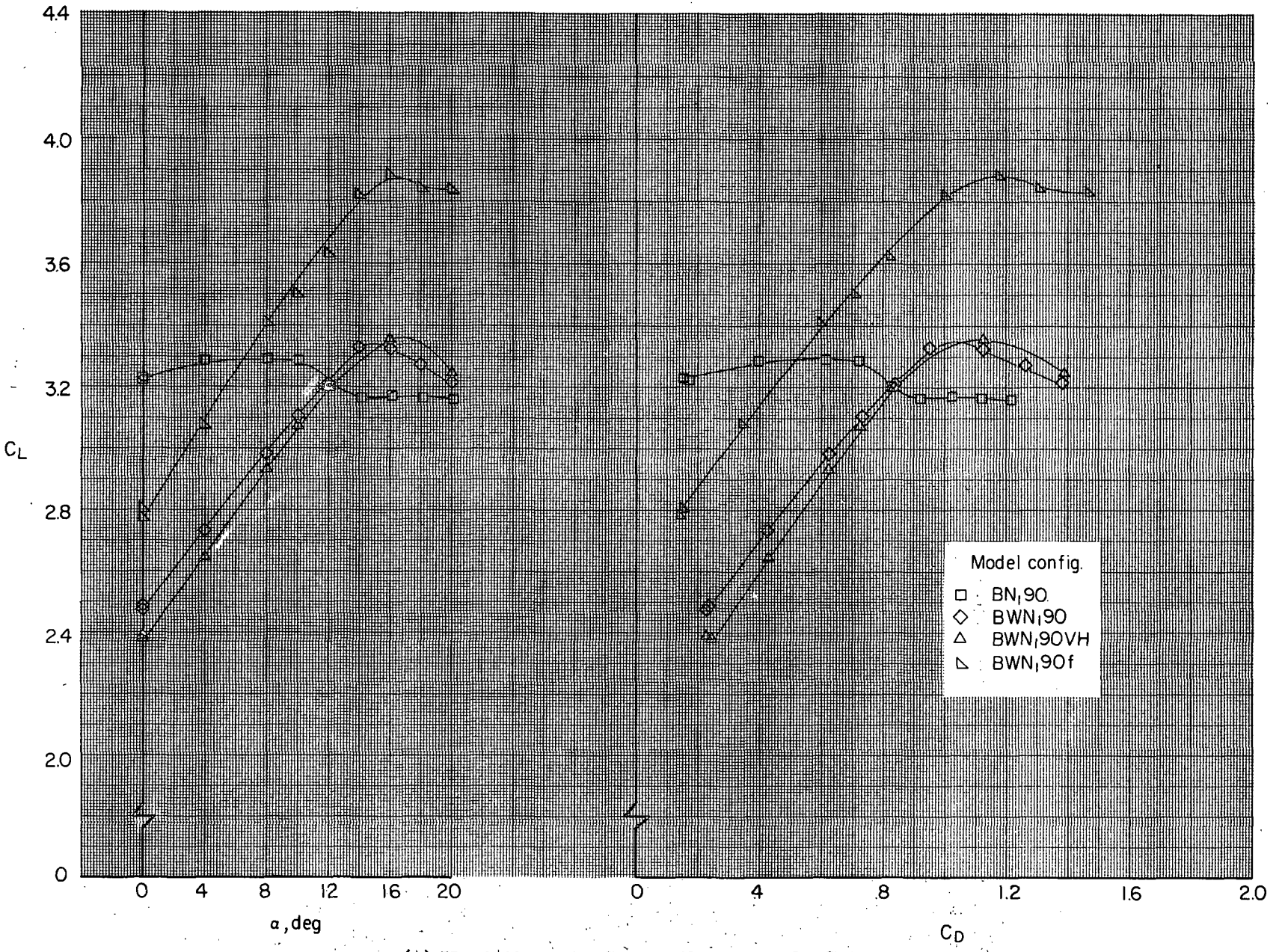
(b) Variation of C_m with α and C_L.

Figure 16.- Continued.



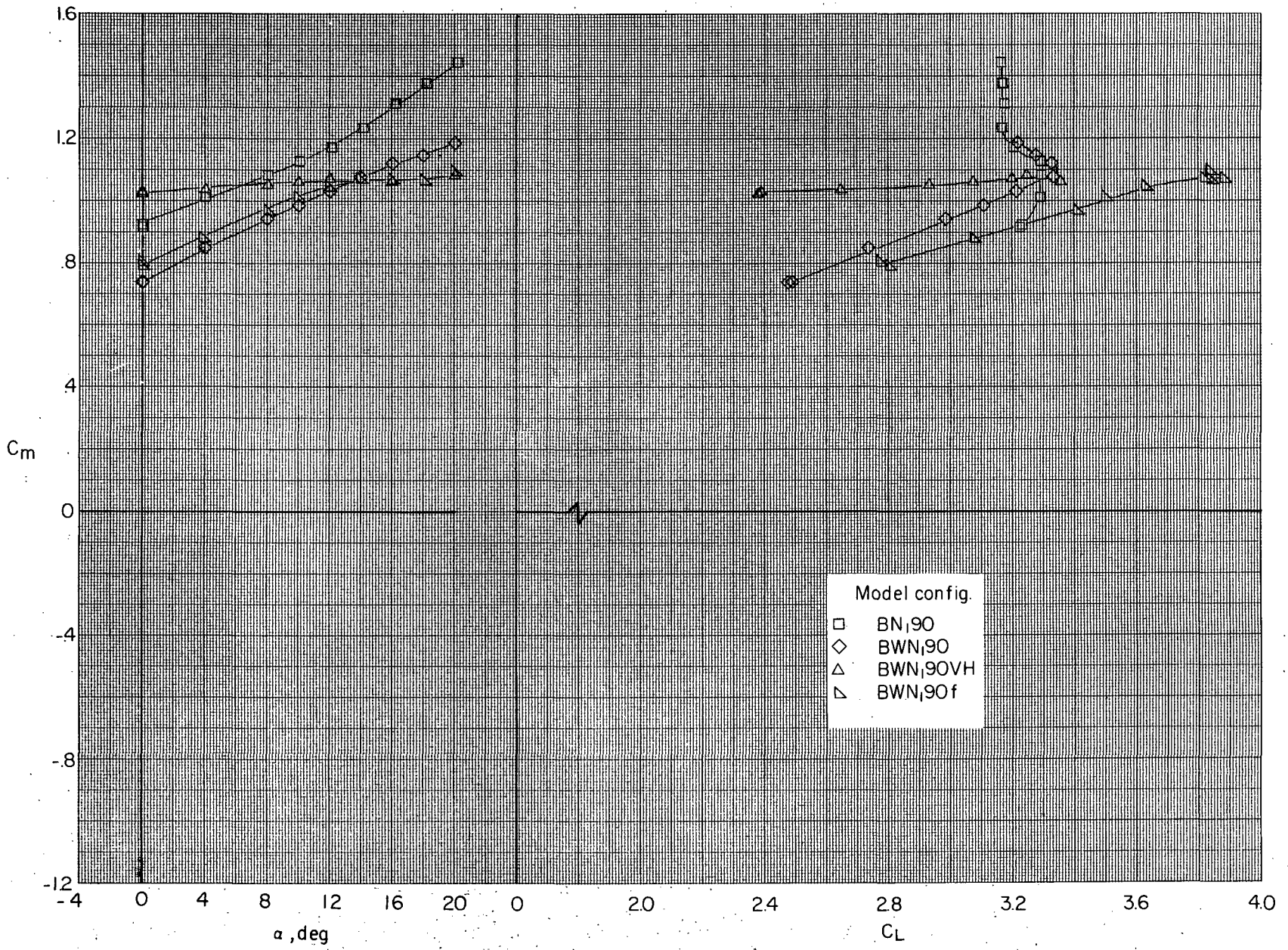
(c) Variation of L/T, D/T, and M_Y/TD_e with α.

Figure 16.- Concluded.



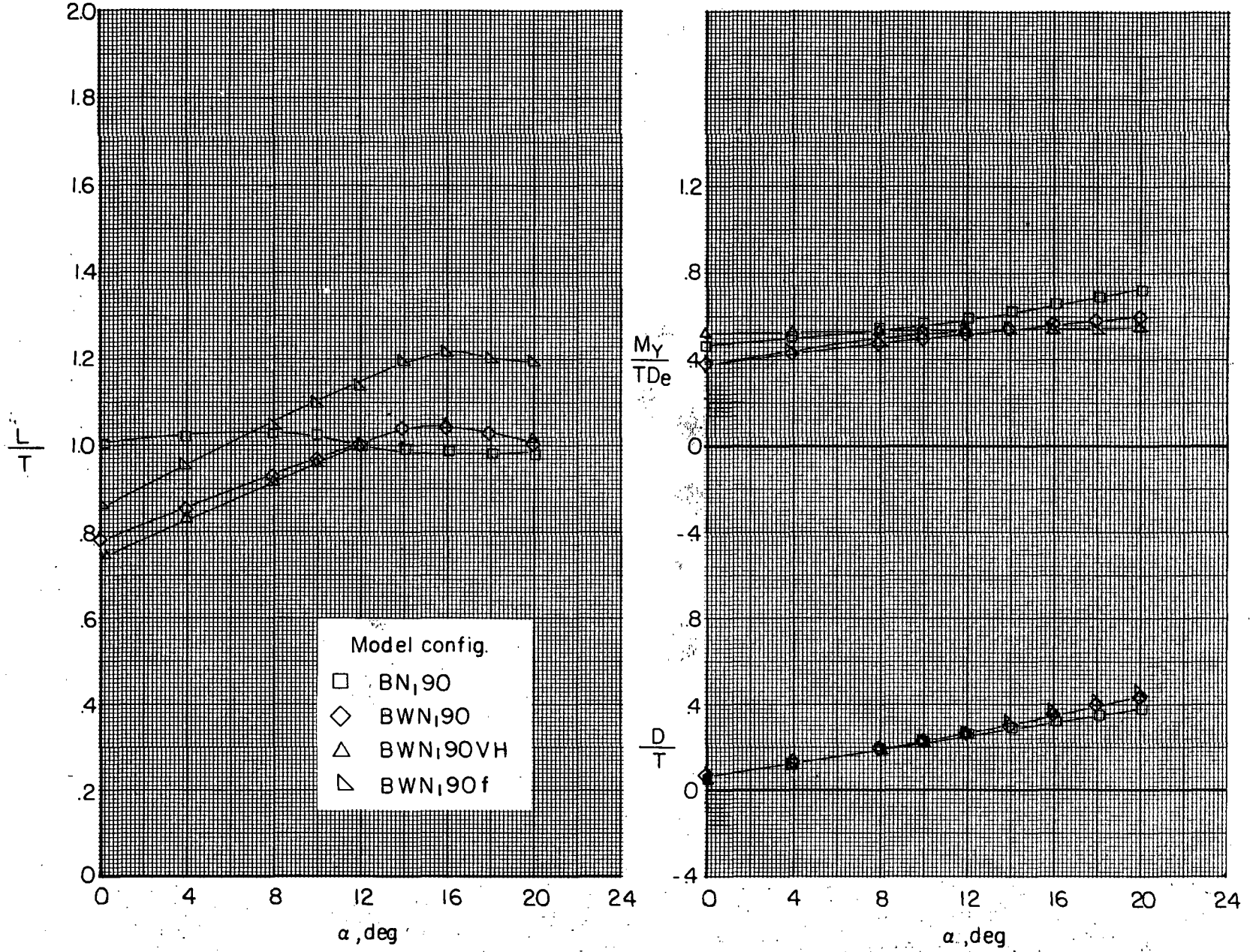
(a) Variation of C_L with α and C_D.

Figure 17.- Effect of model components on longitudinal aerodynamic characteristics of front vectored-thrust configuration with power. $\left(V_\infty/V_j\right)_e = 0.2$.



(b) Variation of C_m with α and C_L.

Figure 17.- Continued.



(c) Variation of L/T, D/T, and M_Y/TD_e with α.

Figure 17.- Concluded.

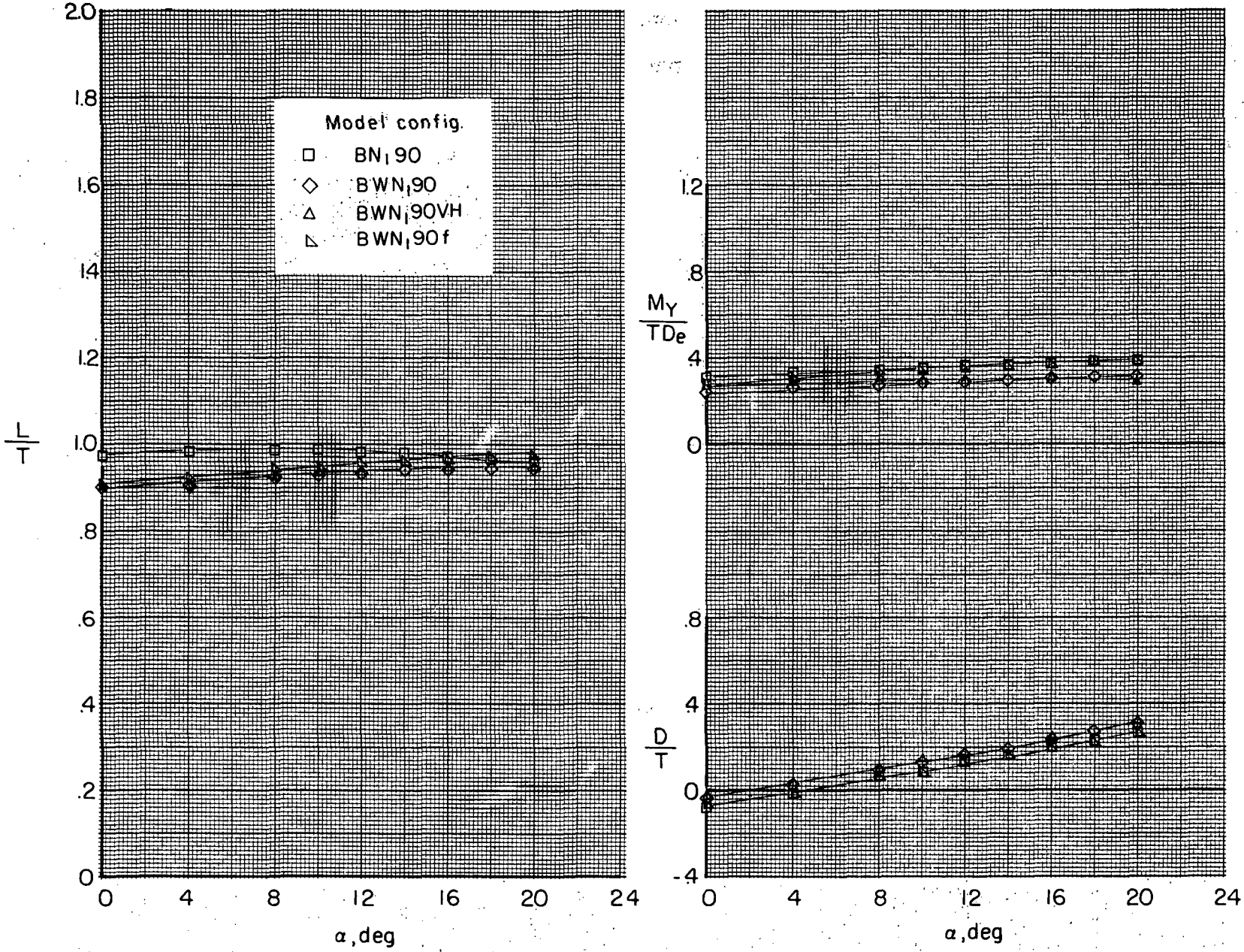


Figure 18.- Effect of model components on longitudinal aerodynamic characteristics of front vectored-thrust configuration with power. $\left(V_\infty/V_j\right)_e = 0.1$.

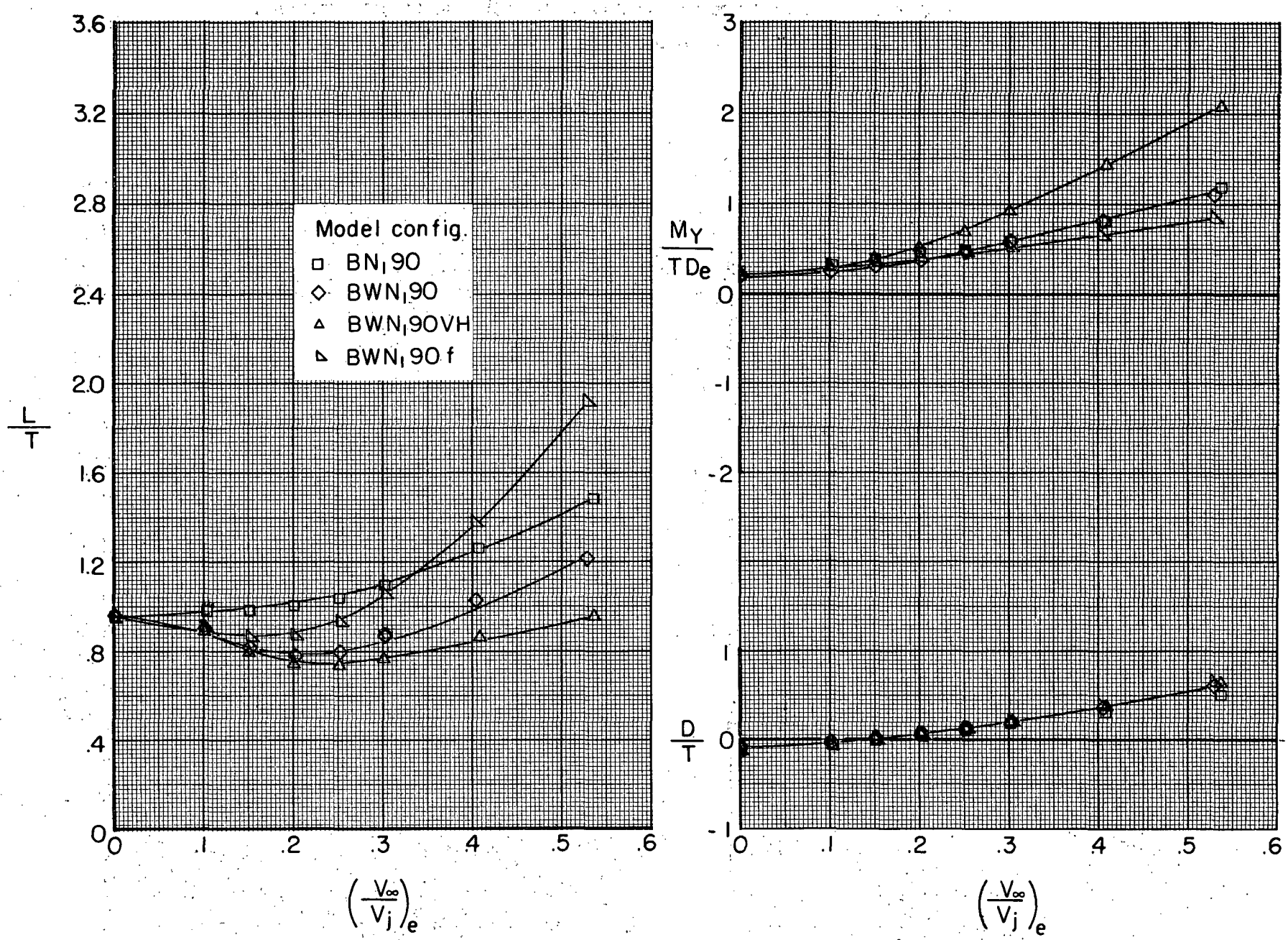


Figure 19.- Effect of model components on longitudinal aerodynamic characteristics of front vectored-thrust configuration with power at an angle of attack of 0^{o}.

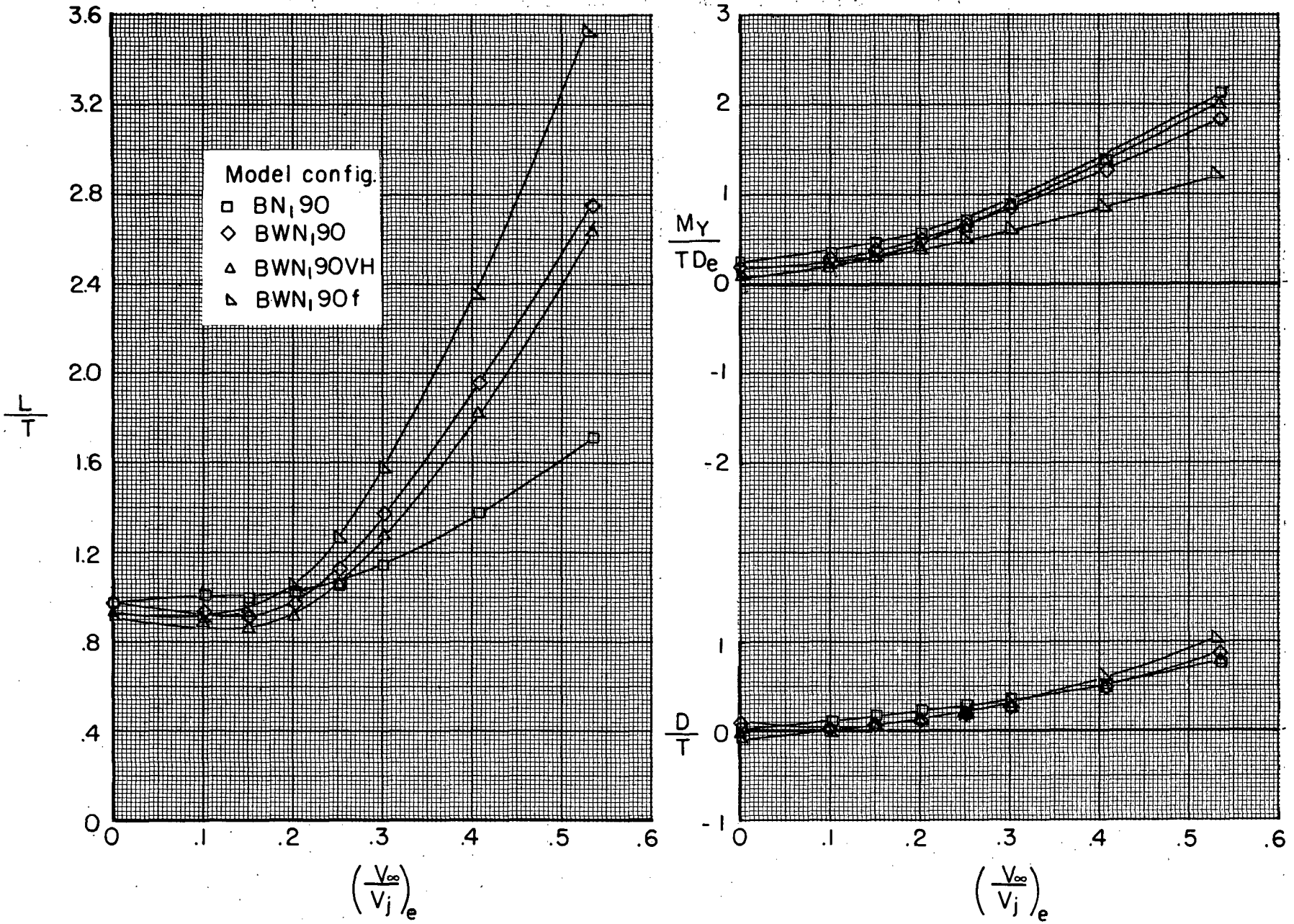


Figure 20.- Effect of model components on longitudinal aerodynamic characteristics of front vectored-thrust configuration with power at an angle of attack of 10^{o}.

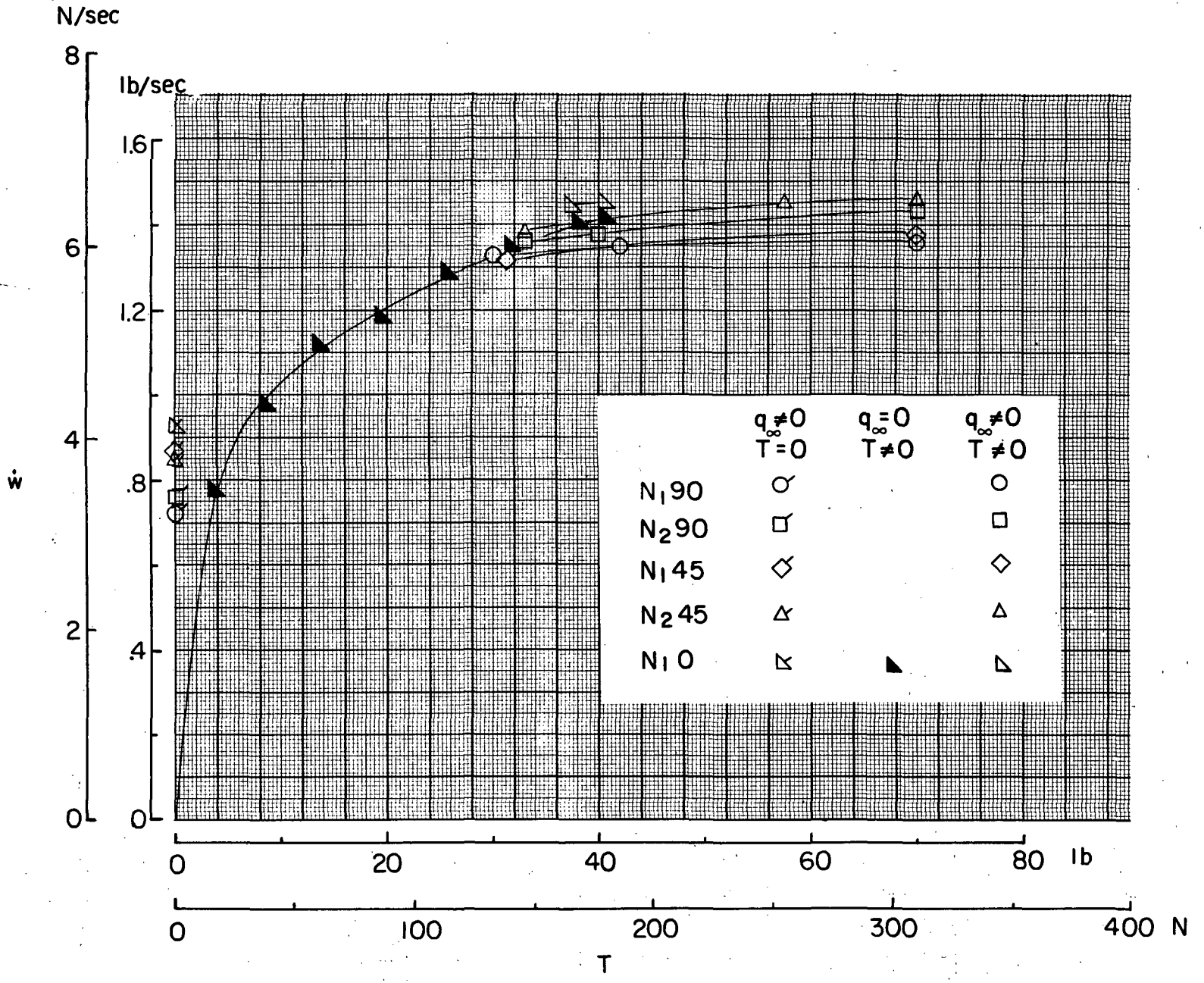
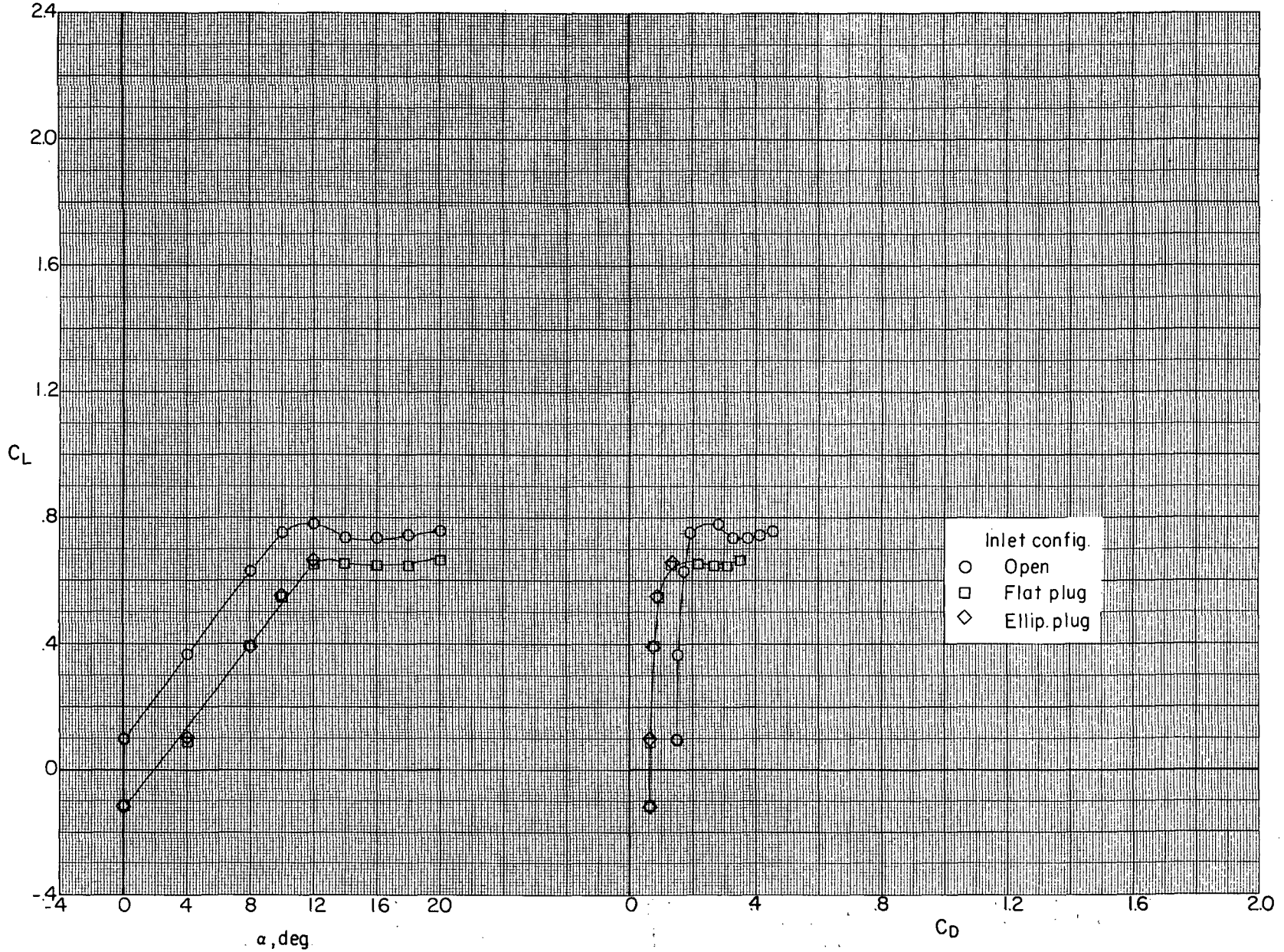
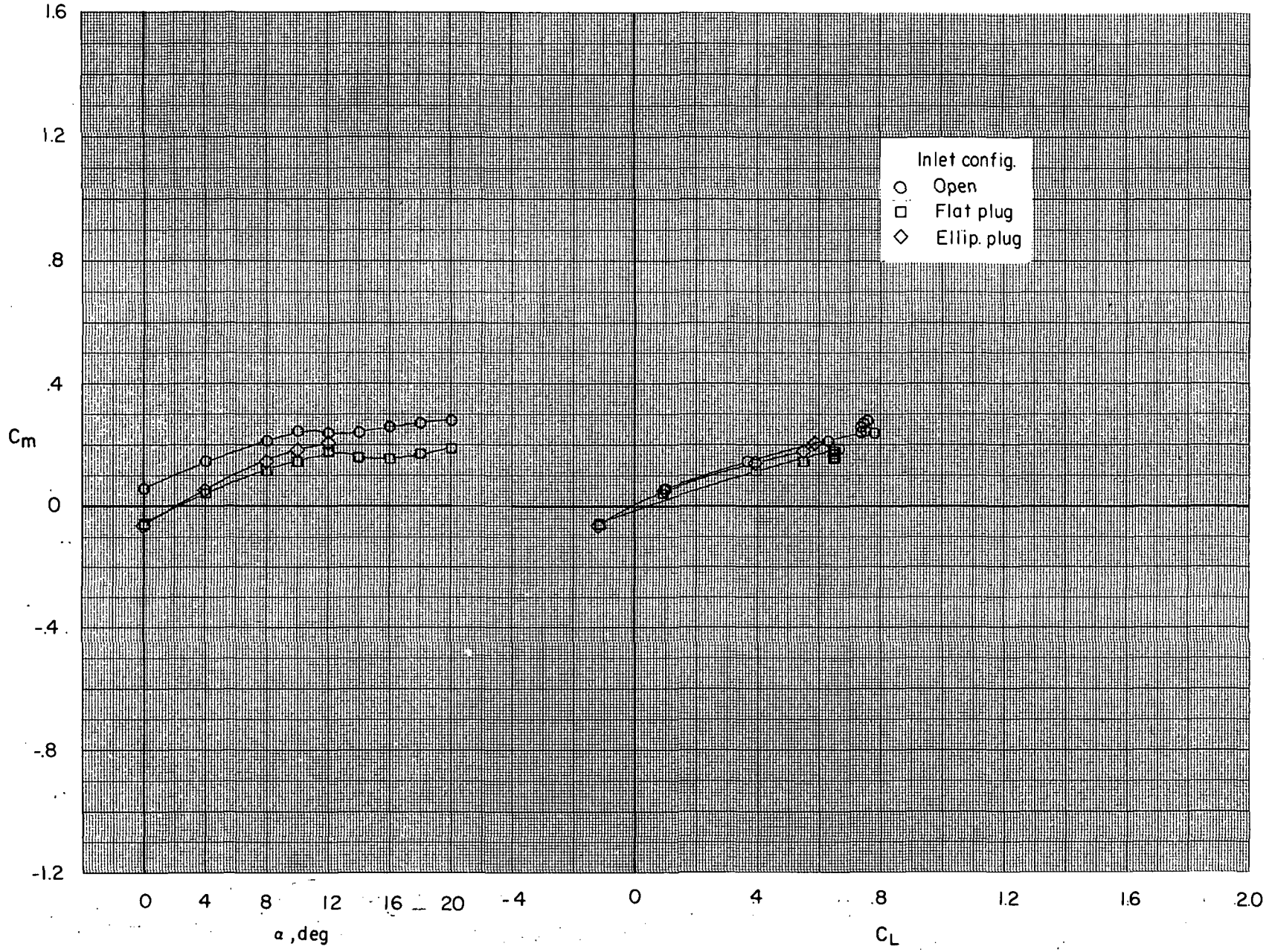


Figure 21. - Inlet weight flow rate for one engine simulator.



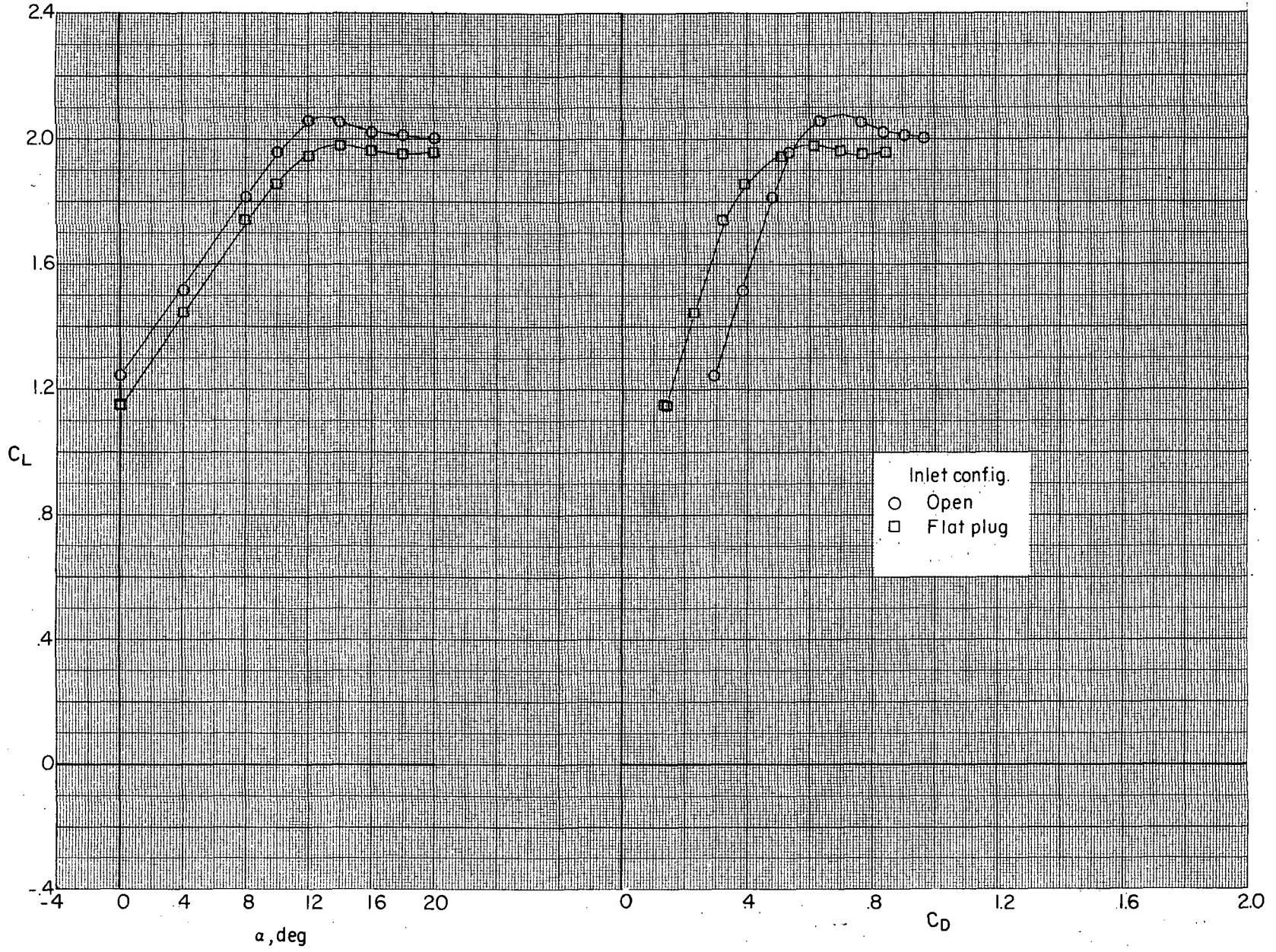
(a) Variation of C_L with α and C_D.

Figure 22.- Effect of closing inlets on longitudinal aerodynamic characteristics of $BWN_1 90$ configuration without power. $\left(V_\infty/V_j\right)_e = \infty$.



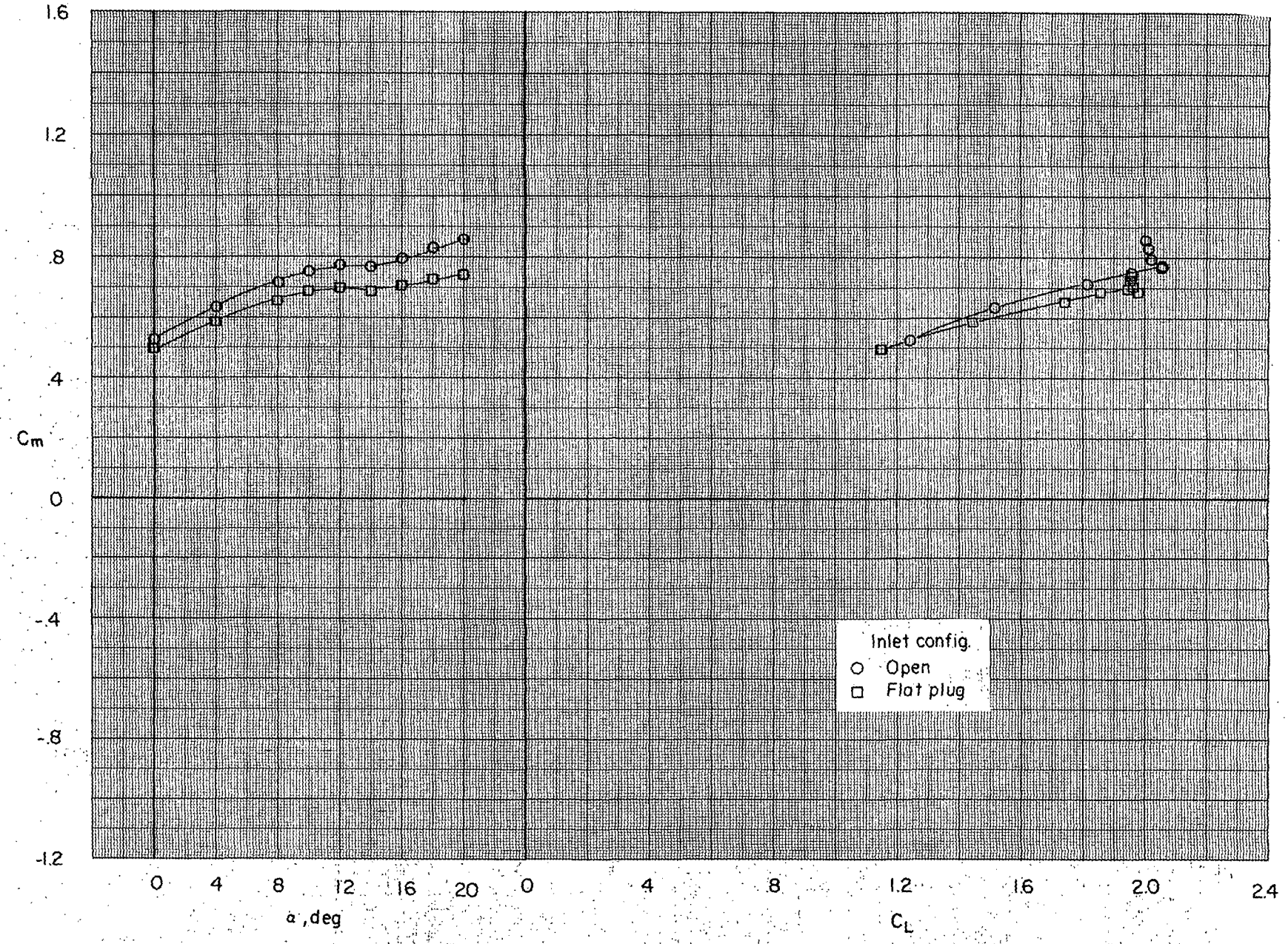
(b) Variation of C_m with α and C_L.

Figure 22.- Concluded.



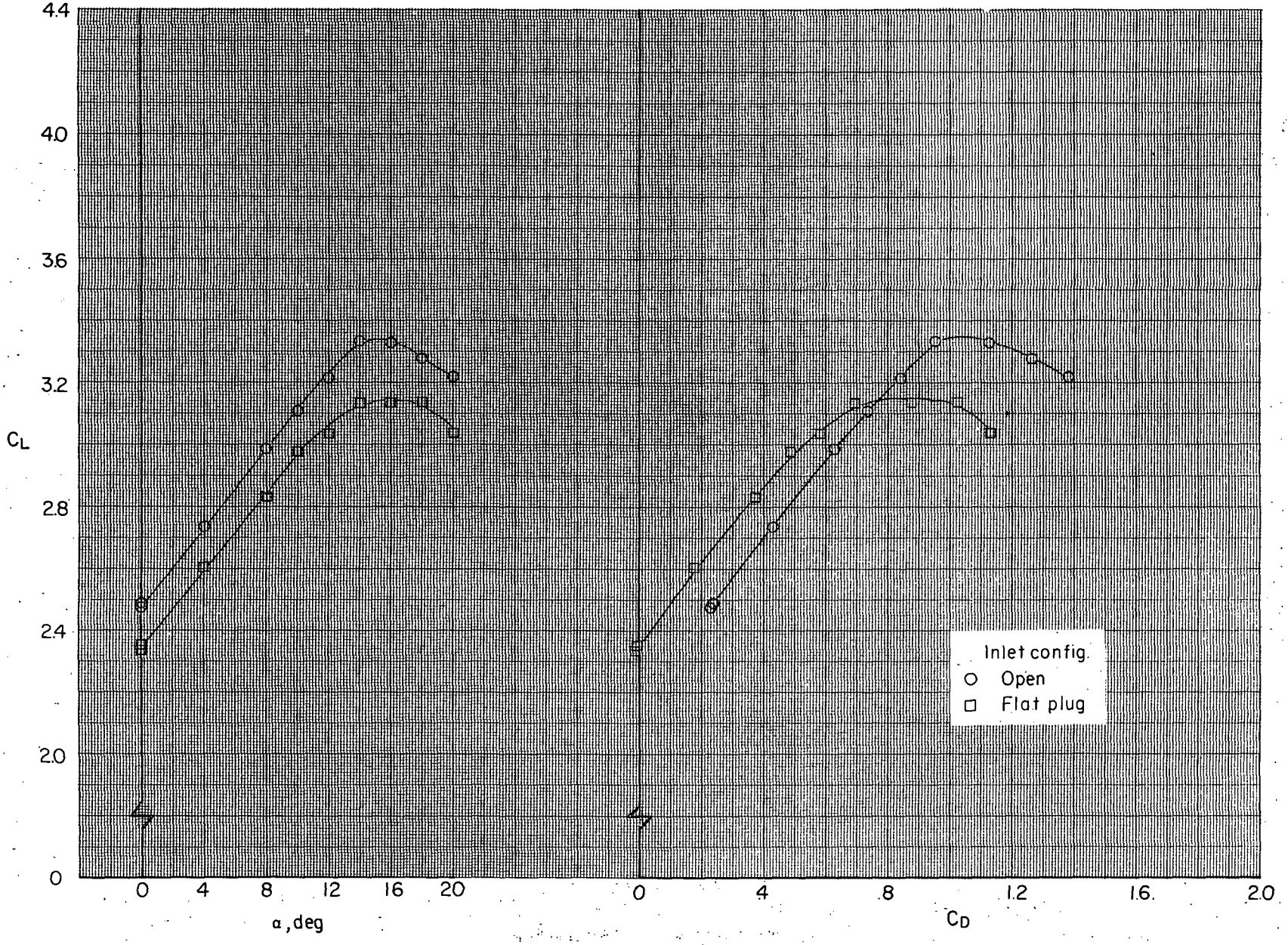
(a) Variation of C_L with α and C_D.

Figure 23.- Effect of closing inlets on longitudinal aerodynamic characteristics of $BWN_1 90$ configuration with power. $\left(V_\infty/V_j\right)_e = 0.3$.



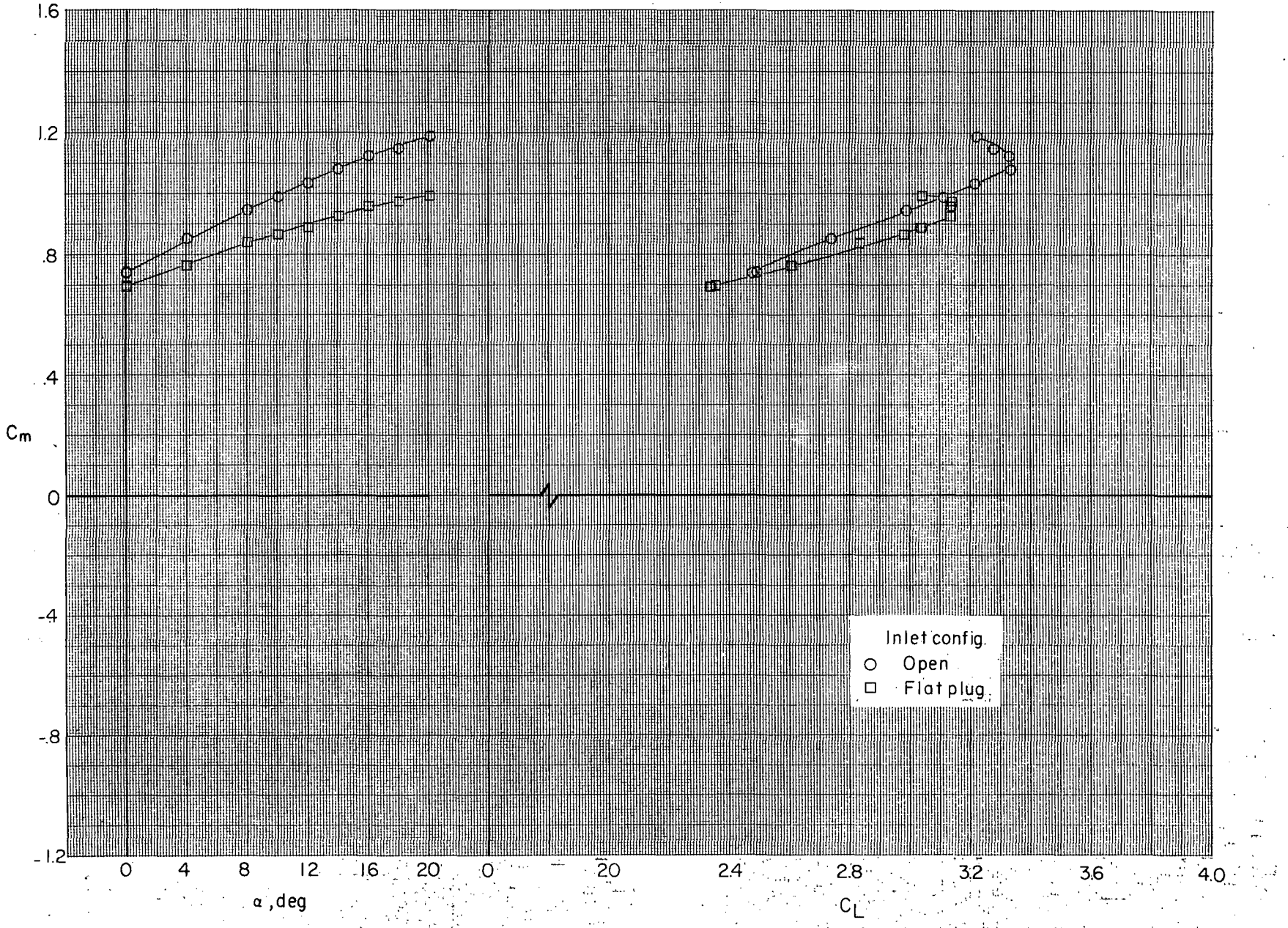
(b) Variation of C_m with α and C_L.

Figure 23.- Concluded.



(a) Variation of C_L with α and C_D.

Figure 24.- Effect of closing inlets on longitudinal aerodynamic characteristics of $BWN_1 90$ configuration with power. $\left(V_\infty/V_j\right)_e = 0.2$.



(b) Variation of C_m with α and C_L.

Figure 24.- Concluded.

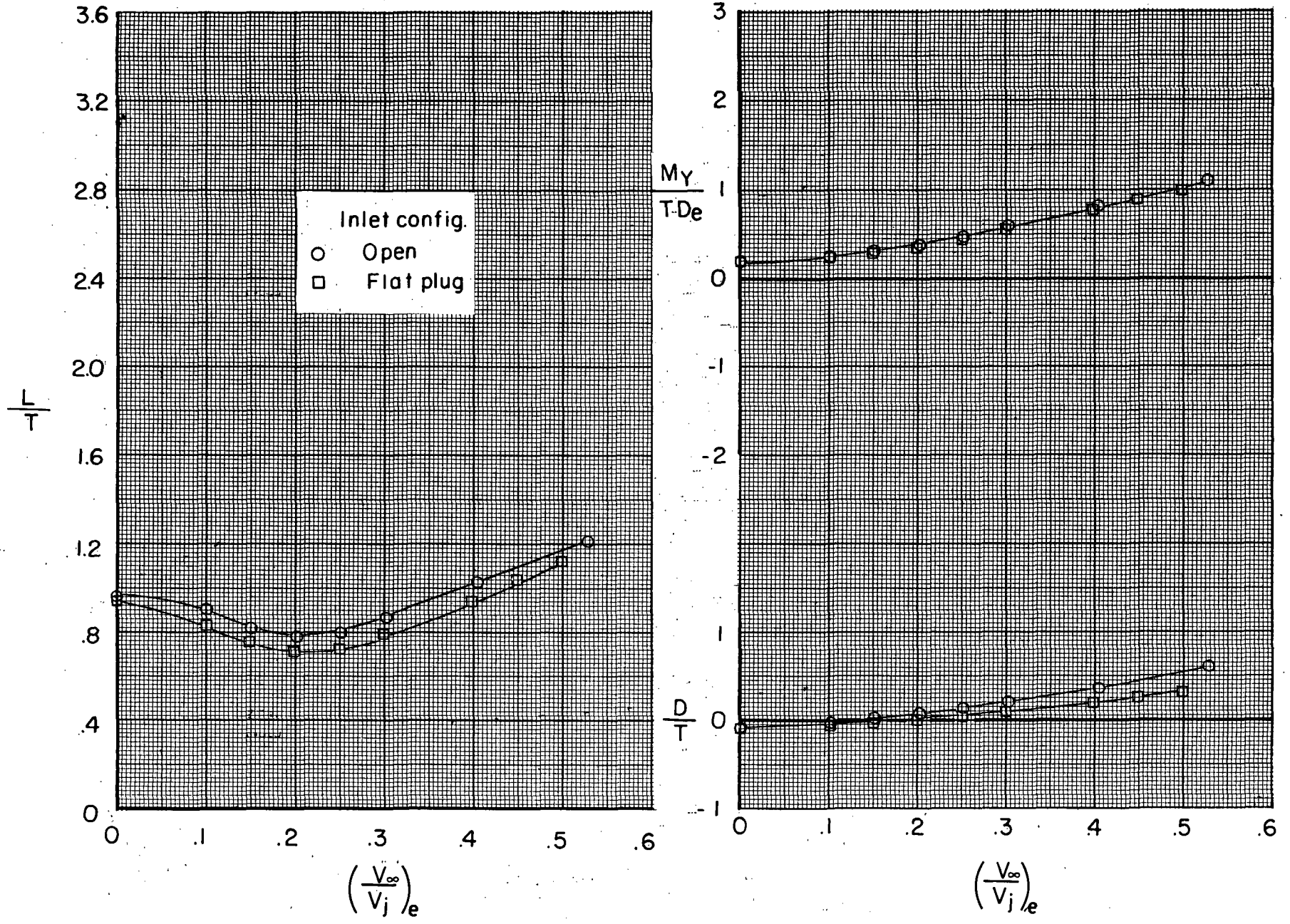


Figure 25.- Effect of closing inlets on longitudinal aerodynamic characteristics of $BWN_1 90$ configuration at an angle of attack of 0^o with power.

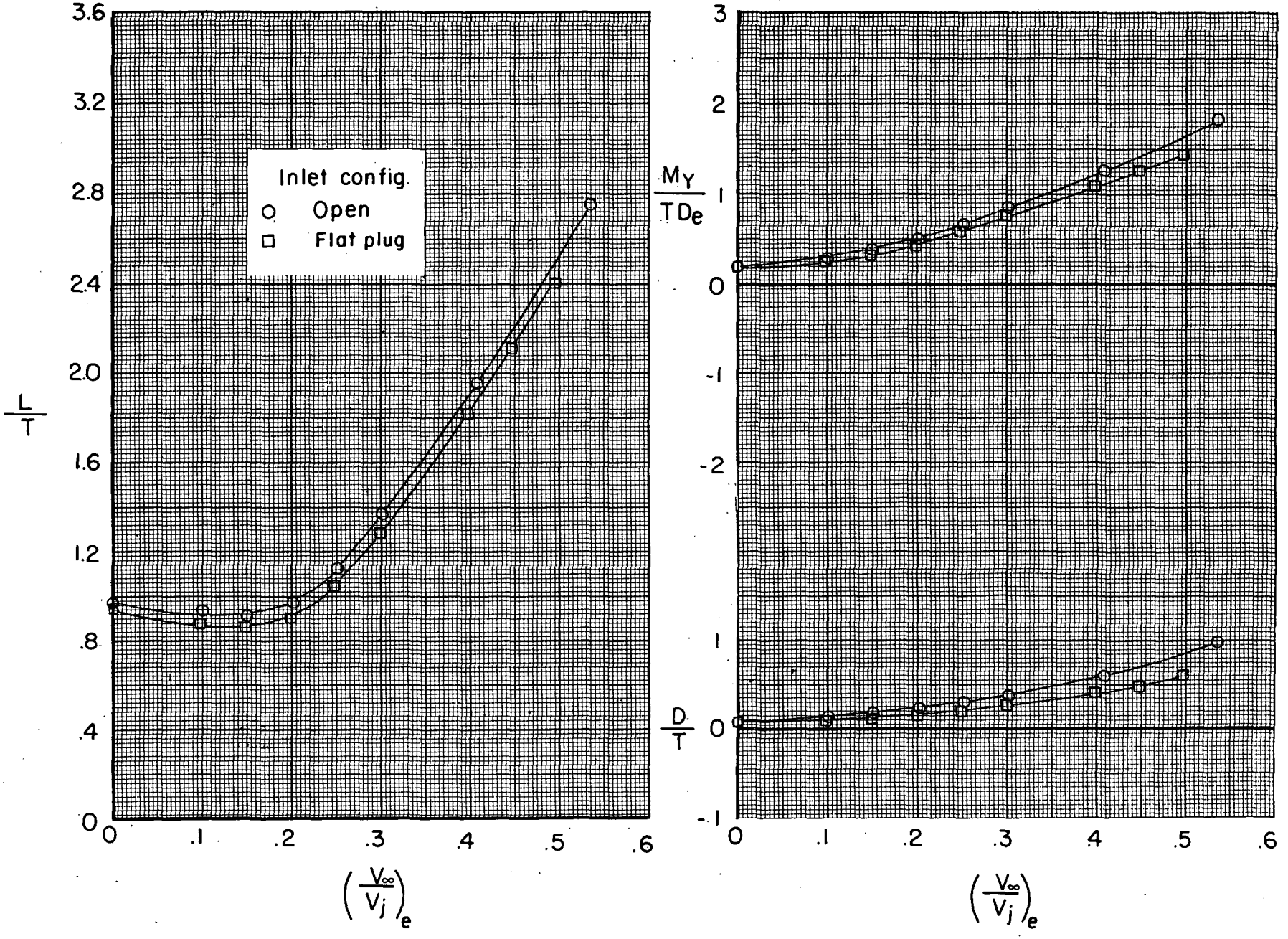
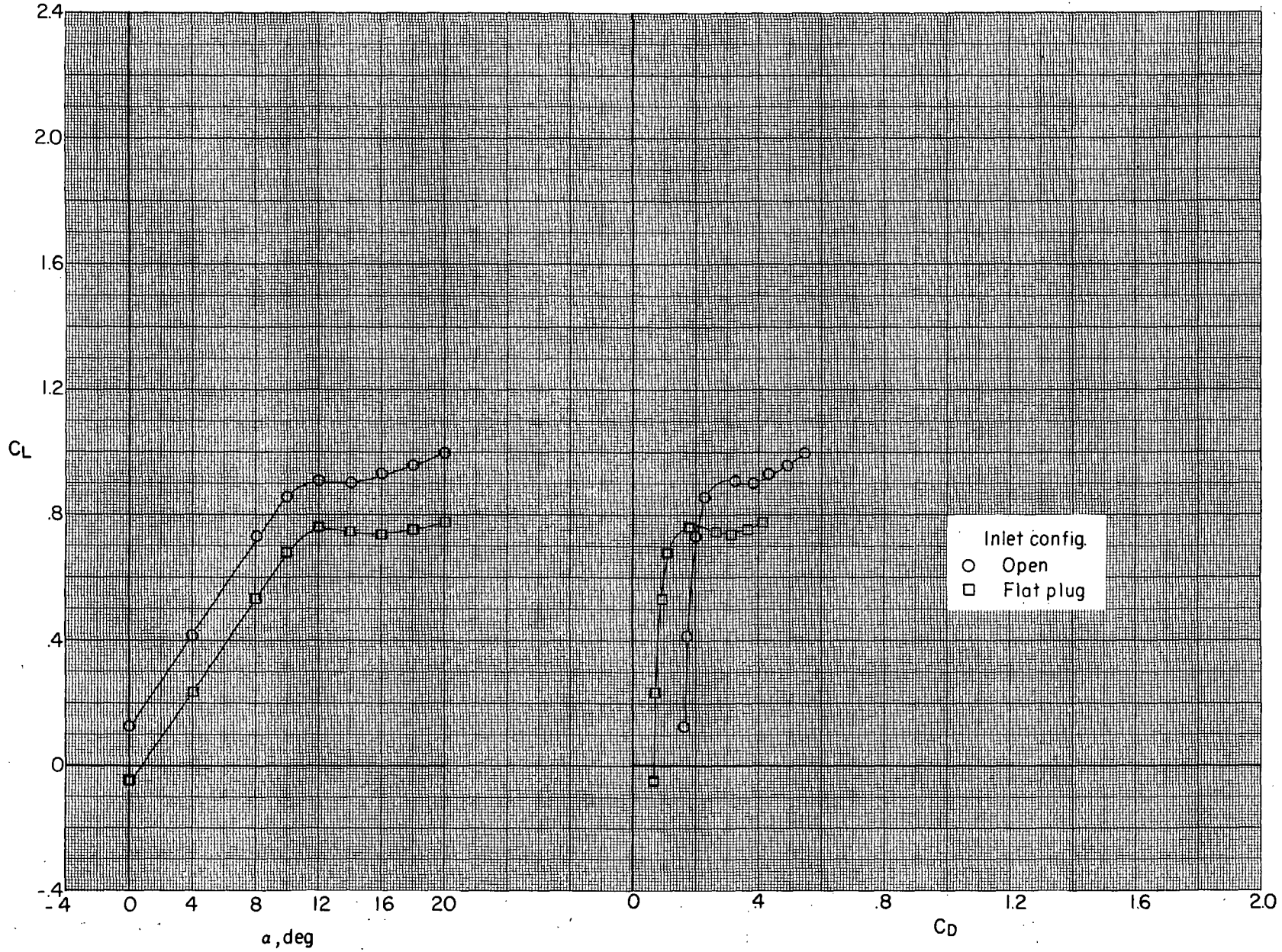
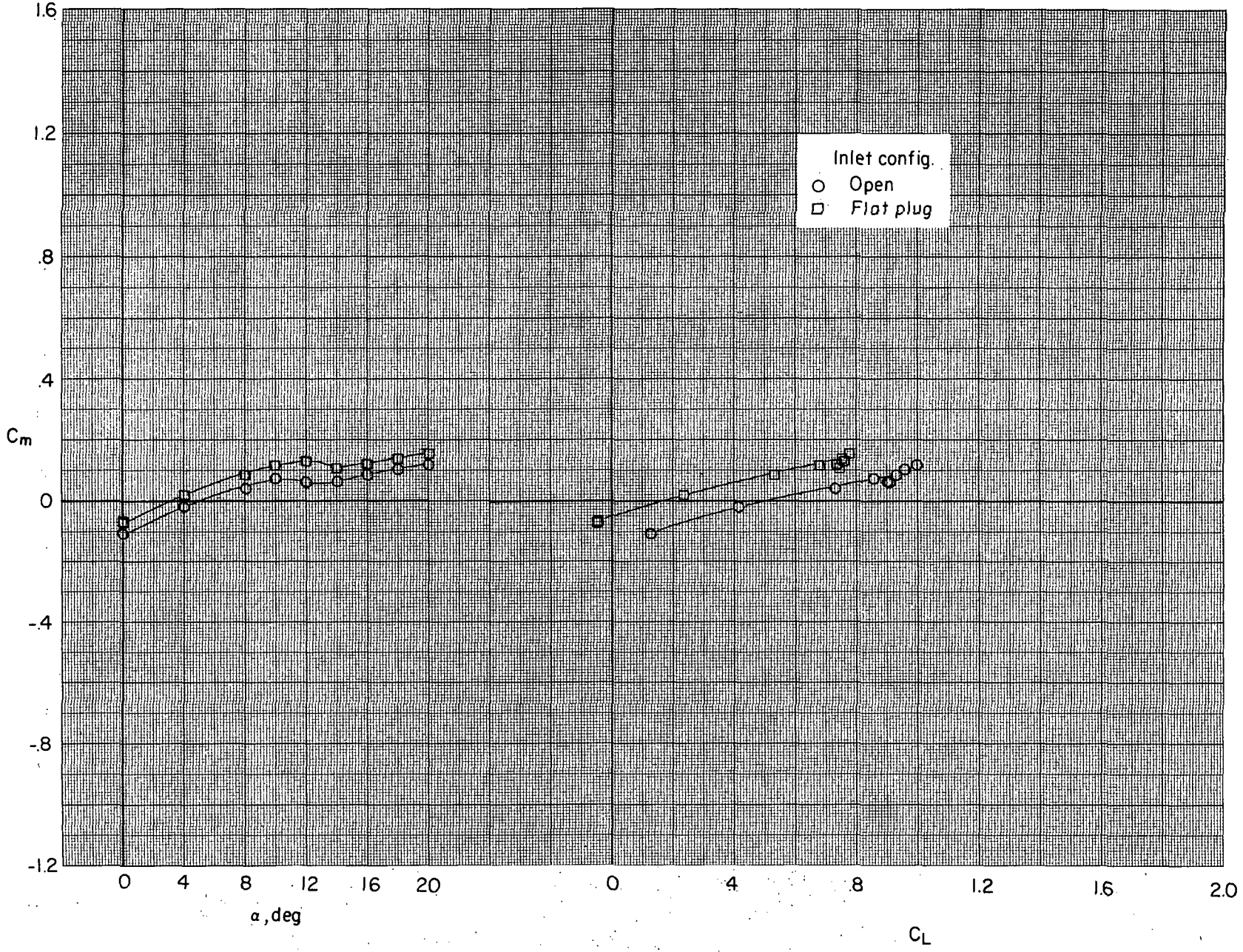


Figure 26.- Effect of closing inlets on longitudinal aerodynamic characteristics of $BWN_1 90$ configuration at an angle of attack of 10^o with power.



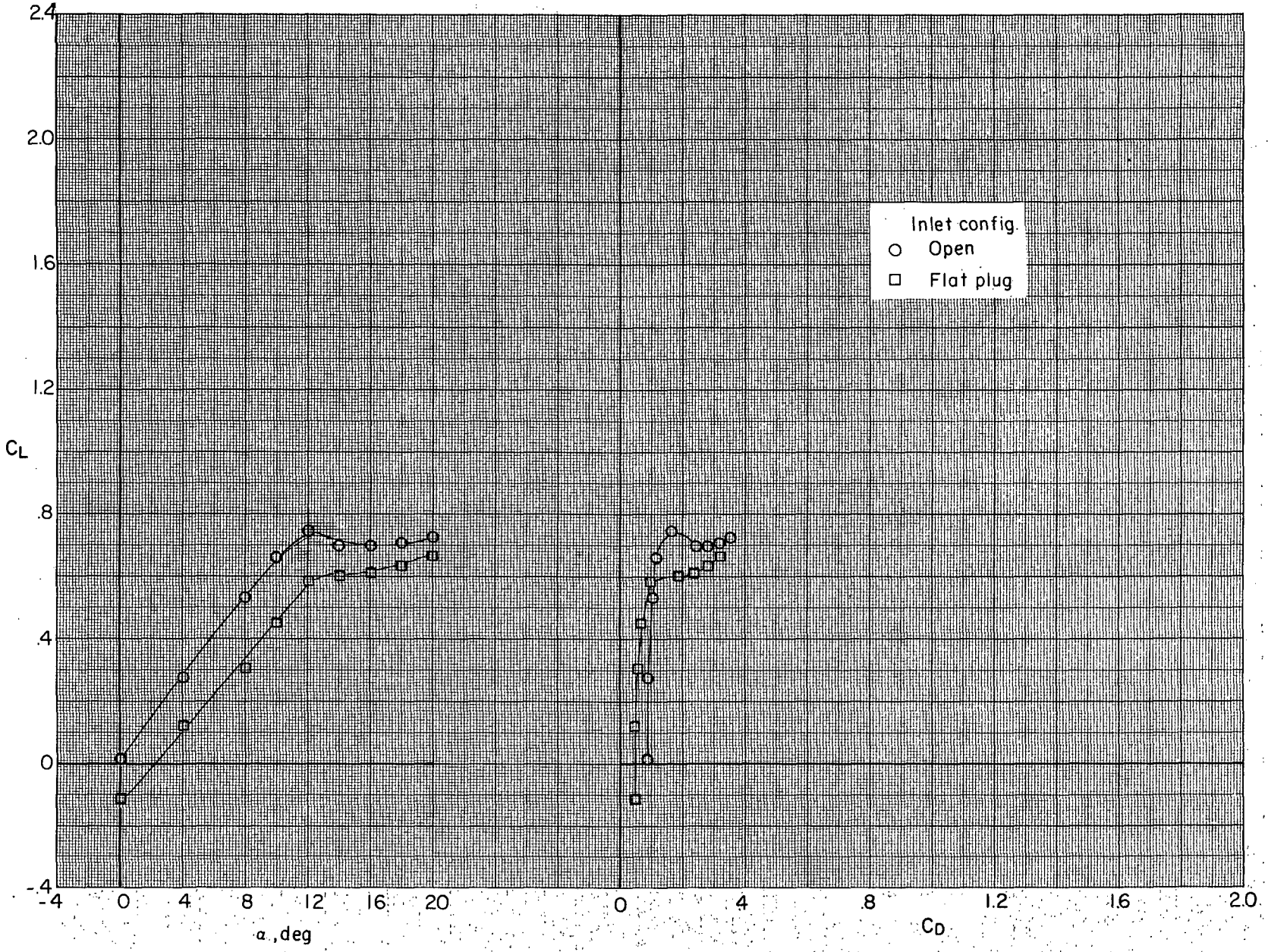
(a) Variation of C_L with α and C_D.

Figure 27.- Effect of closing inlets on longitudinal aerodynamic characteristics of $BWN_2 90$ configuration without power. $\left(V_\infty/V_j\right)_e = \infty$.



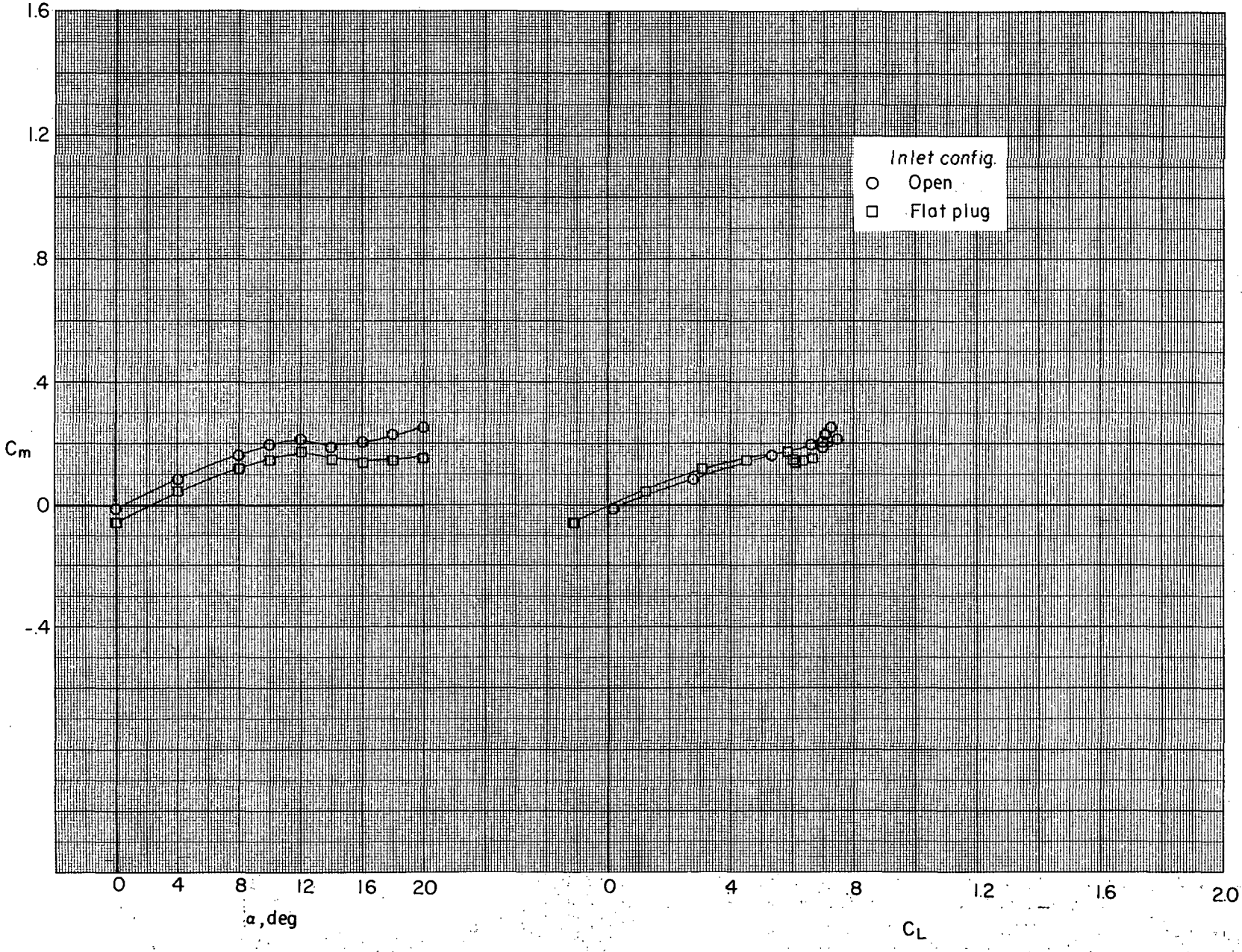
(b) Variation of C_m with α and C_L.

Figure 27.- Concluded.



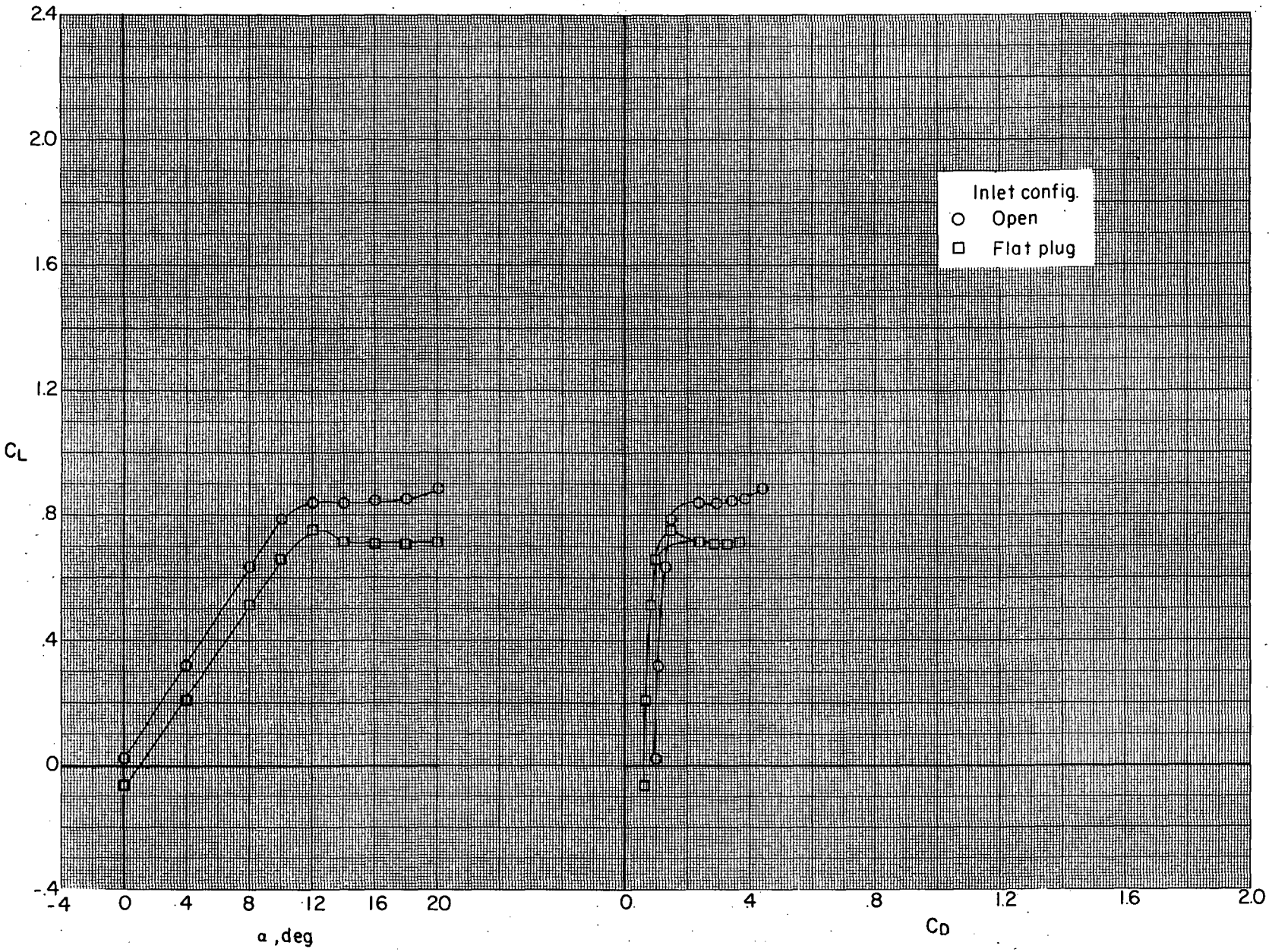
(a) Variation of C_L with α and C_D.

Figure 28. - Effect of closing inlets on longitudinal aerodynamic characteristics of $BWN_1 45$ configuration without power. $\left(V_\infty/V_j\right)_e = \infty$.



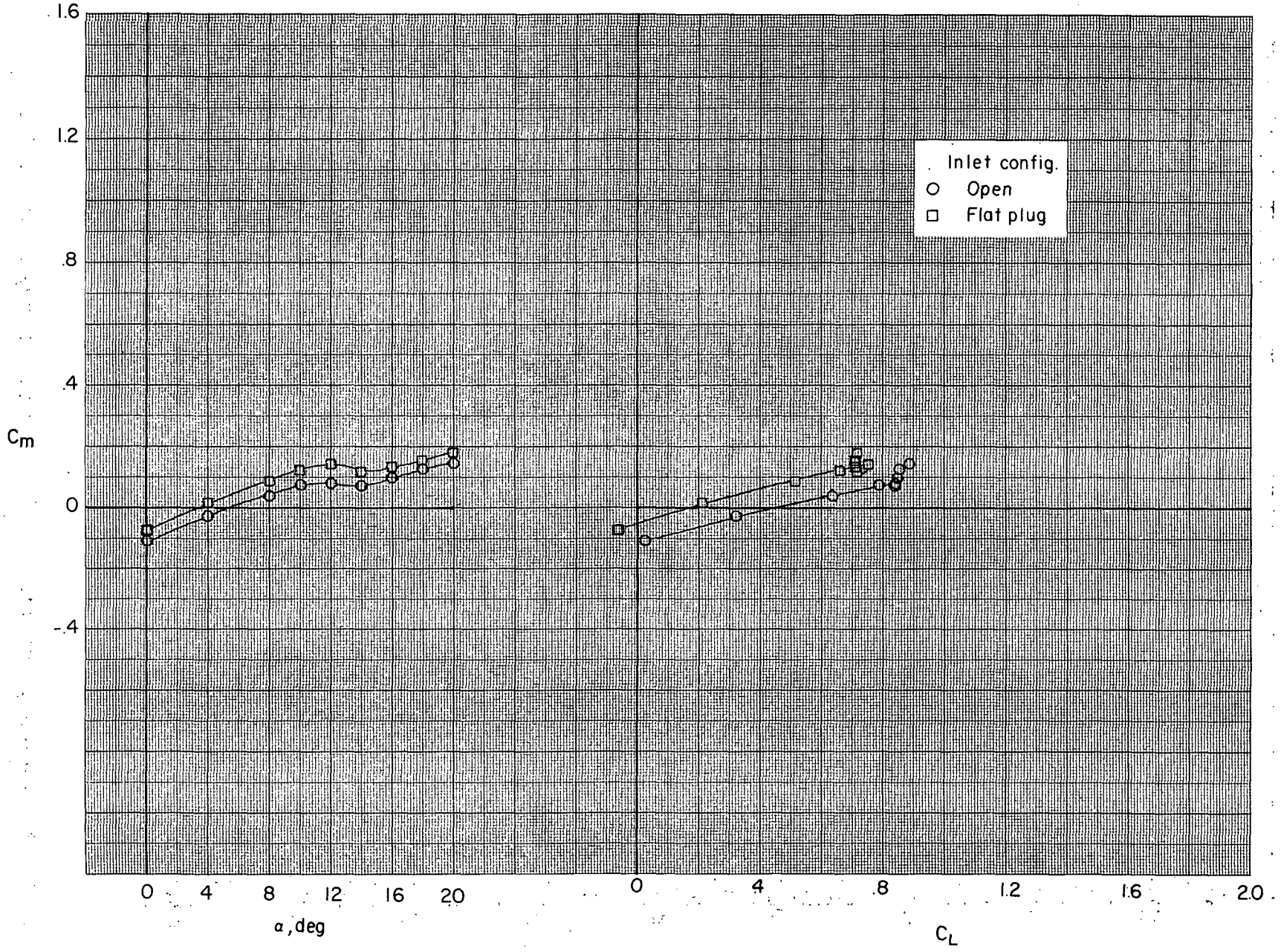
(b) Variation of C_m with α and C_L.

Figure 28.- Concluded.



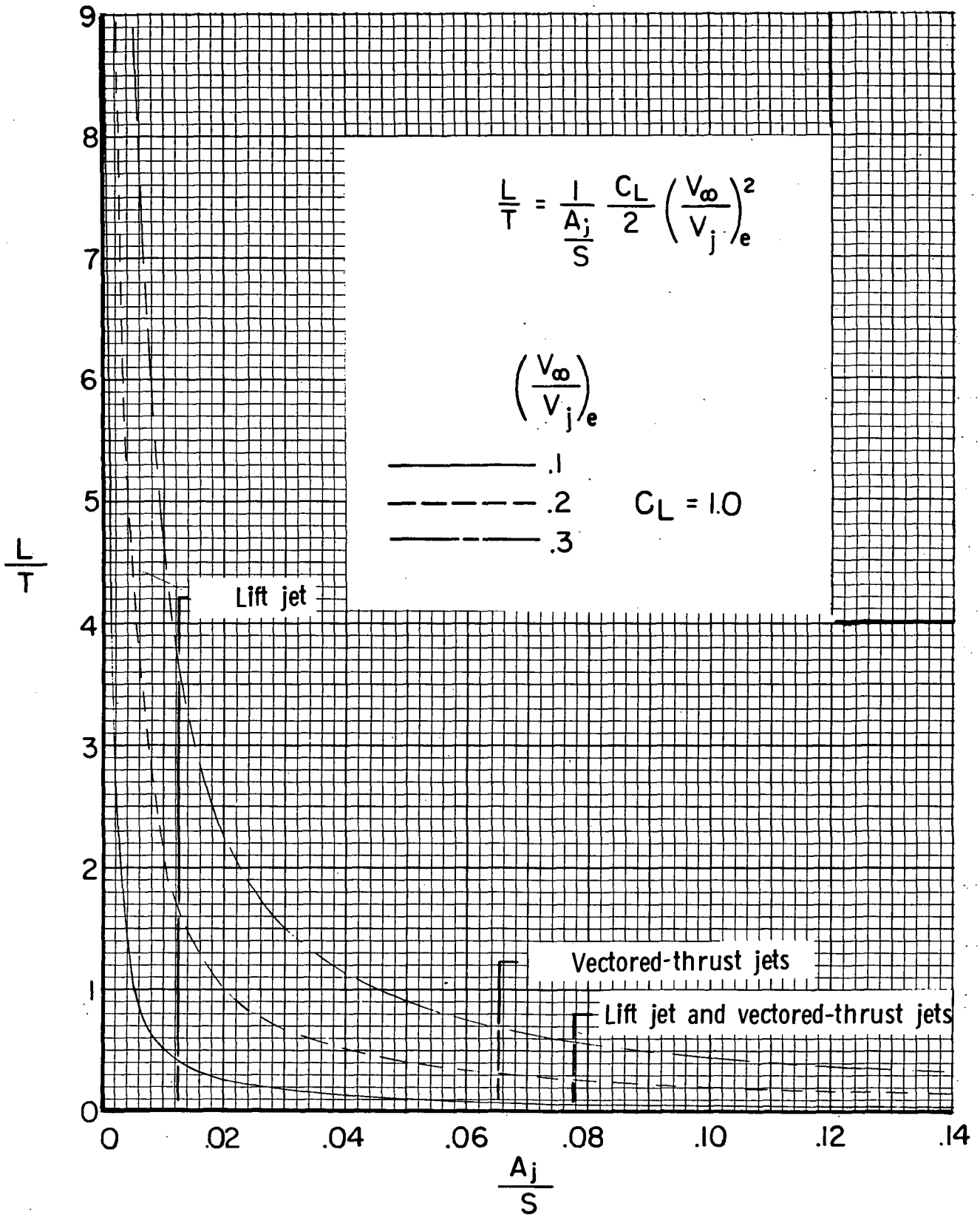
(a) Variation of C_L with α and C_D.

Figure 29.- Effect of closing inlets on longitudinal aerodynamic characteristics of $BWN_2 45$ configuration without power: $\left(V_\infty/V_j\right)_e = \infty$.



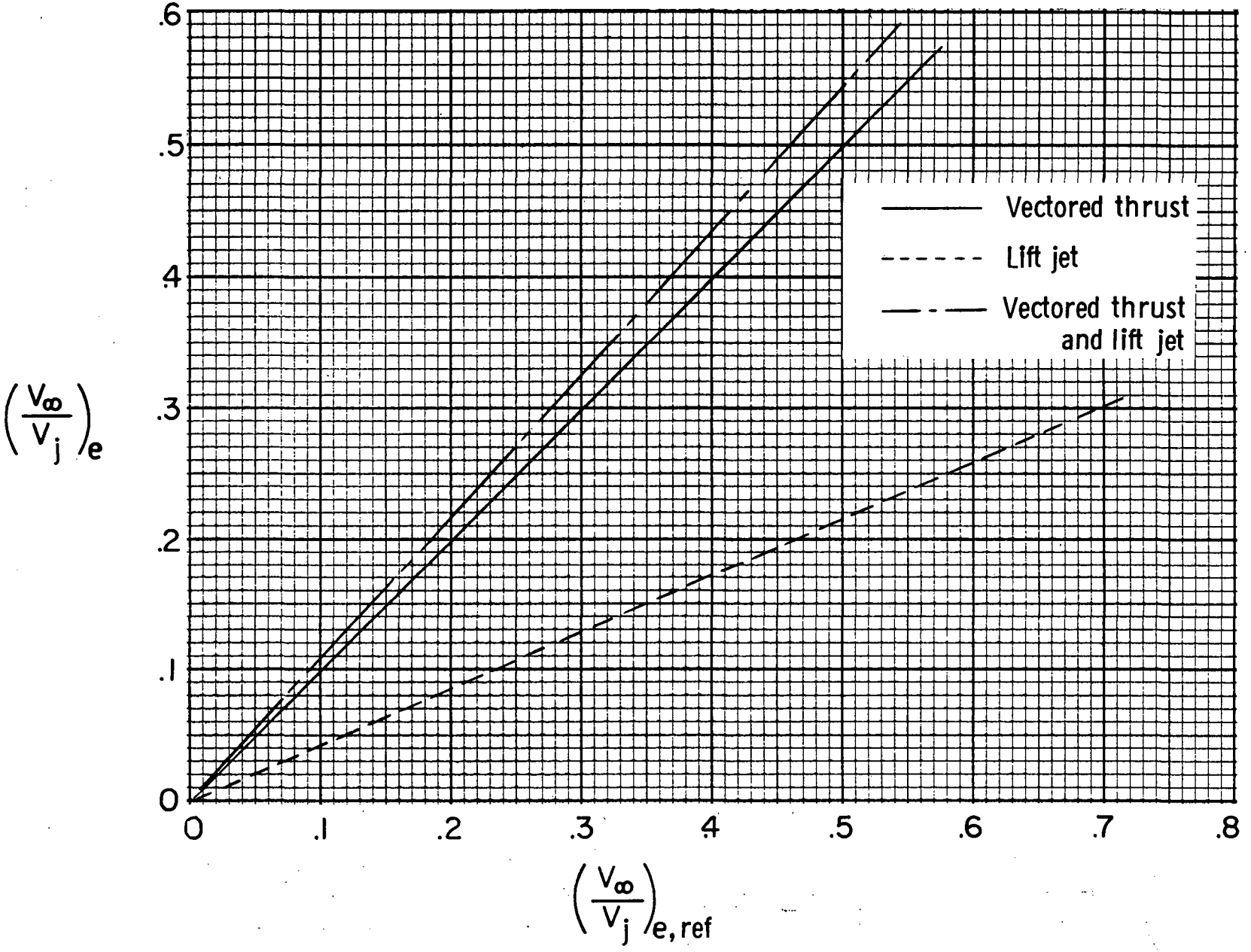
(b) Variation of C_m with α and C_L.

Figure 29.- Concluded.



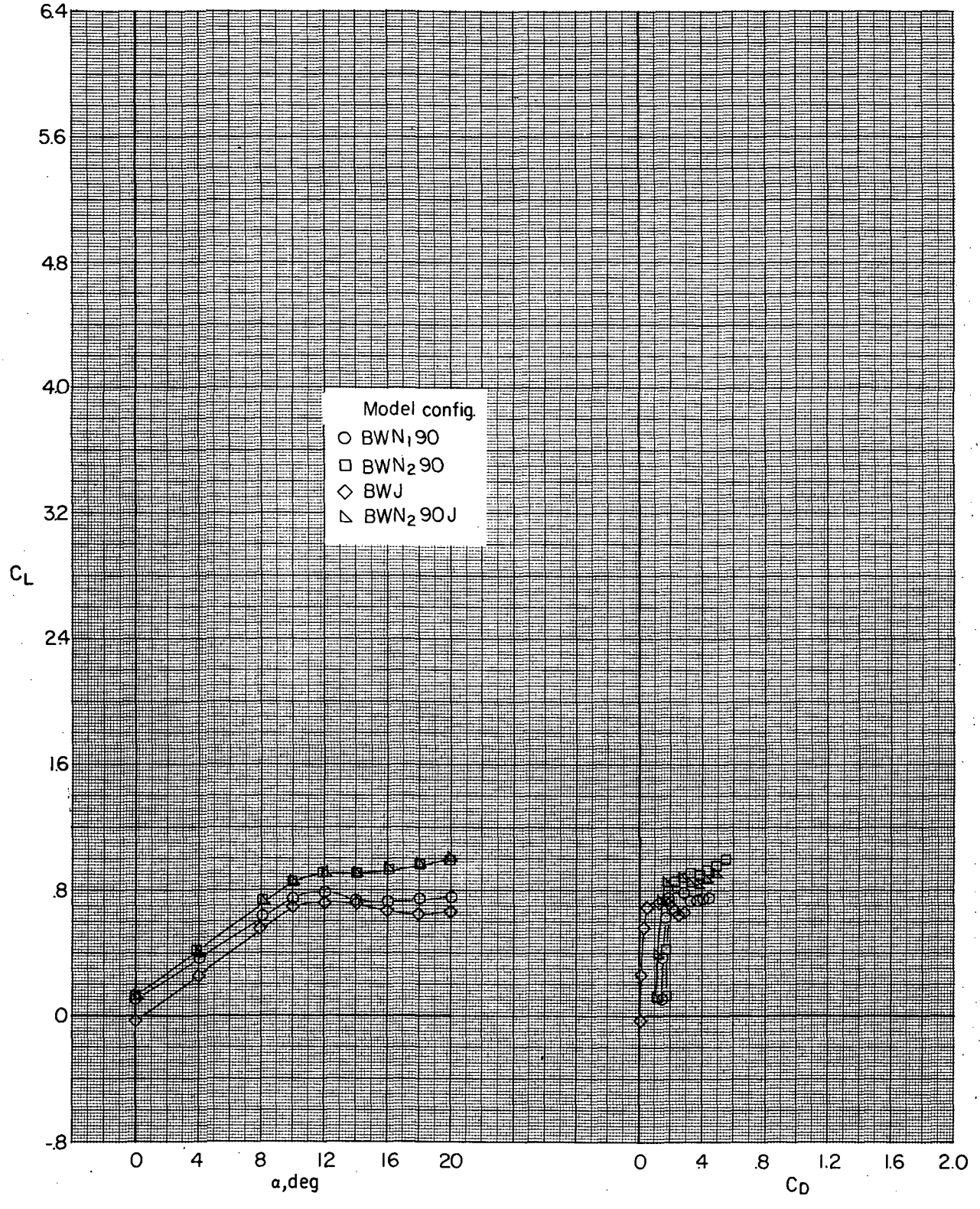
(a) Effect of ratio of jet area to wing area on ratio of wing lift to jet lift.

Figure 30.- Effect of geometry and speed on lift-thrust ratio.



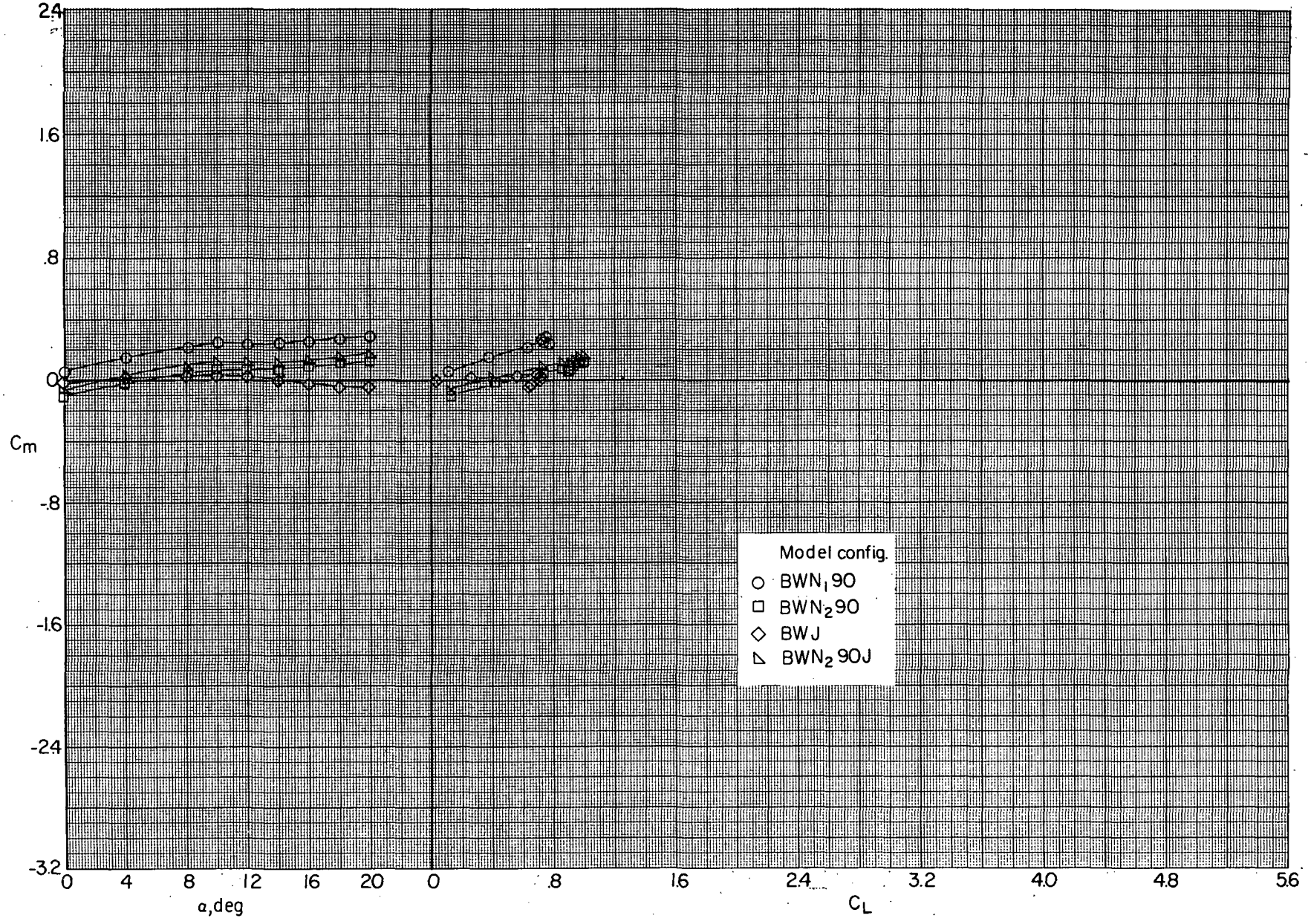
(b) Effective velocity ratio for various configurations as a function of a reference effective velocity ratio.

Figure 30.- Concluded.



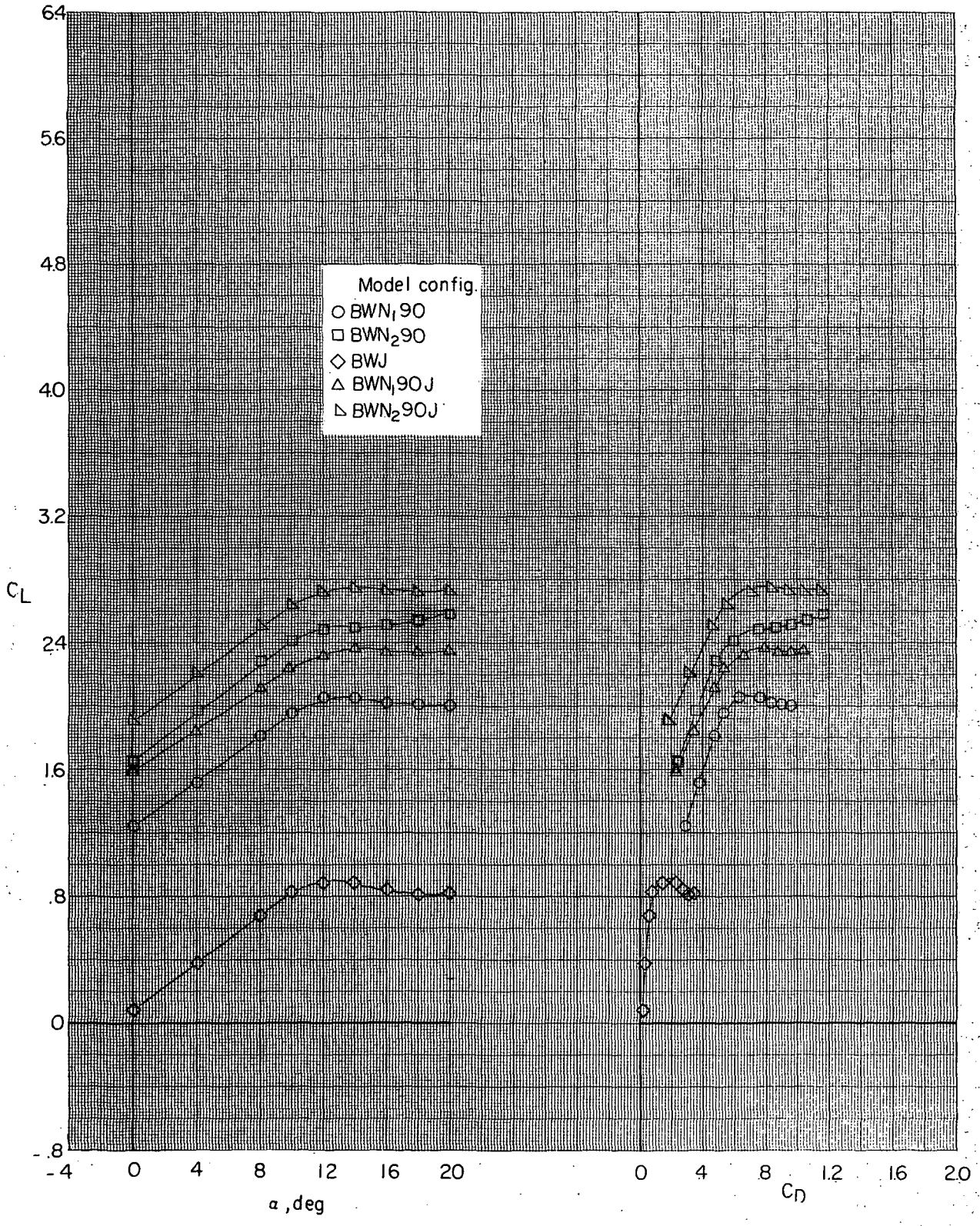
(a) Variation of C_L with α and C_D.

Figure 31.- Effect of thrust configuration on longitudinal aerodynamic characteristics without power. $\left(V_\infty/V_j\right)_e = \infty$.



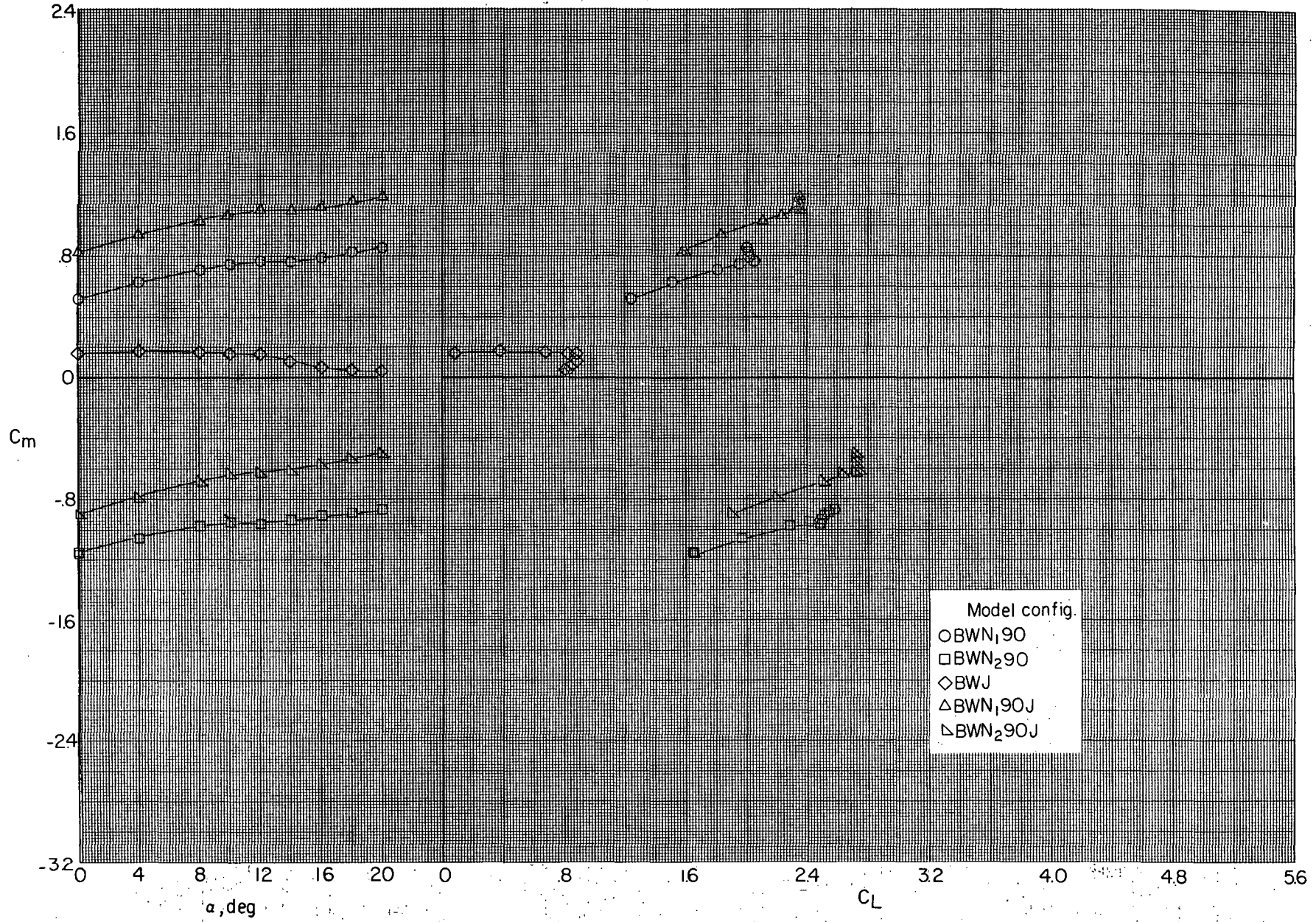
(b) Variation of C_m with α and C_L.

Figure 31.- Concluded.



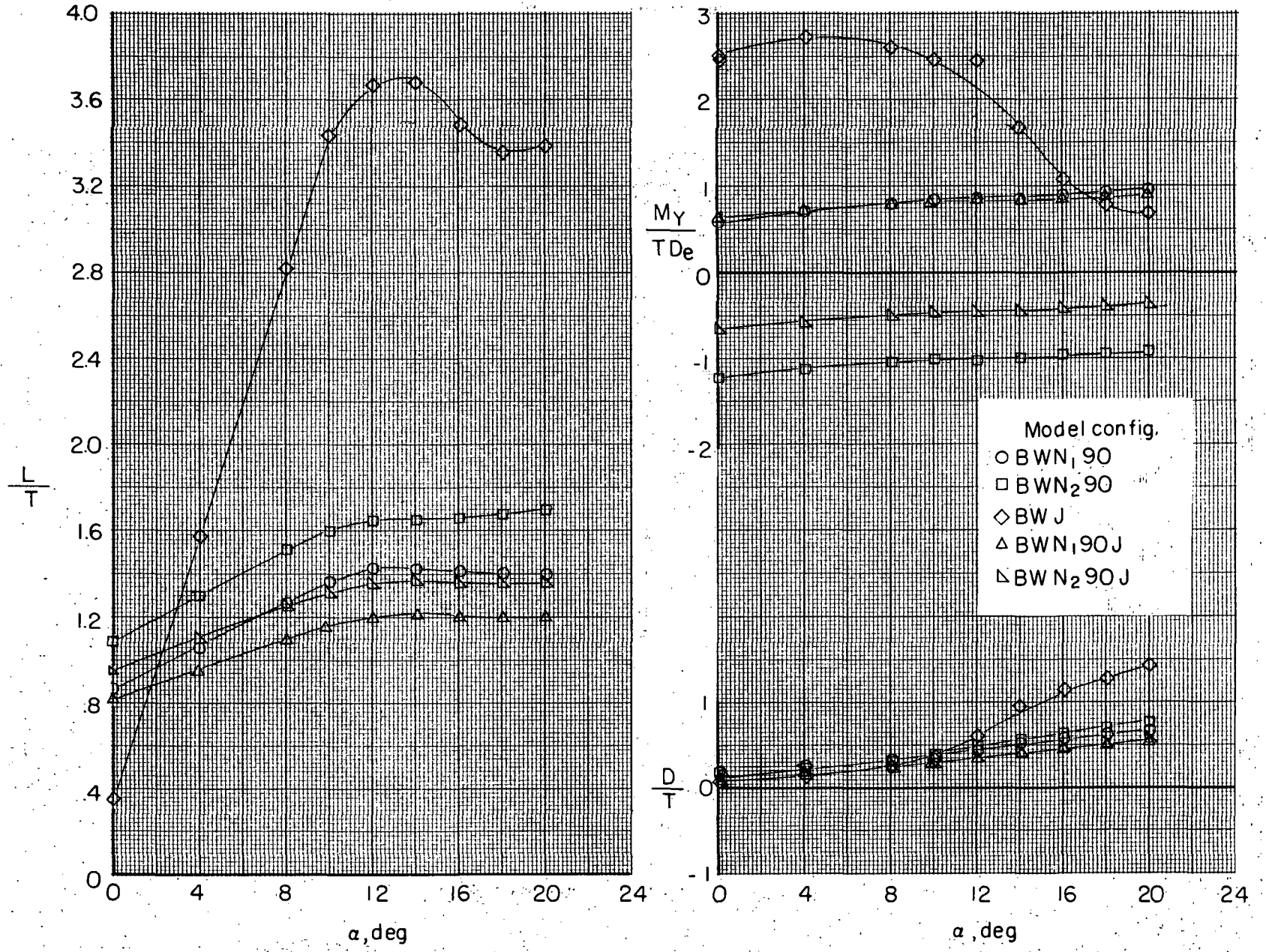
(a) Variation of C_L with α and C_D.

Figure 32.- Effect of thrust configuration on longitudinal aerodynamic characteristics with power. $\left(V_\infty/V_j\right)_e = 0.3$.



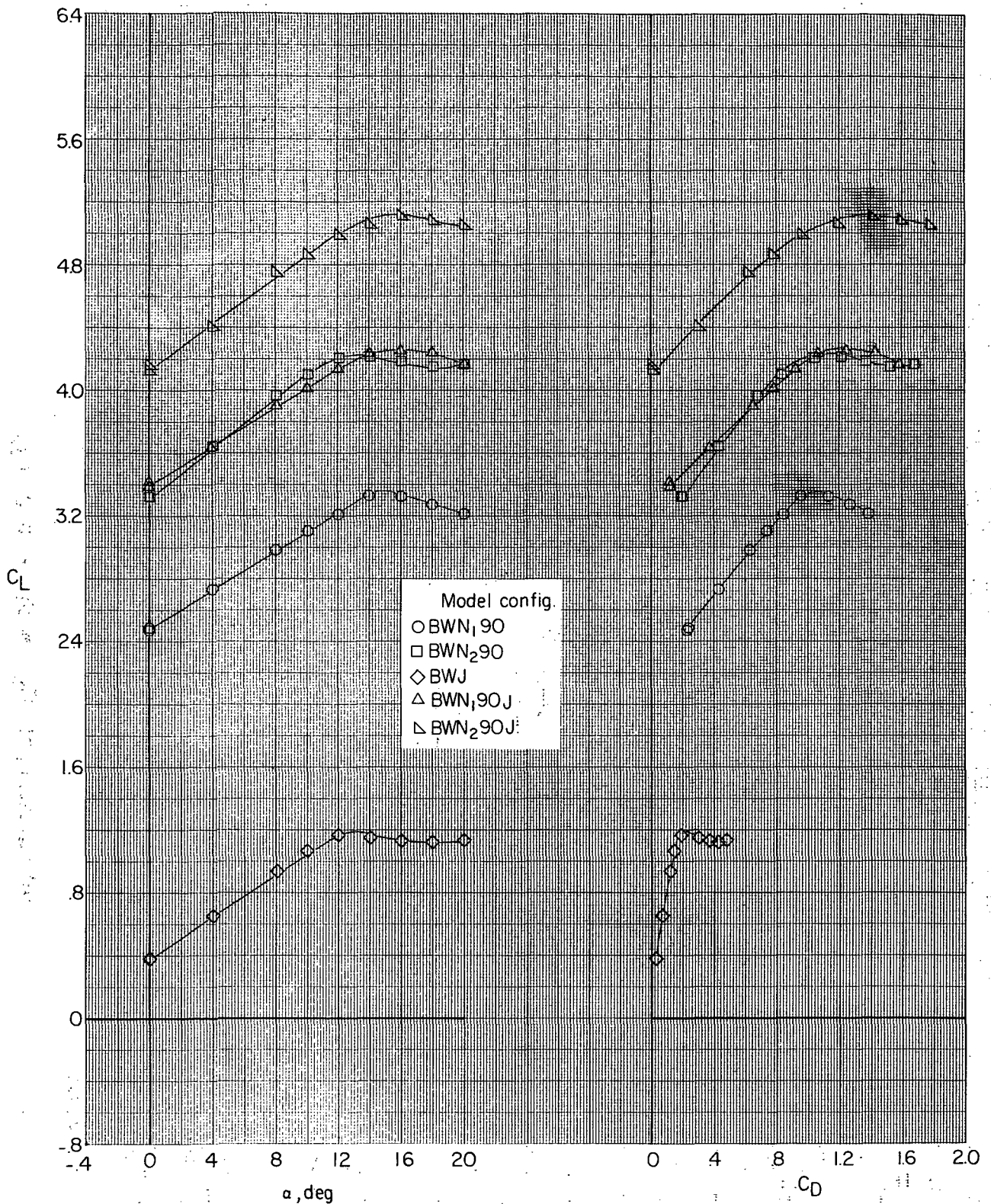
(b) Variation of C_m with α and C_L.

Figure 32.- Continued.



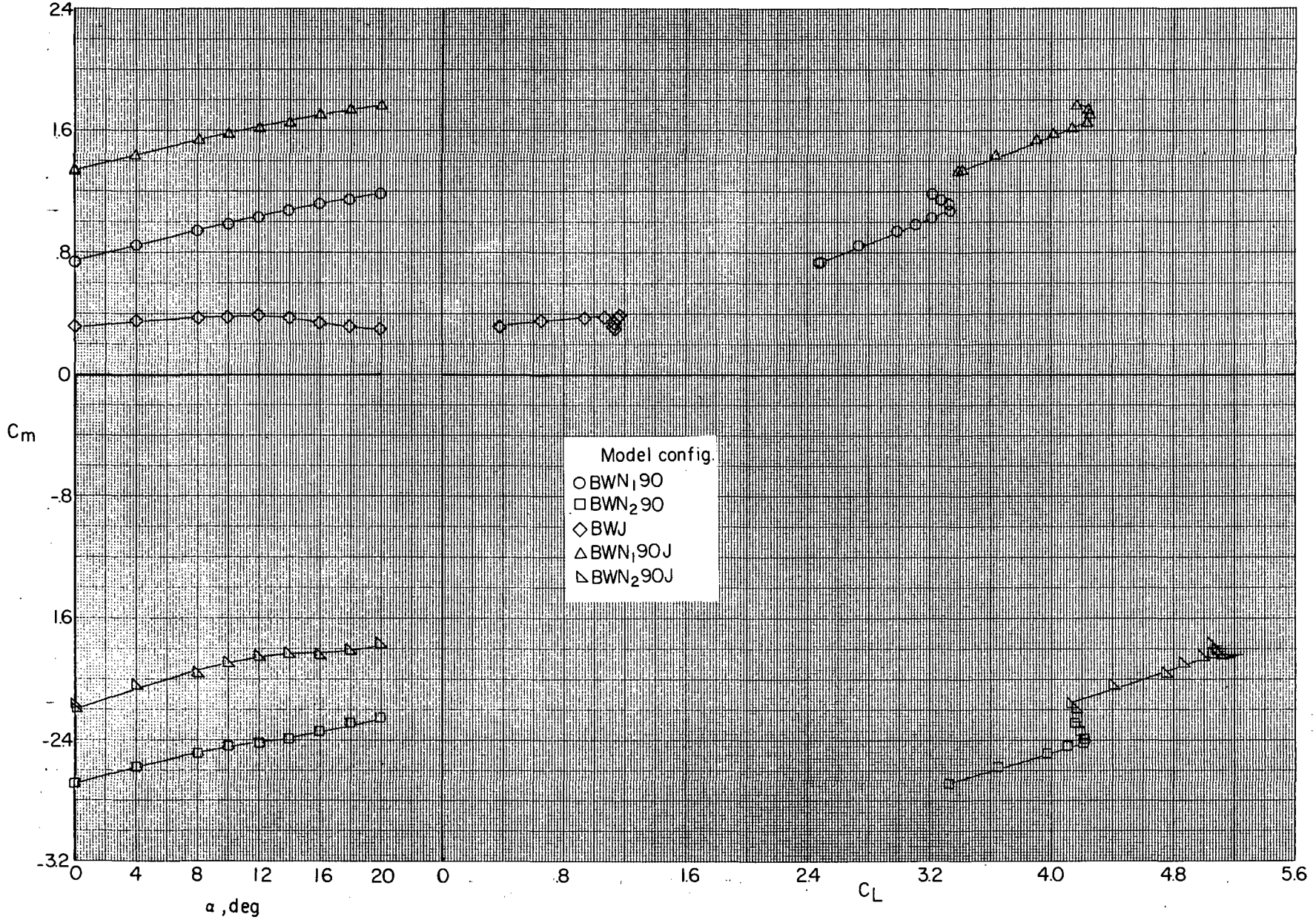
(c) Variation of L/T, D/T, and M_Y/TD_e with α.

Figure 32.- Concluded.



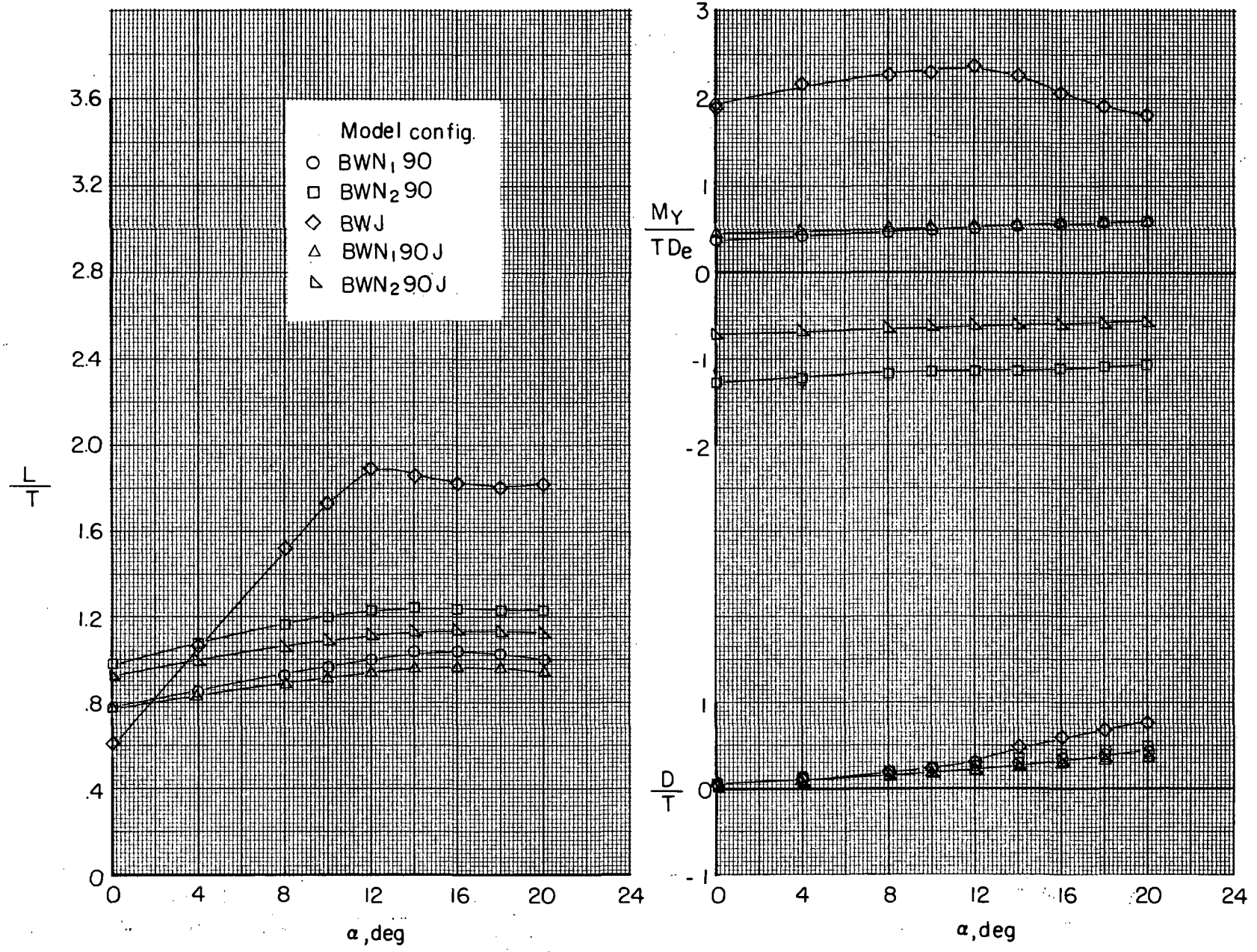
(a) Variation of C_L with α and C_D.

Figure 33.- Effect of thrust configuration on longitudinal aerodynamic characteristics with power. $\left(V_\infty/V_j\right)_e = 0.2$.



(b) Variation of C_m with α and C_L.

Figure 33.- Continued.



(c) Variation of L/T, D/T, and M_Y/TD_e with α.

Figure 33.- Concluded.

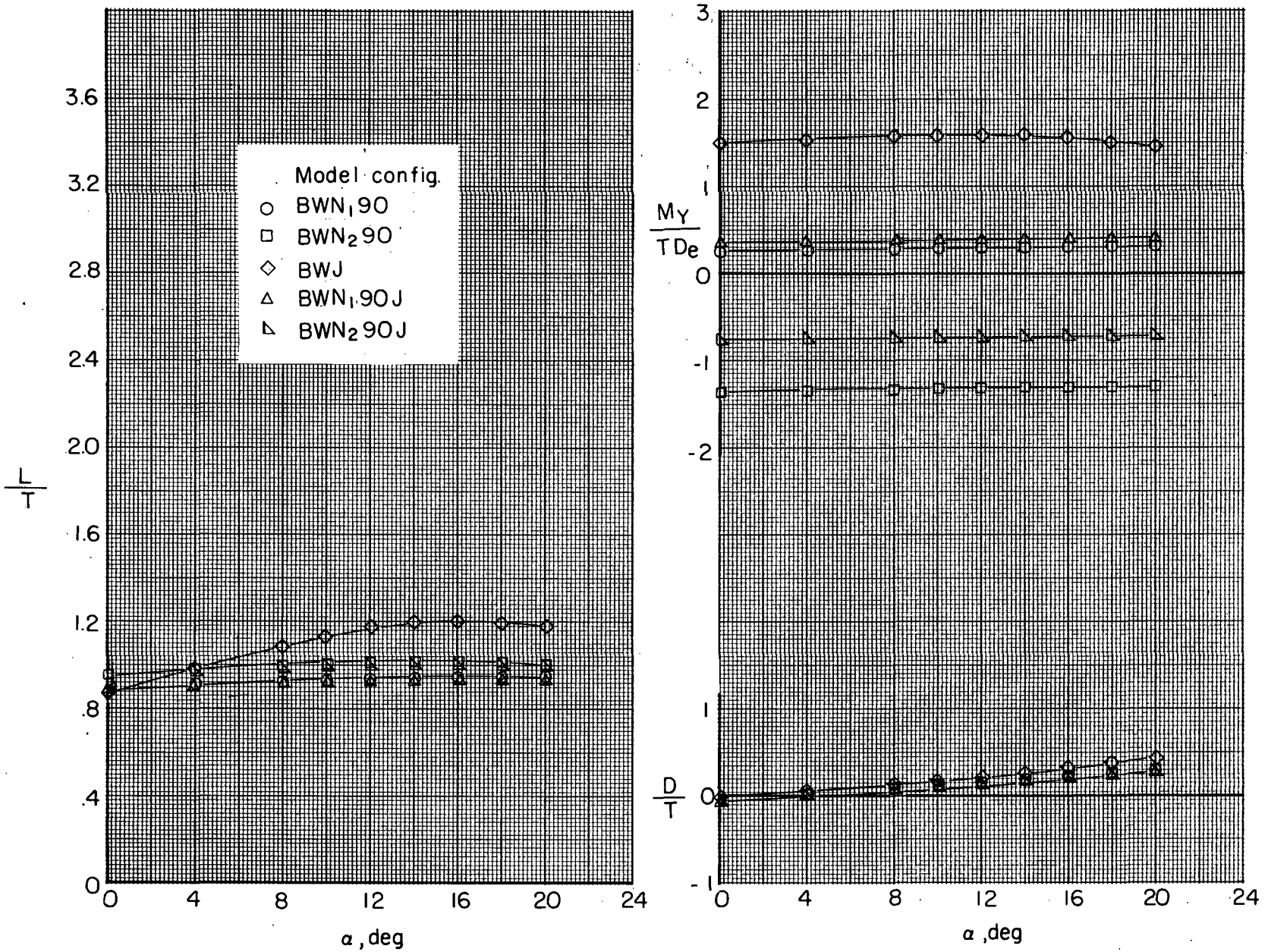


Figure 34.- Effect of thrust configuration on longitudinal aerodynamic characteristics with power. $\left(V_\infty/V_j\right)_e = 0.1$.

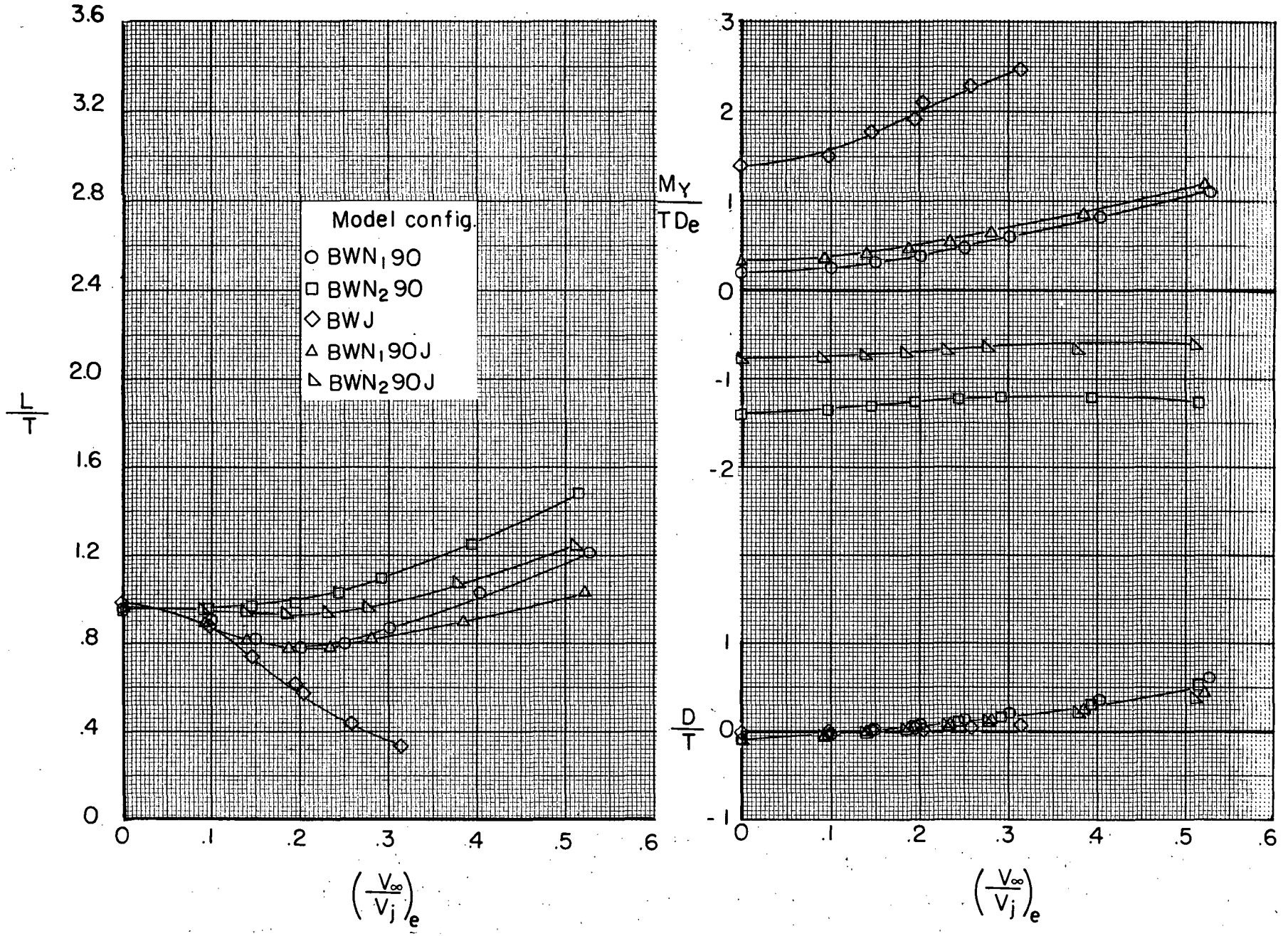


Figure 35.- Effect of thrust configuration on longitudinal aerodynamic characteristics at an angle of attack of 0^{o} with power.

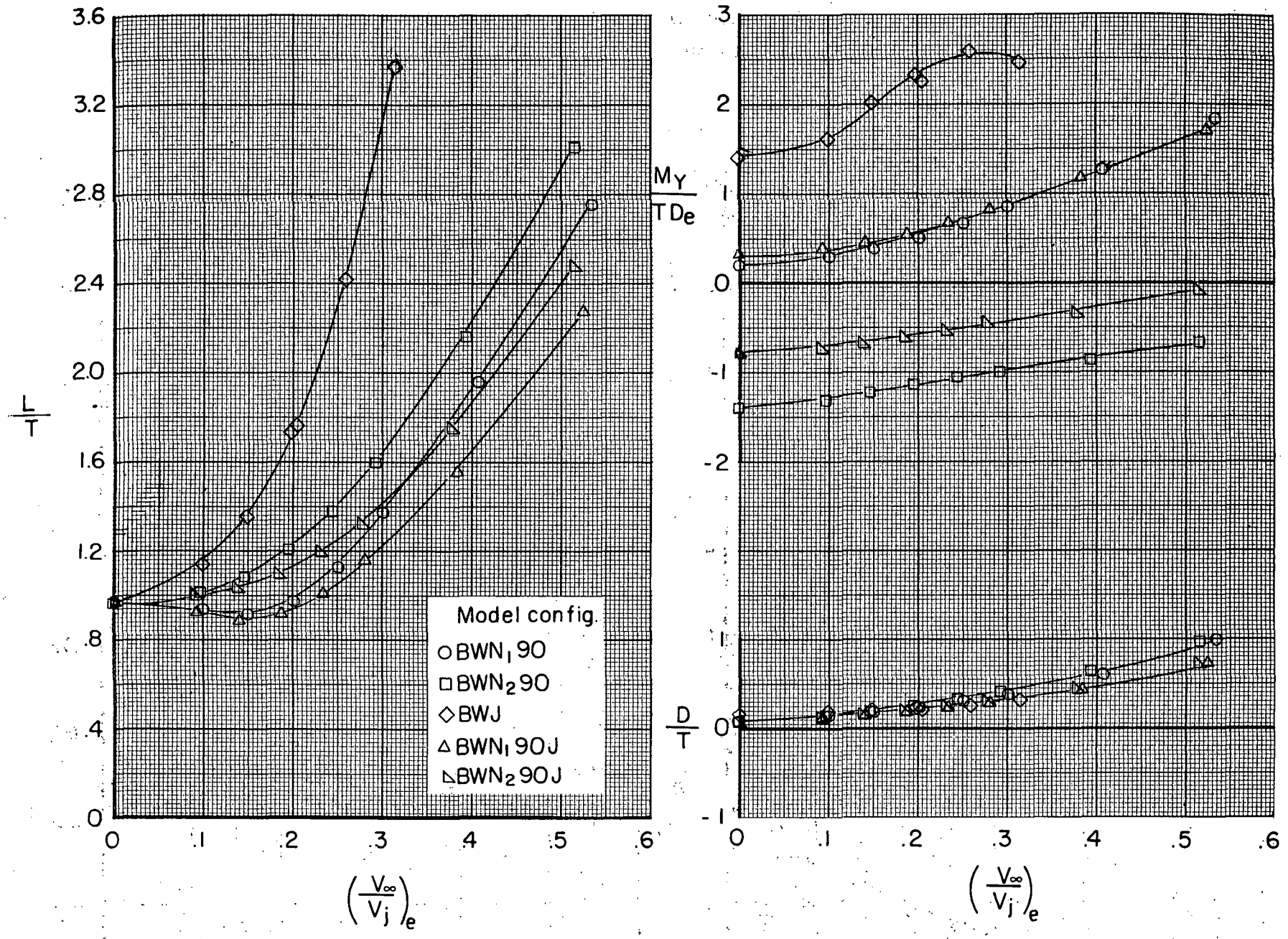
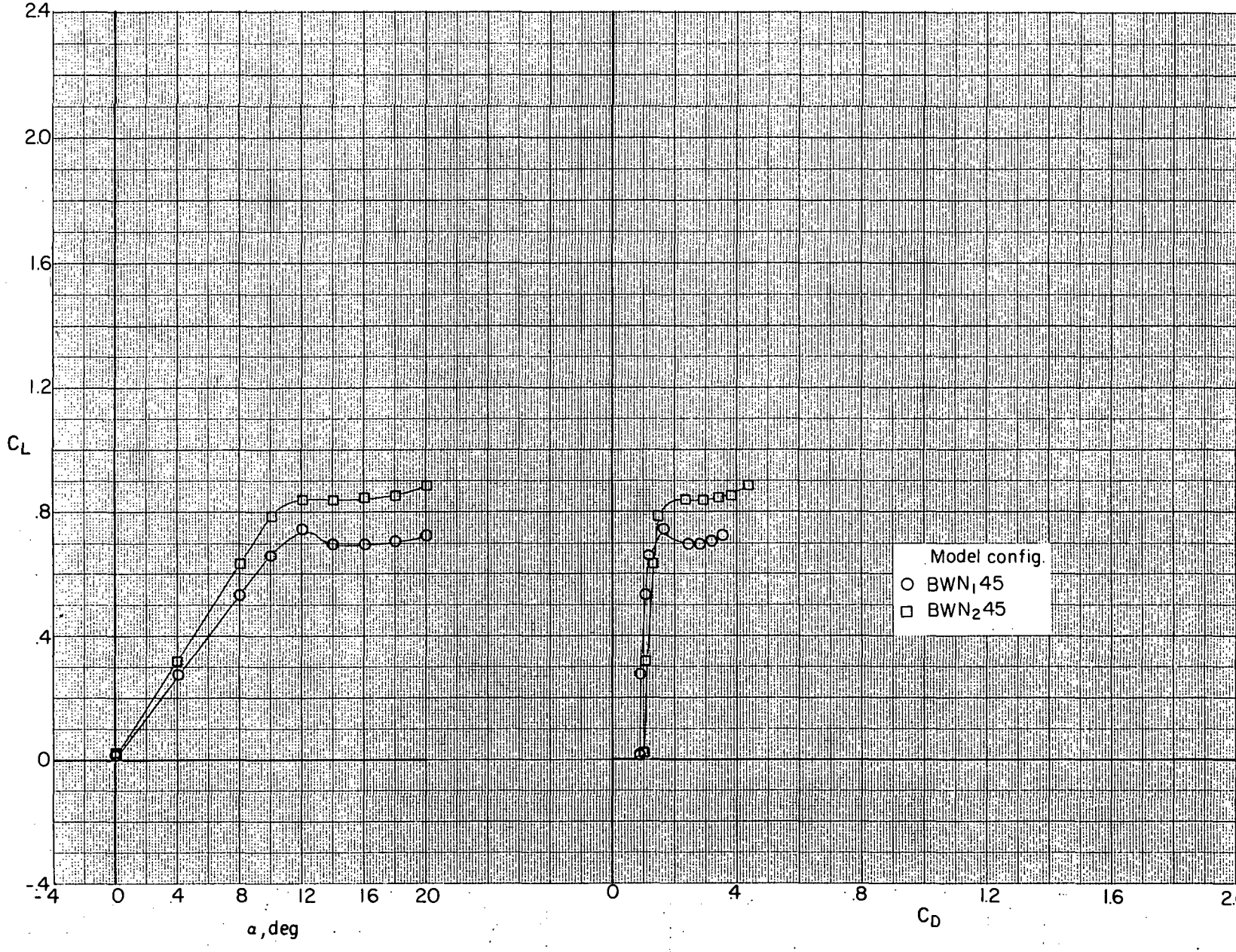
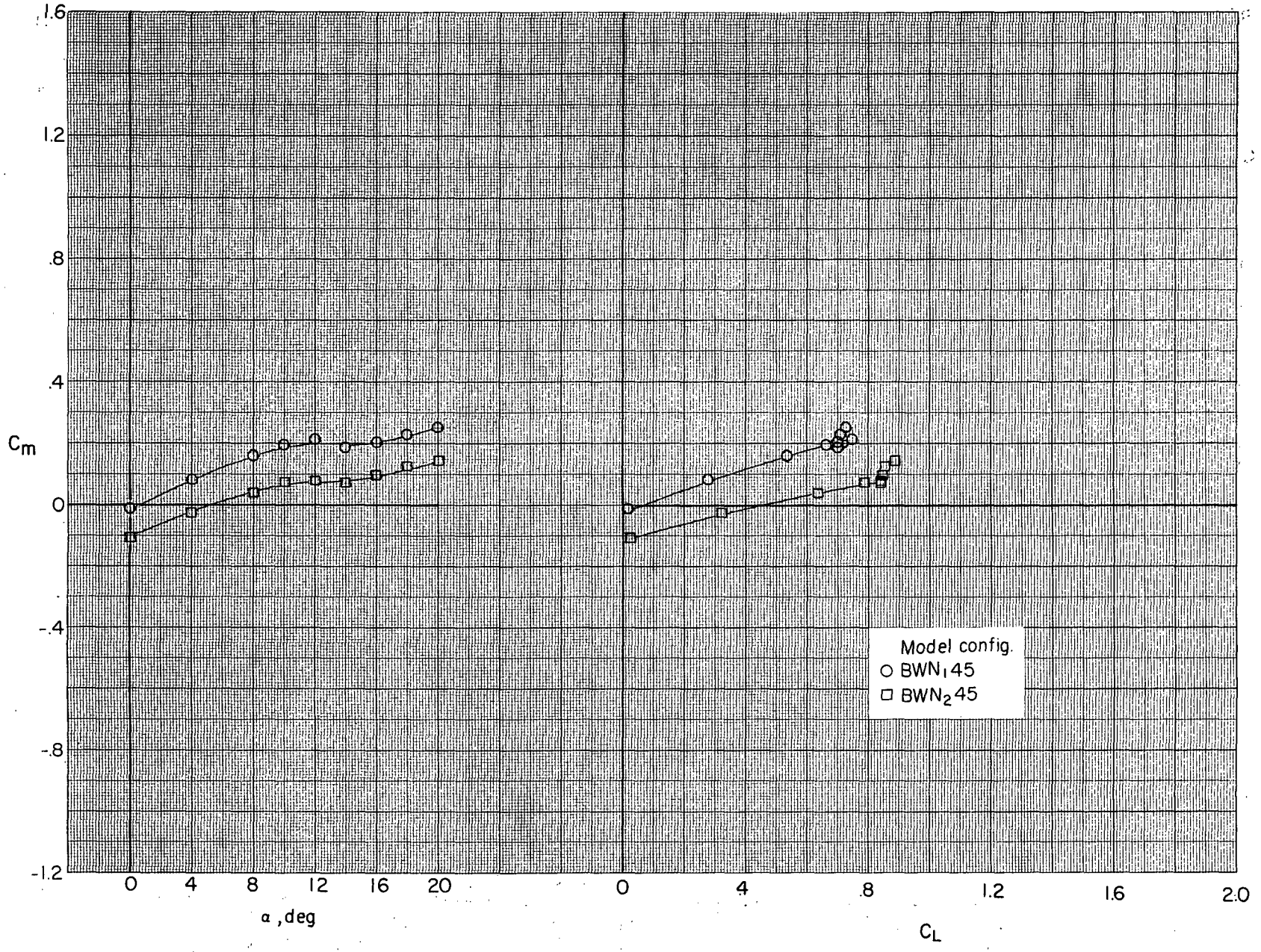


Figure 36.- Effect of thrust configuration on longitudinal aerodynamic characteristics at an angle of attack of 10^{o} with power.



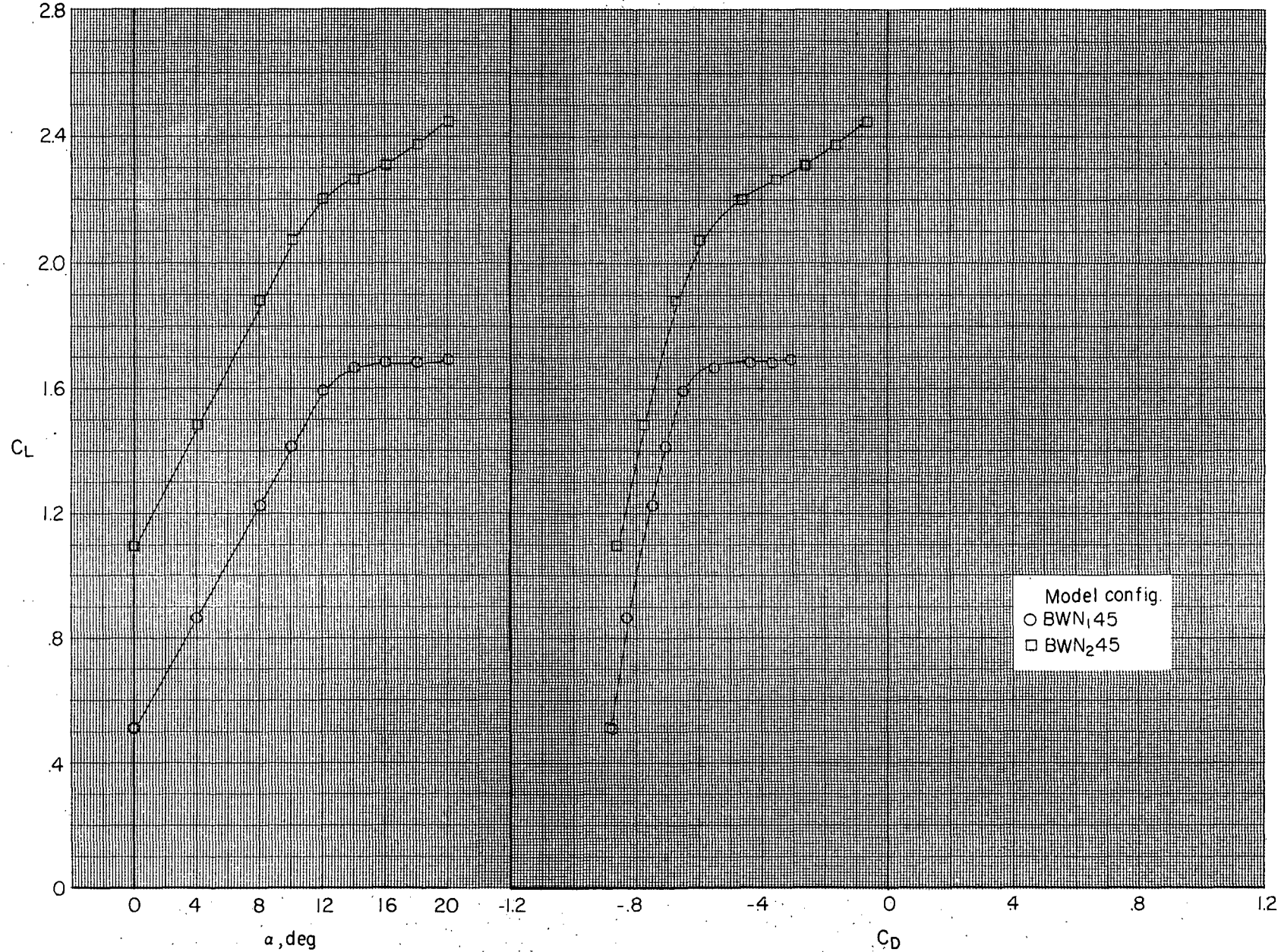
(a) Variation of C_L with α and C_D.

Figure 37.- Effect of thrust configuration on longitudinal aerodynamic characteristics without power. $\left(V_\infty/V_j\right)_e = \infty$.



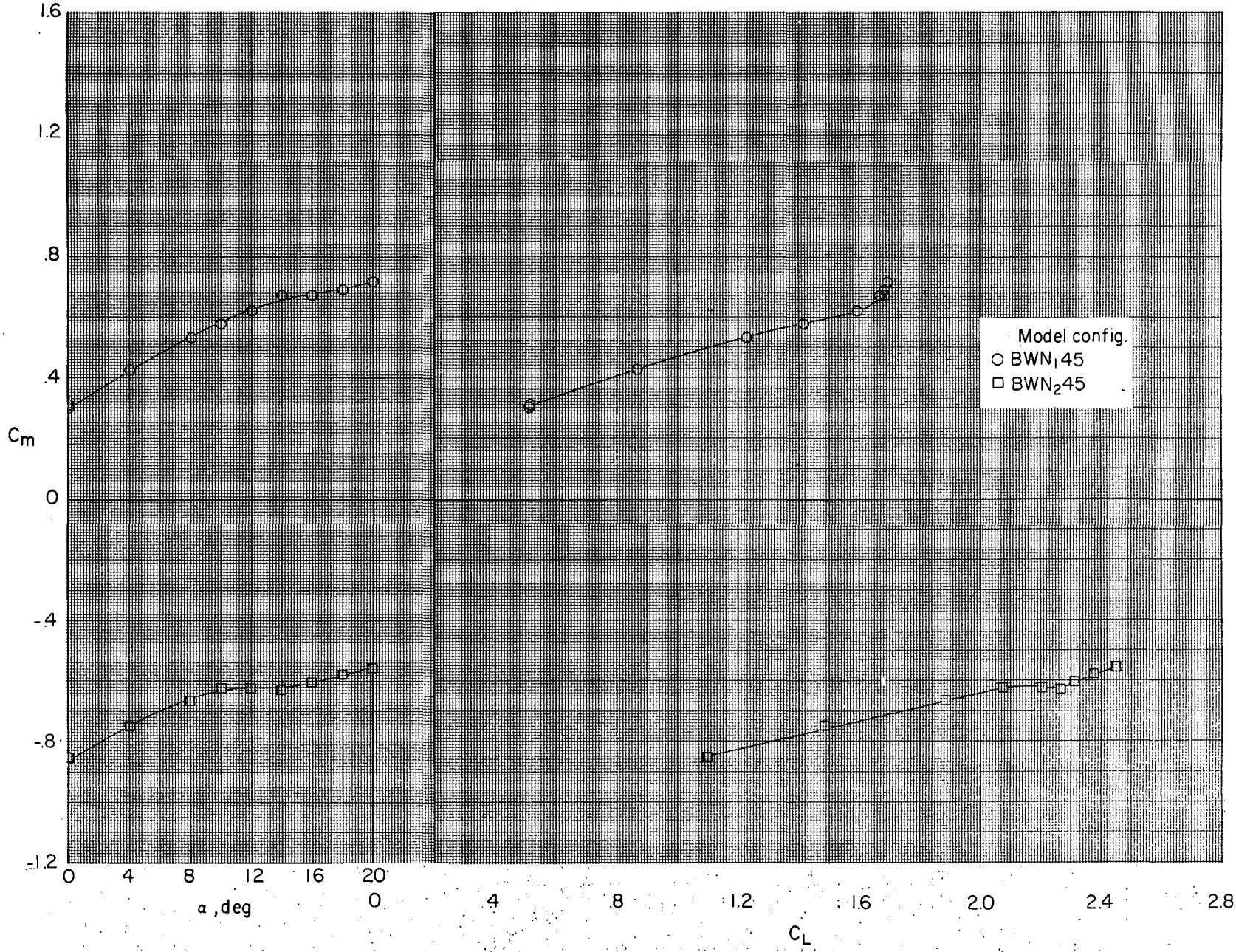
(b) Variation of C_m with α and C_L.

Figure 37.- Concluded.



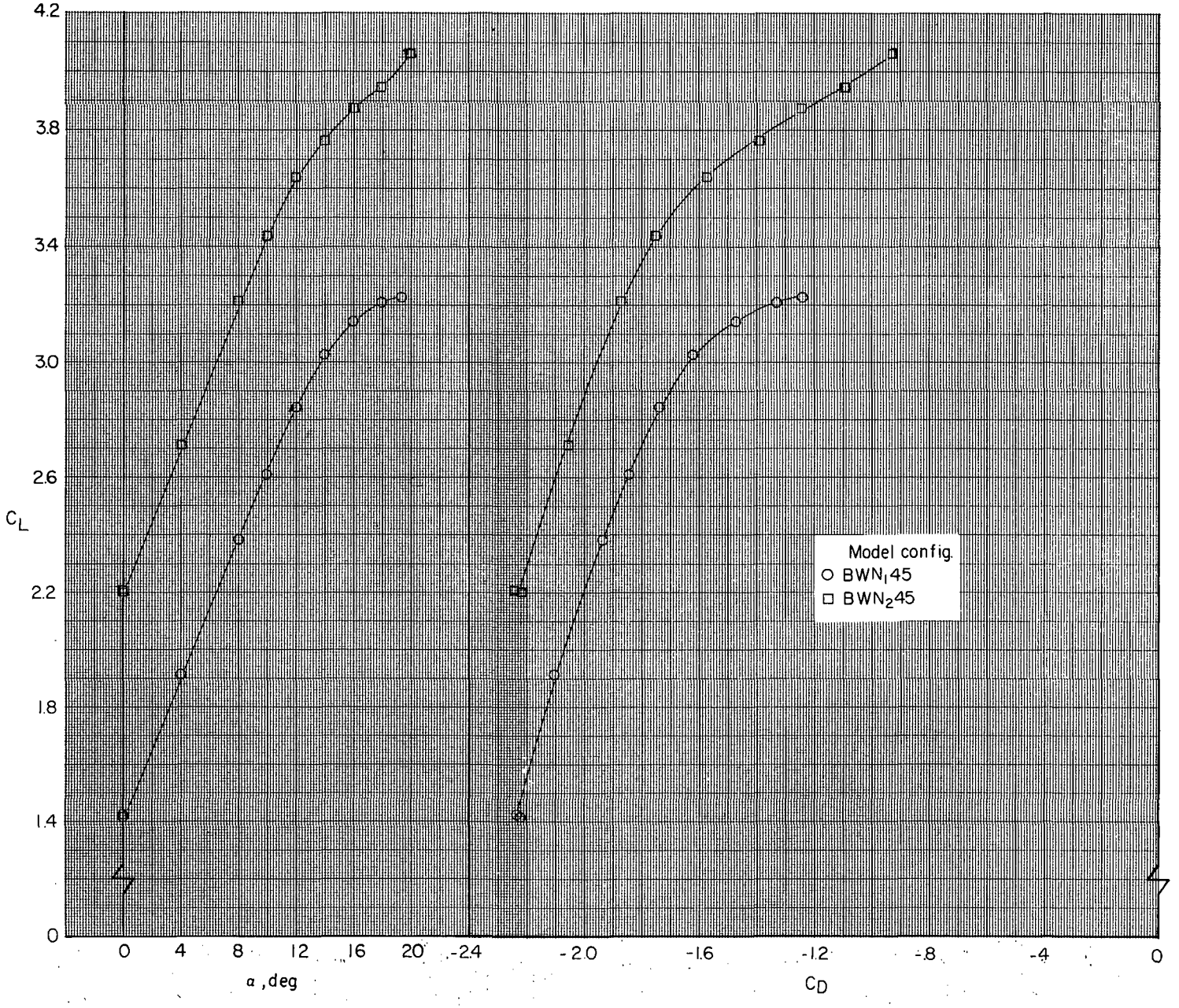
(a) Variation of C_L with α and C_D.

Figure 38.- Effect of thrust configuration on longitudinal aerodynamic characteristics with power. $\left(V_\infty/V_j\right)_e = 0.3$.



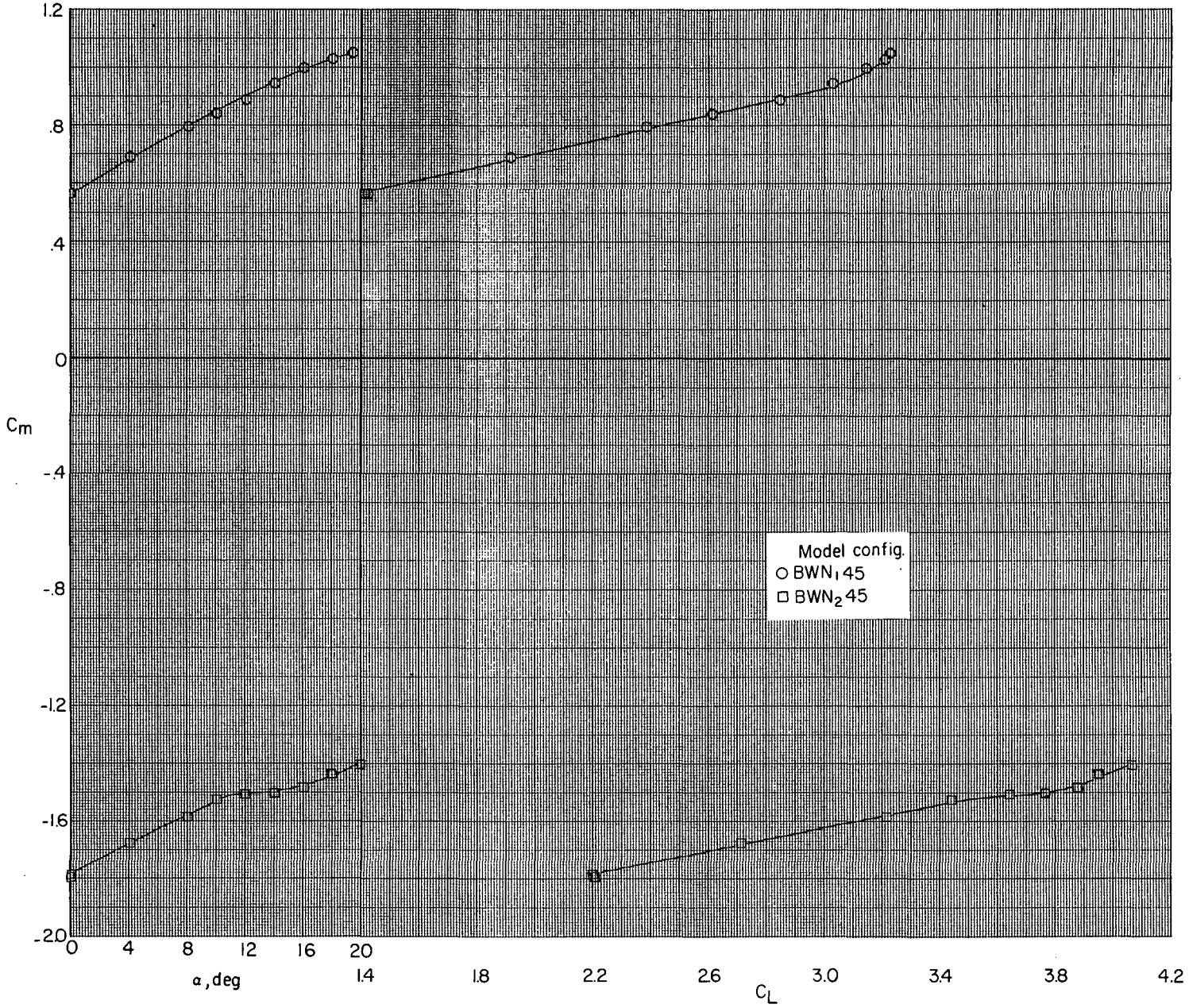
(b) Variation of C_m with α and C_L.

Figure 38.- Concluded.



(a) Variation of C_L with α and C_D.

Figure 39.- Effect of thrust configuration on longitudinal aerodynamic characteristics with power. $\left(V_\infty/V_j\right)_e = 0.2$.



(b) Variation of C_m with α and C_L.

Figure 39. - Concluded.

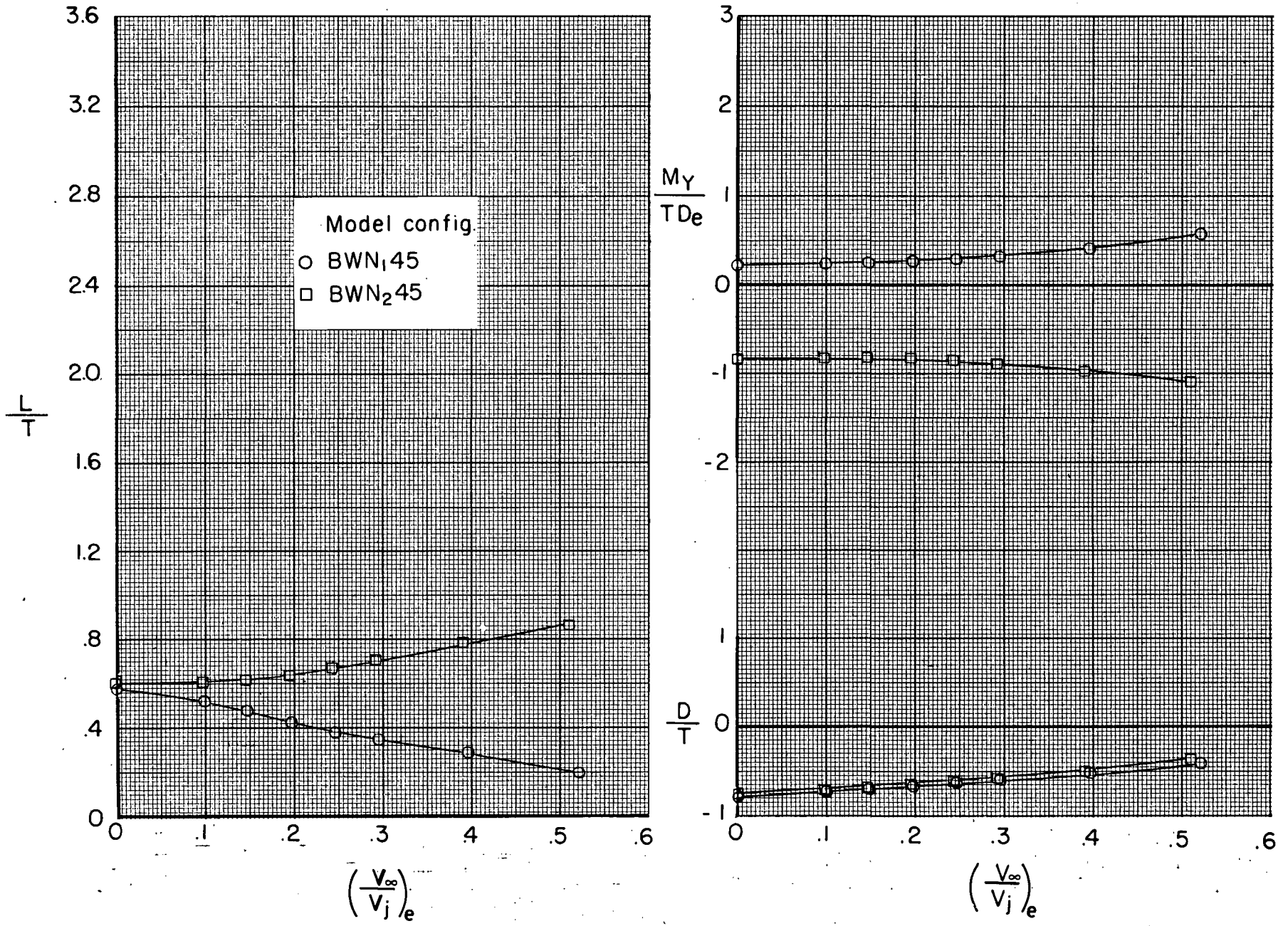


Figure 40.- Effect of thrust configuration on longitudinal aerodynamic characteristics at an angle of attack of 0^{o} with power.

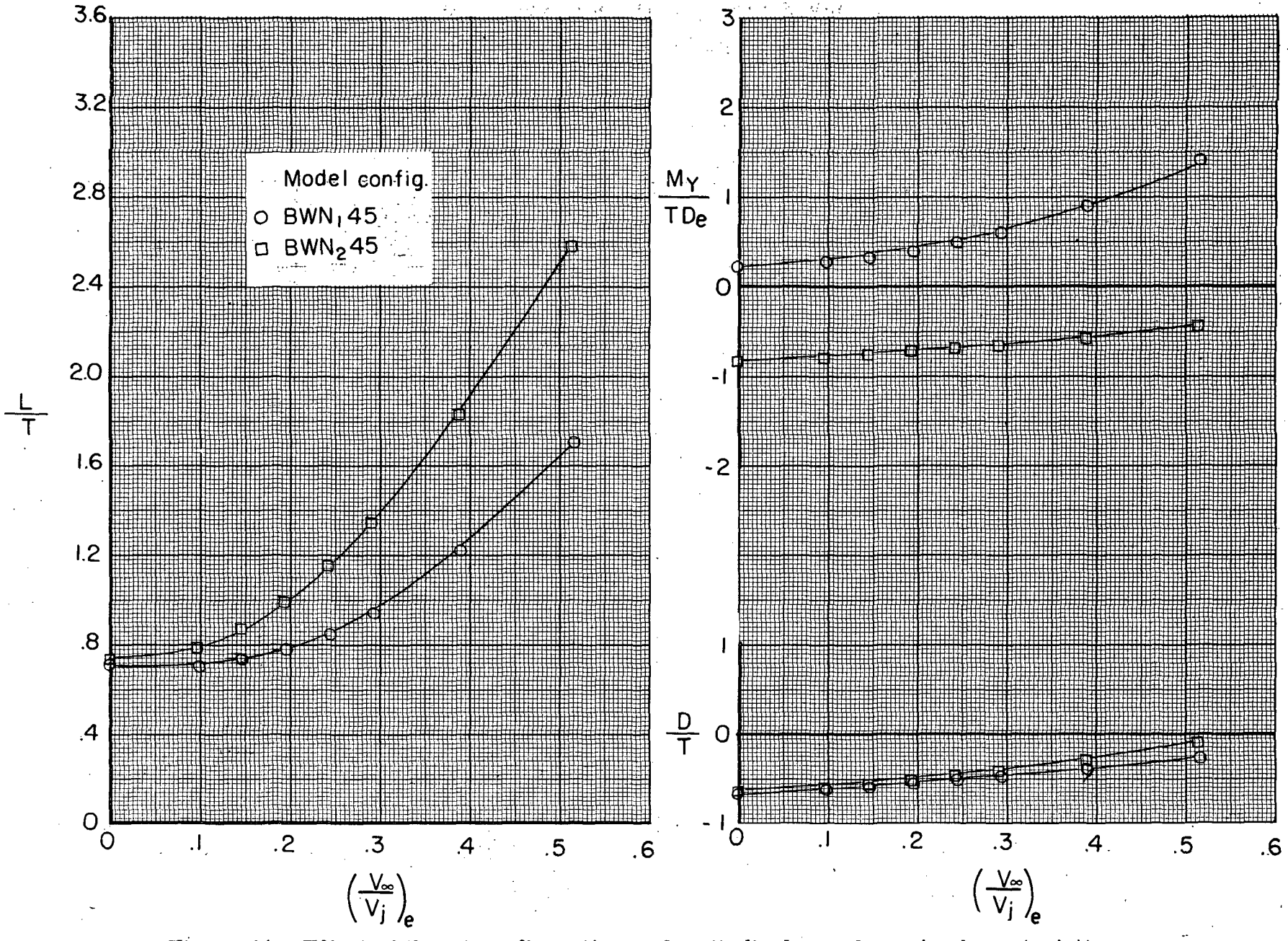
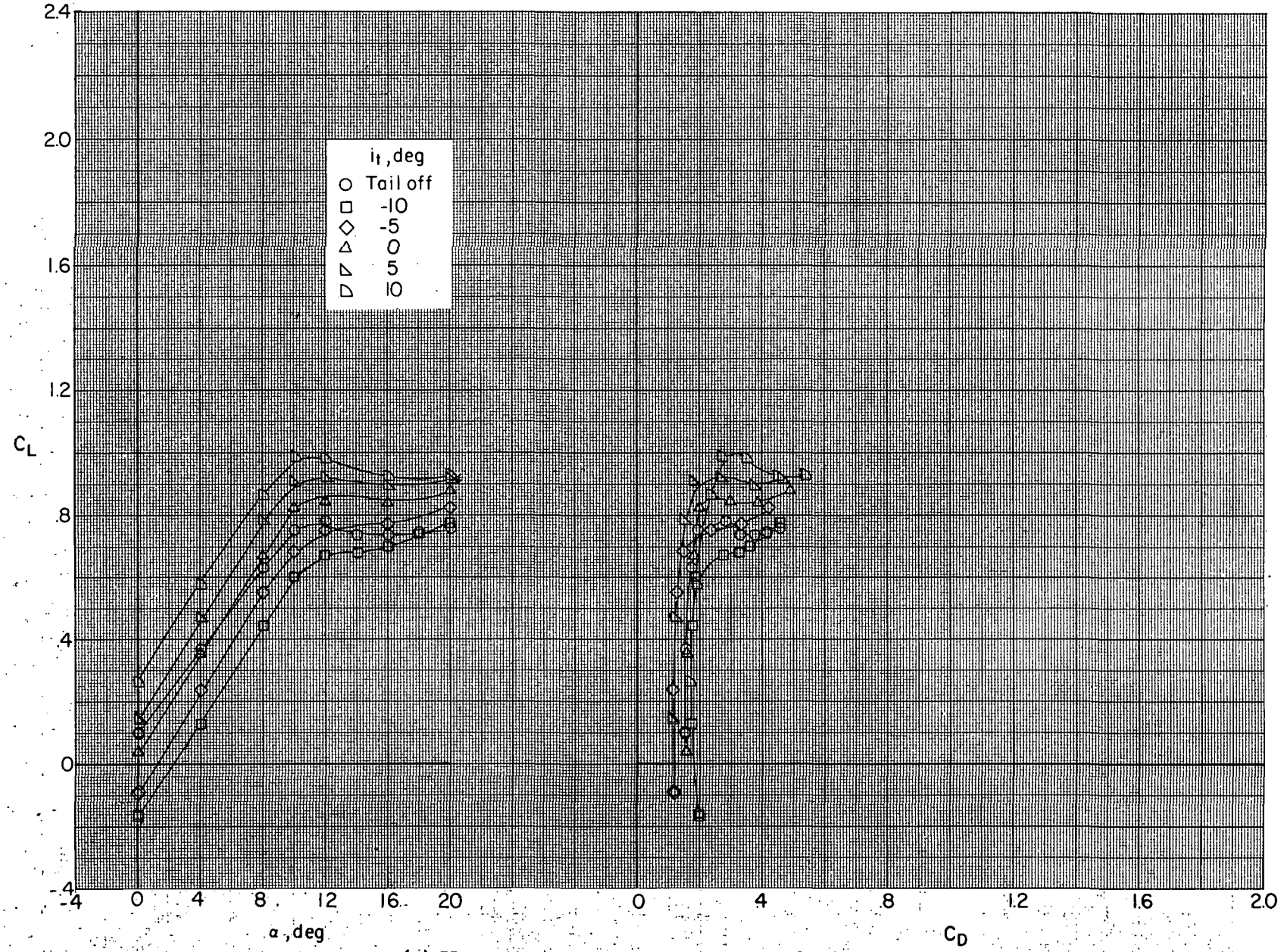
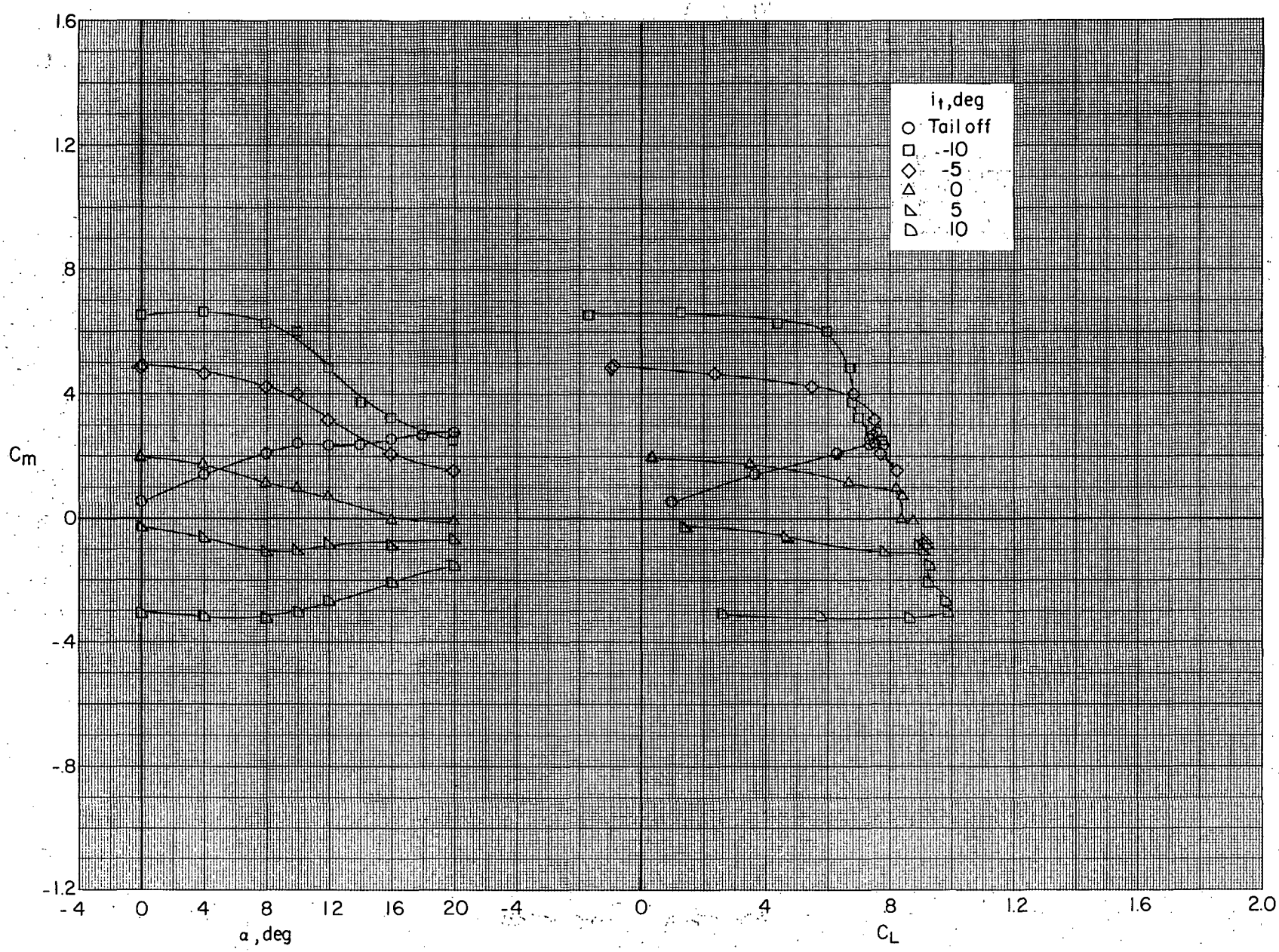


Figure 41.- Effect of thrust configuration on longitudinal aerodynamic characteristics at an angle of attack of 10^{o} with power.



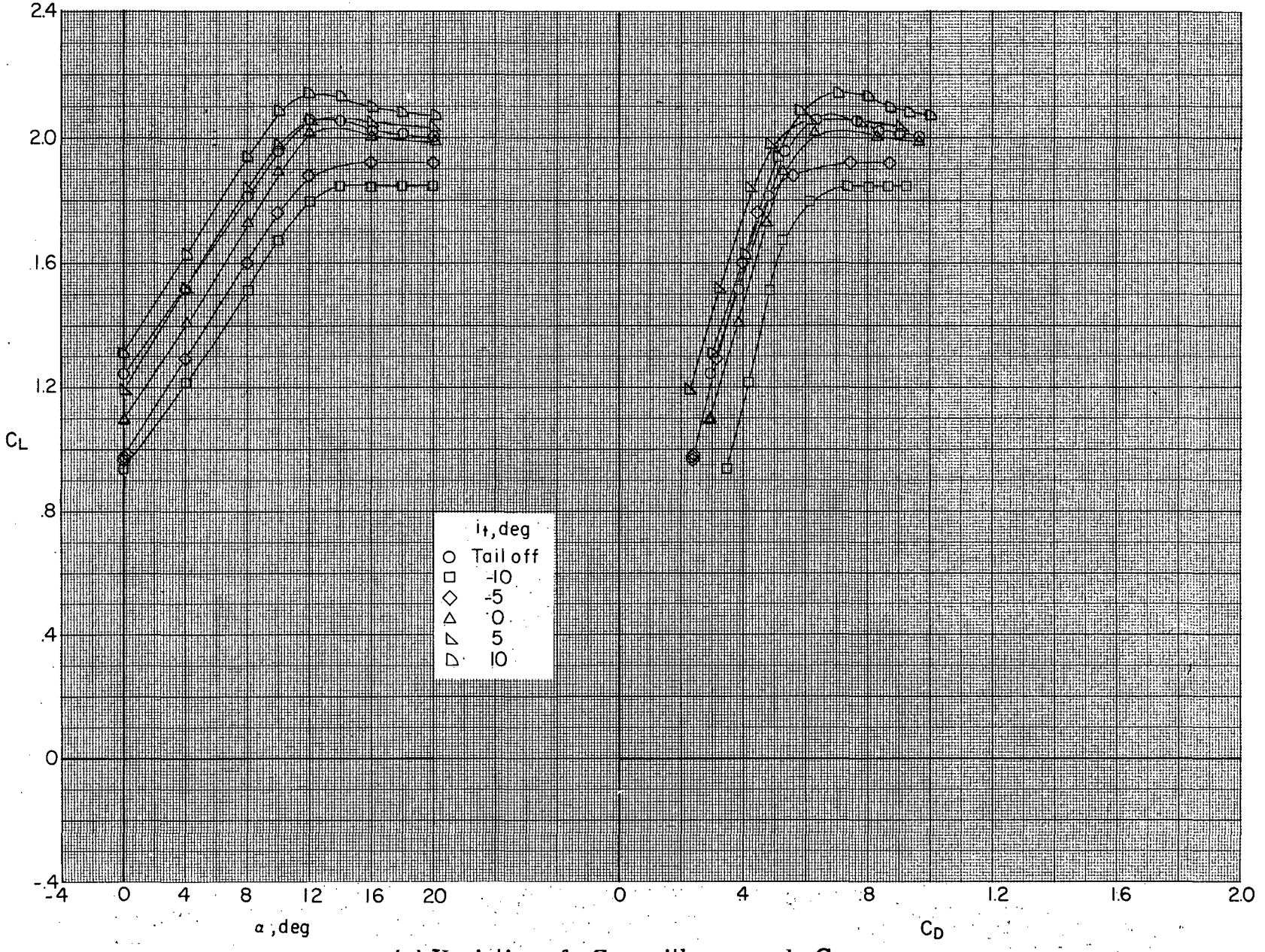
(a) Variation of C_L with α and C_D.

Figure 42.- Effect of tail incidence on longitudinal aerodynamic characteristics of $BWN_1 90VH$ configuration without power. $\left(V_\infty / V_j\right)_e = \infty$.



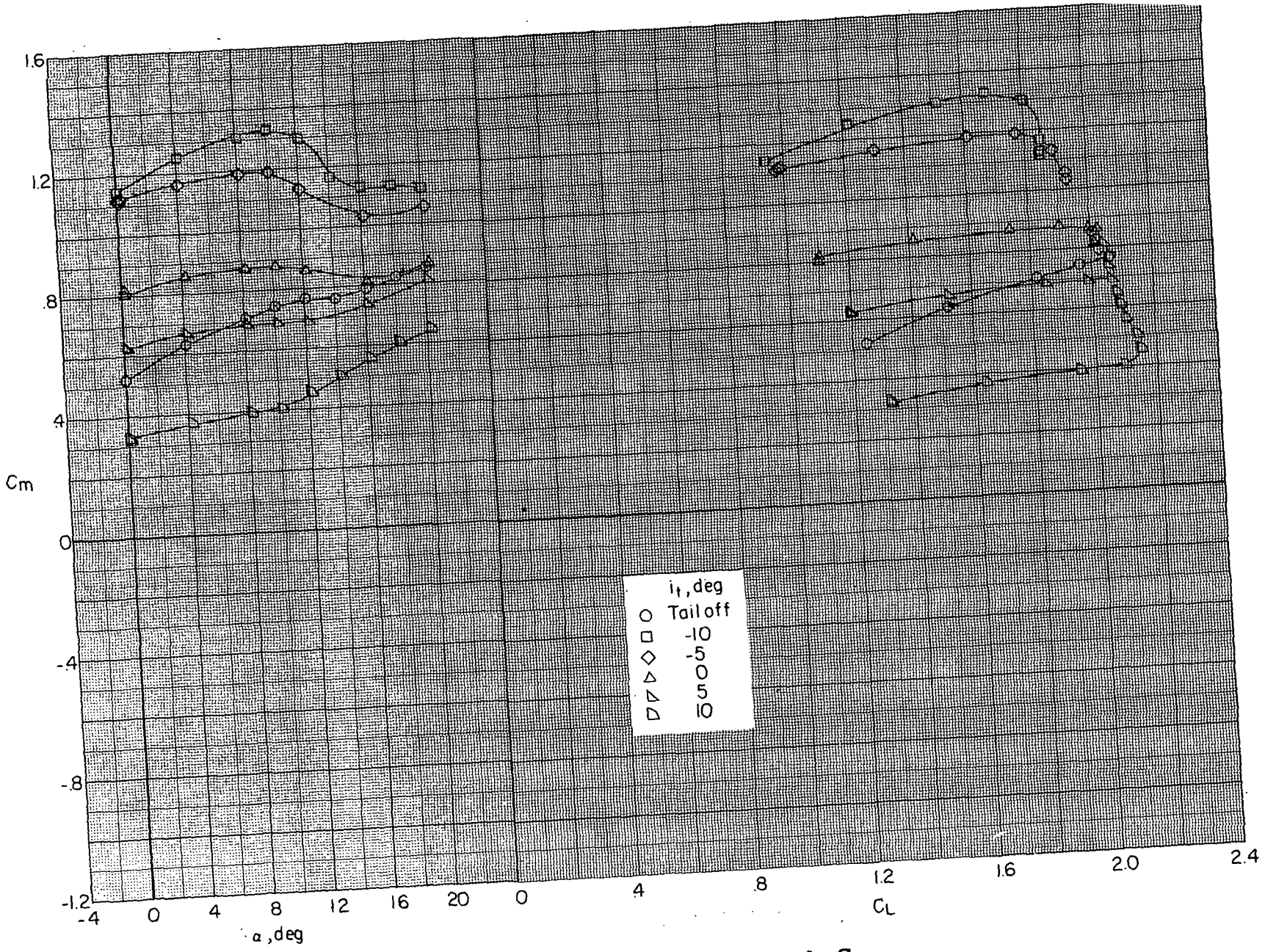
(b) Variation of C_m with α and C_L.

Figure 42.- Concluded.



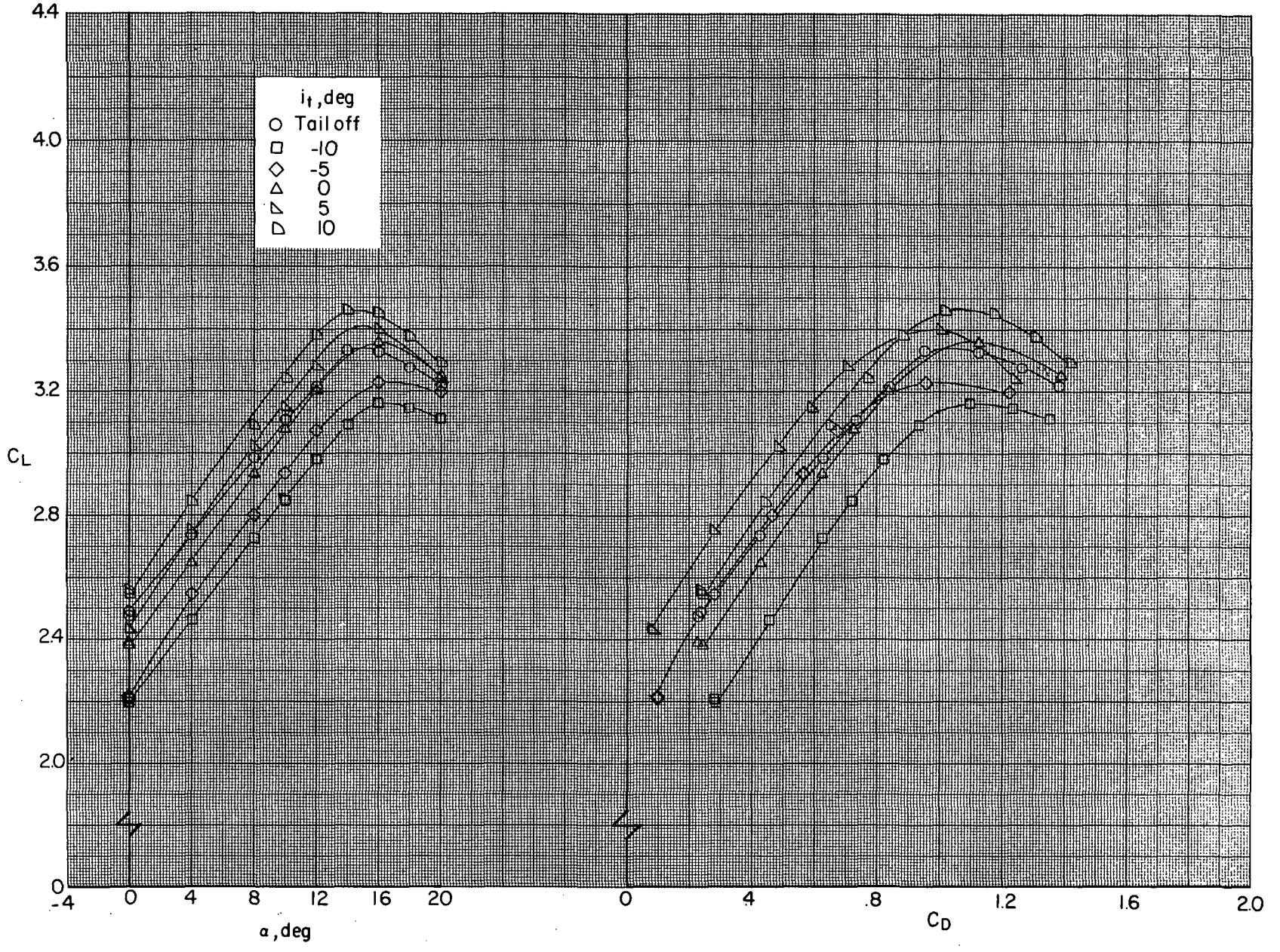
(a) Variation of C_L with α and C_D.

Figure 43.- Effect of tail incidence on longitudinal aerodynamic characteristics of $BWN_1 90VH$ configuration with power. $\left(V_\infty / V_j\right)_e = 0.3$.



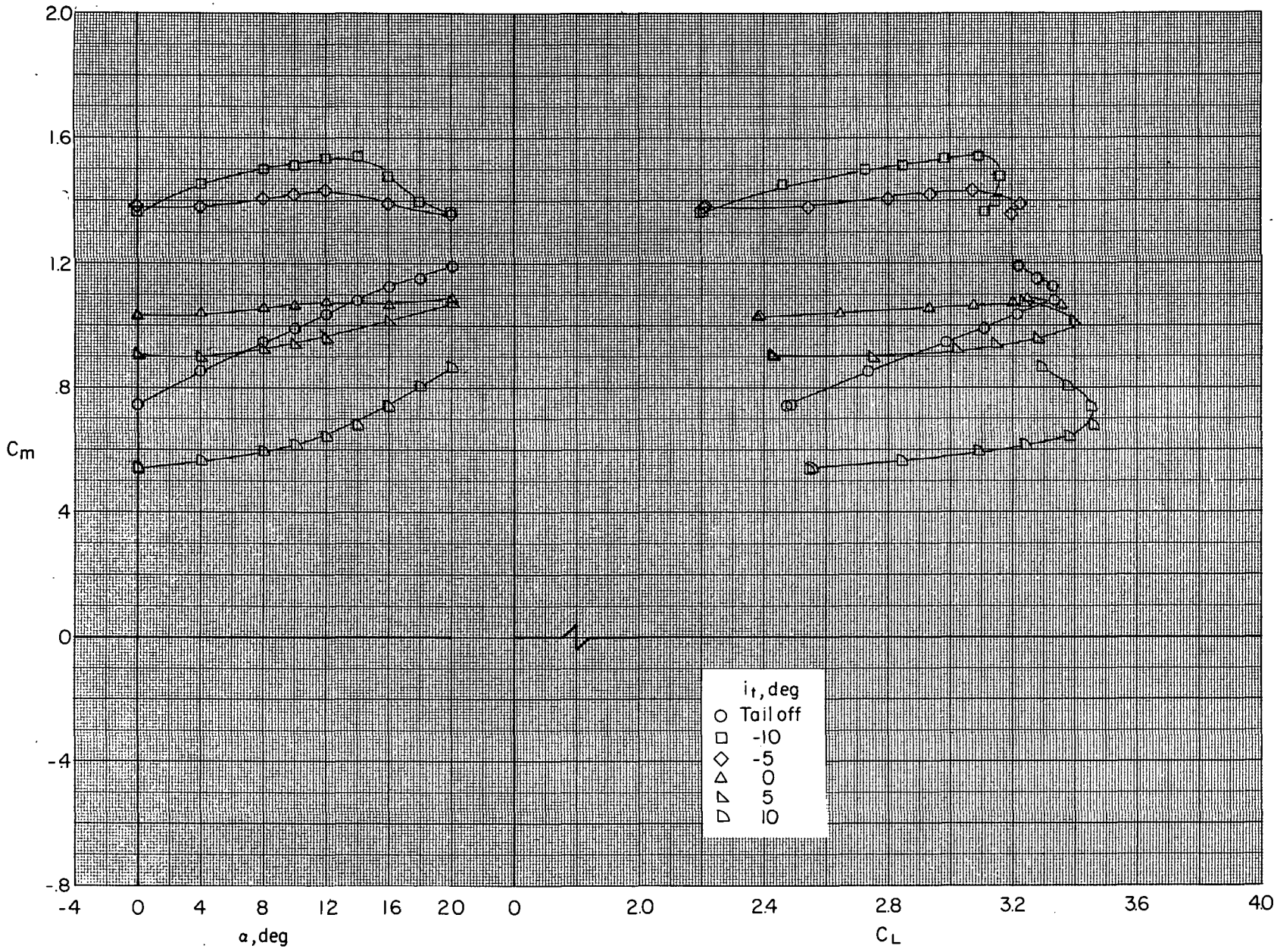
(b) Variation of C_m with α and C_L.

Figure 43.- Concluded.



(a) Variation of C_L with α and C_D.

Figure 44.- Effect of tail incidence on longitudinal aerodynamic characteristics of $BWN_1 90VH$ configuration with power. $\left(V_\infty/V_j\right)_e = 0.2$.



(b) Variation of C_m with α and C_L.

Figure 44.- Concluded.

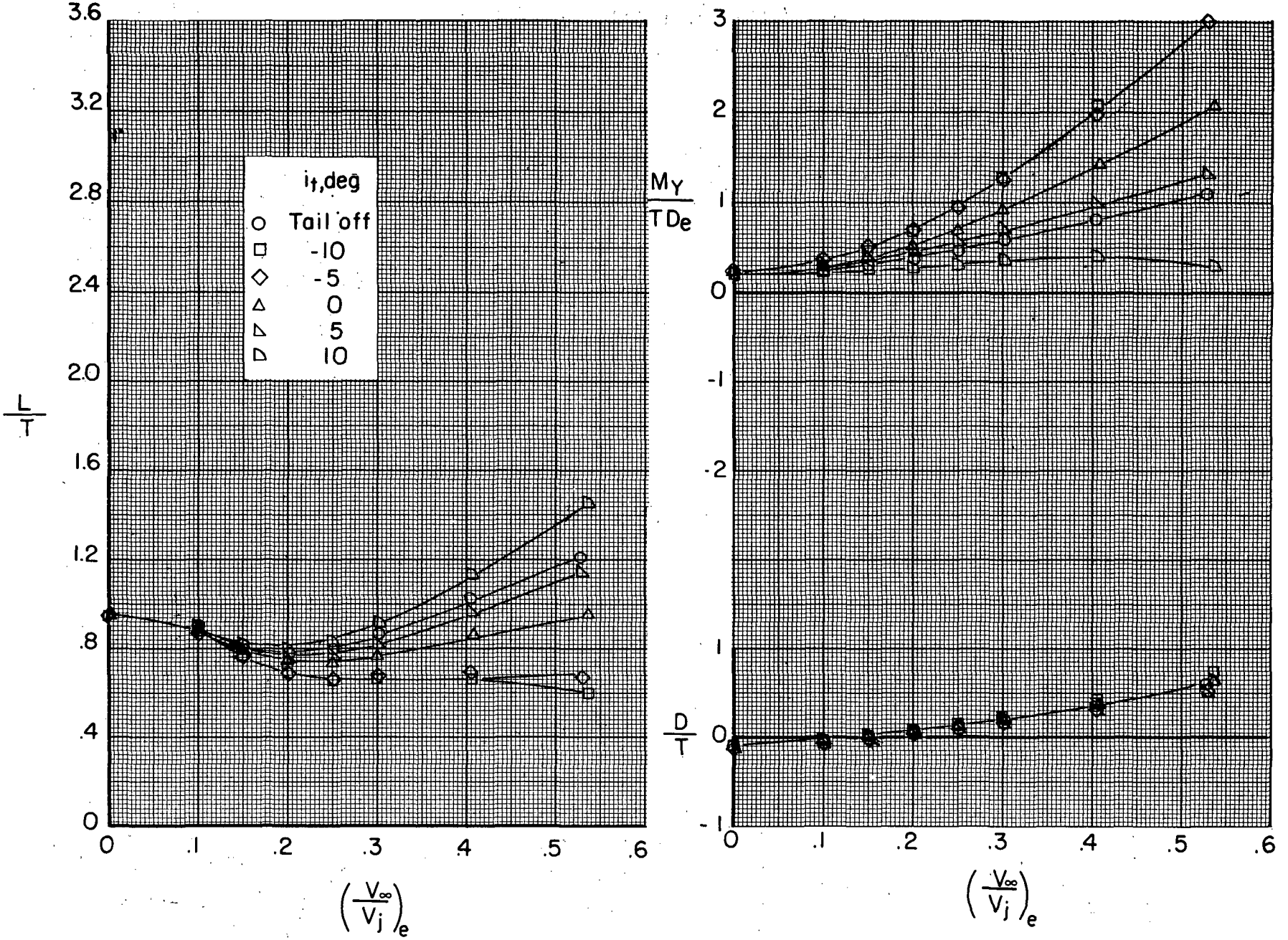


Figure 45.- Effect of tail incidence on longitudinal aerodynamic characteristics of $BWN_1 90VH$ configuration at an angle of attack of 0^o with power.

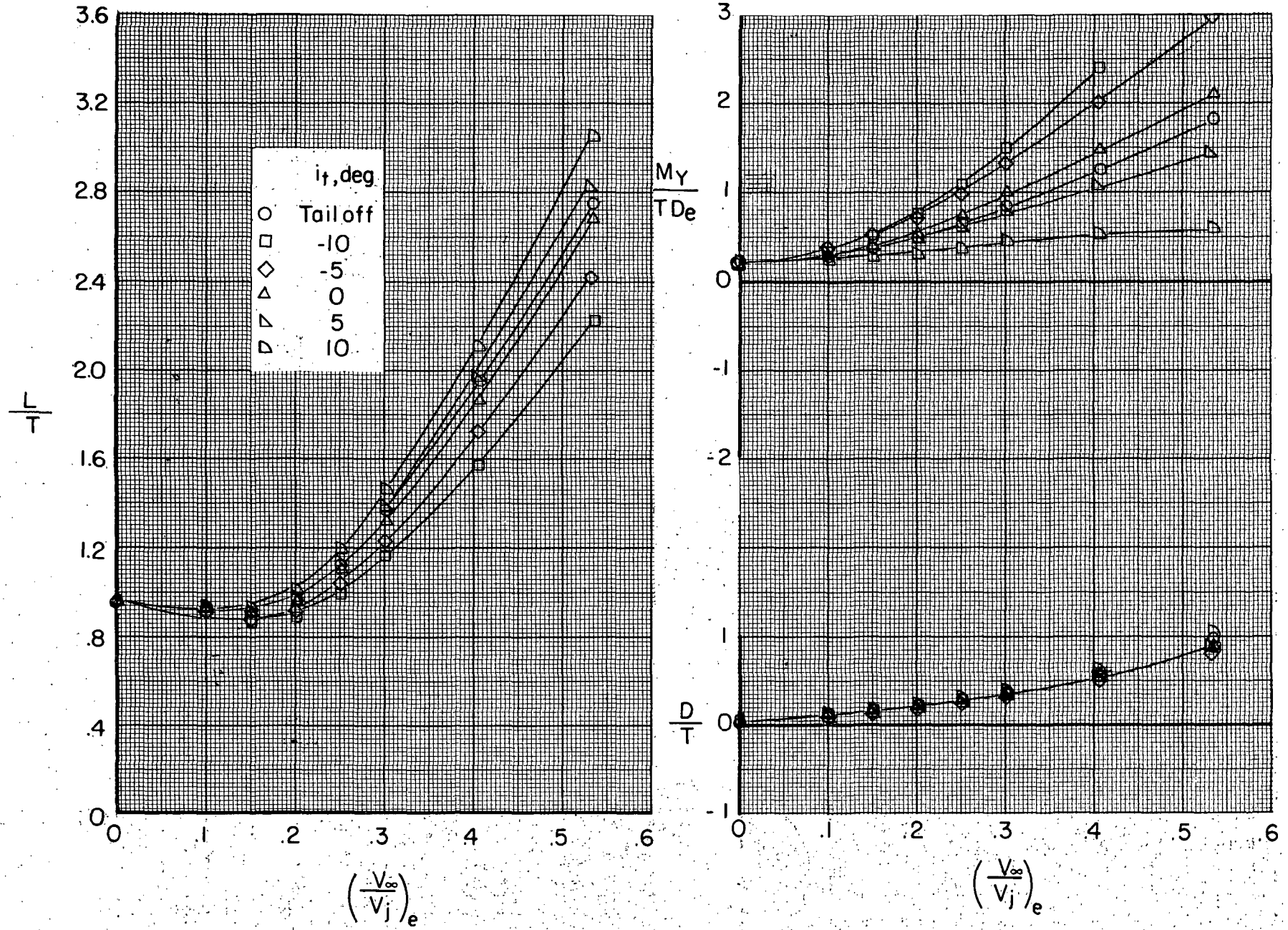
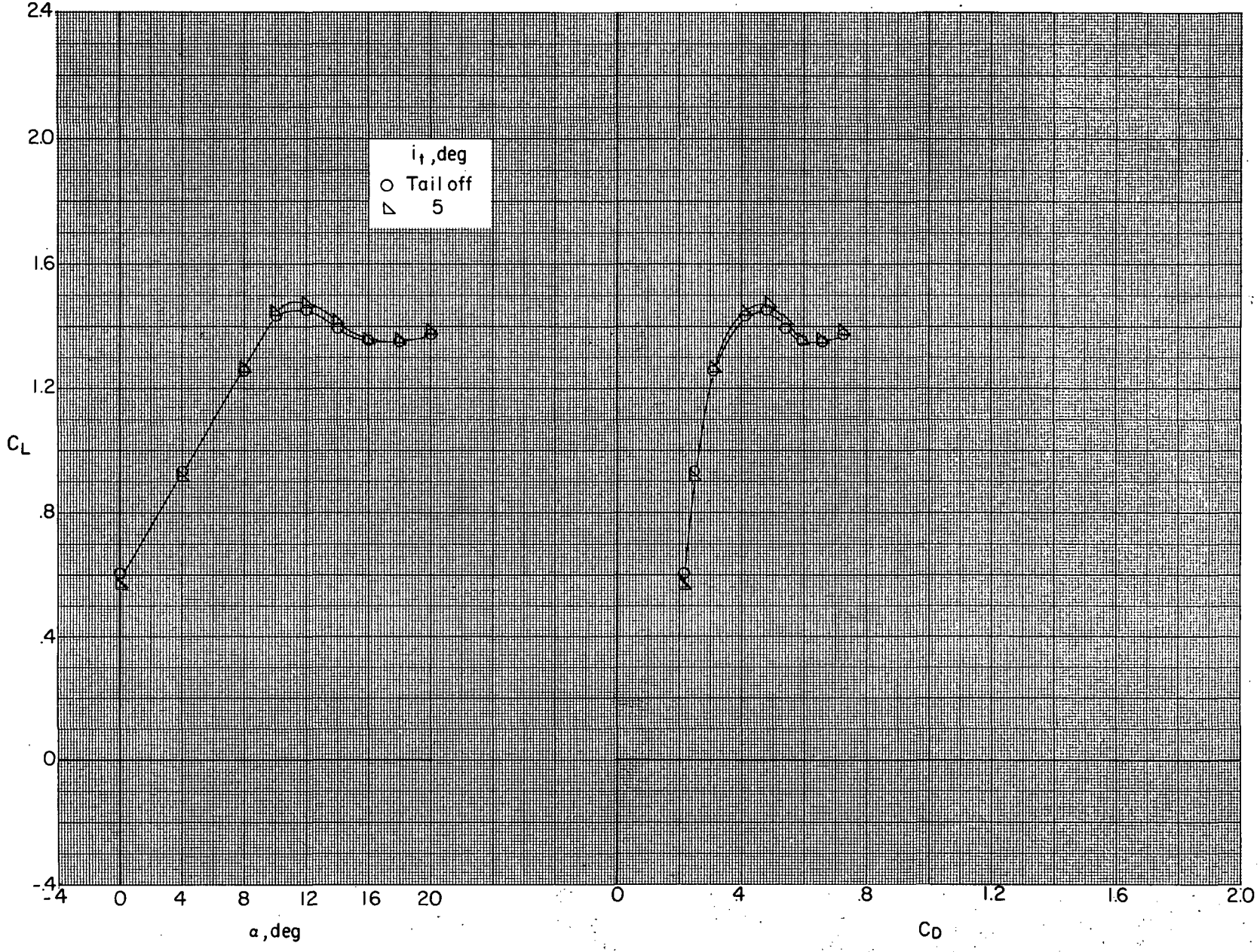
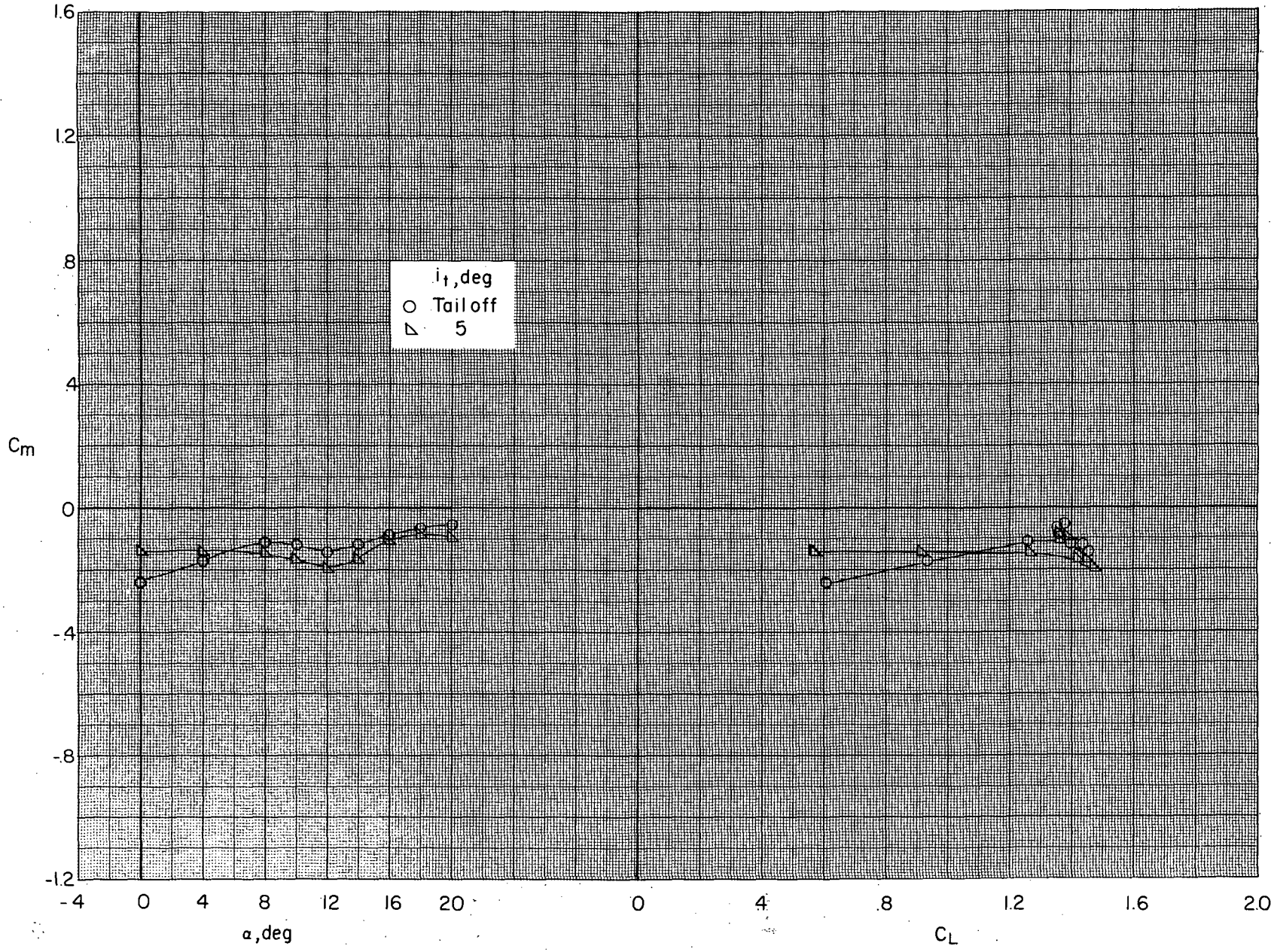


Figure 46.- Effect of tail incidence on longitudinal aerodynamic characteristics of BWN_190VH configuration at an angle of attack of 10^o with power.



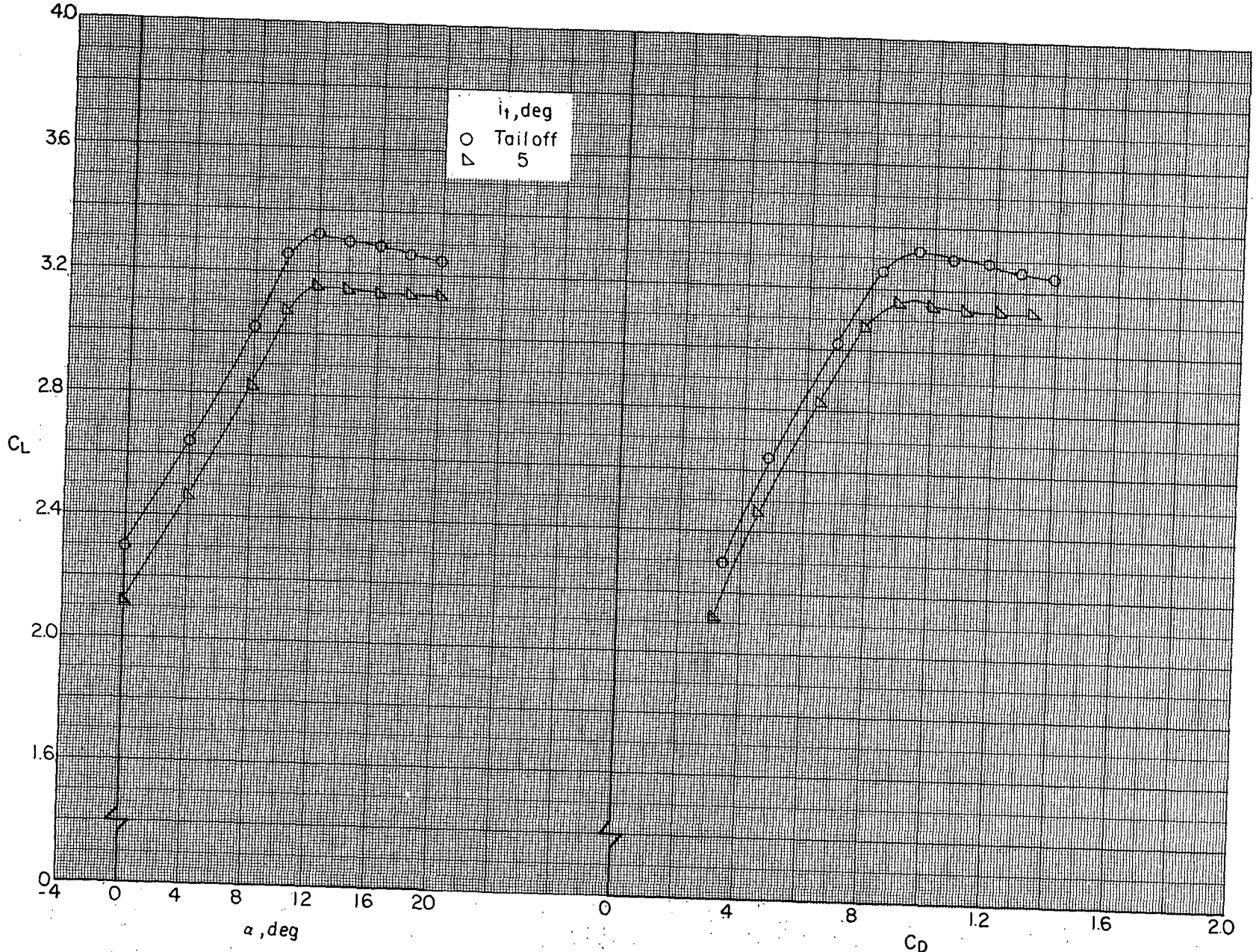
(a) Variation of C_L with α and C_D.

Figure 47.- Effect of tail incidence on longitudinal aerodynamic characteristics of $BWN_2 90VHf$ configuration without power. $\left(V_\infty / V_j\right)_e = \infty$.



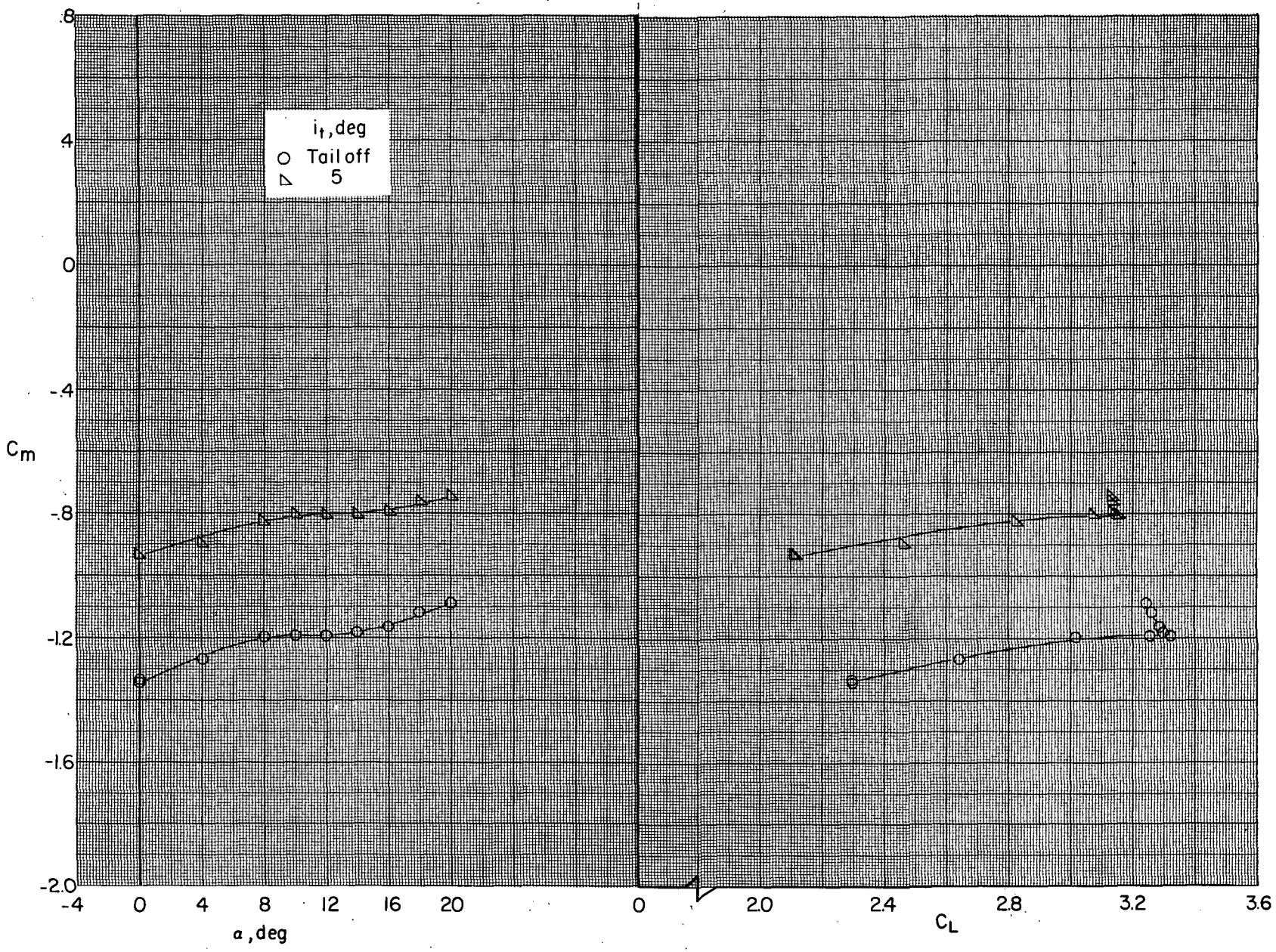
(b) Variation of C_m with α and C_L.

Figure 47.- Concluded.



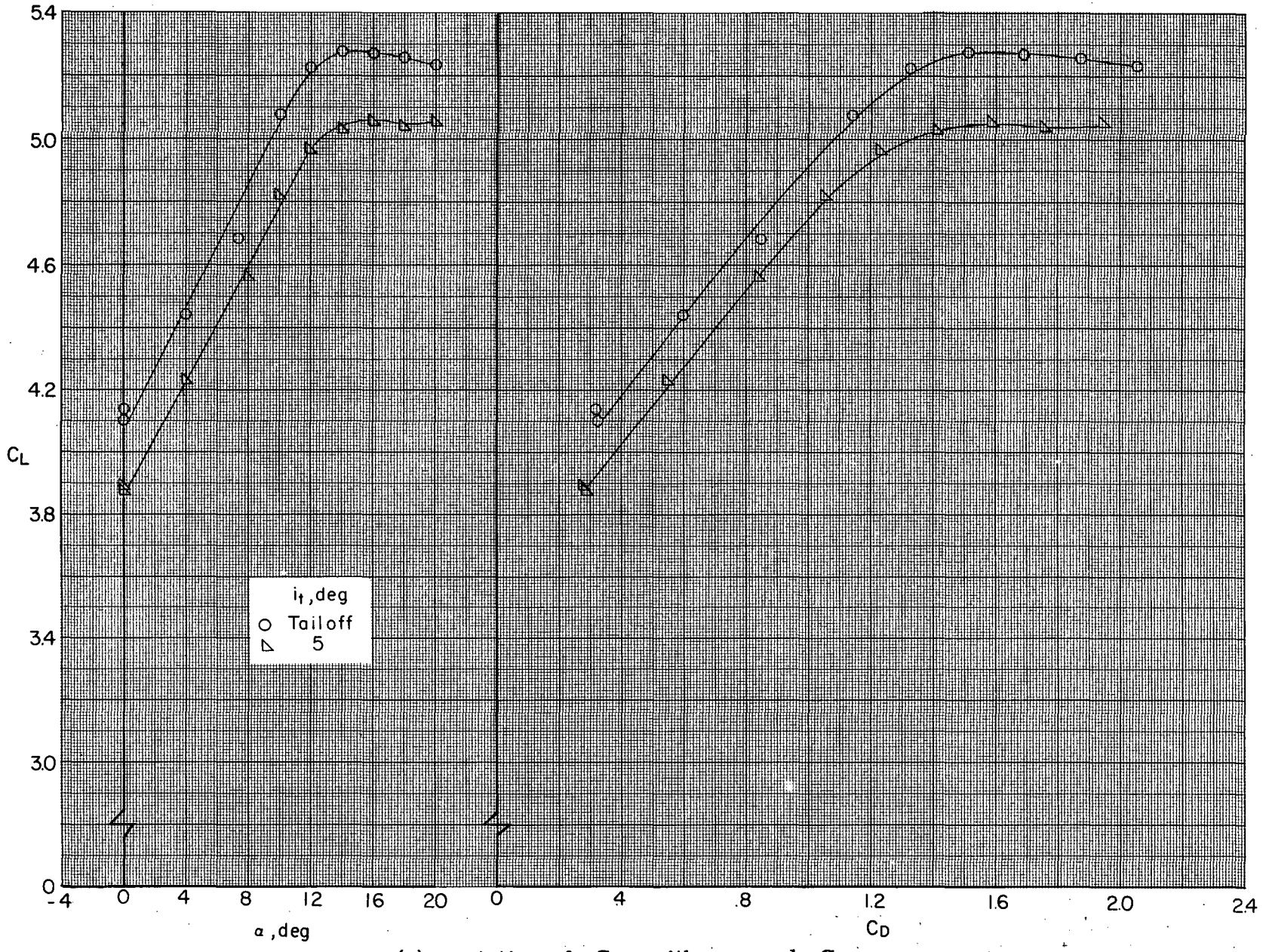
(a) Variation of C_L with α and C_D.

Figure 48.- Effect of tail incidence on longitudinal aerodynamic characteristics of $BWN_2 90 VHf$ configuration with power. $\left(V_\infty/V_j\right)_e = 0.3$.



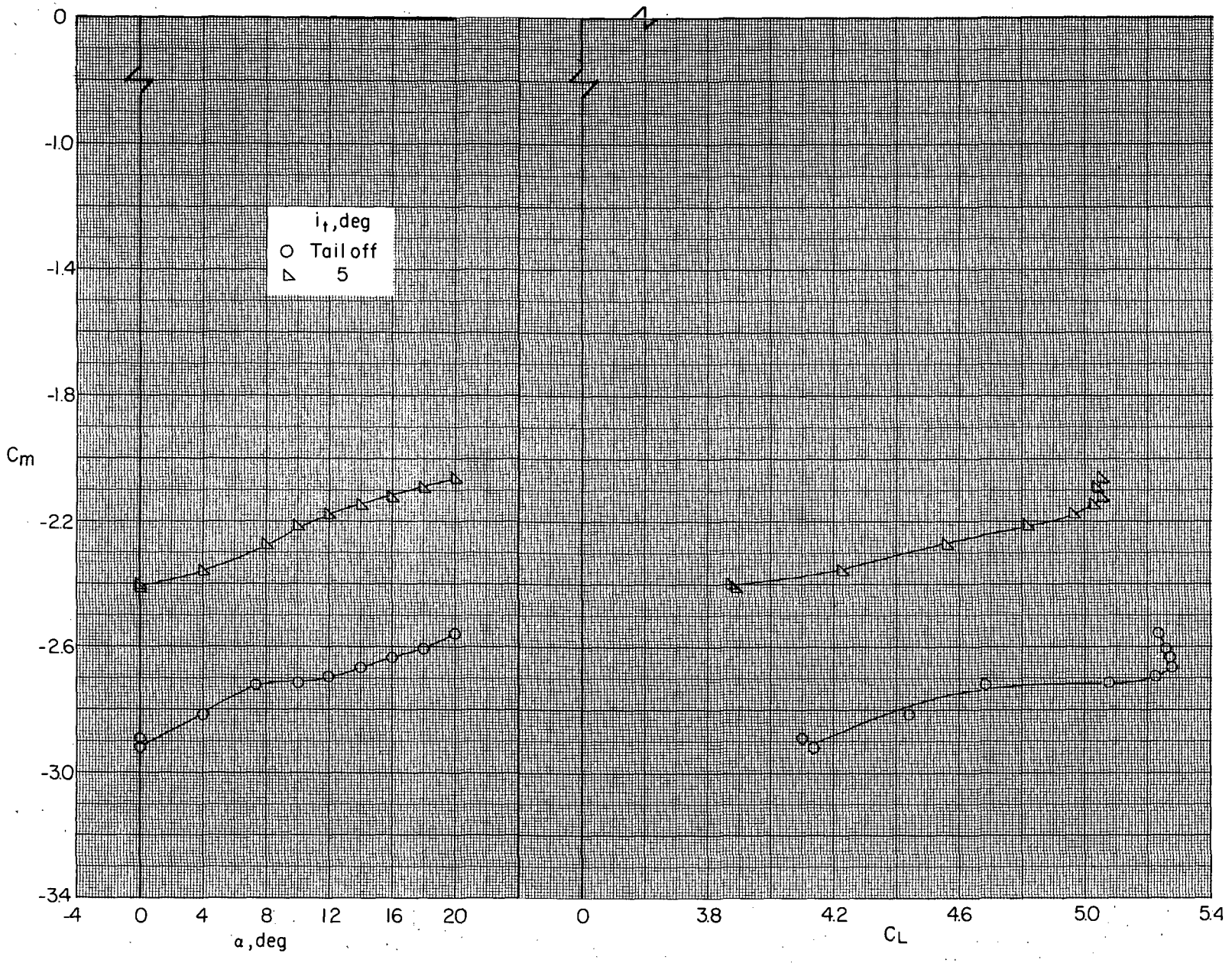
(b) Variation of C_m with α and C_L.

Figure 48. - Concluded.



(a) Variation of C_L with α and C_D.

Figure 49.- Effect of tail incidence on longitudinal aerodynamic characteristics of $BWN_2$90VHf configuration with power. $\left(V_\infty/V_j\right)_e = 0.2$.



(b) Variation of C_m with α and C_L.

Figure 49.- Concluded.

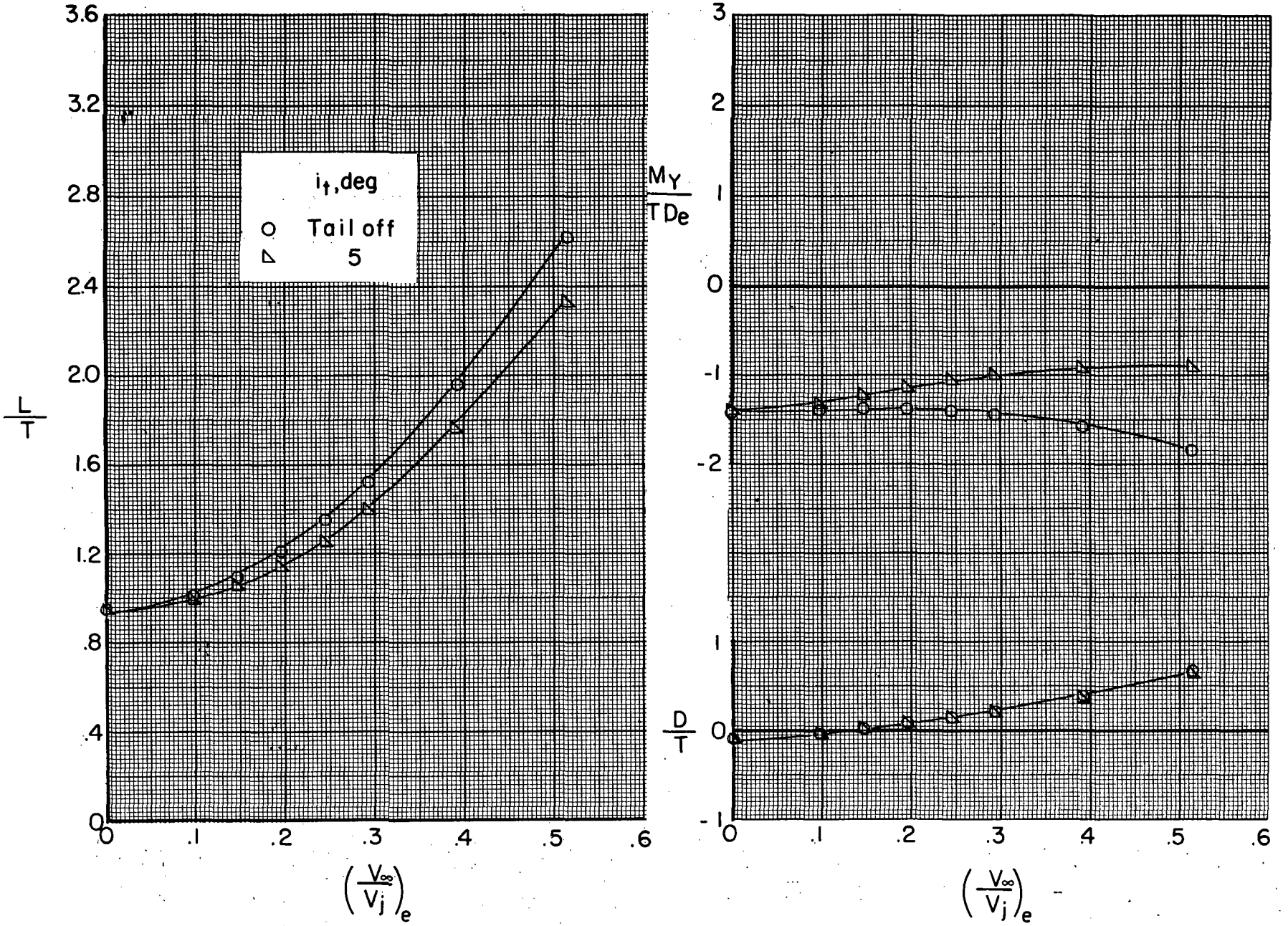


Figure 50.- Effect of tail incidence on longitudinal aerodynamic characteristics of $BWN_2$90VHf configuration at an angle of attack of 0^o with power.

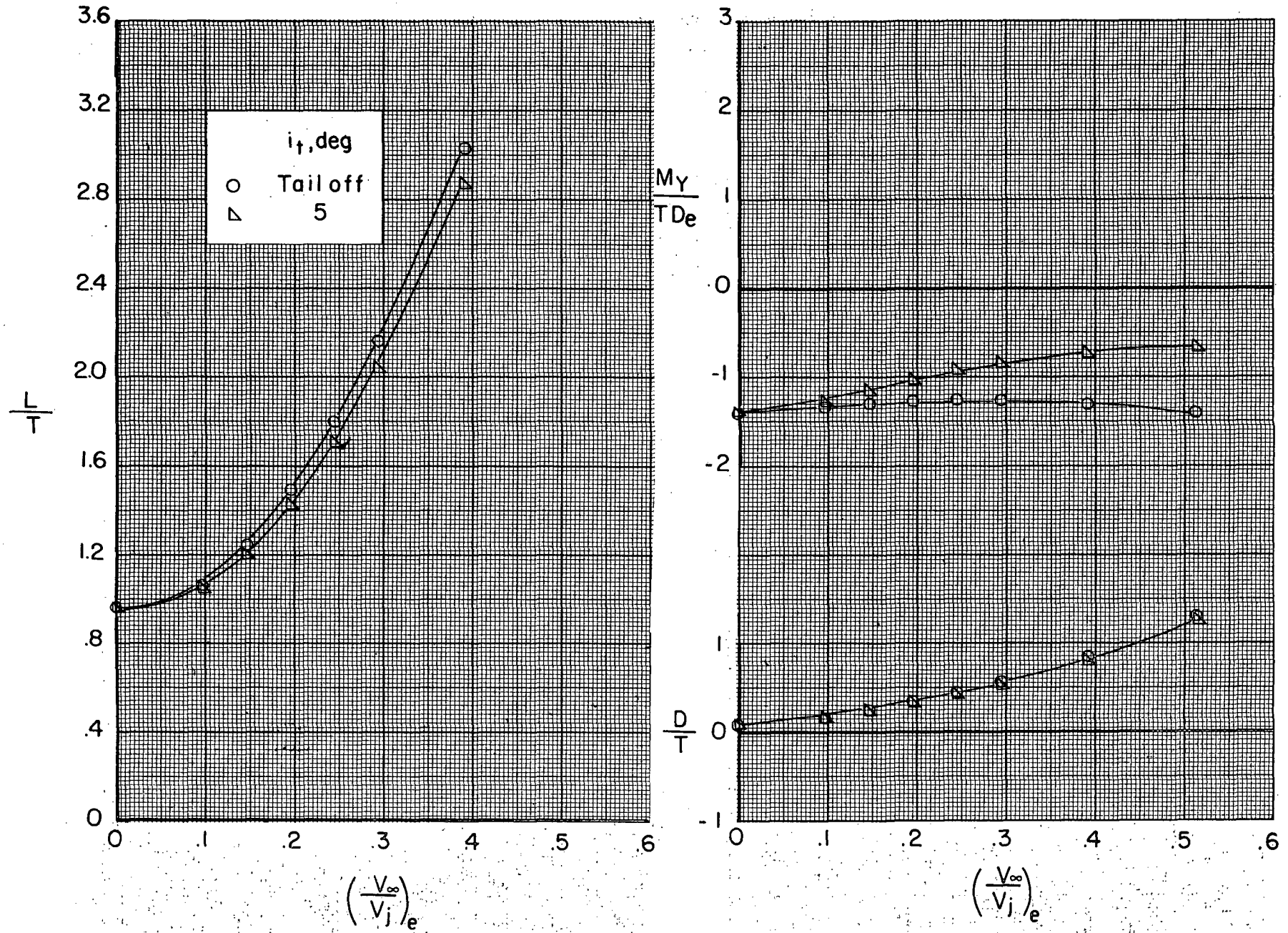
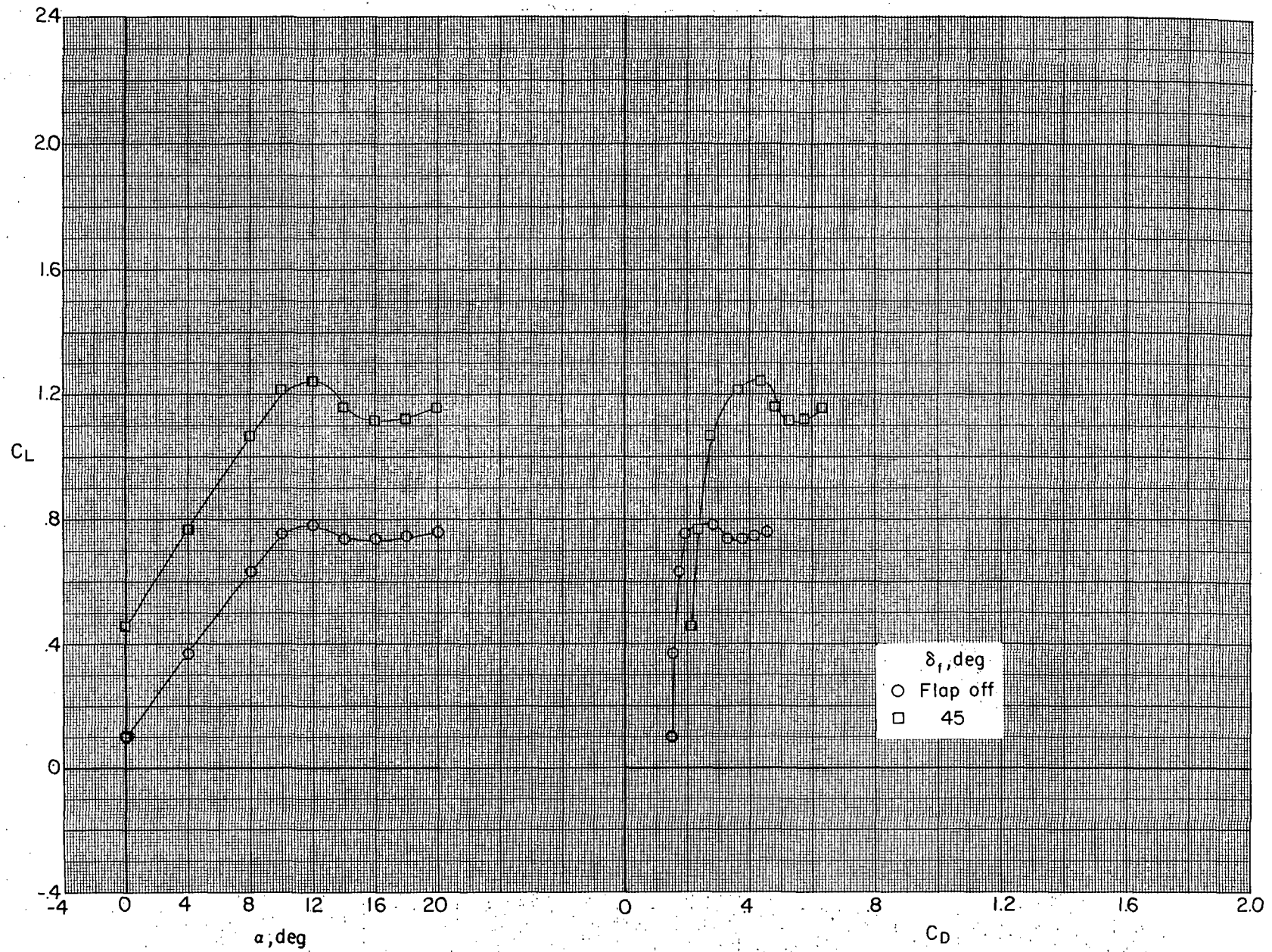
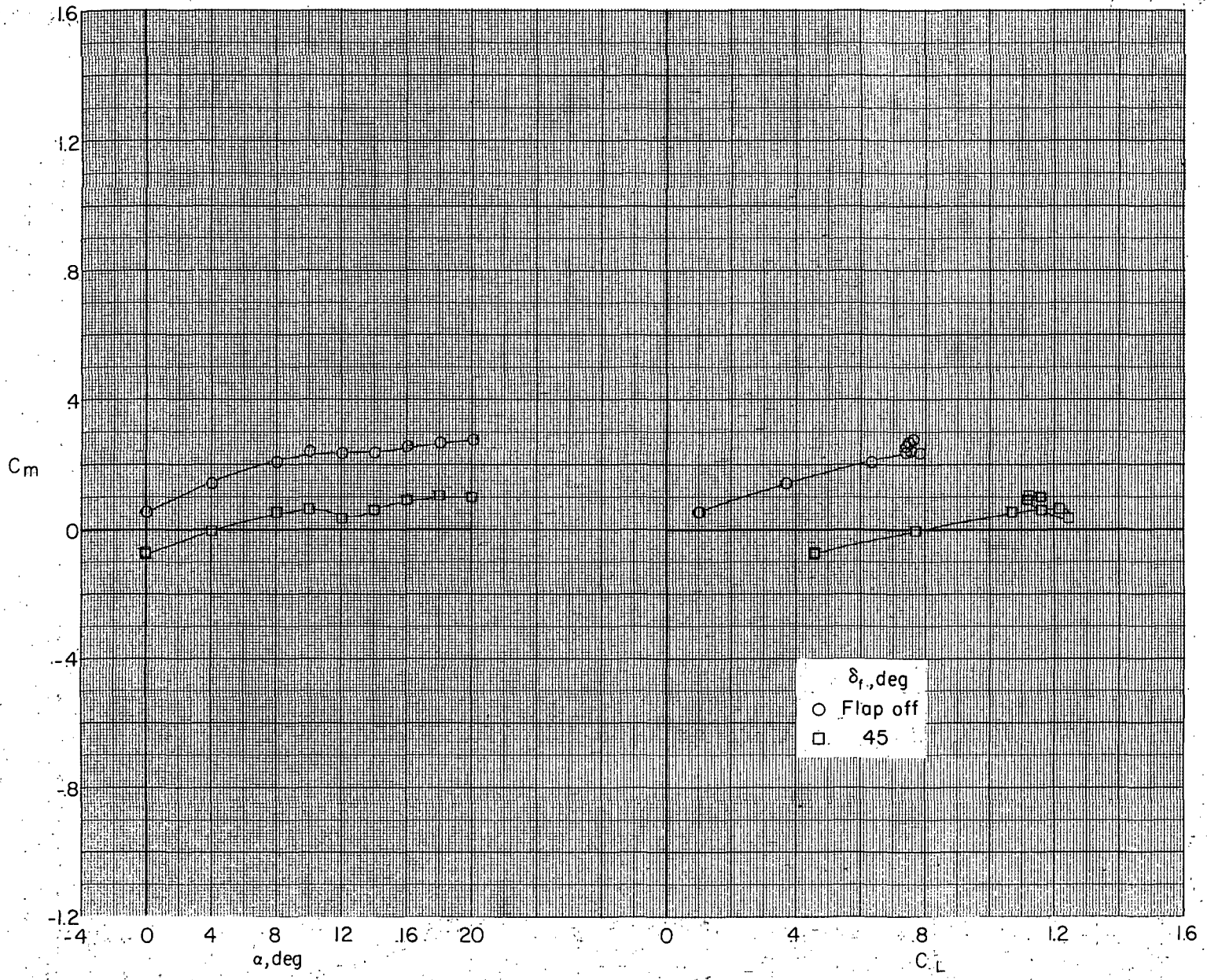


Figure 51.- Effect of tail incidence on longitudinal aerodynamic characteristics of BWN_2VHf configuration at an angle of attack of 10^o with power.



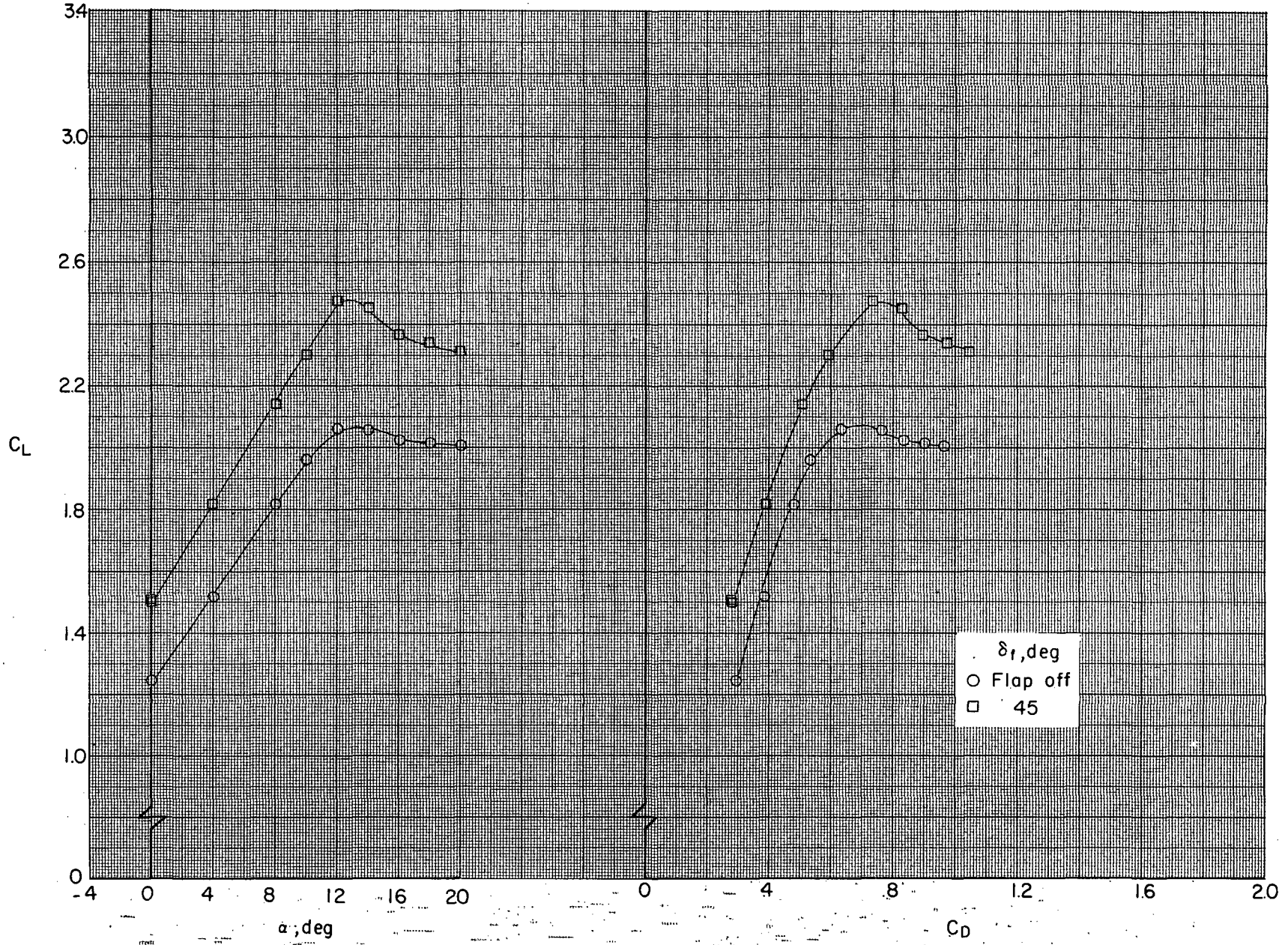
(a) Variation of C_L with α and C_D.

Figure 52.- Effect of flaps on longitudinal characteristics of $BWN_1 90$ configuration without power. $\left(V_\infty/V_j\right)_e = \infty$.



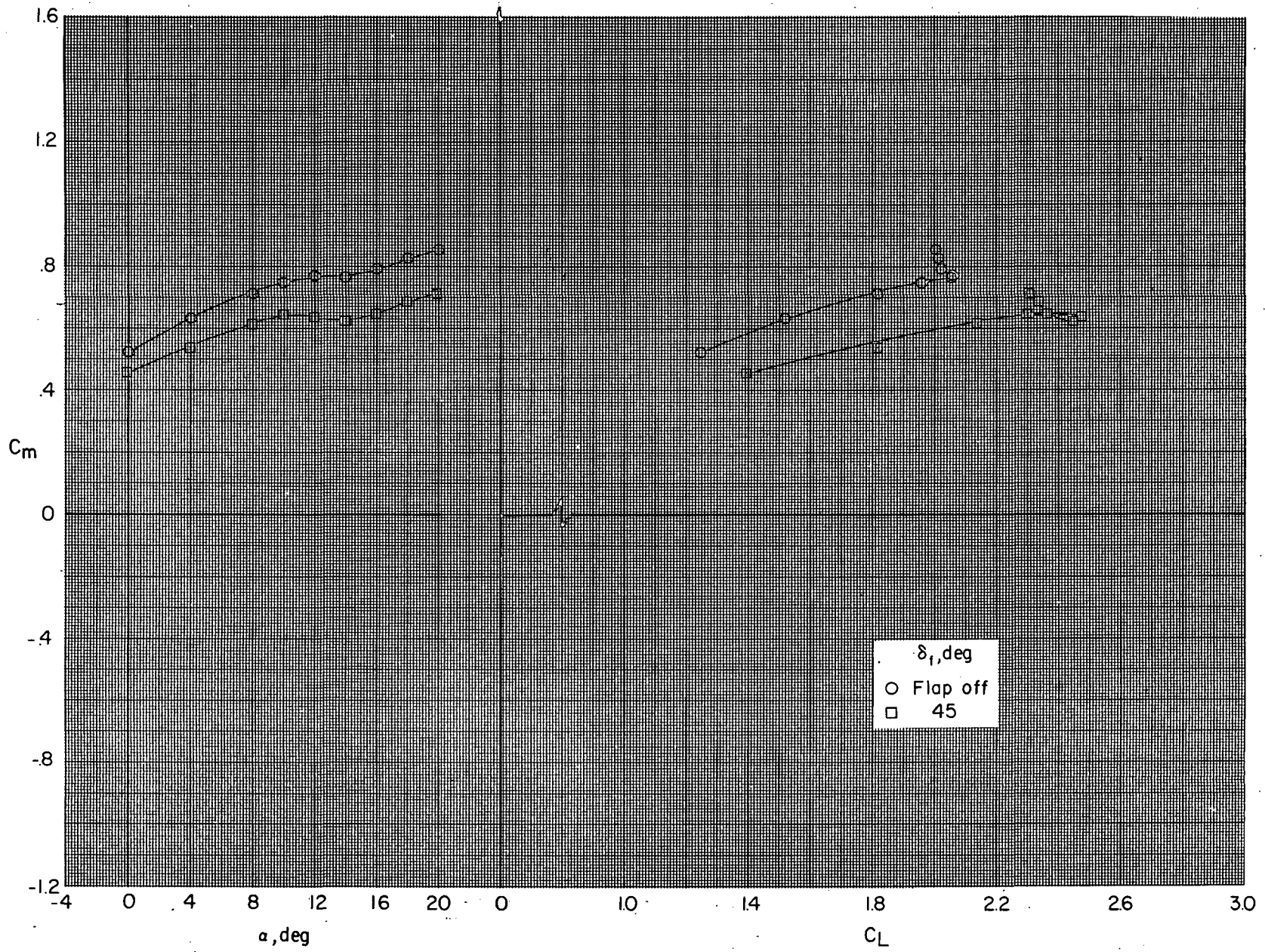
(b) Variation of C_m with α and C_L.

Figure 52.- Concluded.



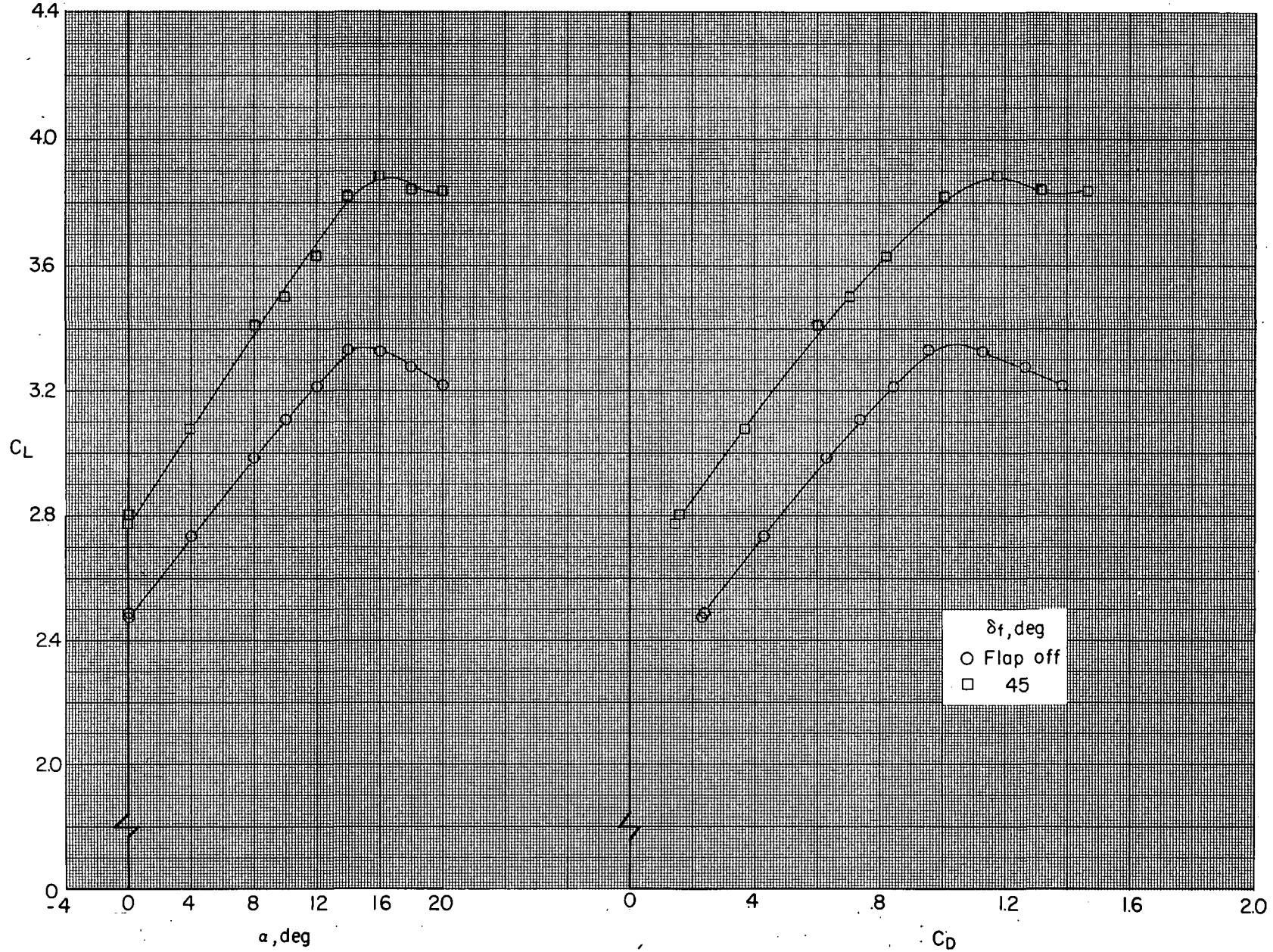
(a) Variation of C_L with α and C_D.

Figure 53.- Effect of flaps on longitudinal characteristics of $BWN_1 90$ configuration with power. $\left(V_\infty/V_j\right)_e = 0.3$.



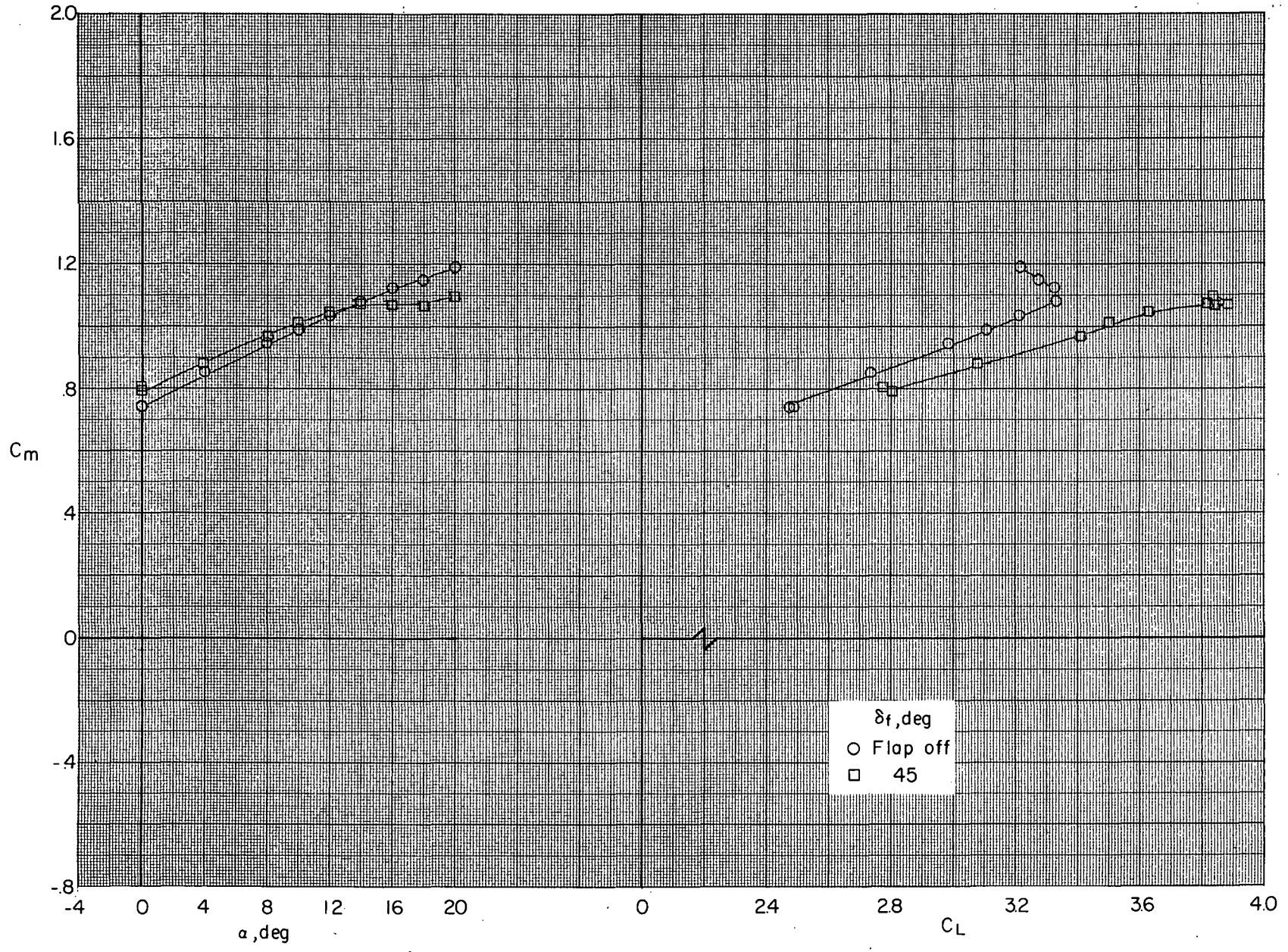
(b) Variation of C_m with α and C_L.

Figure 53.- Concluded.



(a) Variation of C_L with α and C_D.

Figure 54.- Effect of flaps on longitudinal characteristics of $BWN_1 90$ configuration with power. $\left(V_\infty/V_j\right)_e = 0.2$.



(b) Variation of C_m with α and C_L.

Figure 54.- Concluded.

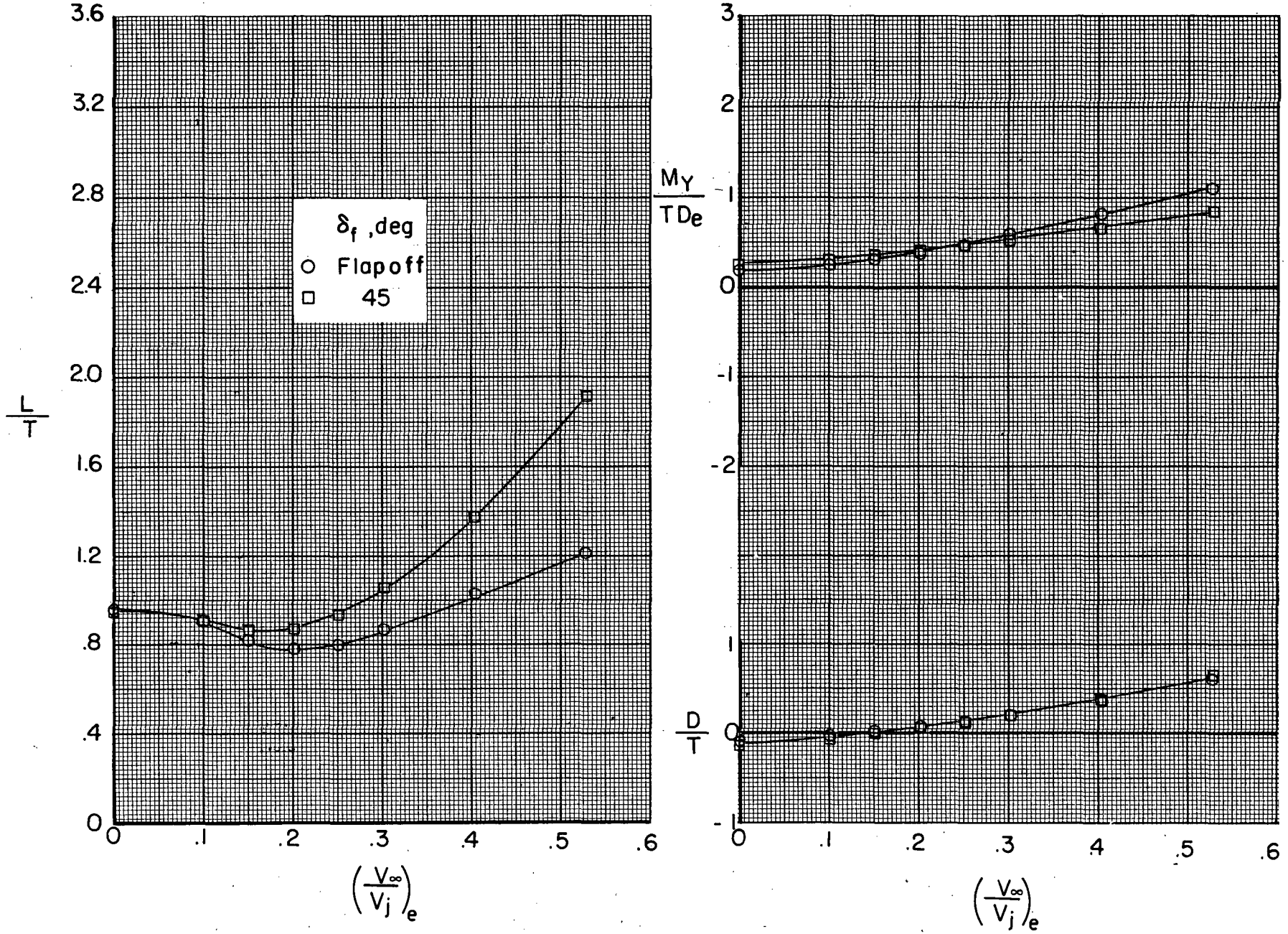


Figure 55.- Effect of flaps on longitudinal characteristics of $BWN_1 90$ configuration at an angle of attack of 0^o with power.

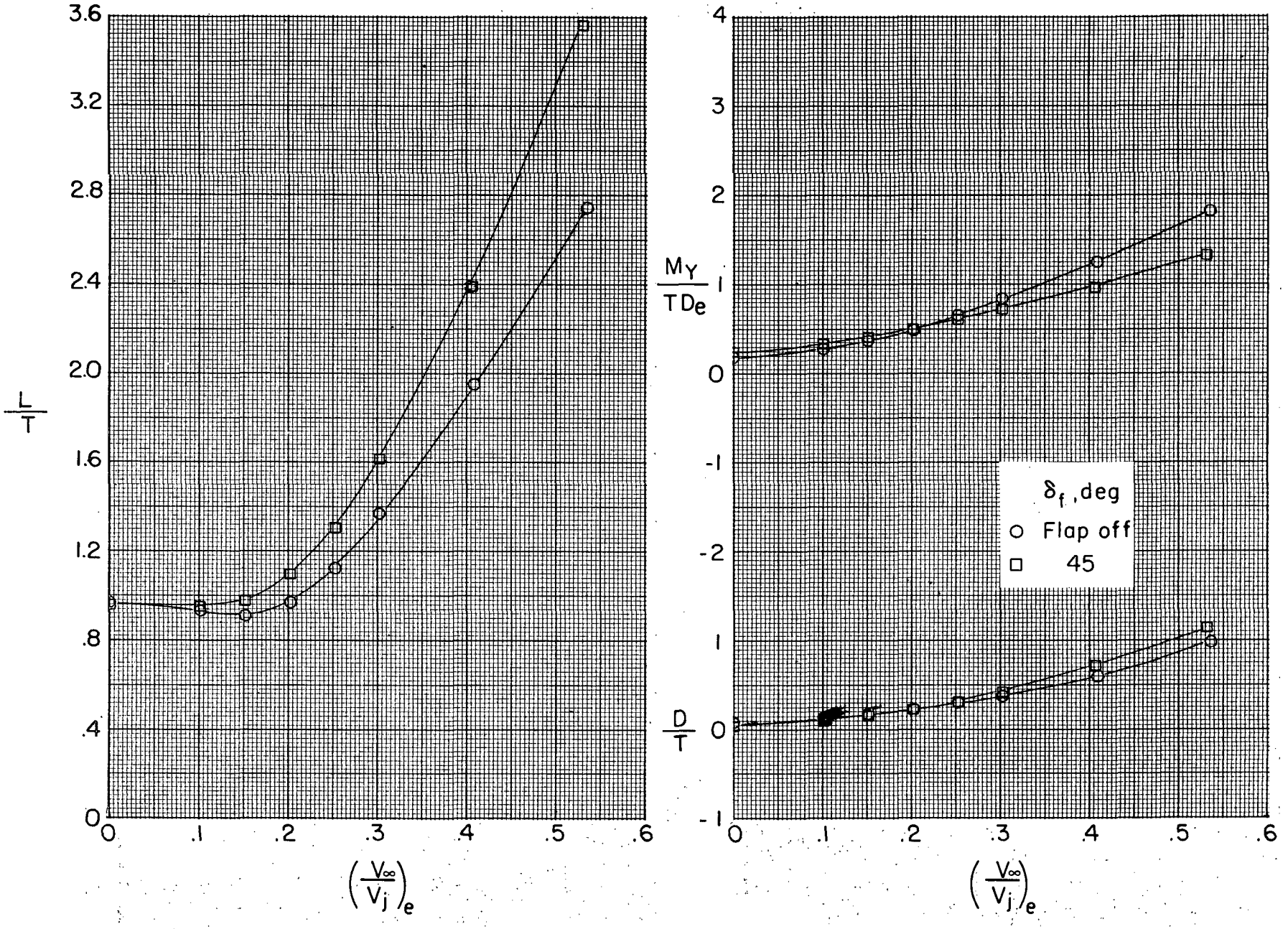
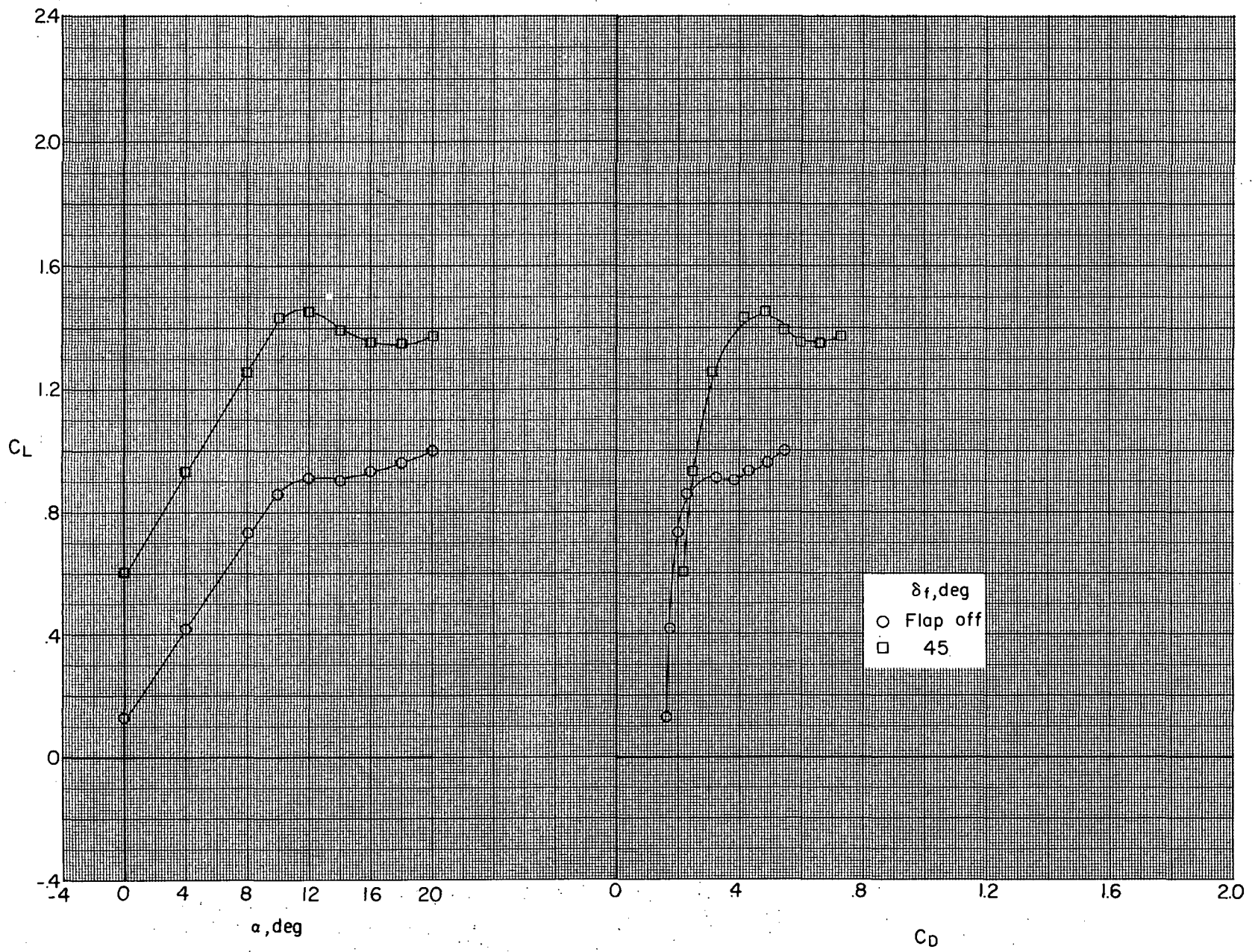
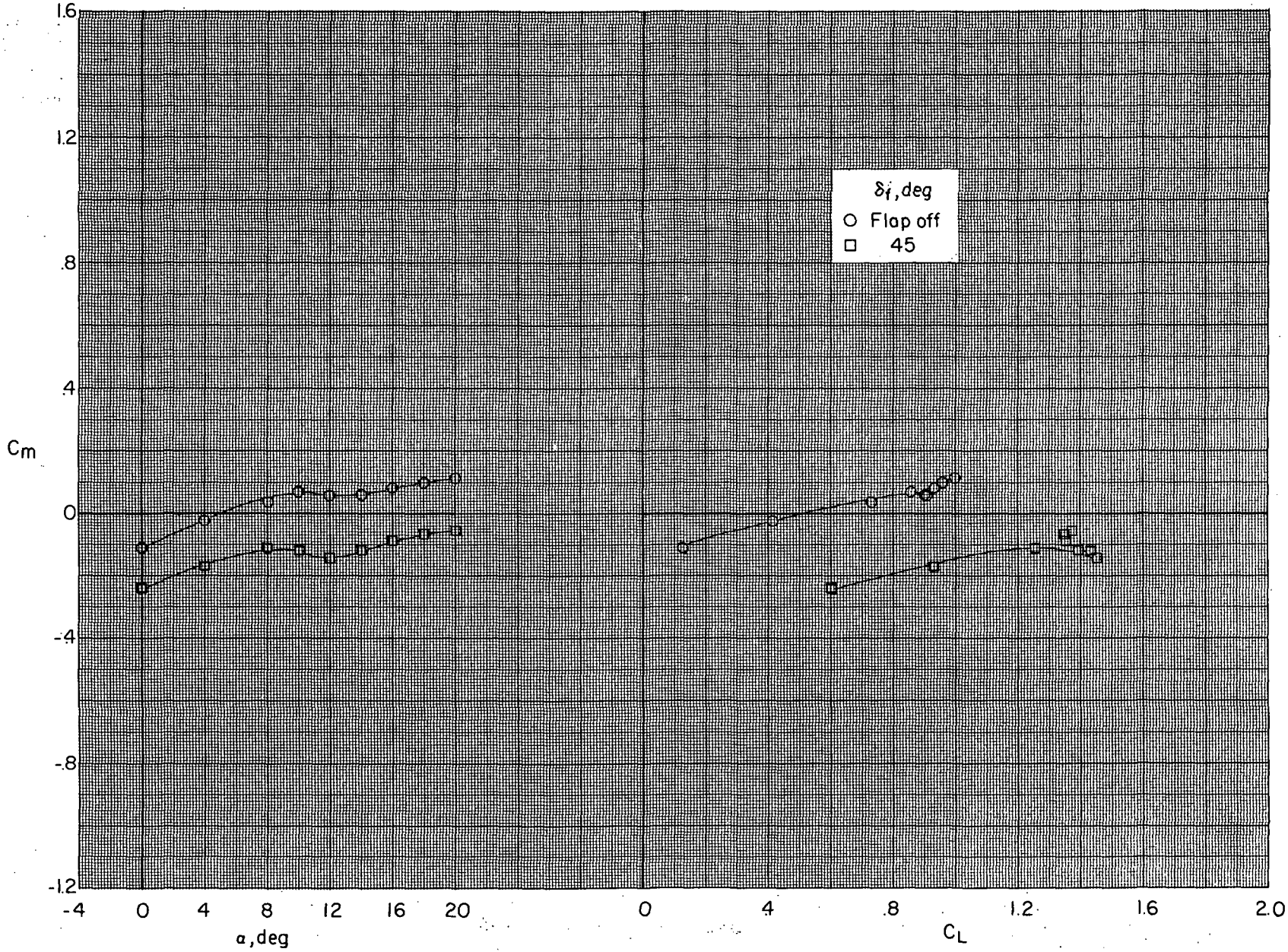


Figure 56.- Effect of flaps on longitudinal characteristics of $BWN_1 90$ configuration at an angle of attack of 10^0 with power.



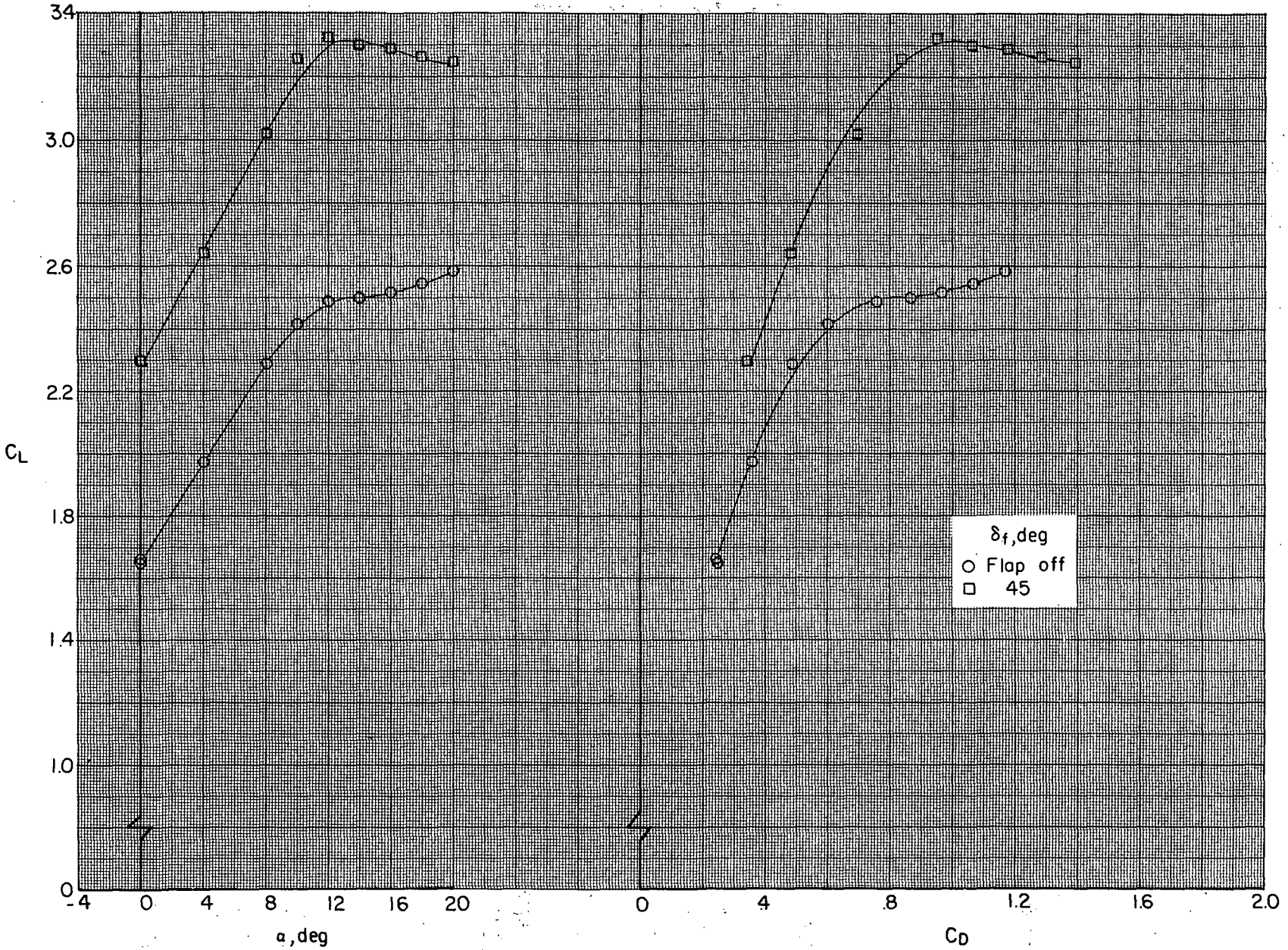
(a) Variation of C_L with α and C_D.

Figure 57.- Effect of flaps on longitudinal characteristics of $BWN_2 90$ configuration without power. $\left(V_\infty/V_j\right)_e = \infty$.



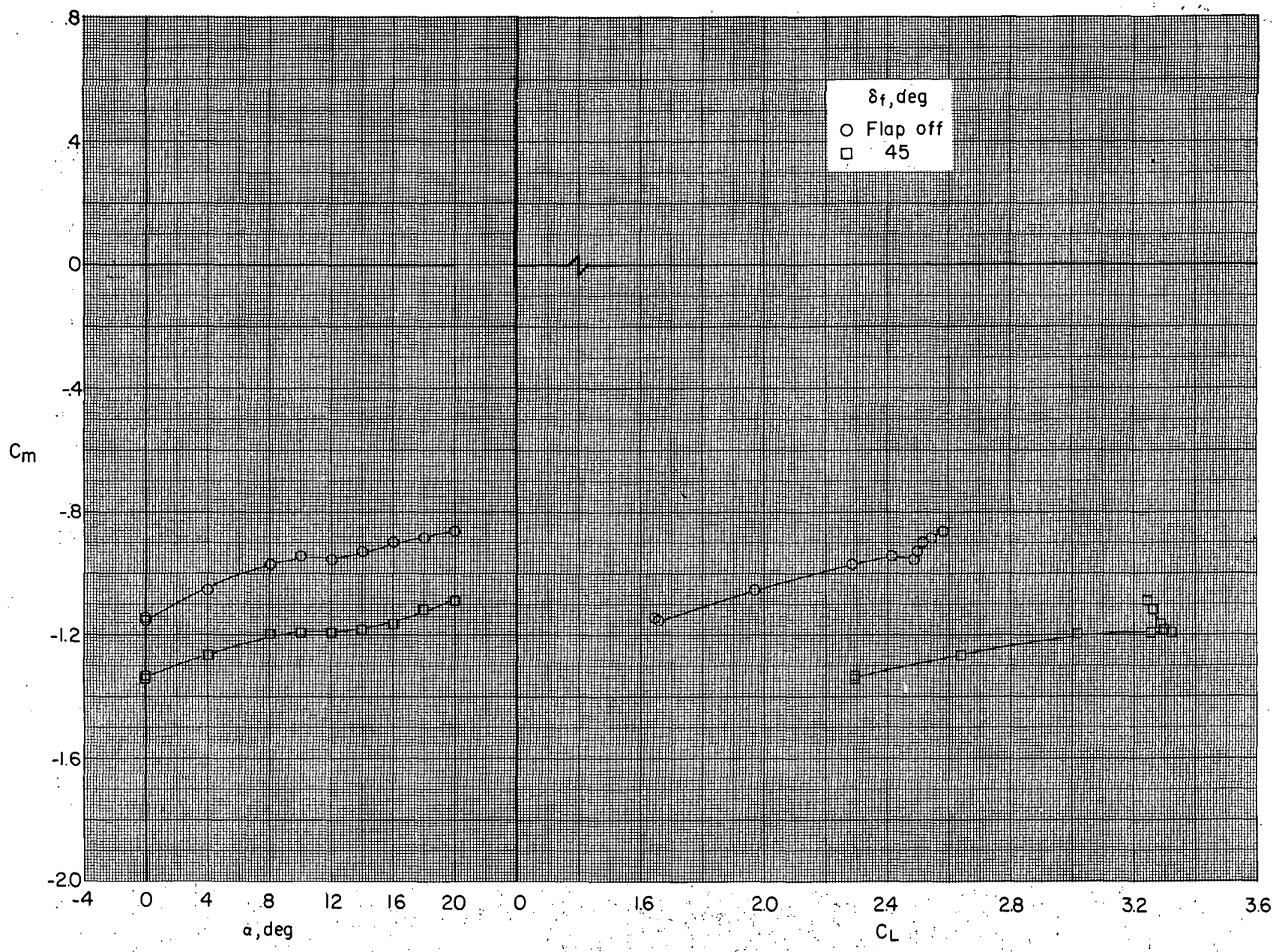
(b) Variation of C_m with α and C_L.

Figure 57.- Concluded.



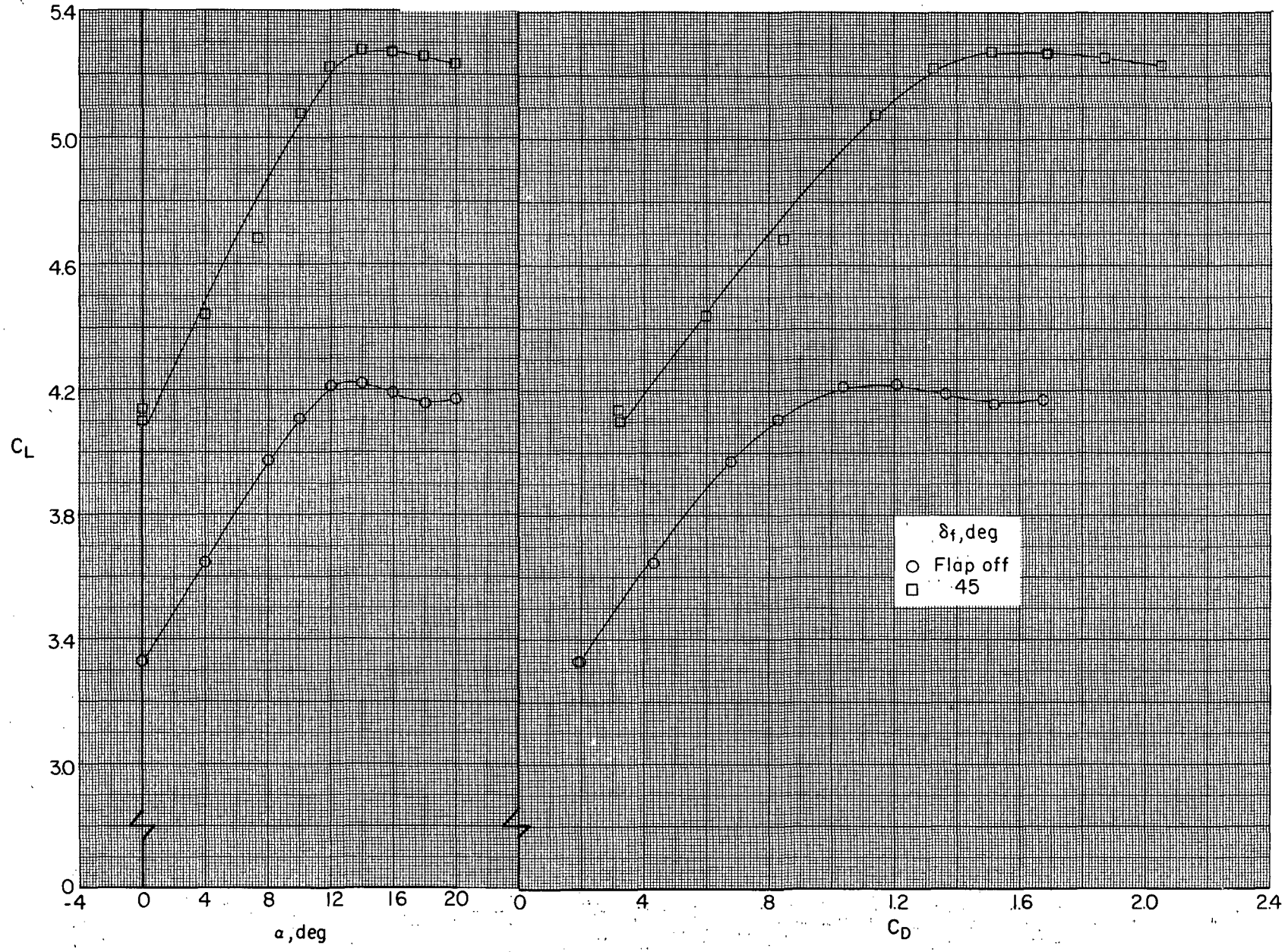
(a) Variation of C_L with α and C_D.

Figure 58.- Effect of flaps on longitudinal characteristics of $BWN_2 90$ configuration with power. $\left(V_\infty/V_j\right)_e = 0.3$.



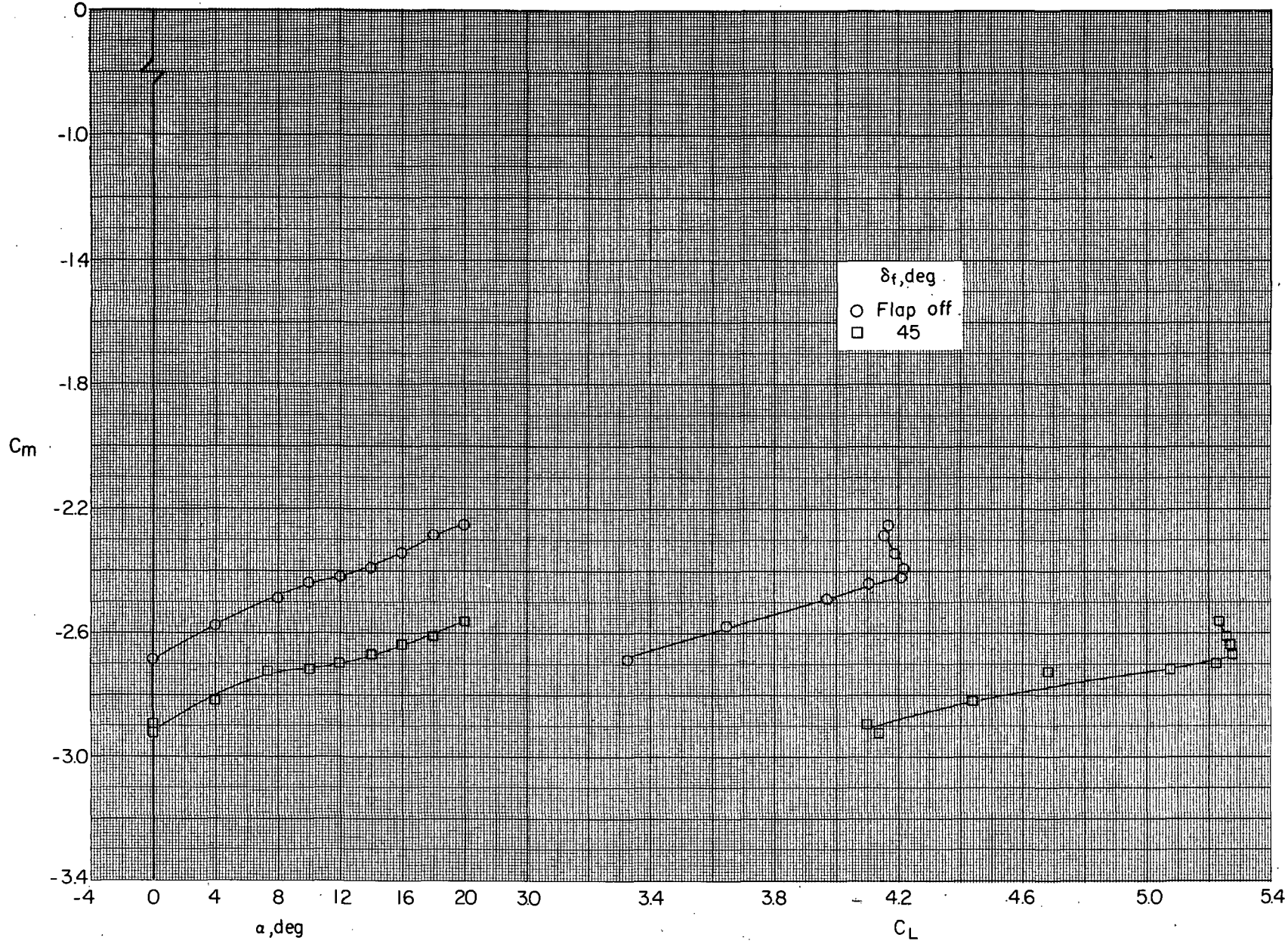
(b) Variation of C_m with α and C_L.

Figure 58.- Concluded.



(a) Variation of C_L with α and C_D.

Figure 59.- Effect of flaps on longitudinal characteristics of $BWN_2 90$ configuration with power. $\left(V_\infty/V_j\right)_e = 0.2$.



(b) Variation of C_m with α and C_L.

Figure 59.- Concluded.

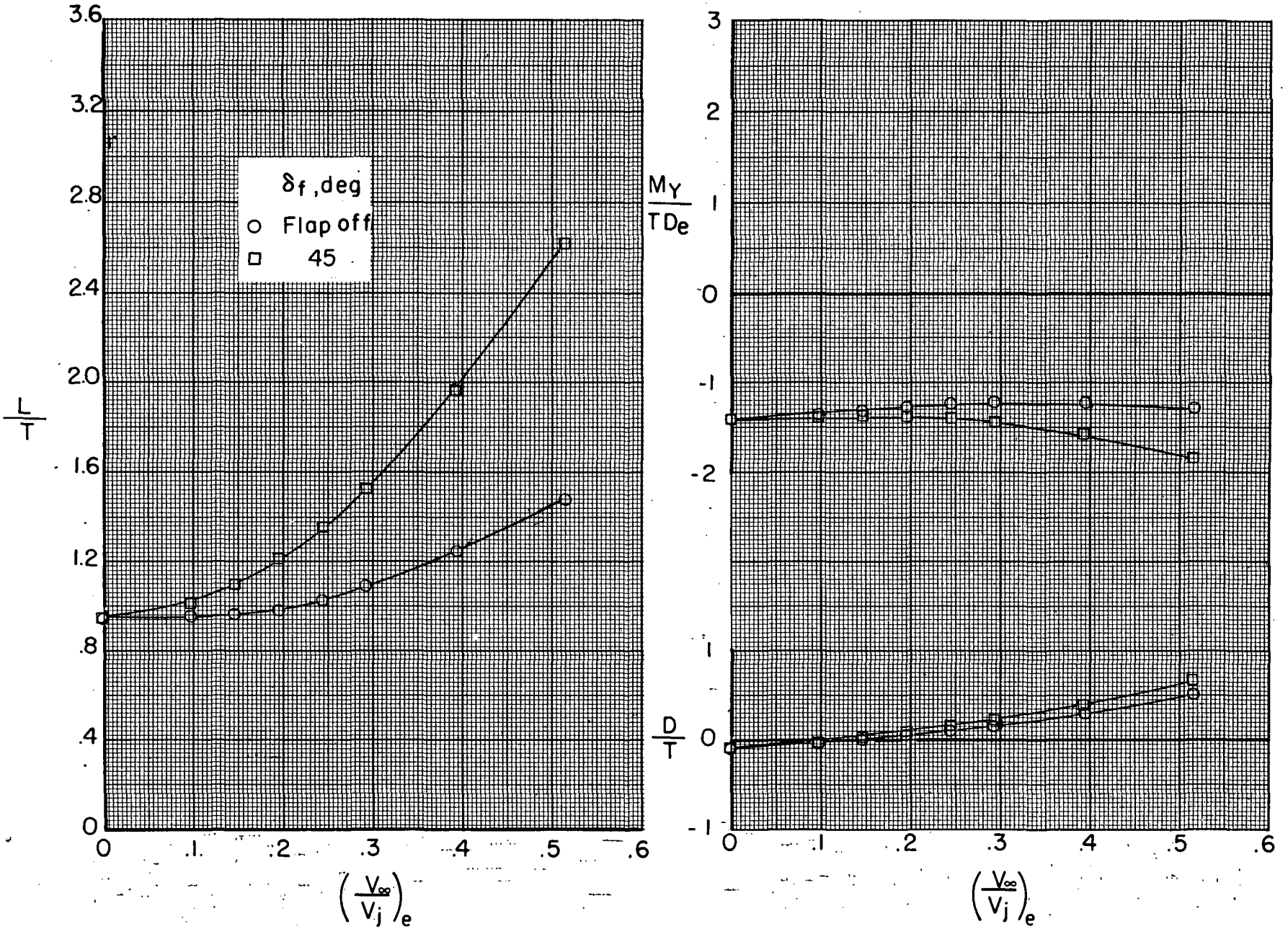


Figure 60.- Effect of flaps on longitudinal characteristics of $BWN_2 90$ configuration at an angle of attack of 0^o with power.

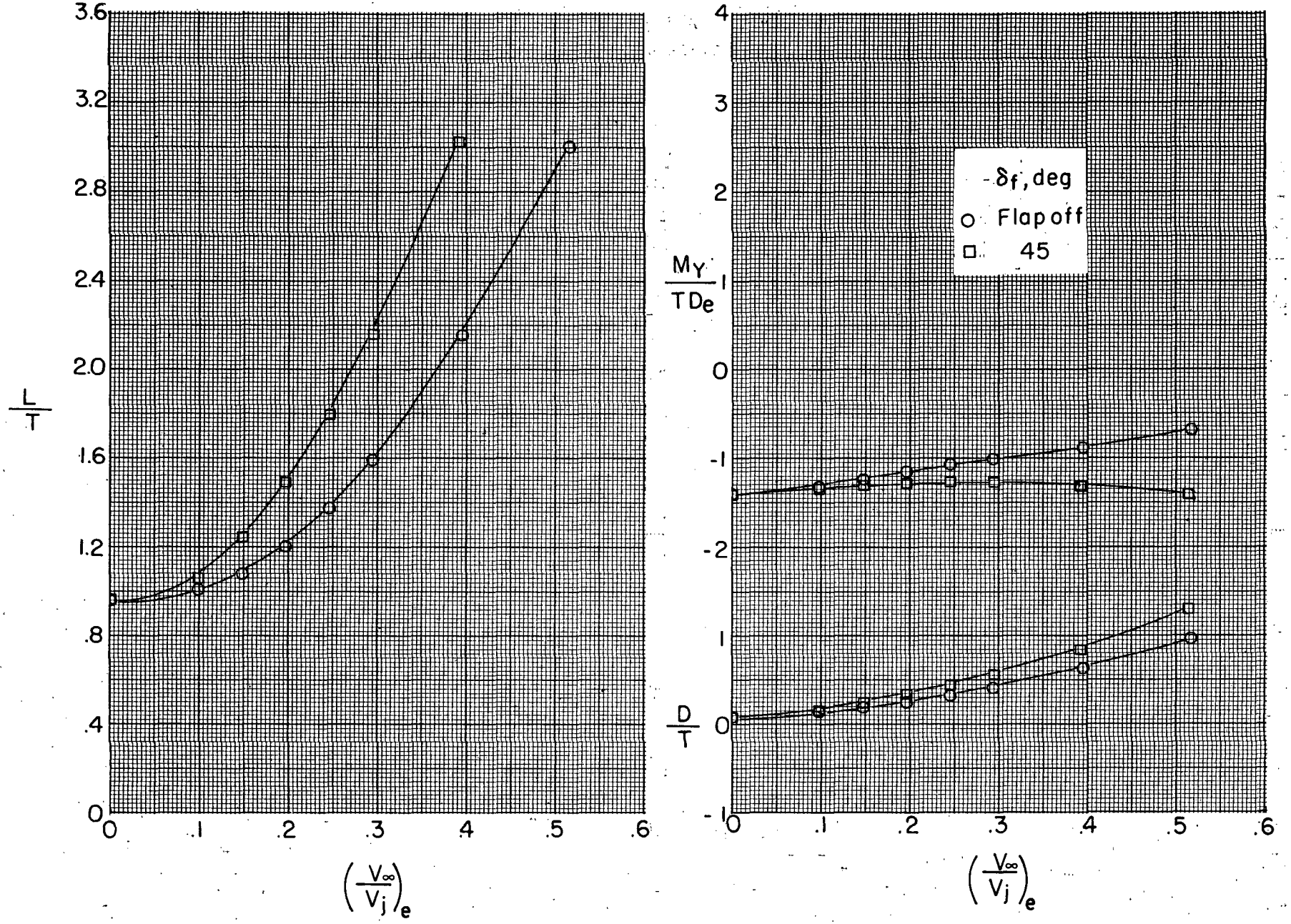
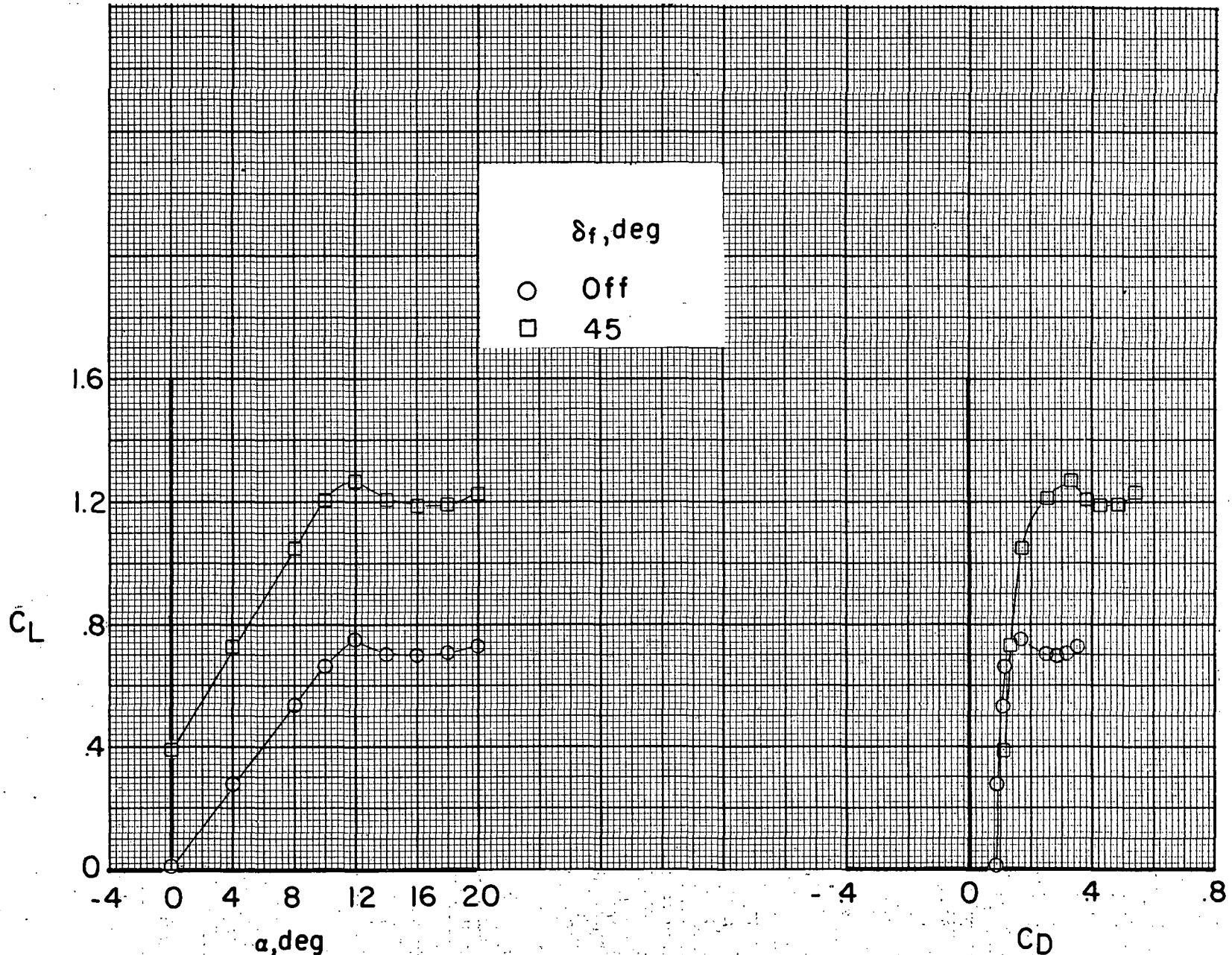
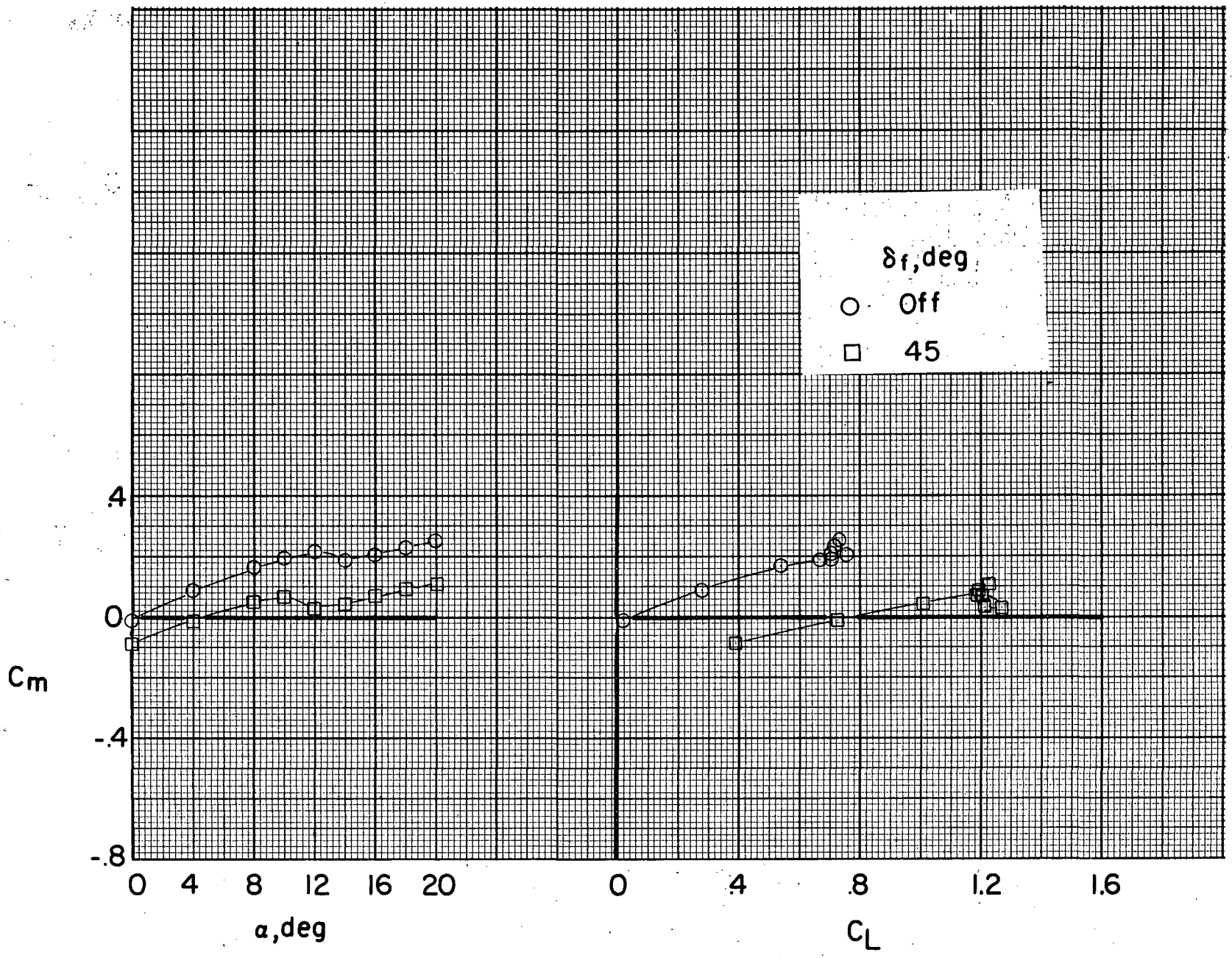


Figure 61.- Effect of flaps on longitudinal characteristics of $BWN_2 90$ configuration at an angle of attack of 10^o with power.



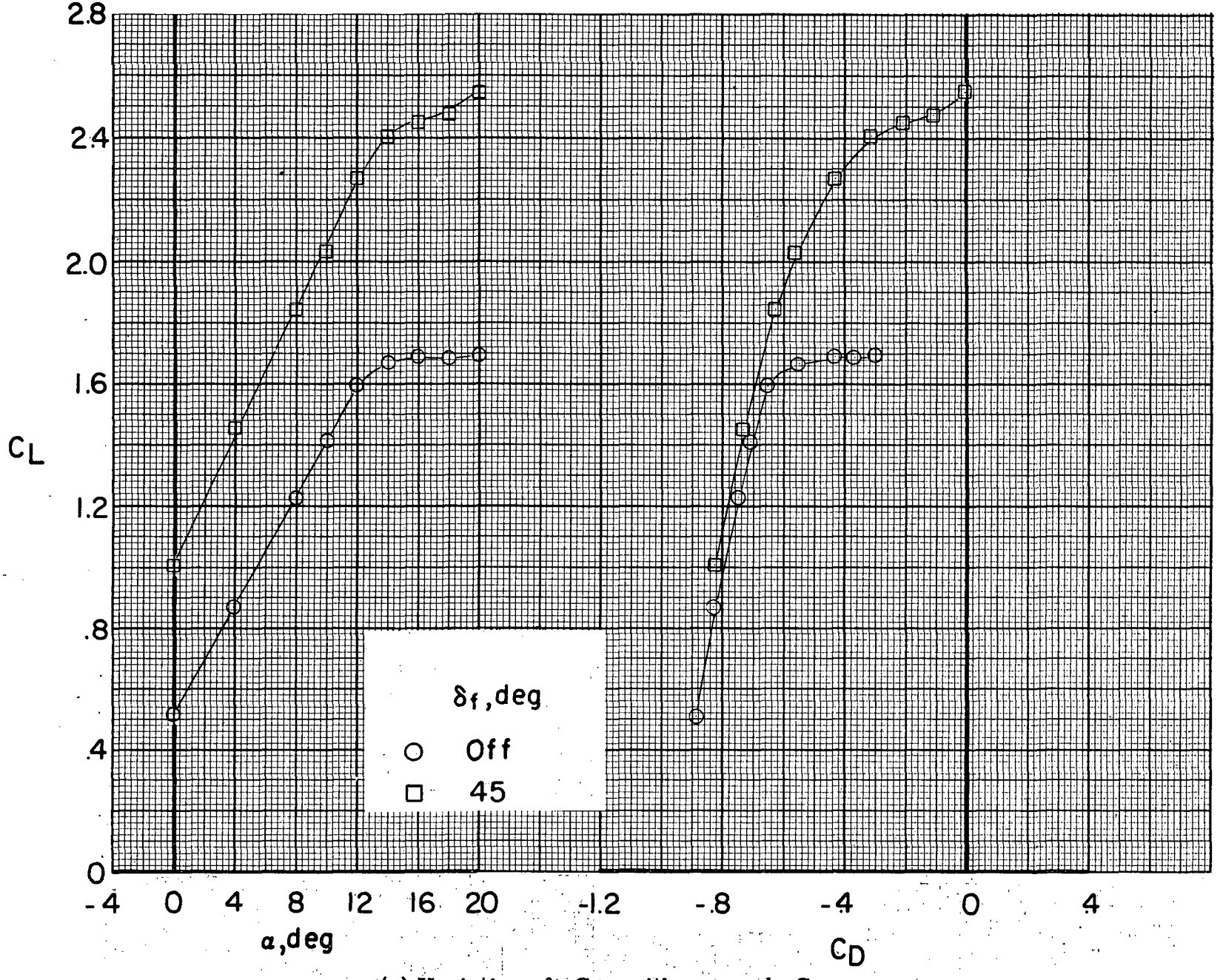
(a) Variation of C_L with α and C_D.

Figure 62.- Effect of flaps on longitudinal characteristics for $BWN_1 45f$ configuration. $\left(V_\infty/V_j\right)_e = \infty$.



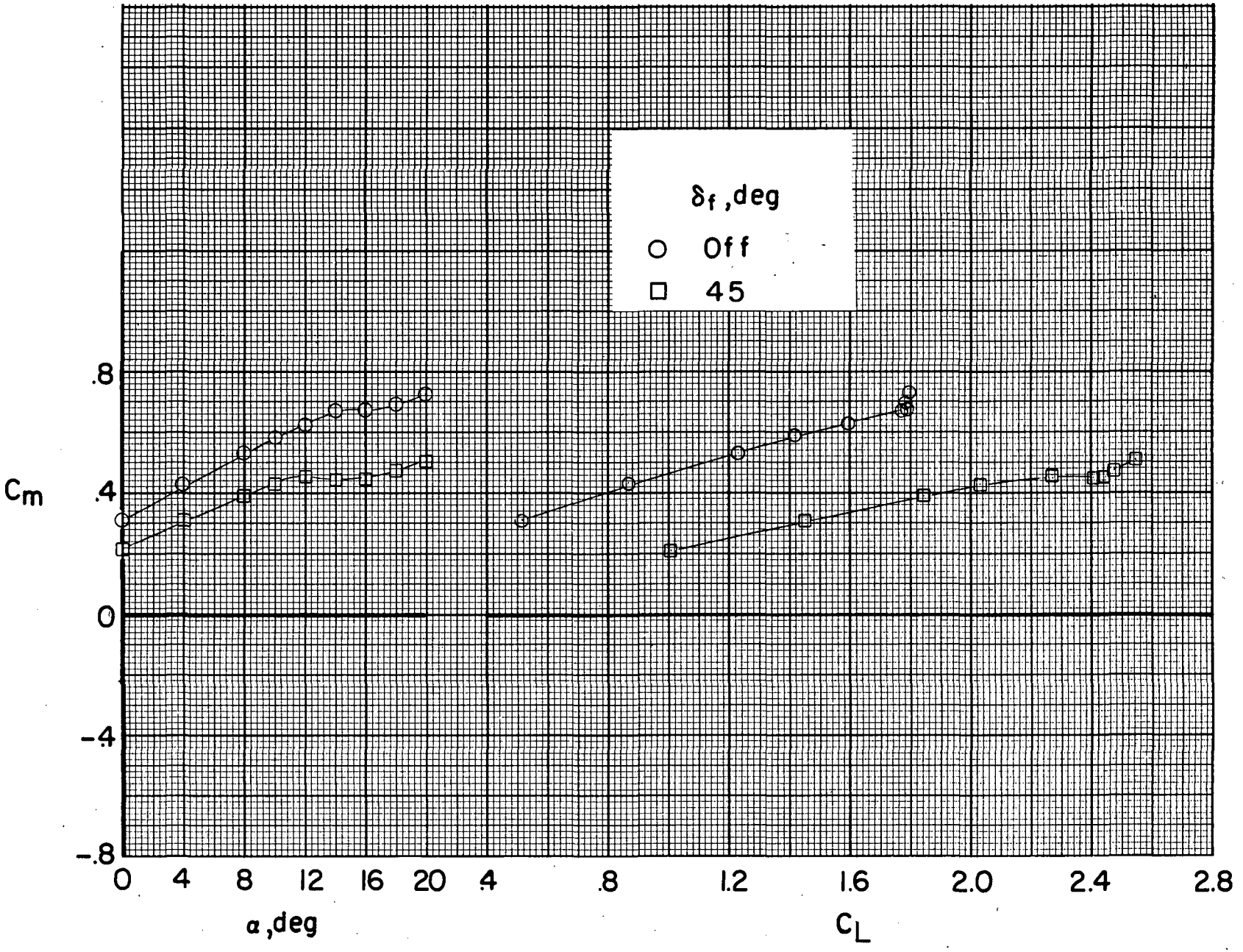
(b) Variation of C_m with α and C_L.

Figure 62.- Concluded.



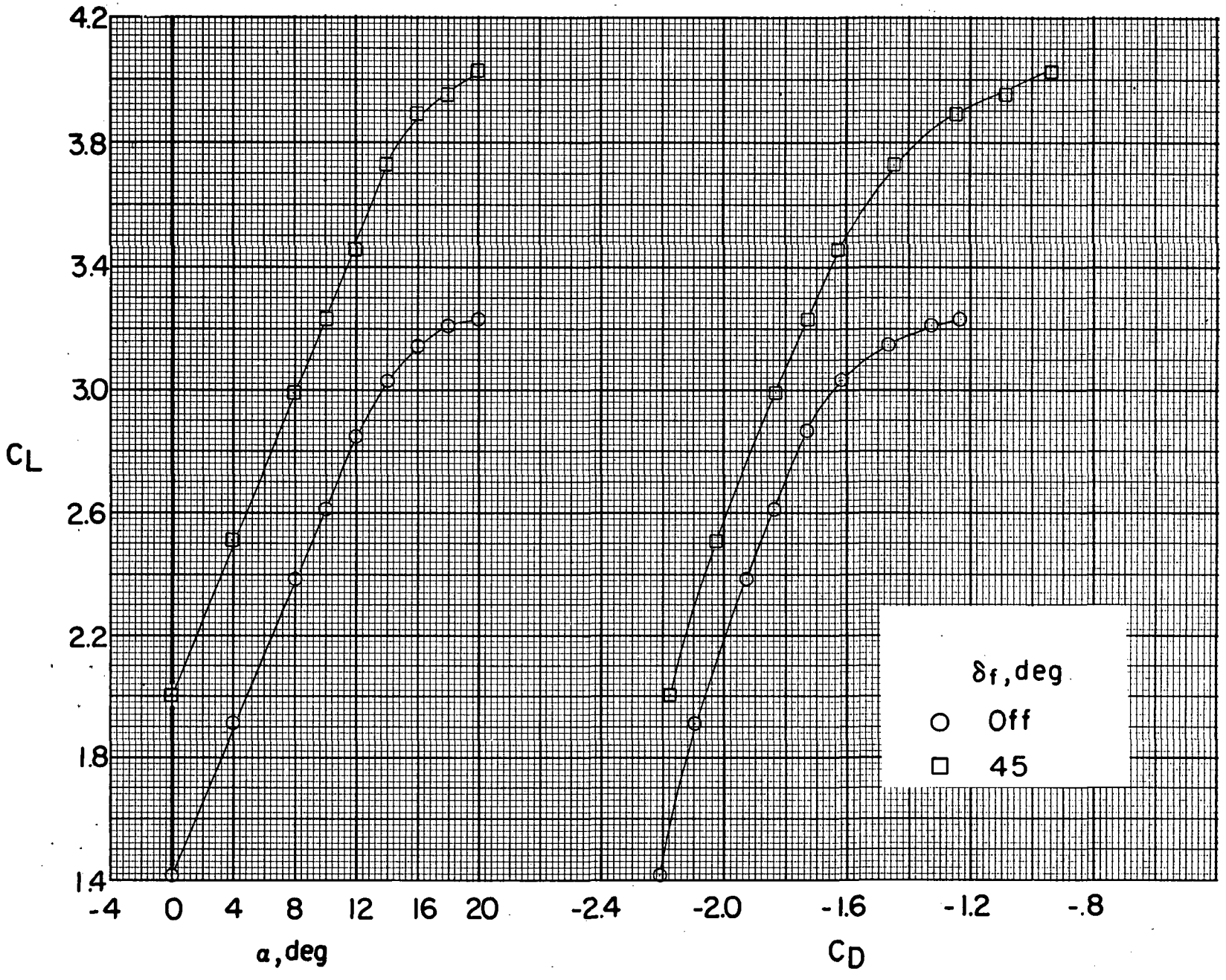
(a) Variation of C_L with α and C_D.

Figure 63.- Effect of flaps on longitudinal characteristics for $BWN_1 45f$ configuration. $\left(V_\infty/V_j\right)_e = 0.3$.



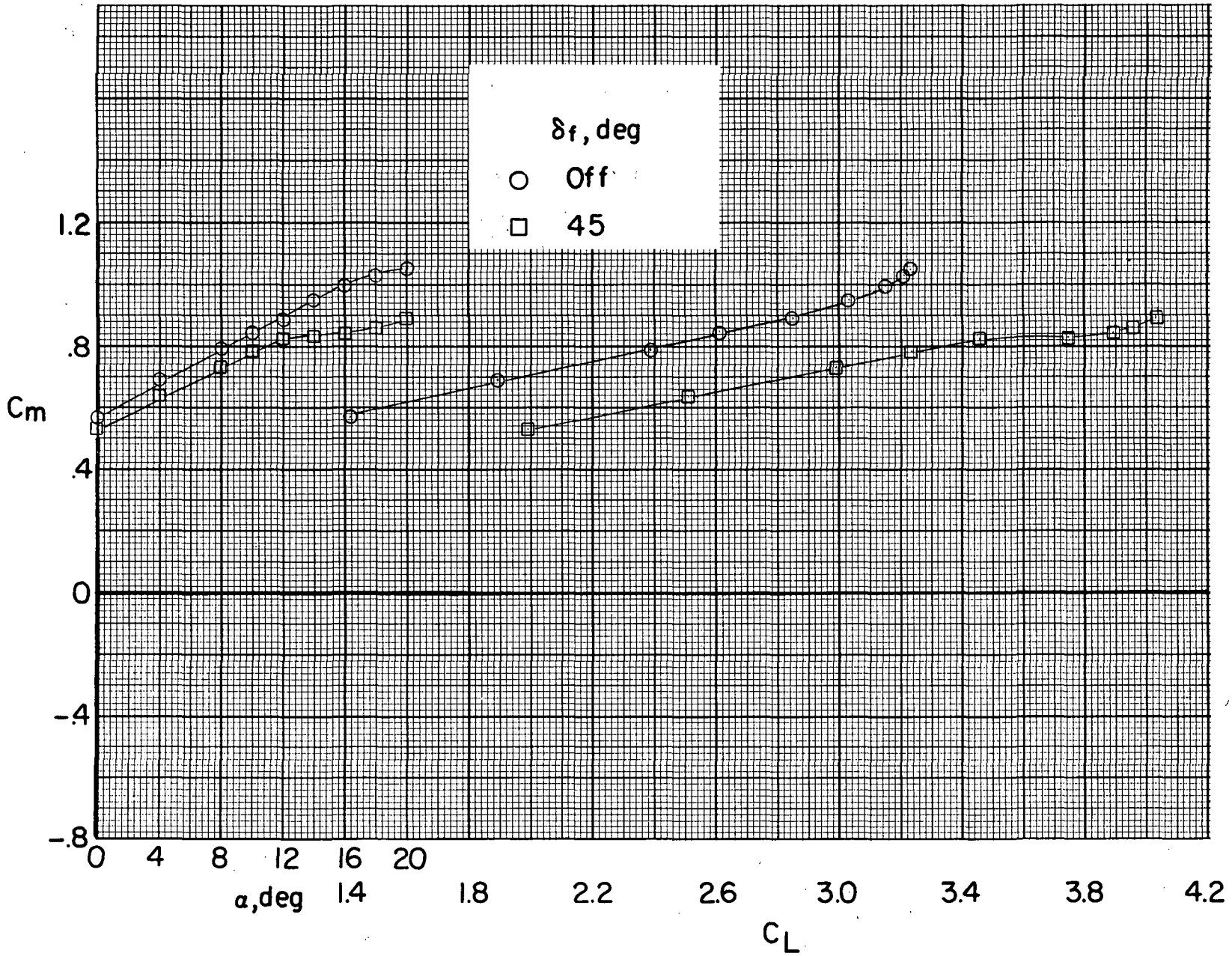
(b) Variation of C_m with α and C_L.

Figure 63.- Concluded.



(a) Variation of C_L with α and C_D.

Figure 64.- Effect of flaps on longitudinal characteristics for $BWN_1 45f$ configuration. $\left(V_\infty/V_j\right)_e = 0.2$.



(b) Variation of C_m with α and C_L.

Figure 64.- Concluded.

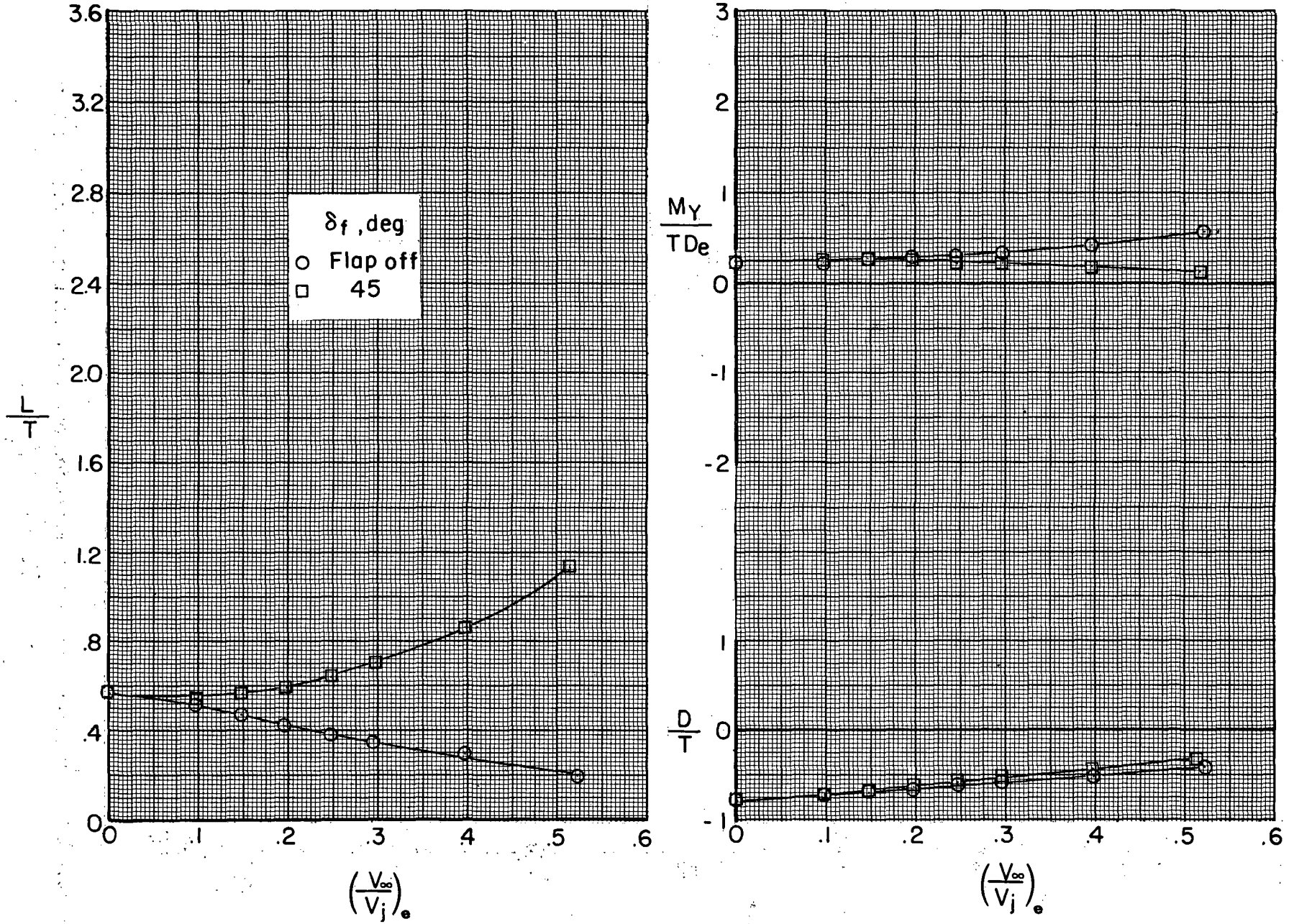


Figure 65.- Effect of flaps on longitudinal characteristics of $BWN_1 45$ configuration at an angle of attack of 0^o with power.

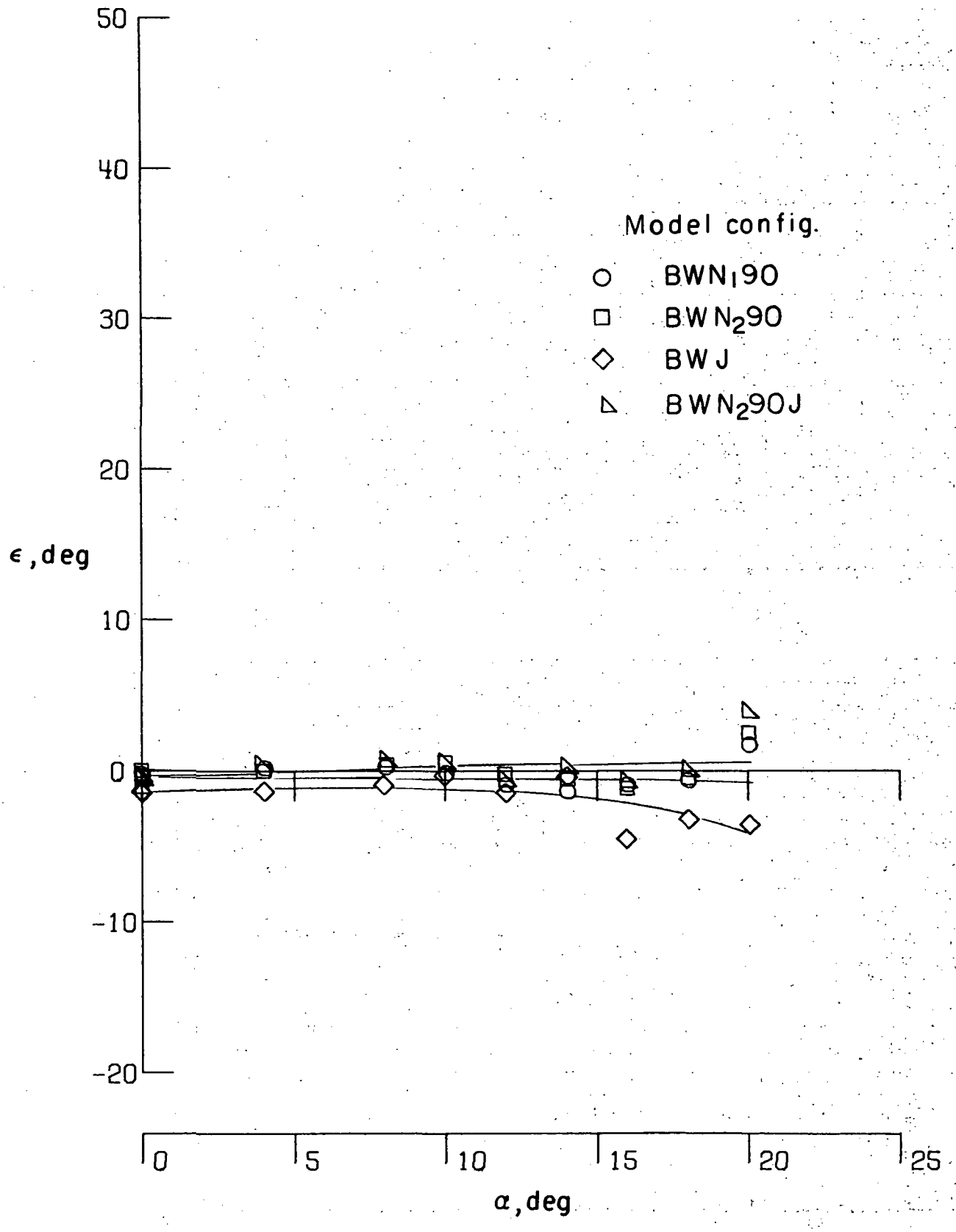


Figure 66.- Effect of thrust location on variation of downwash with angle of attack. $z/\bar{c} = -1.12$; $\left(V_\infty/V_j\right)_e = \infty$.

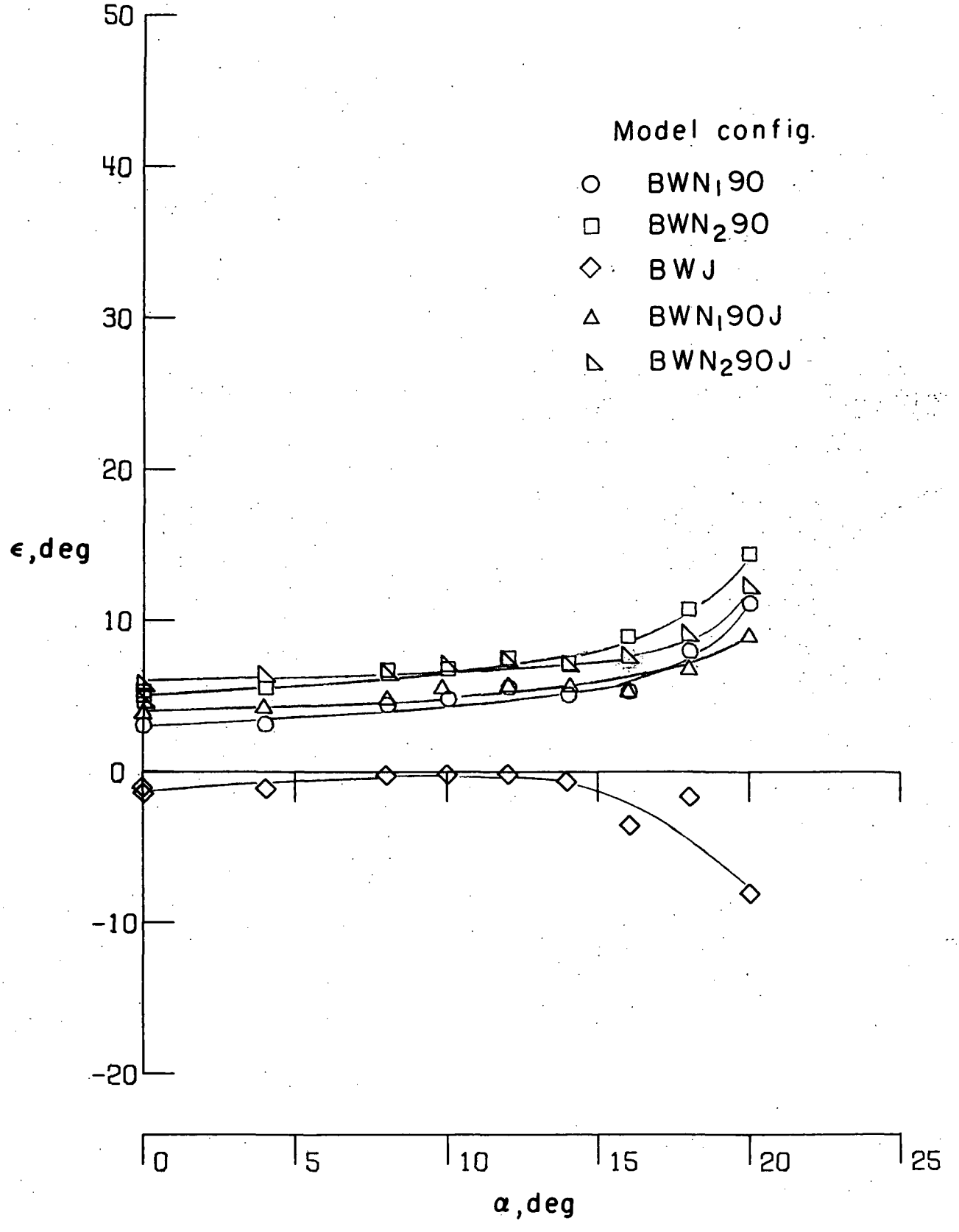


Figure 67.- Effect of thrust location on variation of downwash with angle of attack. $z/\bar{c} = -1.12$; $\left(V_\infty/V_j\right)_e = 0.3$.

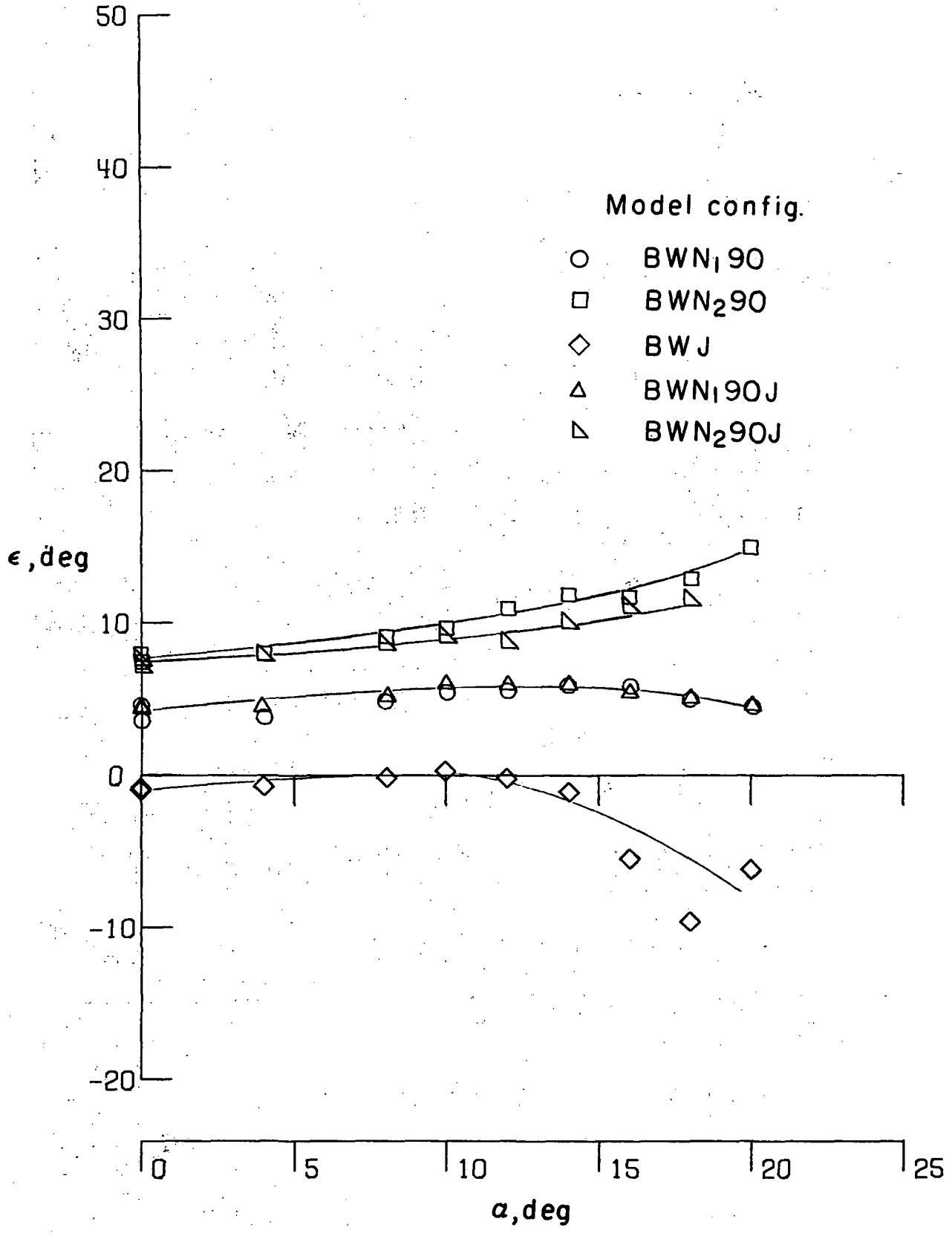


Figure 68.- Effect of thrust location on variation of downwash with angle of attack. $z/\bar{c} = -1.12$; $\left(V_\infty/V_j\right)_e = 0.2$.

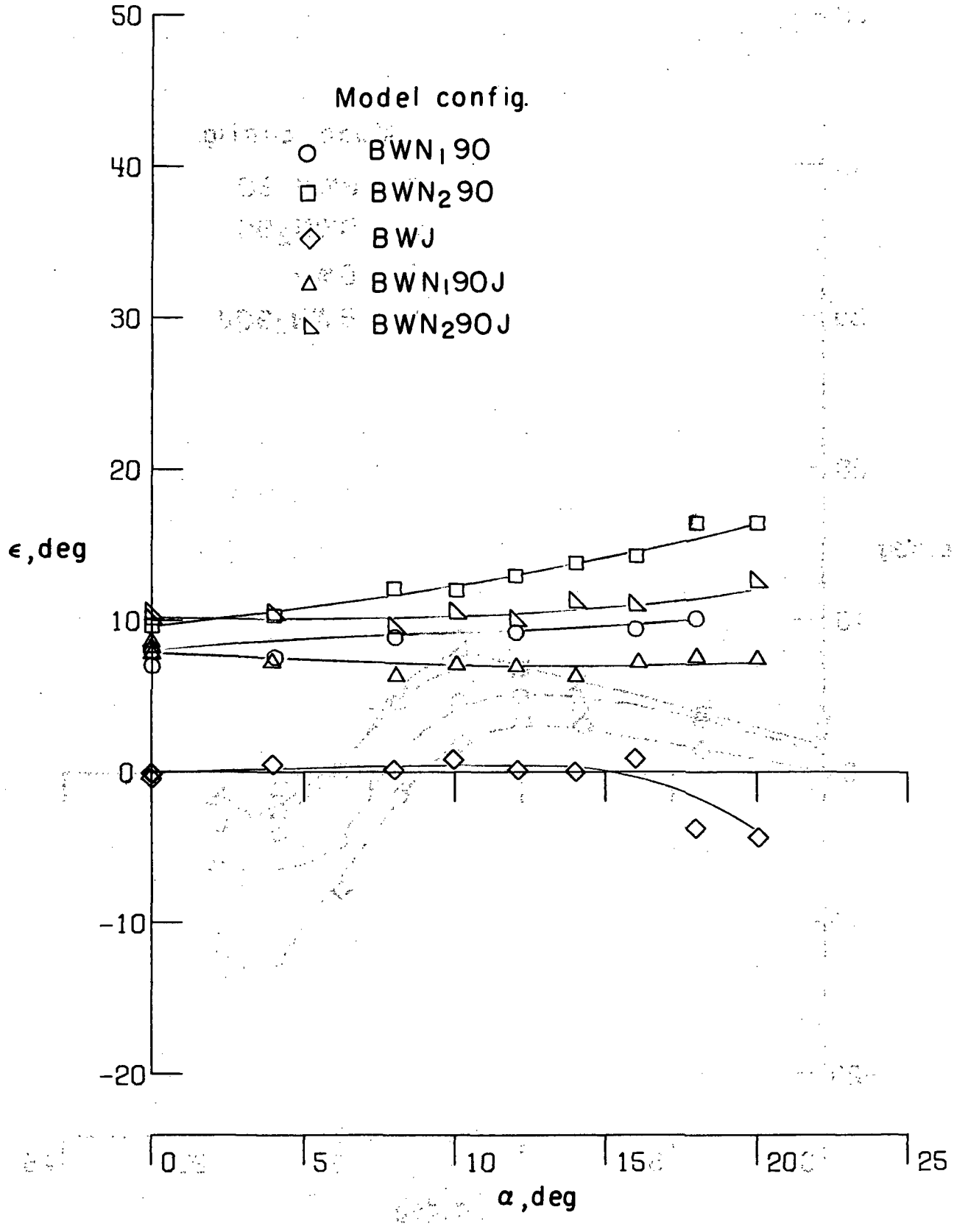


Figure 69.- Effect of thrust location on variation of downwash with angle of attack. $z/\bar{c} = -1.12$; $\left(V_\infty/V_j\right)_e = 0.1$.

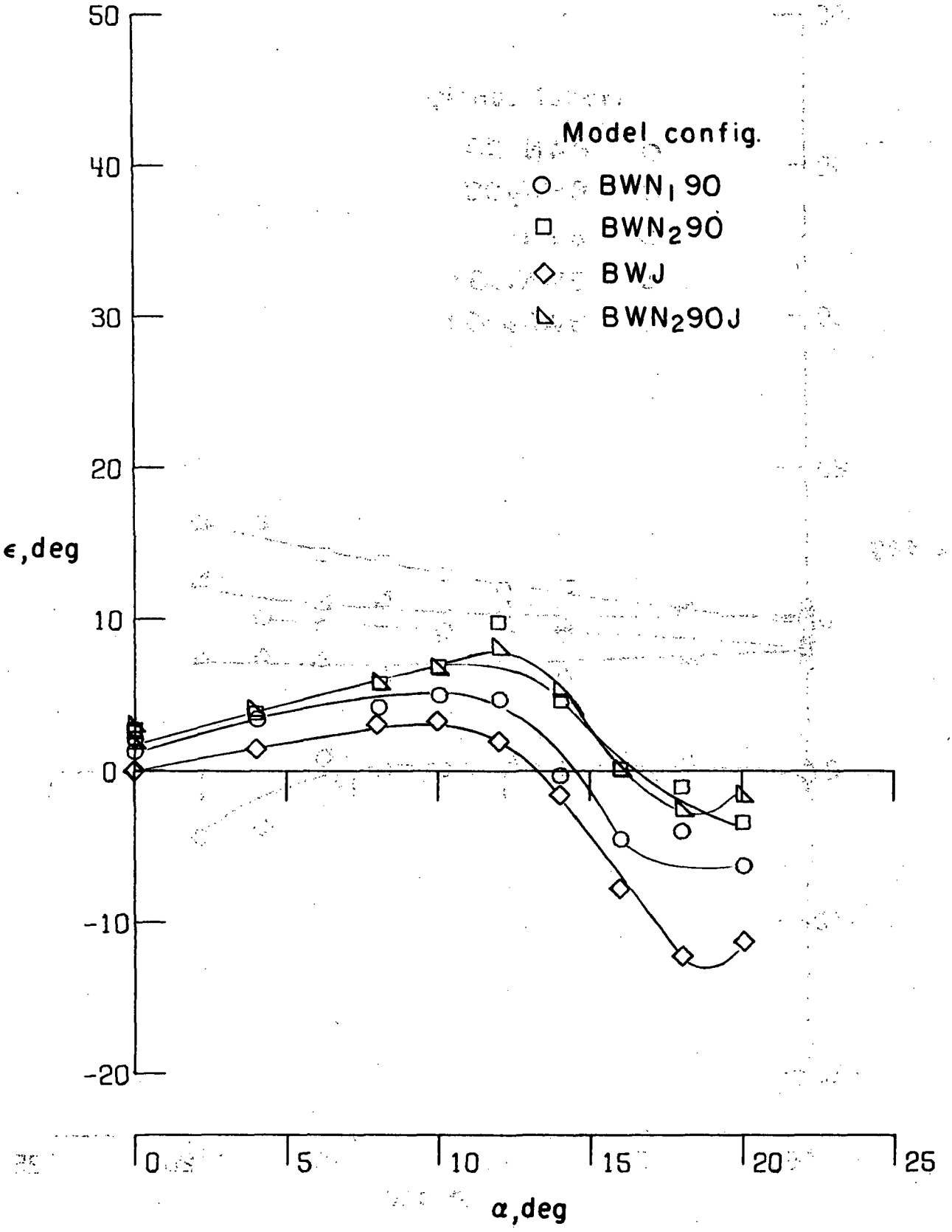


Figure 70.- Effect of thrust location on variation of downwash with angle of attack. $z/\bar{c} = -0.40$; $\left(V_\infty/V_j\right)_e = \infty$.

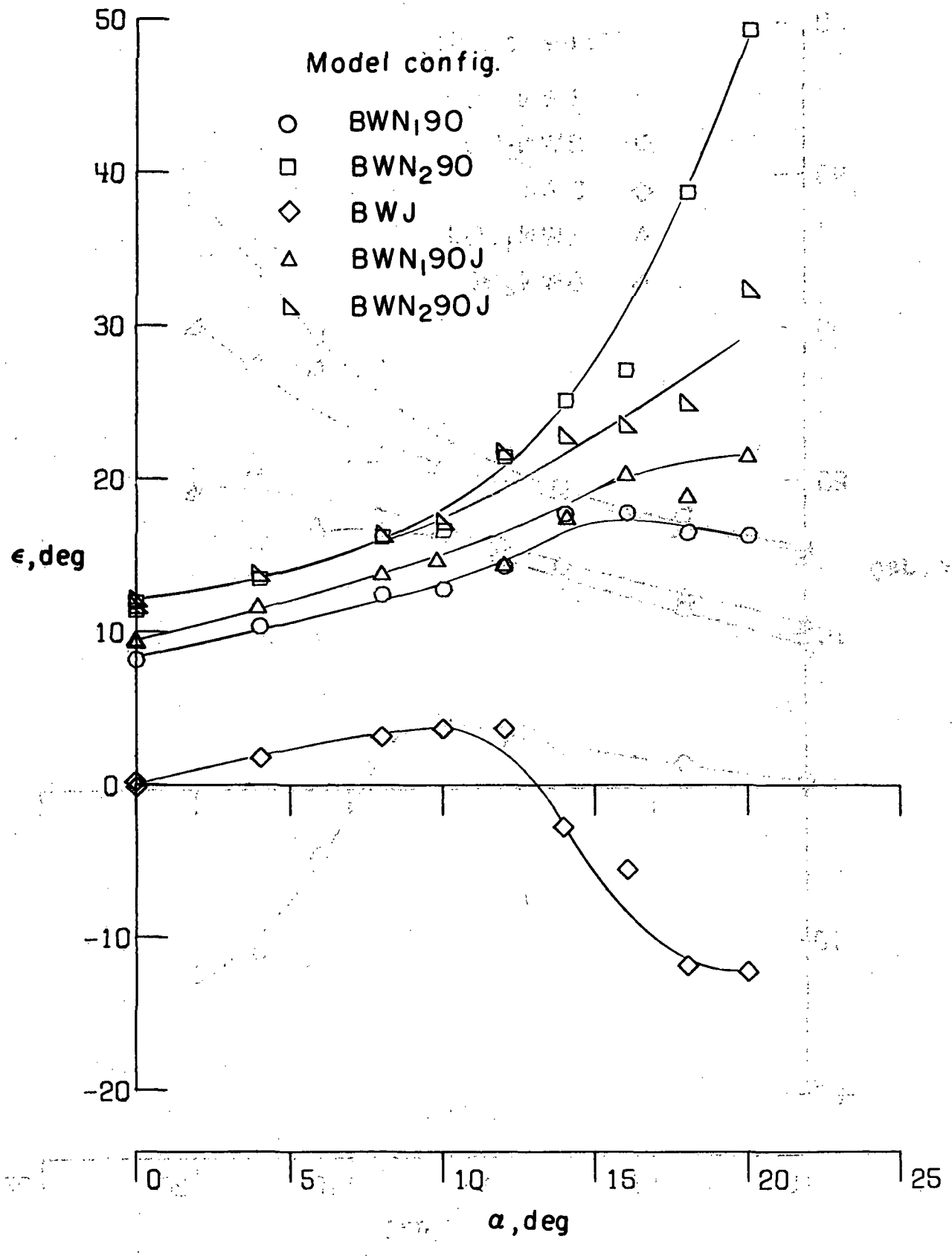


Figure 71.- Effect of thrust location on variation of downwash with angle of attack. $z/\bar{c} = -0.40$; $\left(V_\infty/V_j\right)_e = 0.3$.

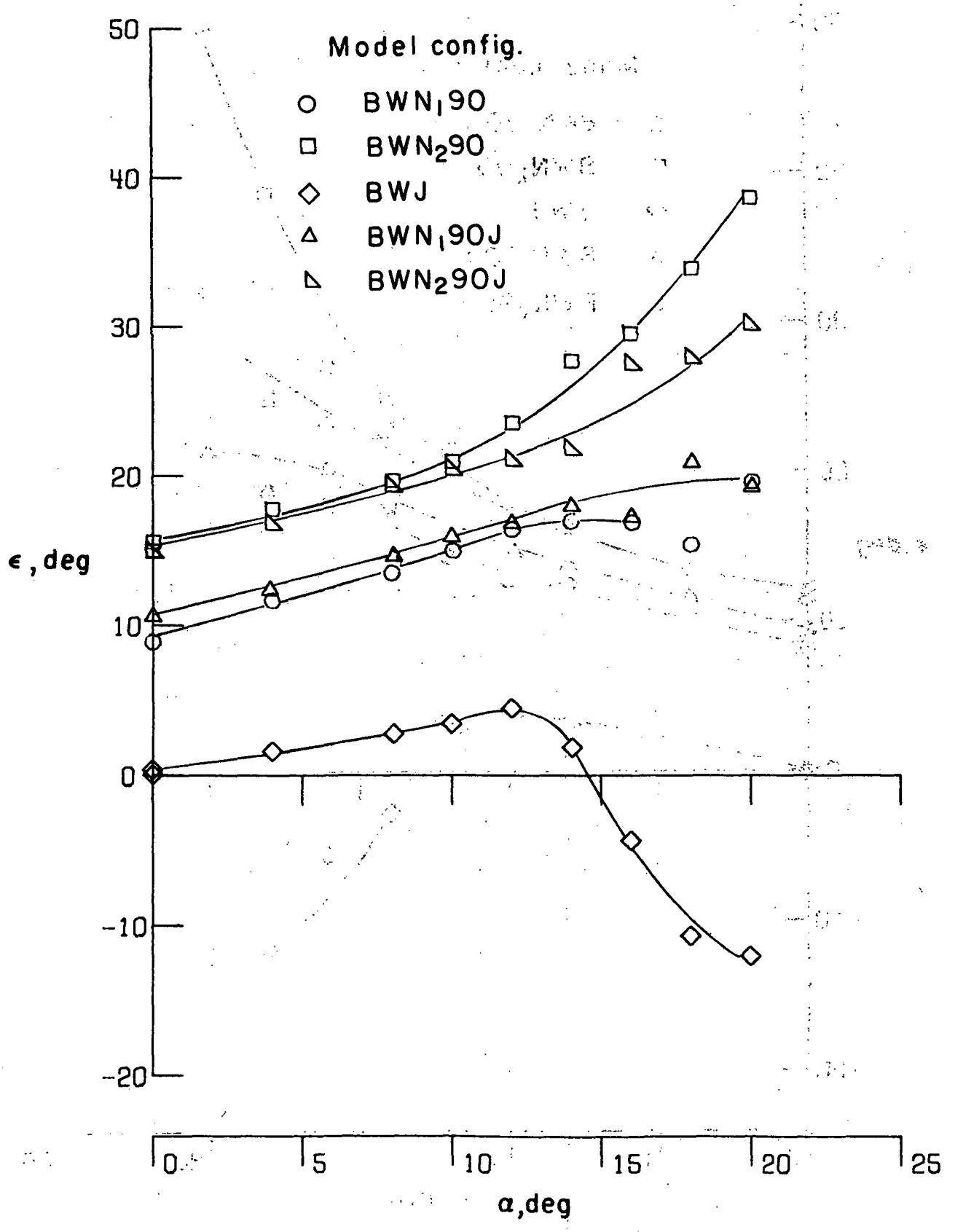


Figure 72.- Effect of thrust location on variation of downwash with angle of attack. $z/\bar{c} = -0.40$; $\left(V_\infty/V_j\right)_e = 0.2$.

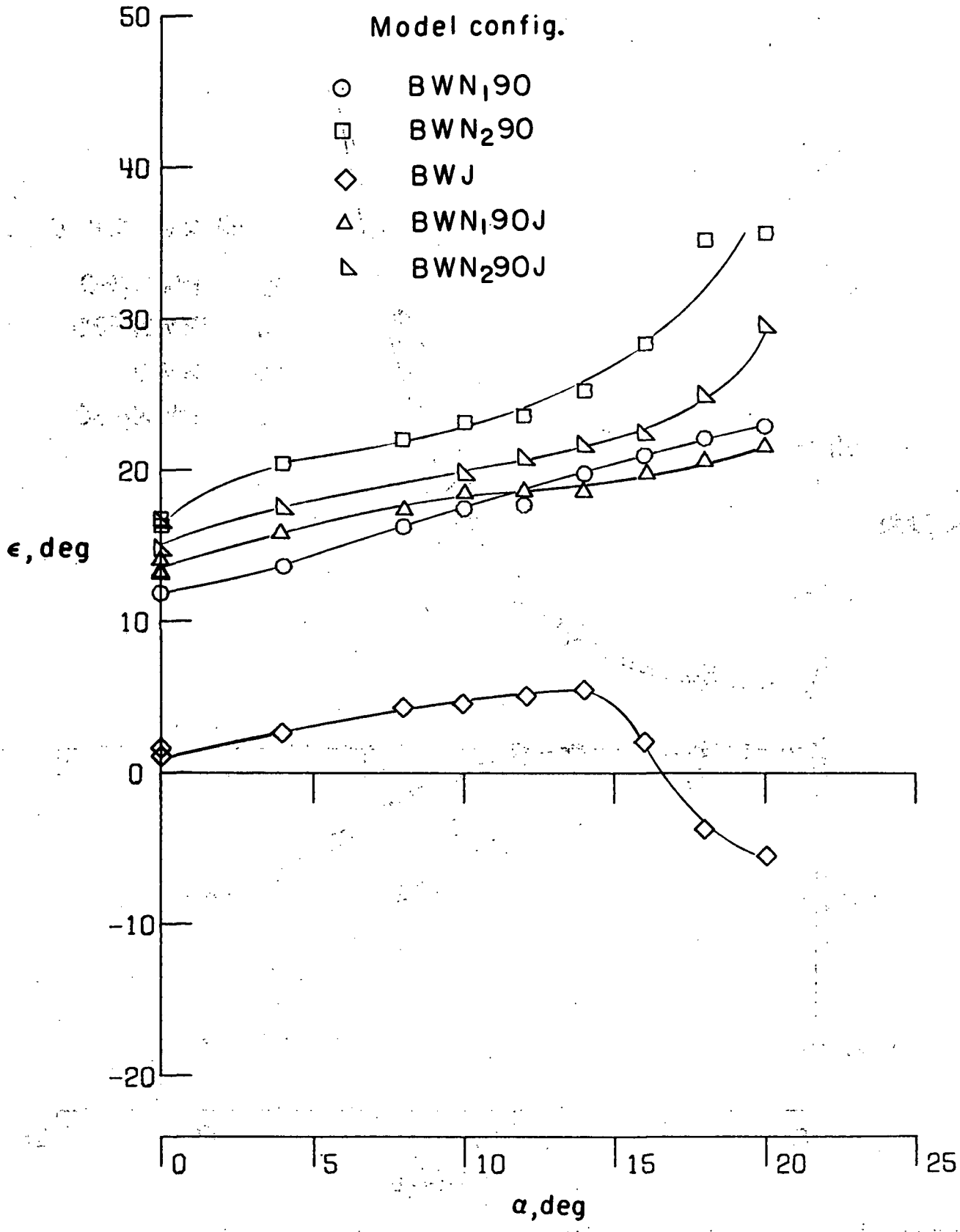


Figure 73.- Effect of thrust location on variation of downwash with angle of attack. $z/\bar{c} = -0.40$; $\left(V_\infty/V_j\right)_e = 0.1$.

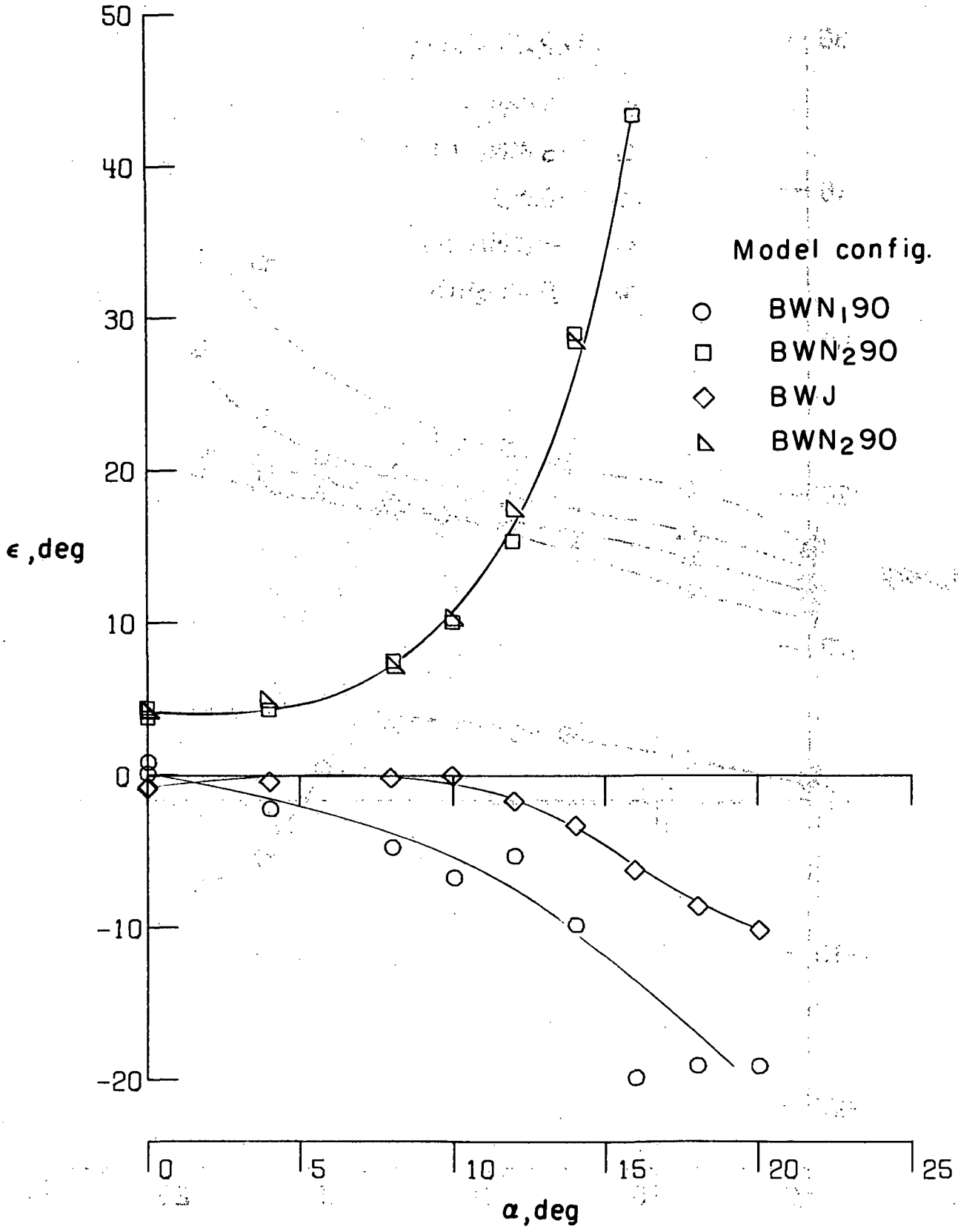


Figure 74.- Effect of thrust location on variation of downwash with angle of attack. $z/\bar{c} = 0.32$; $\left(V_\infty/V_j\right)_e = \infty$.

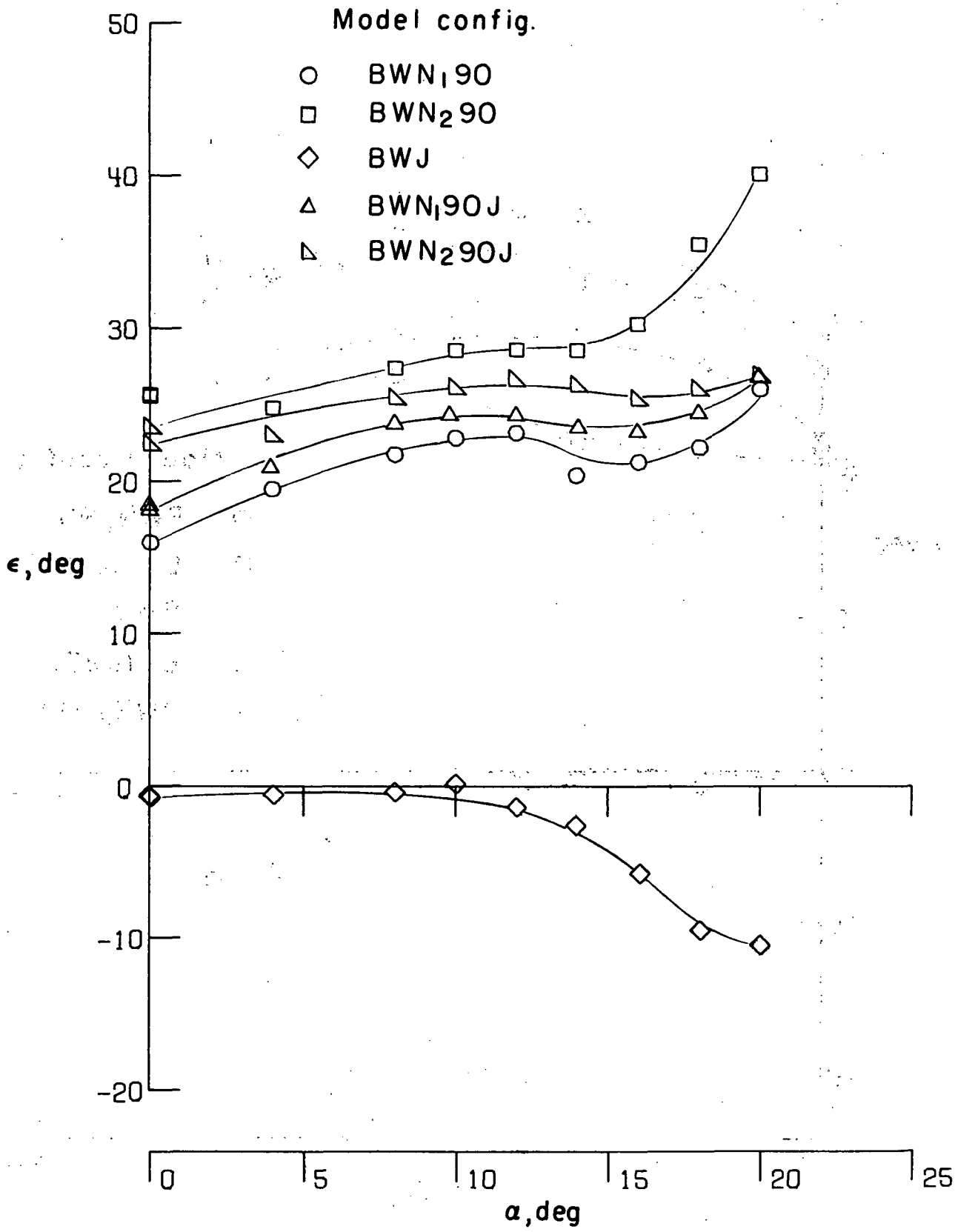


Figure 75.- Effect of thrust location on variation of downwash with angle of attack. $z/\bar{c} = 0.32$; $\left(V_\infty/V_j\right)_e = 0.3$.

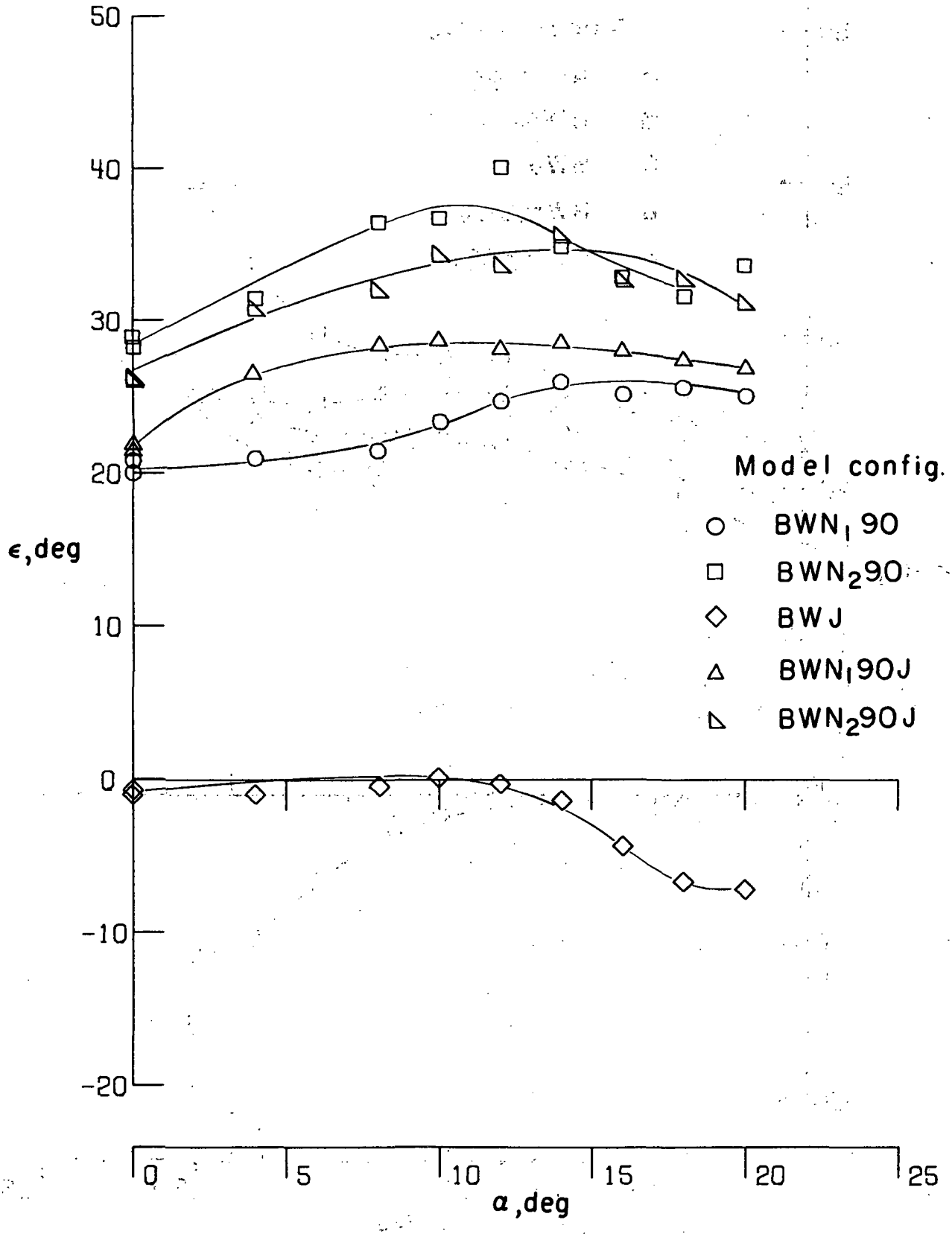


Figure 76.- Effect of thrust location on variation of downwash with angle of attack. $z/\bar{c} = 0.32$; $\left(V_\infty/V_j\right)_e = 0.2$.

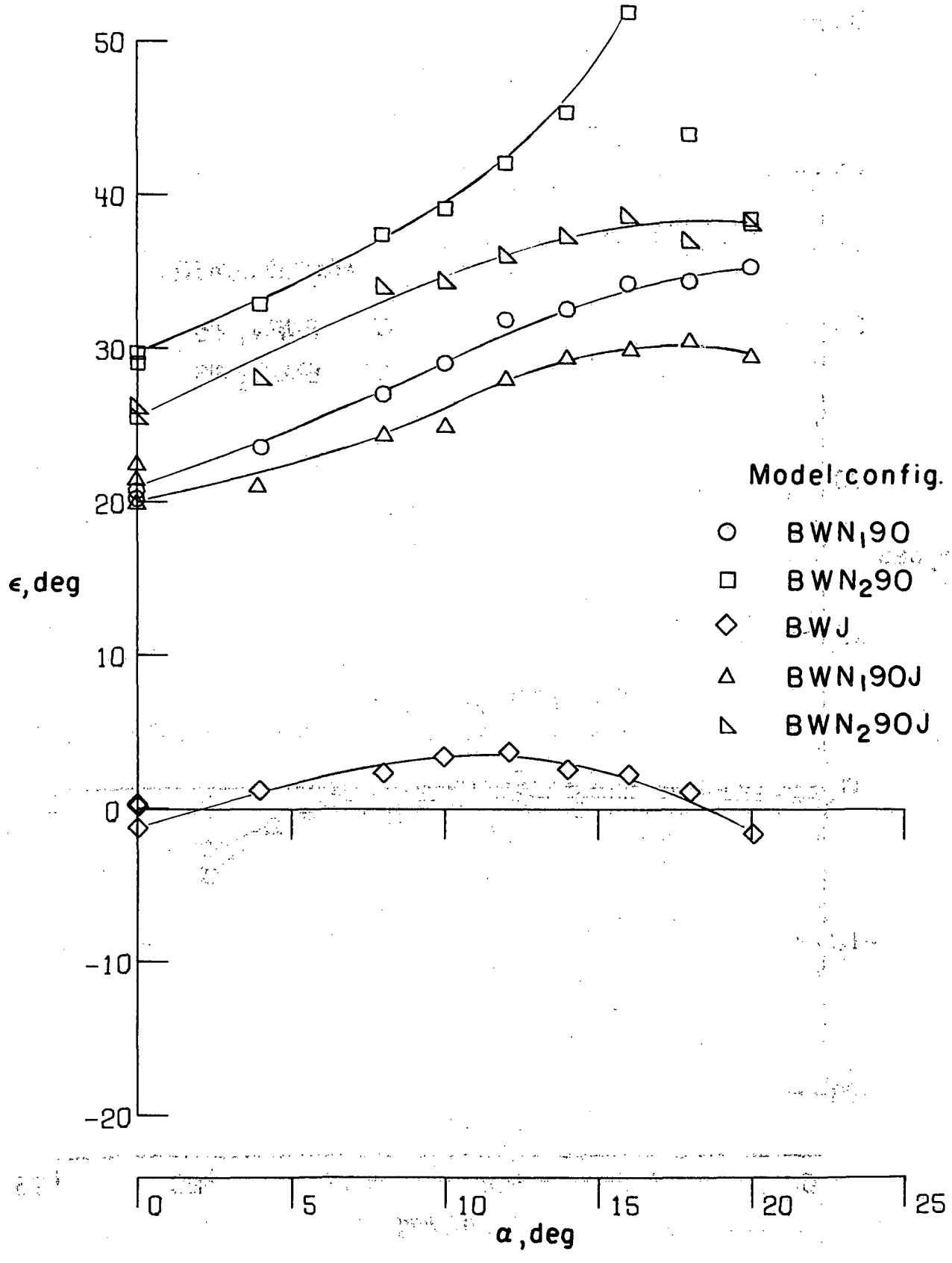


Figure 77.- Effect of thrust location on variation of downwash with angle of attack. $z/\bar{c} = 0.32$; $\left(V_\infty/V_j\right)_e = 0.1$.

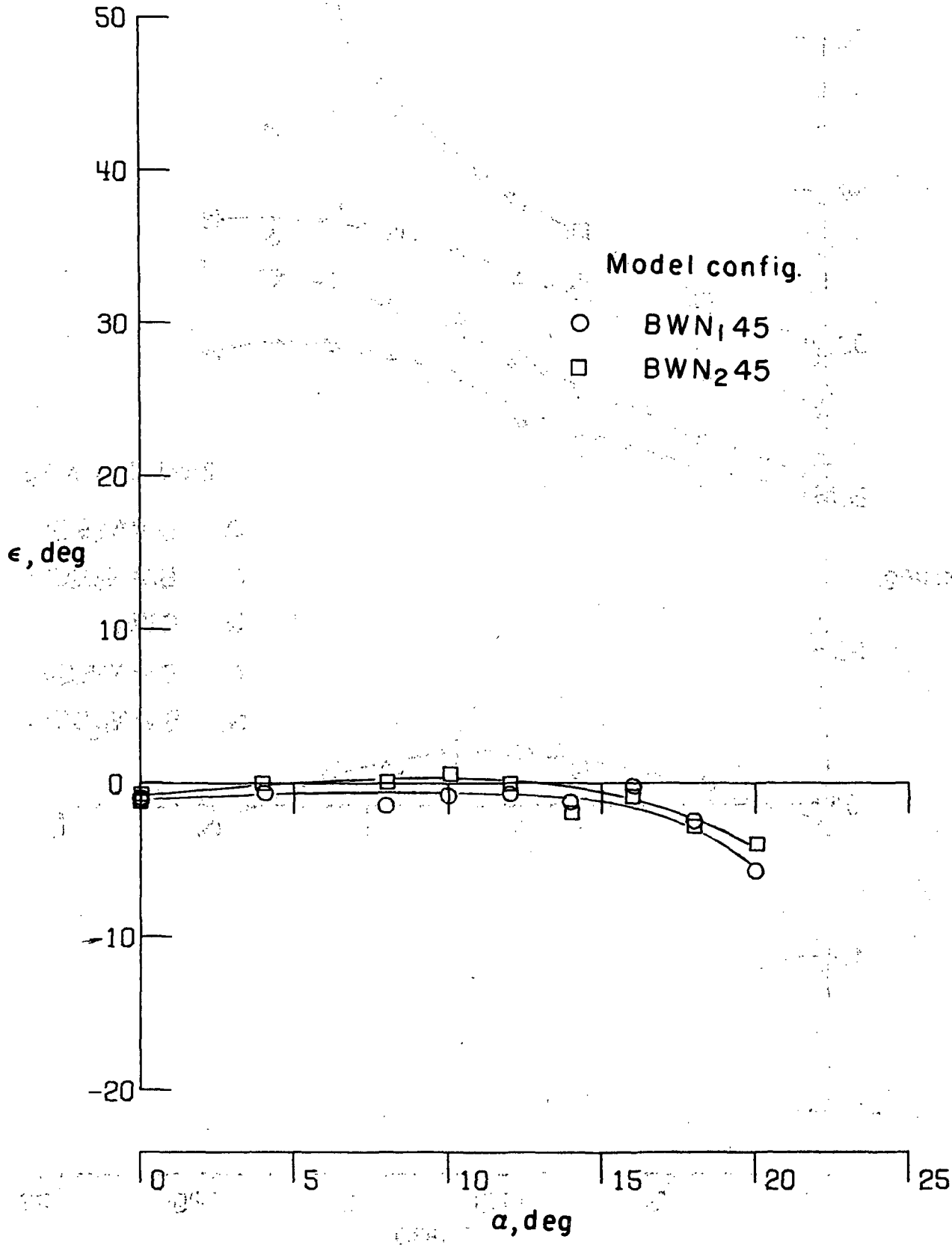


Figure 78.- Effect of thrust location on variation of downwash with angle of attack. $z/\bar{c} = -1.12$; $\left(V_\infty/V_j\right)_e = \infty$.

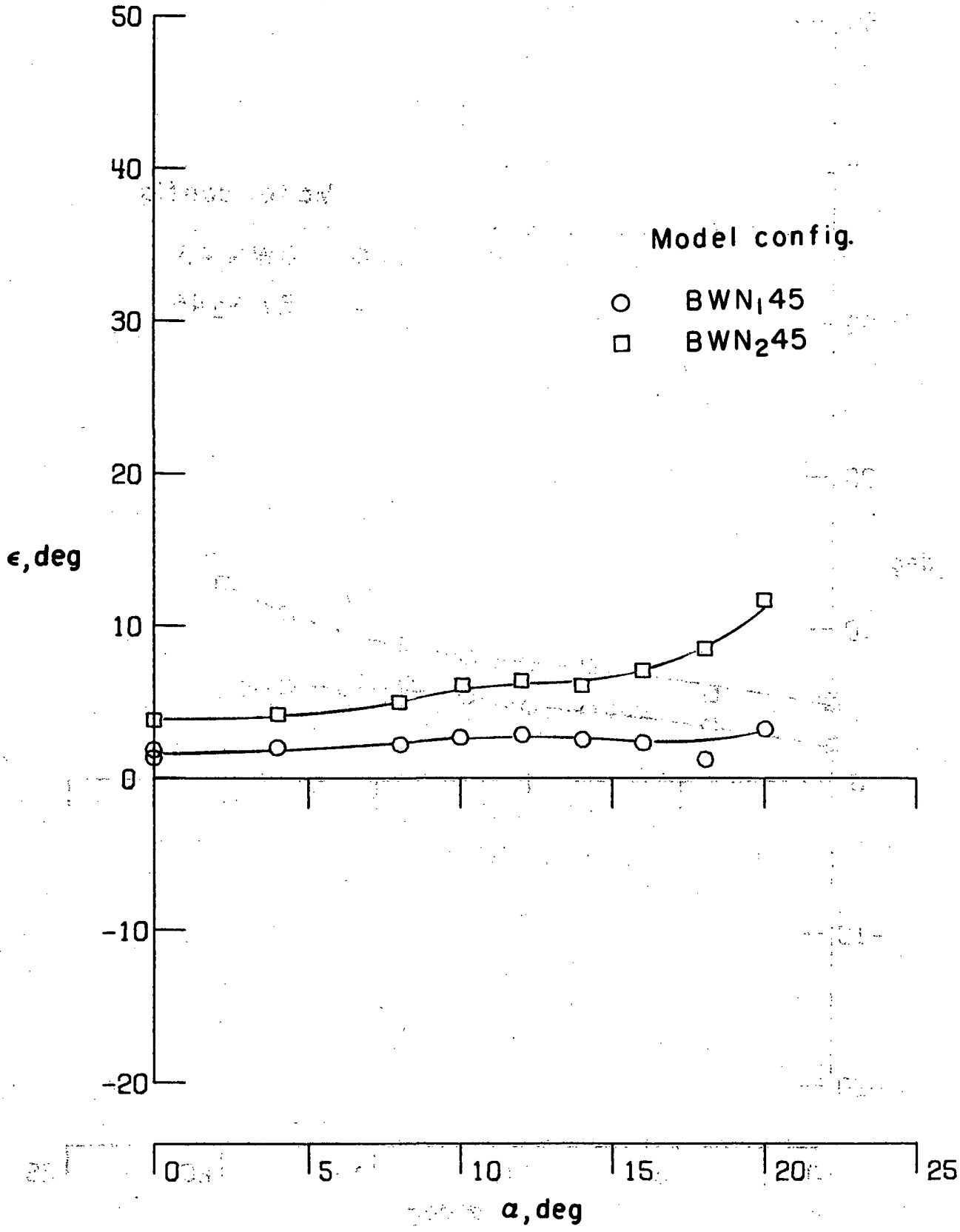


Figure 79.- Effect of thrust location on variation of downwash with angle of attack. $z/\bar{c} = -1.12$; $\left(V_\infty/V_j\right)_e = 0.3$.

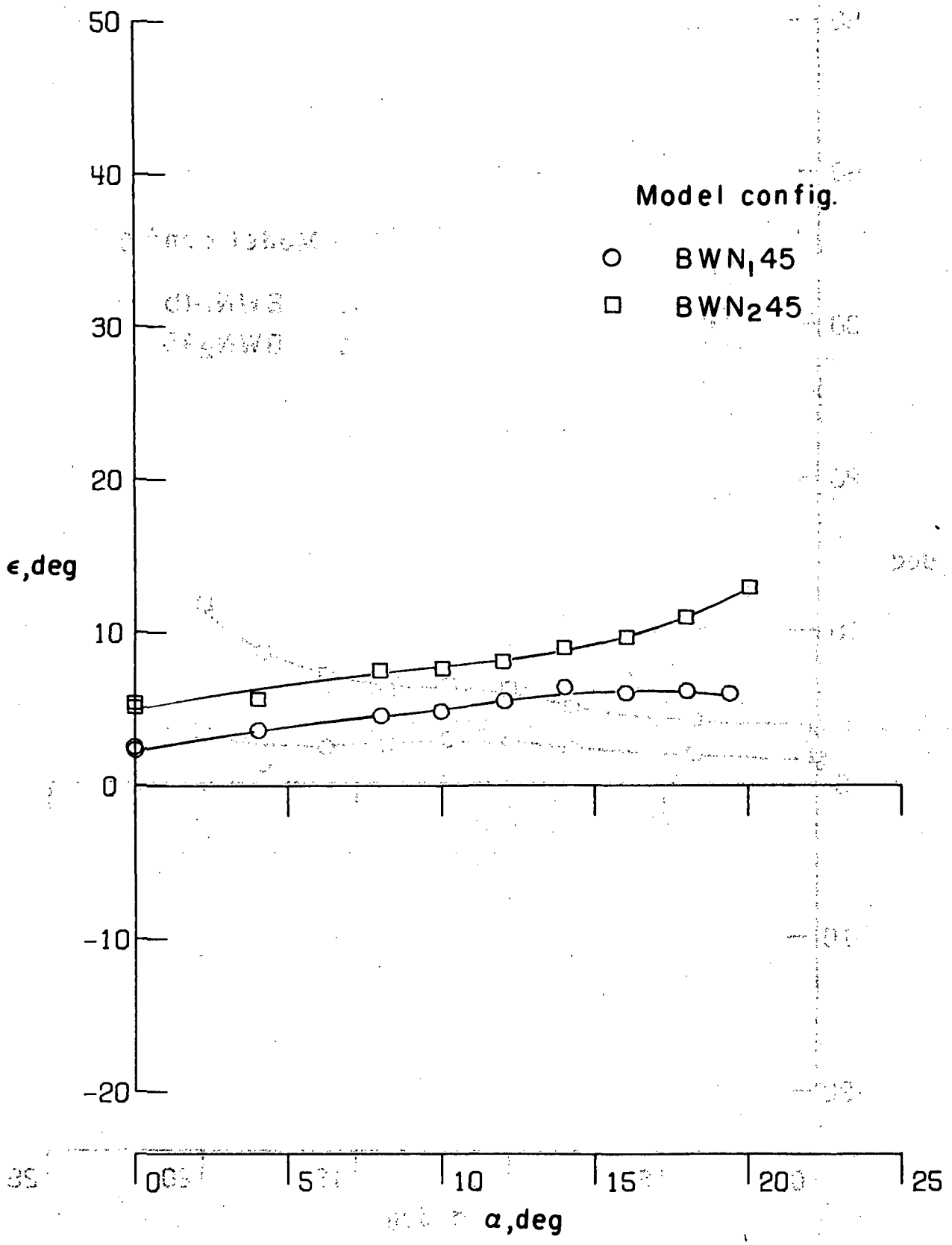


Figure 80. - Effect of thrust location on variation of downwash with angle of attack. $z/\bar{c} = -1.12$; $\left(V_\infty/V_j\right)_e = 0.2$.

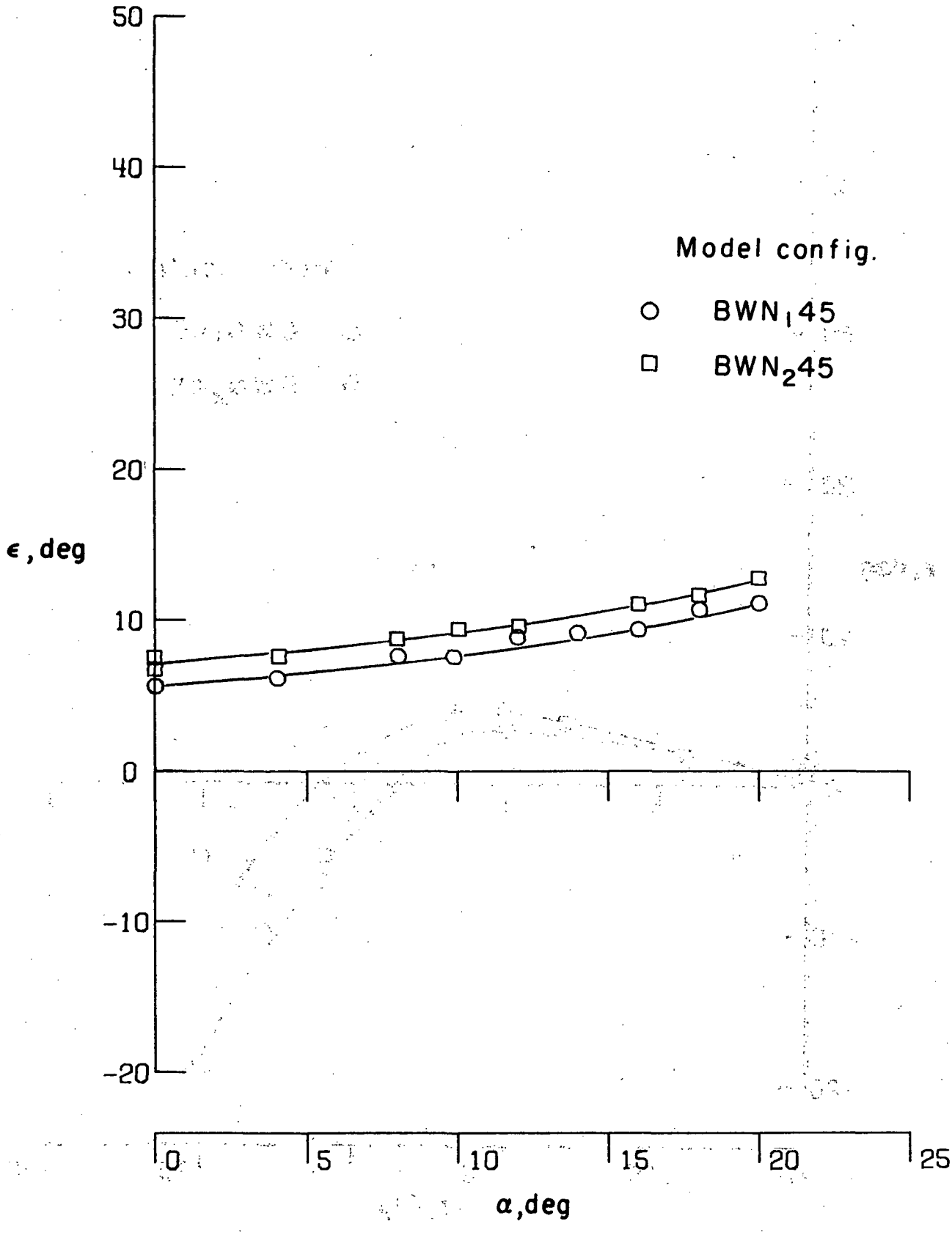


Figure 81.- Effect of thrust location on variation of downwash with angle of attack. $z/\bar{c} = -1.12$; $\left(V_\infty/V_j\right)_e = 0.1$.

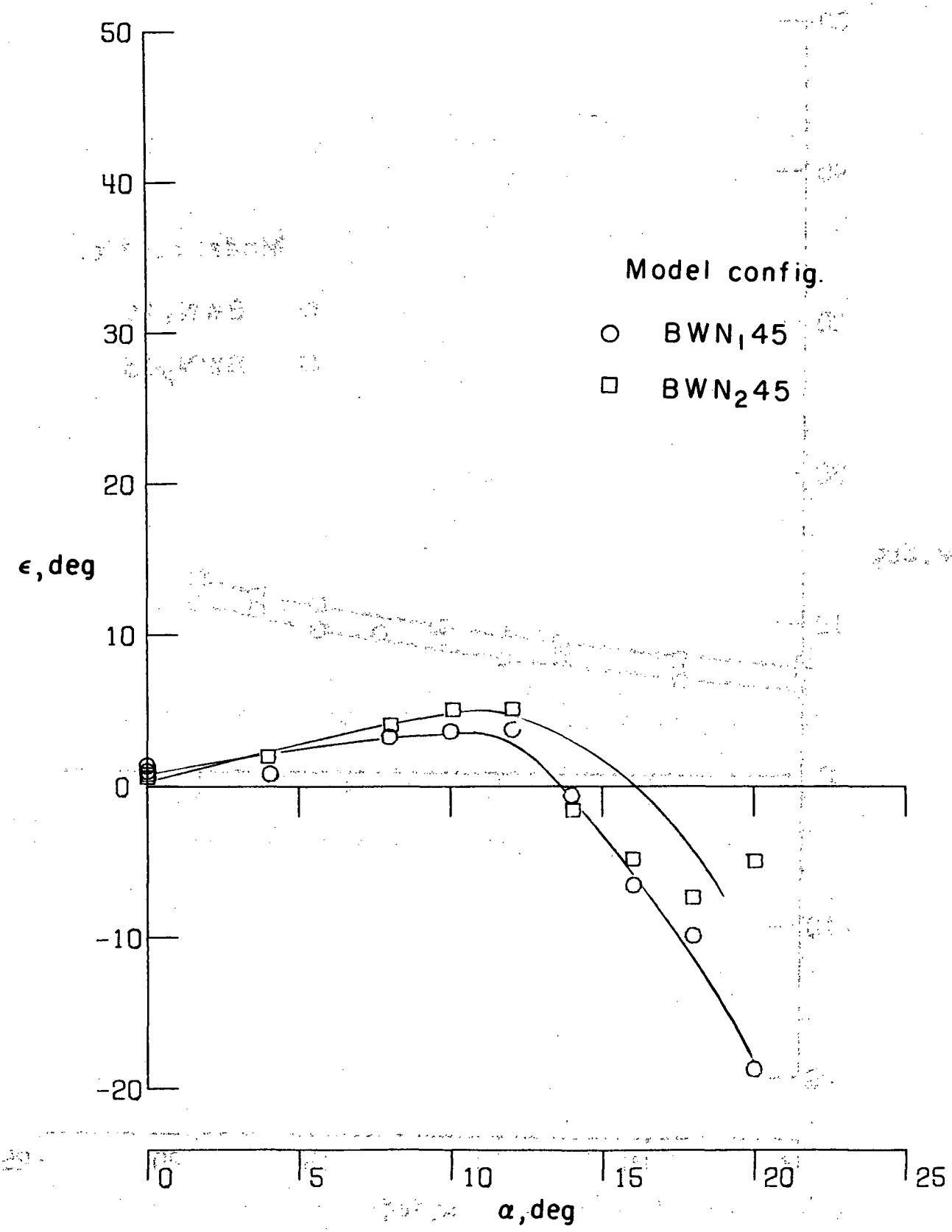


Figure 82. - Effect of thrust location on variation of downwash with angle of attack. $z/\bar{c} = -0.40$; $\left(V_\infty/V_j\right)_e = \infty$.

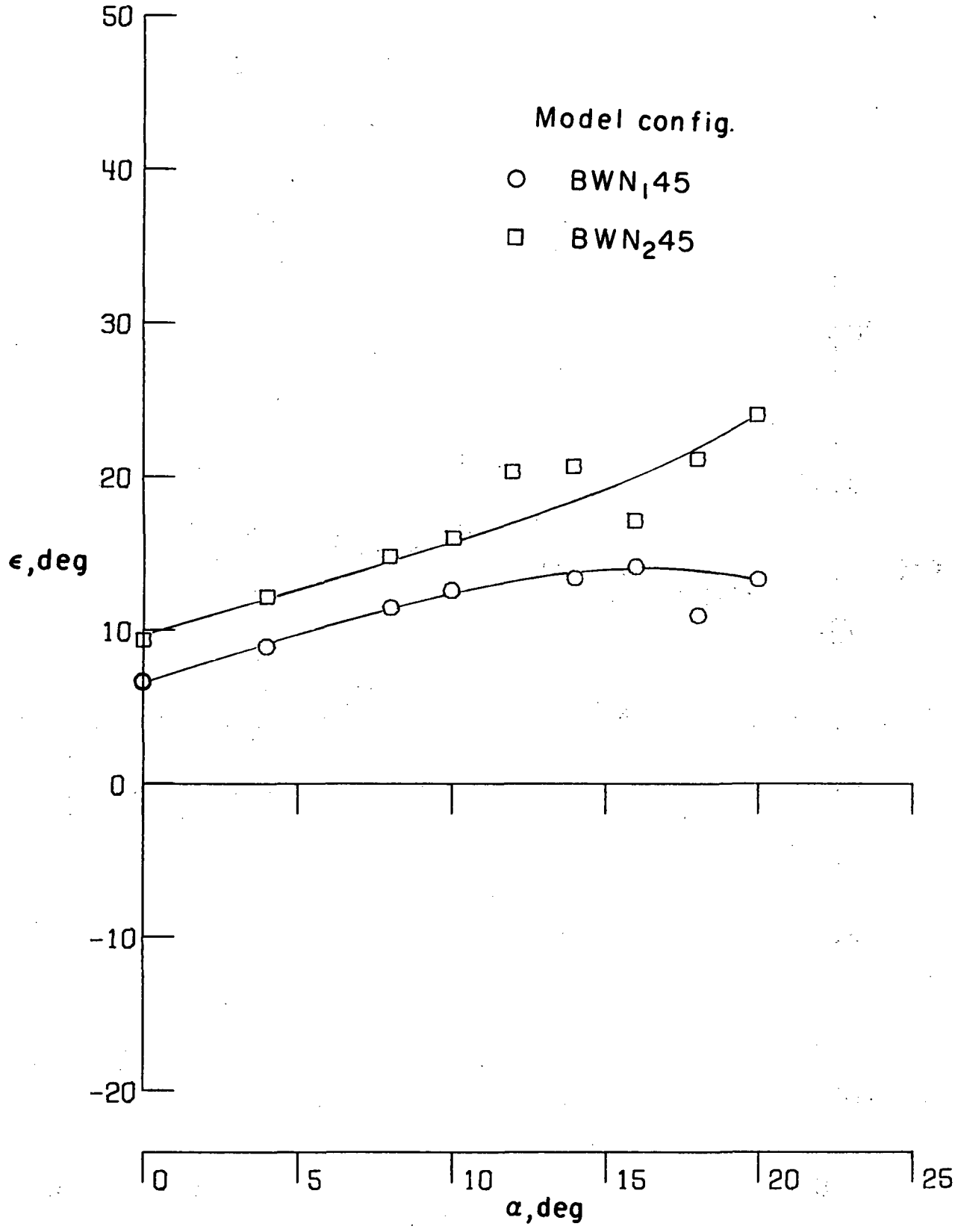


Figure 83.- Effect of thrust location on variation of downwash with angle of attack. $z/\bar{c} = -0.40$; $\left(V_\infty/V_j\right)_e = 0.3$.

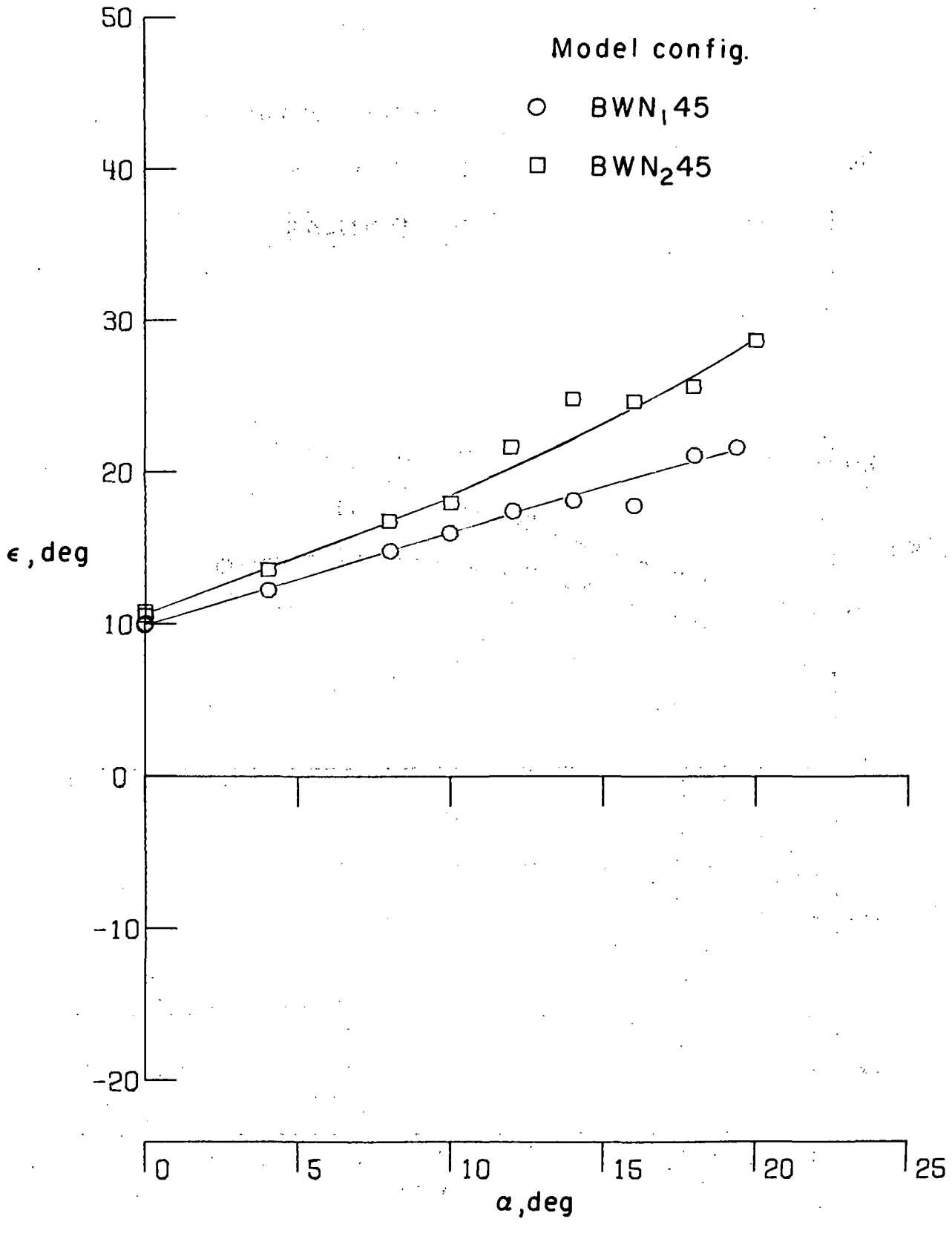


Figure 84.- Effect of thrust location on variation of downwash with angle of attack. $z/\bar{c} = -0.40$; $\left(V_\infty/V_j\right)_e = 0.2$.

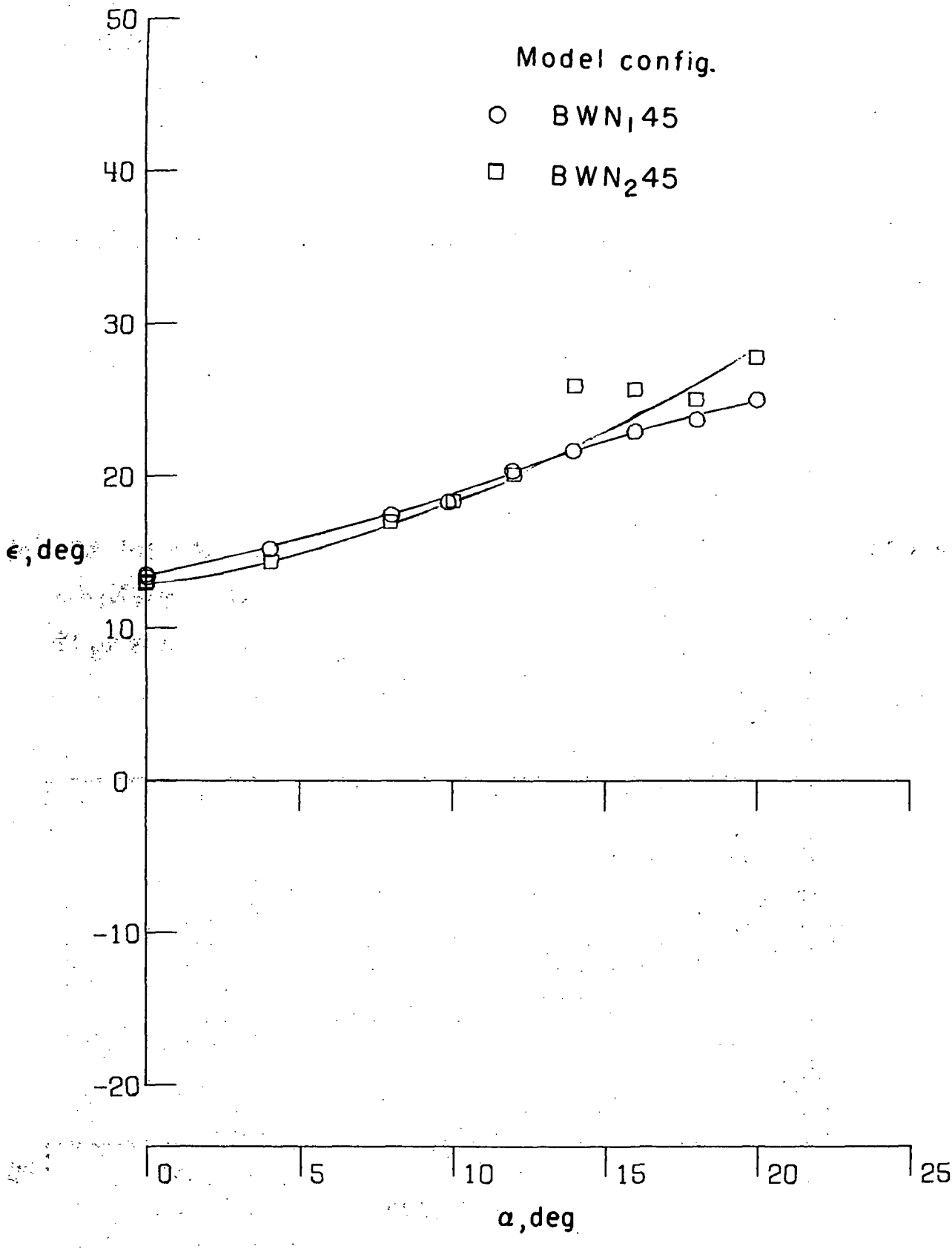


Figure 85.- Effect of thrust location on variation of downwash with angle of attack. $z/\bar{c} = -0.40$; $\left(V_\infty/V_j\right)_e = 0.1$.

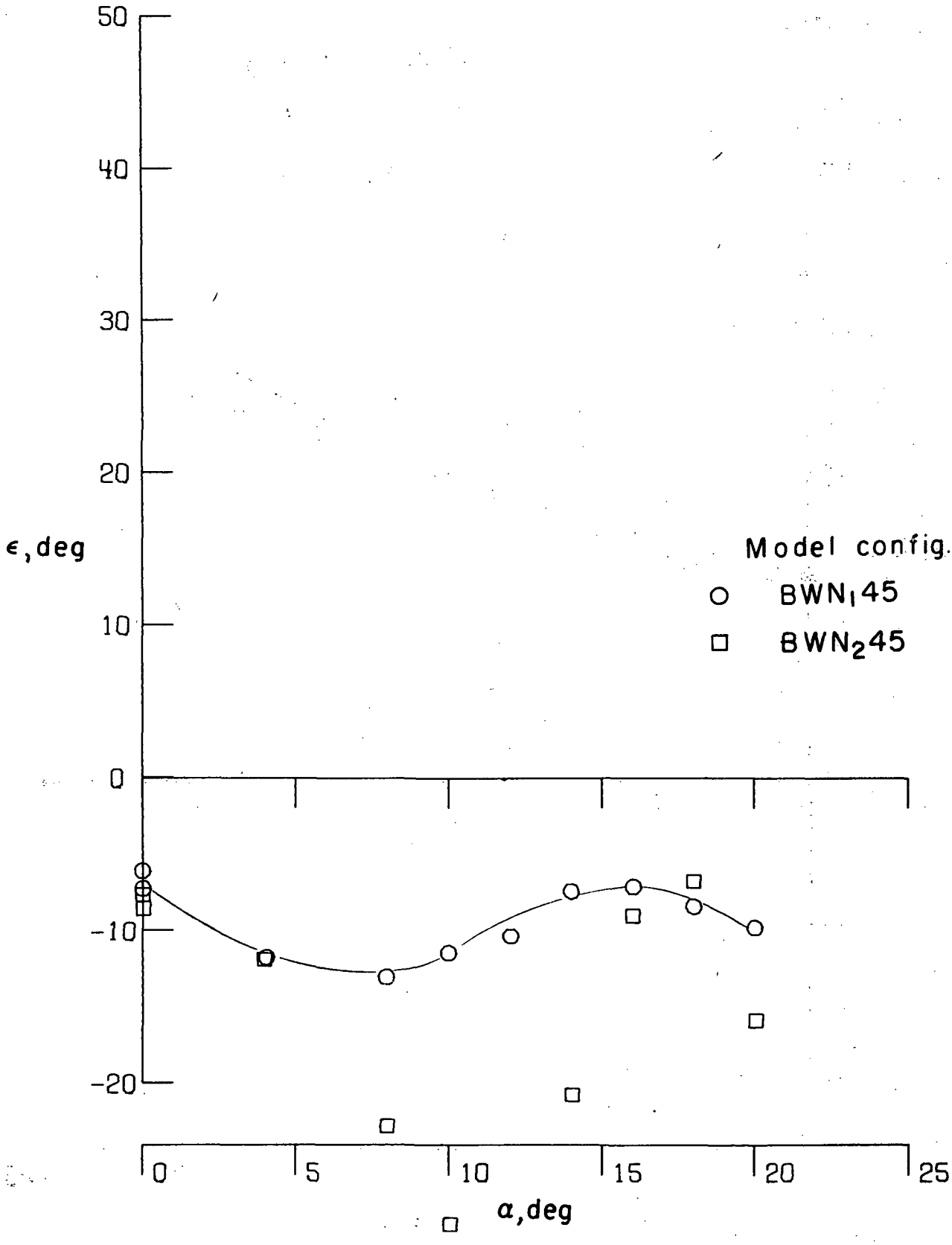


Figure 86.- Effect of thrust location on variation of downwash with angle of attack. $z/\bar{c} = 0.32$; $\left(V_\infty/V_j\right)_e = \infty$.

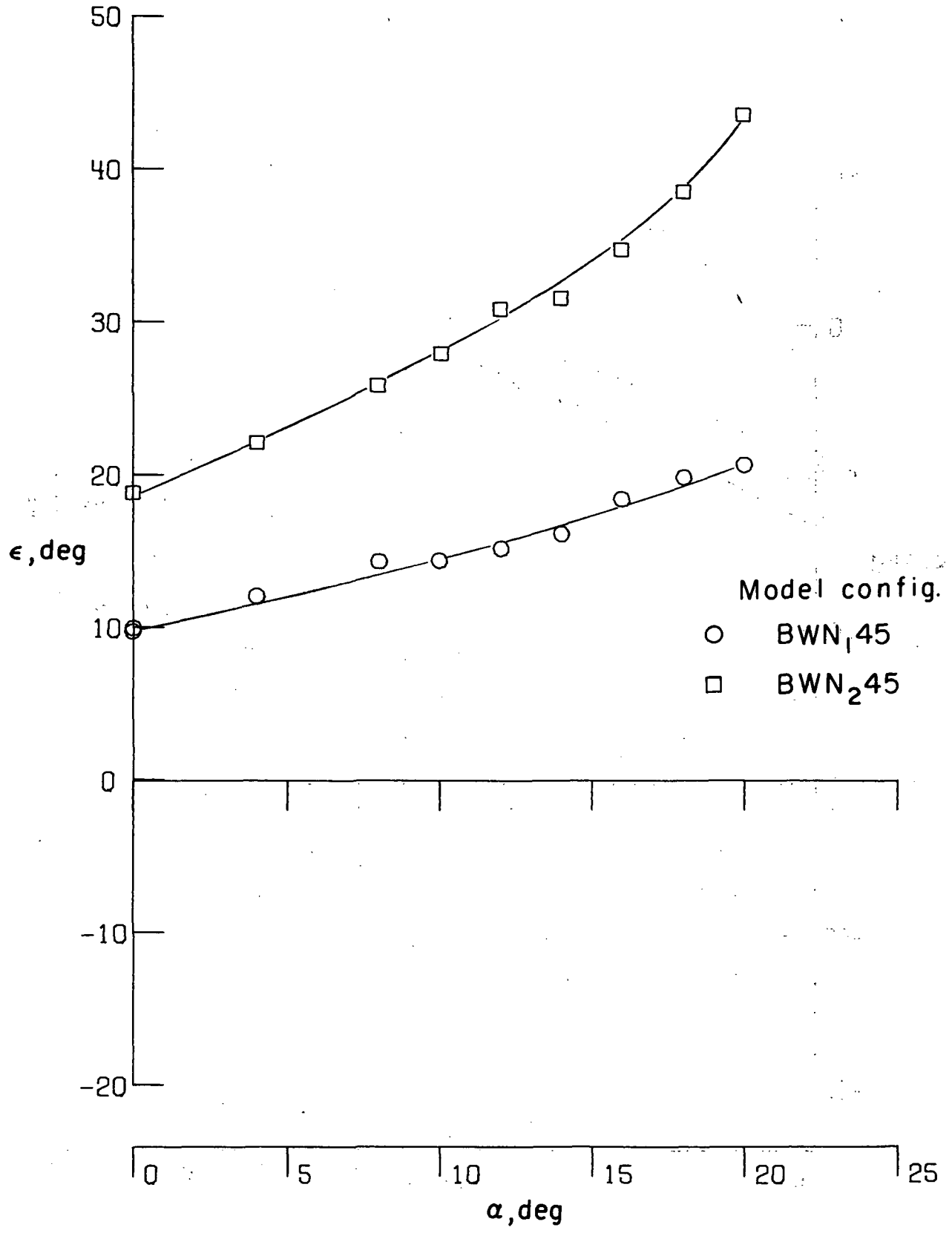


Figure 87.- Effect of thrust location on variation of downwash with angle of attack. $z/\bar{c} = 0.32$; $\left(V_\infty/V_j\right)_e = 0.3$.

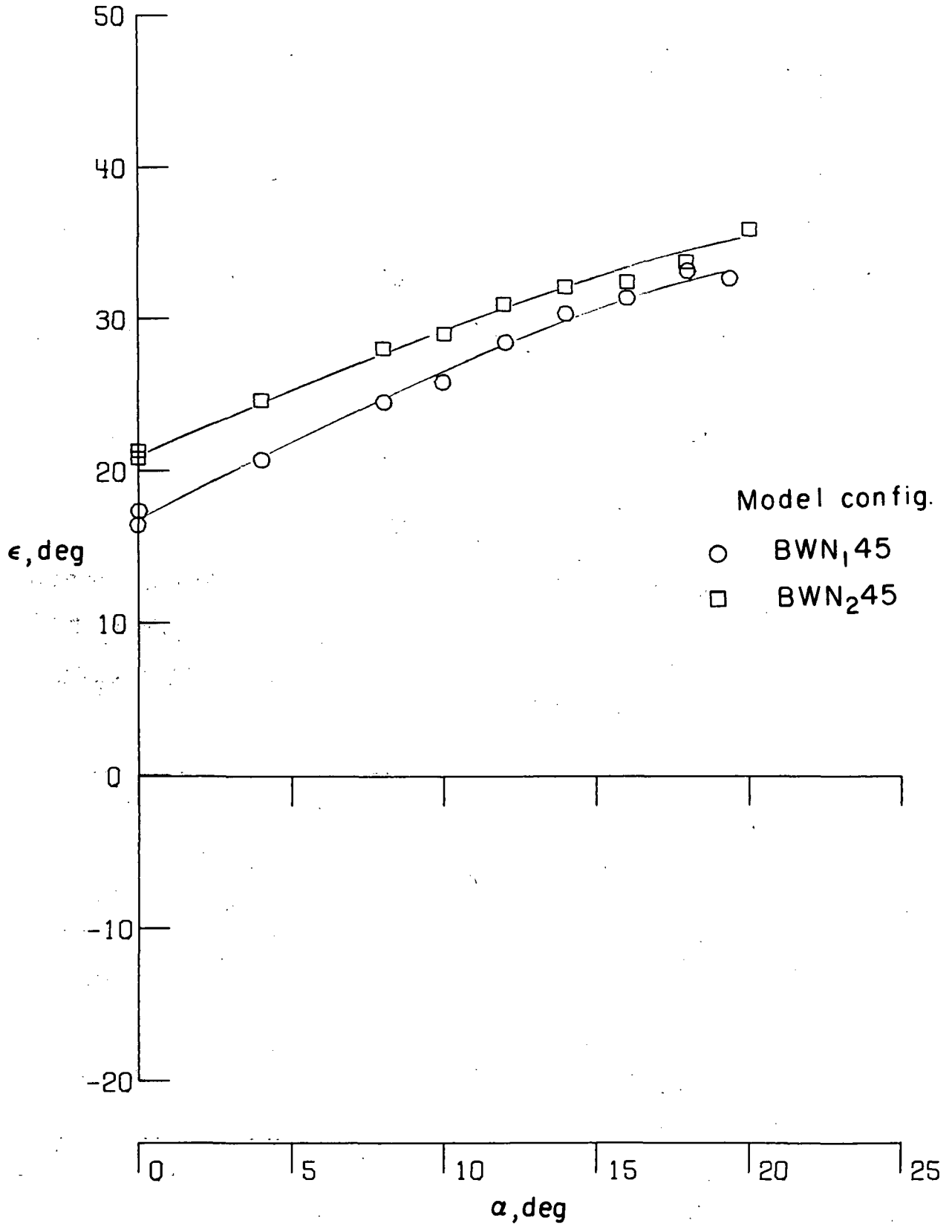


Figure 88.- Effect of thrust location on variation of downwash with angle of attack. $z/\bar{c} = 0.32$; $\left(V_\infty / V_j\right)_e = 0.2$.

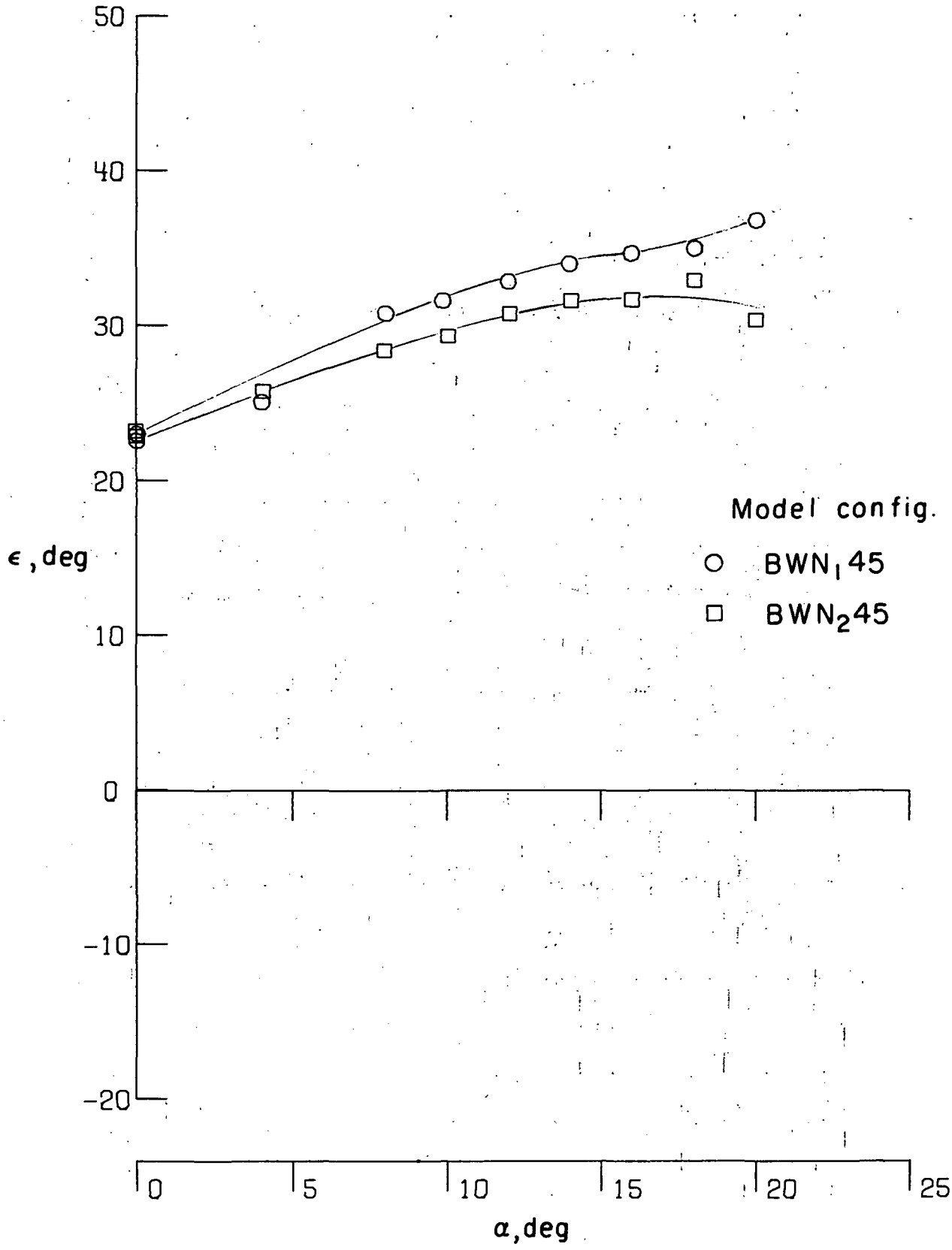
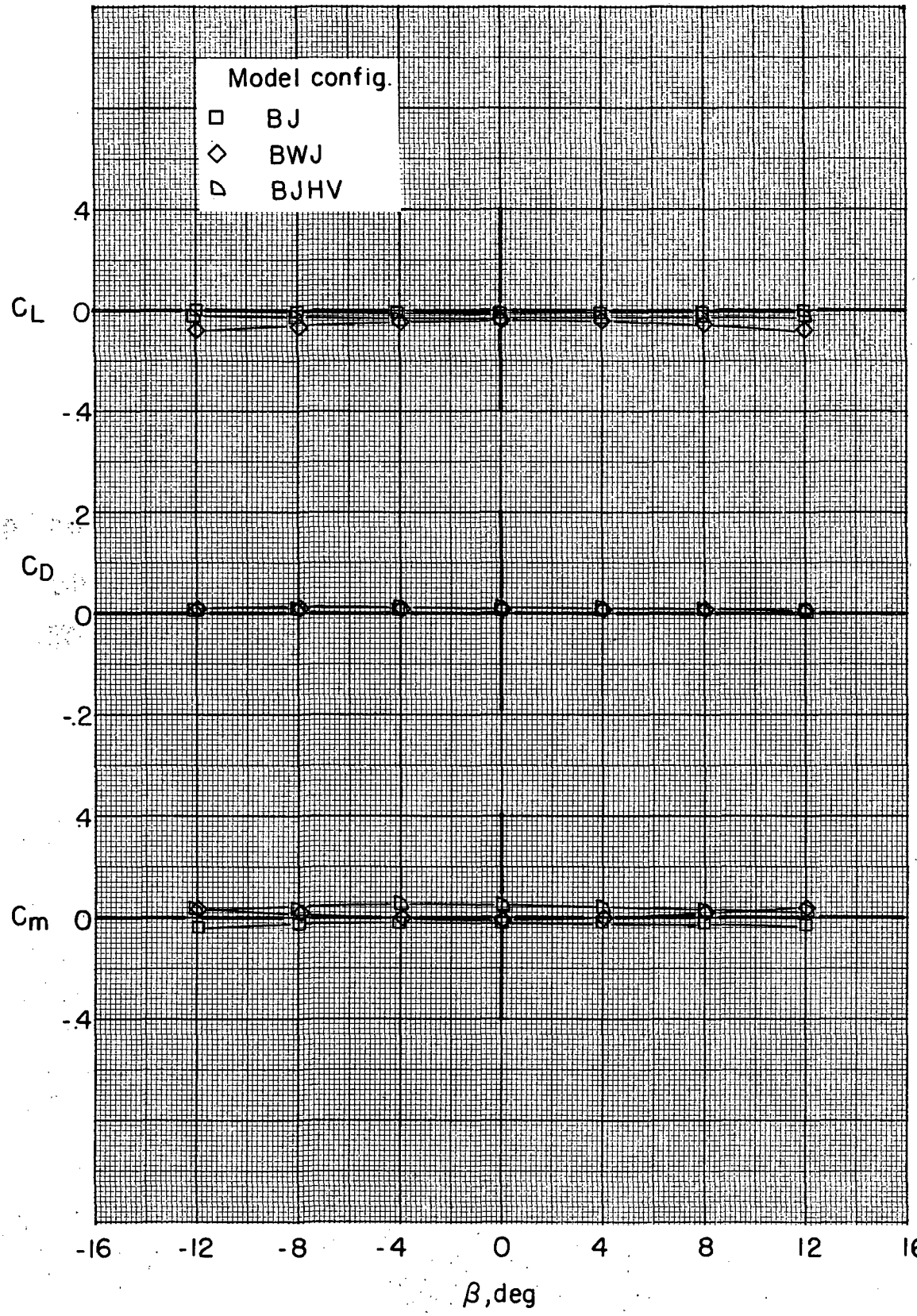
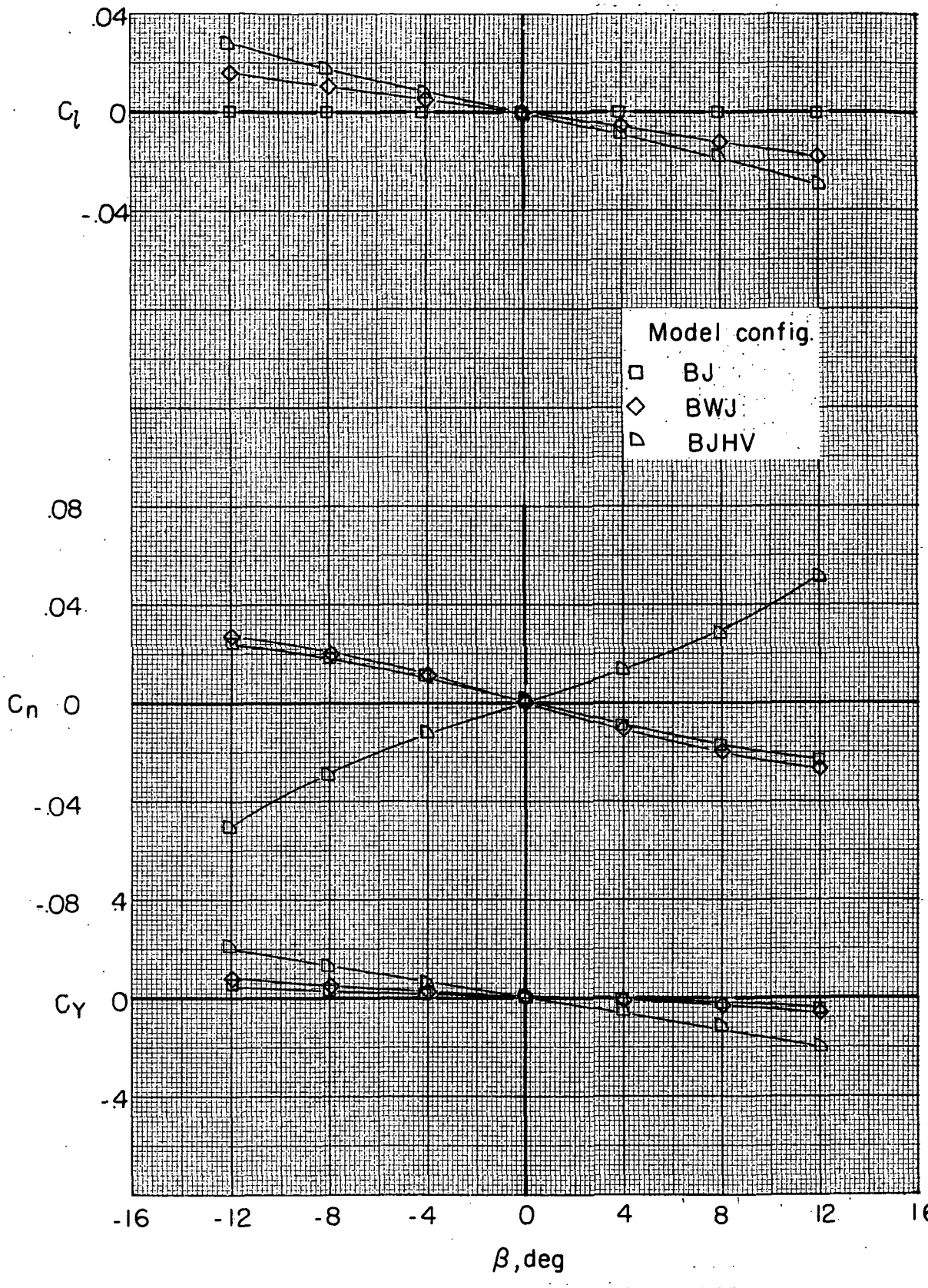


Figure 89.- Effect of thrust location on variation of downwash with angle of attack. $z/\bar{c} = 0.32$; $\left(V_\infty/V_j\right)_e = 0.1$.



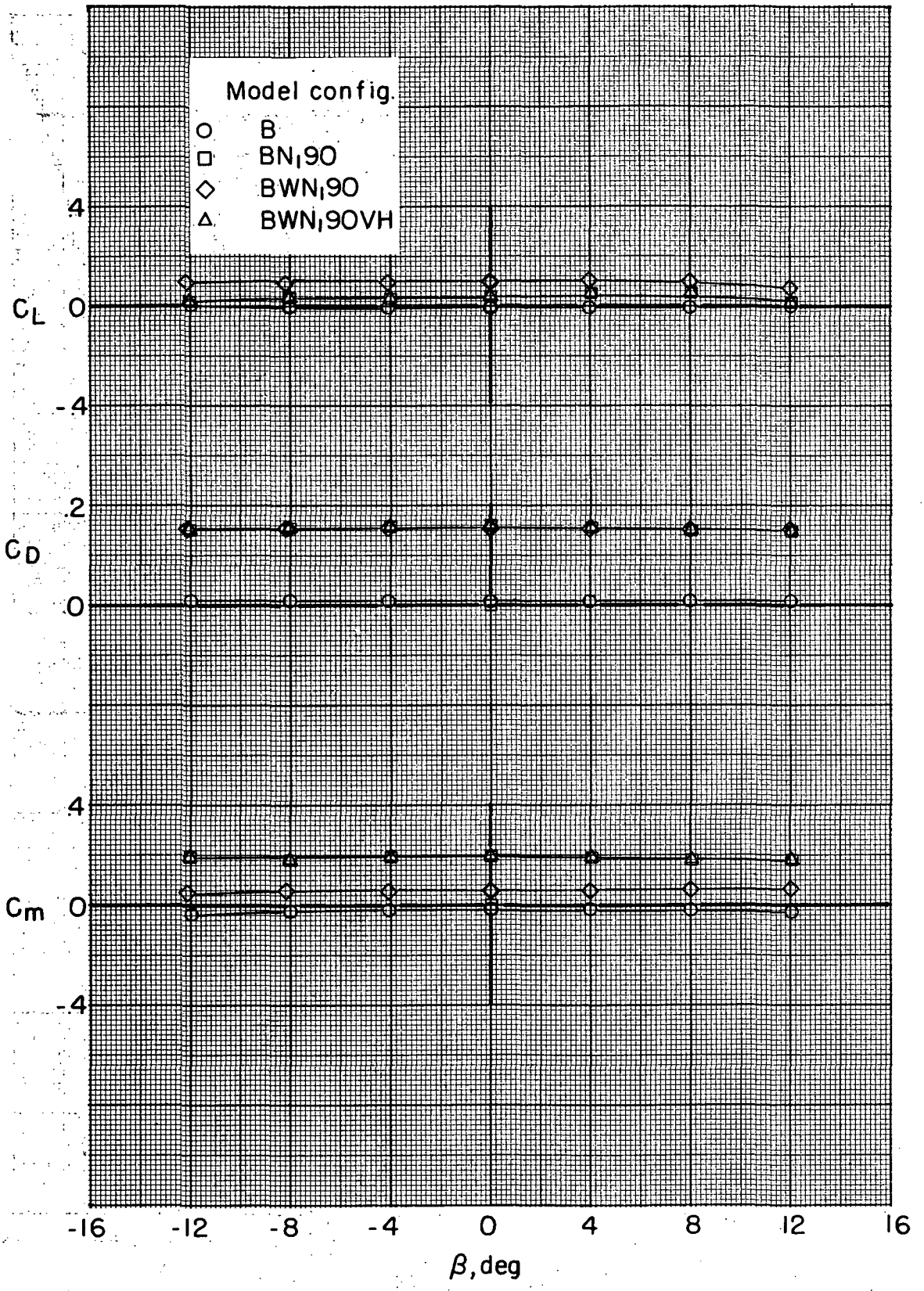
(a) Variation of C_L, C_D, and C_m with β.

Figure 90.- Effect of model components on aerodynamic characteristics in sideslip of lift-jet configuration without power. $\left(V_\infty/V_j\right)_e = \infty$.



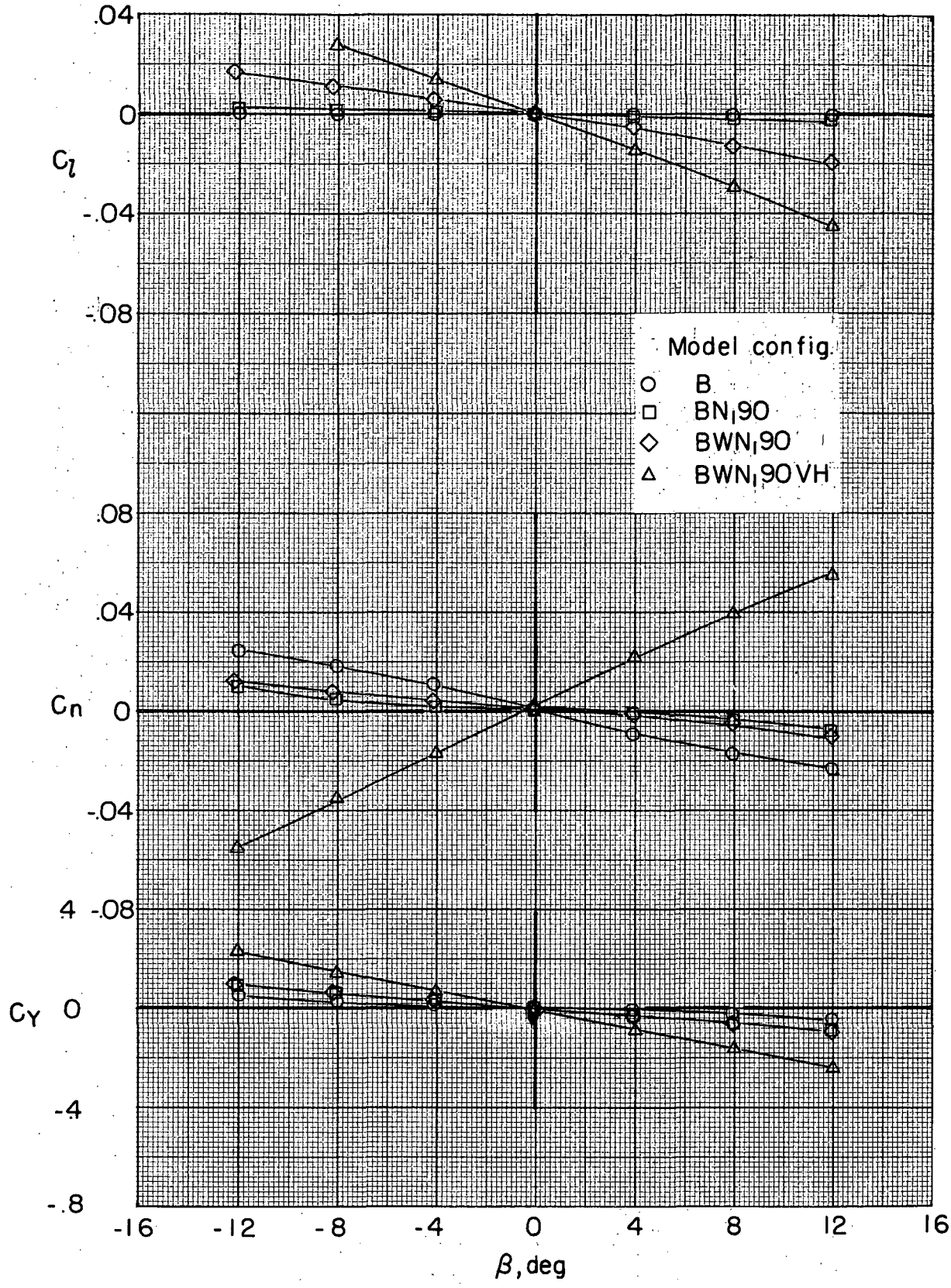
(b) Variation of C_l, C_n, and C_Y with β.

Figure 90.- Concluded.



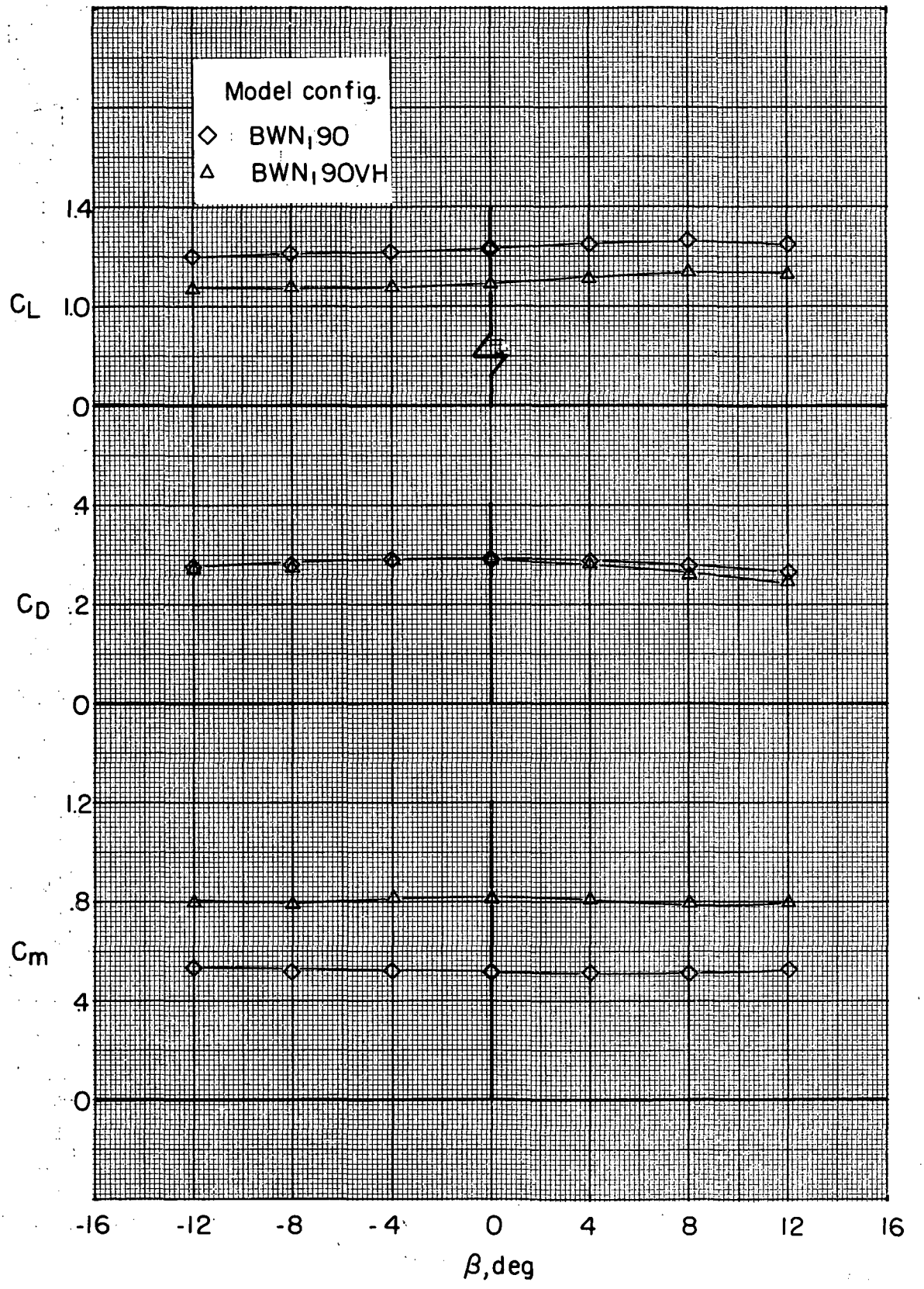
(a) Variation of C_L, C_D, and C_m with β.

Figure 91.- Effect of model components on aerodynamic characteristics in sideslip of front vectored-thrust configuration without power. $\left(V_\infty/V_j\right)_e = \infty$.



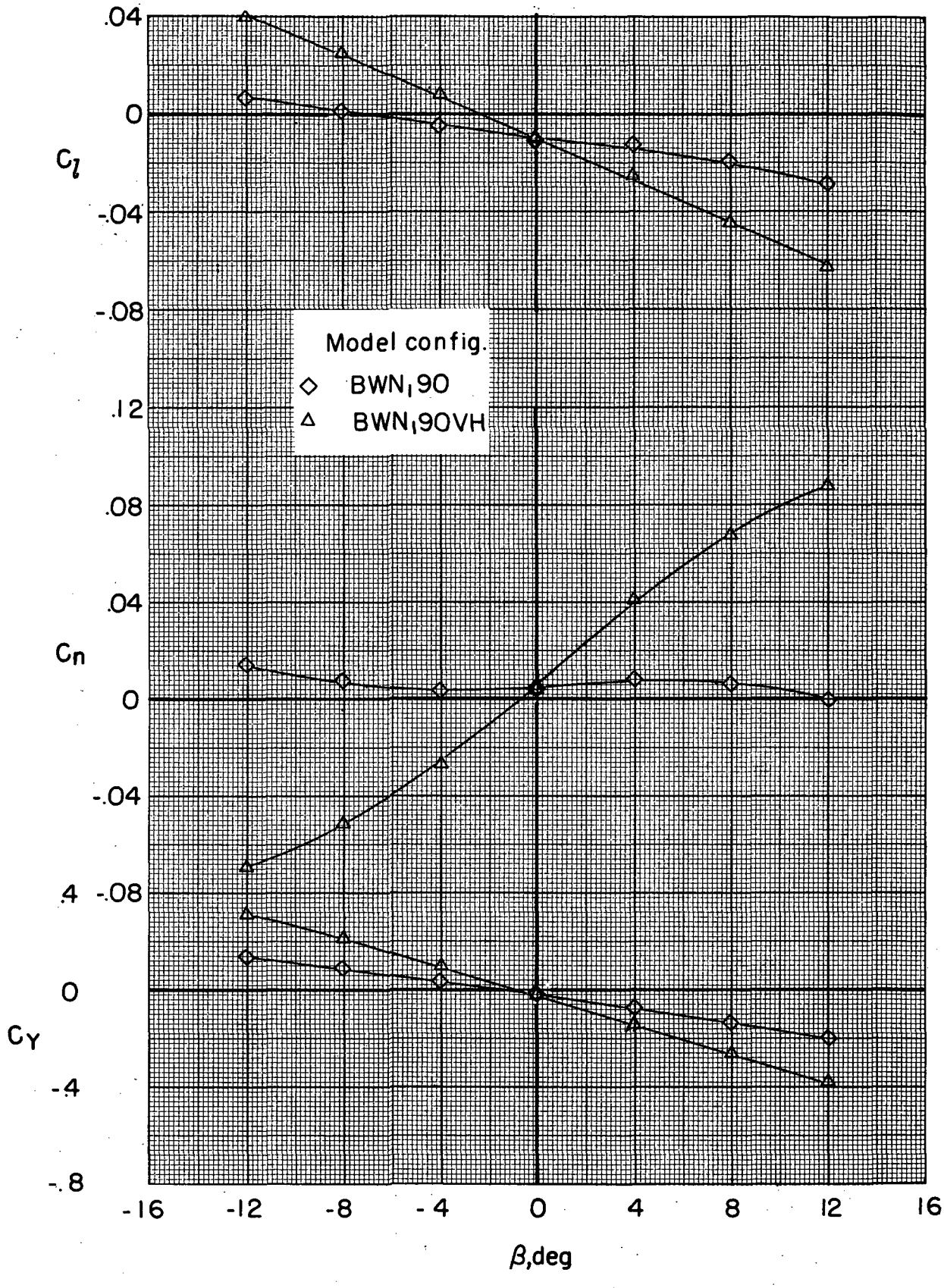
(b) Variation of C_l, C_n, and C_Y with β.

Figure 91.- Concluded.



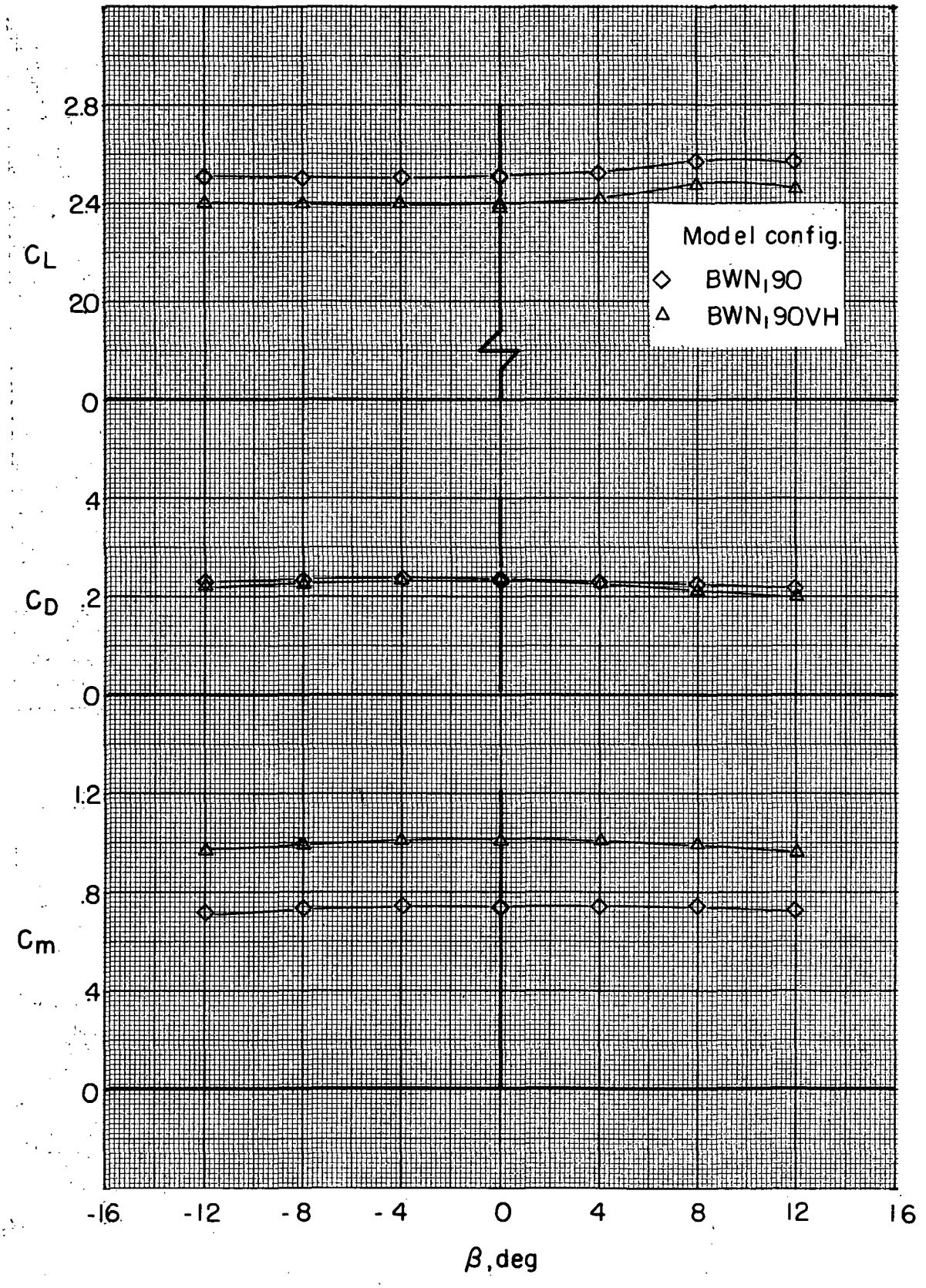
(a) Variation of C_L, C_D, and C_m with β.

Figure 92.- Effect of model components on aerodynamic characteristics in sideslip of front vectored-thrust configuration with power. $\left(V_\infty/V_j\right)_e = 0.3$.



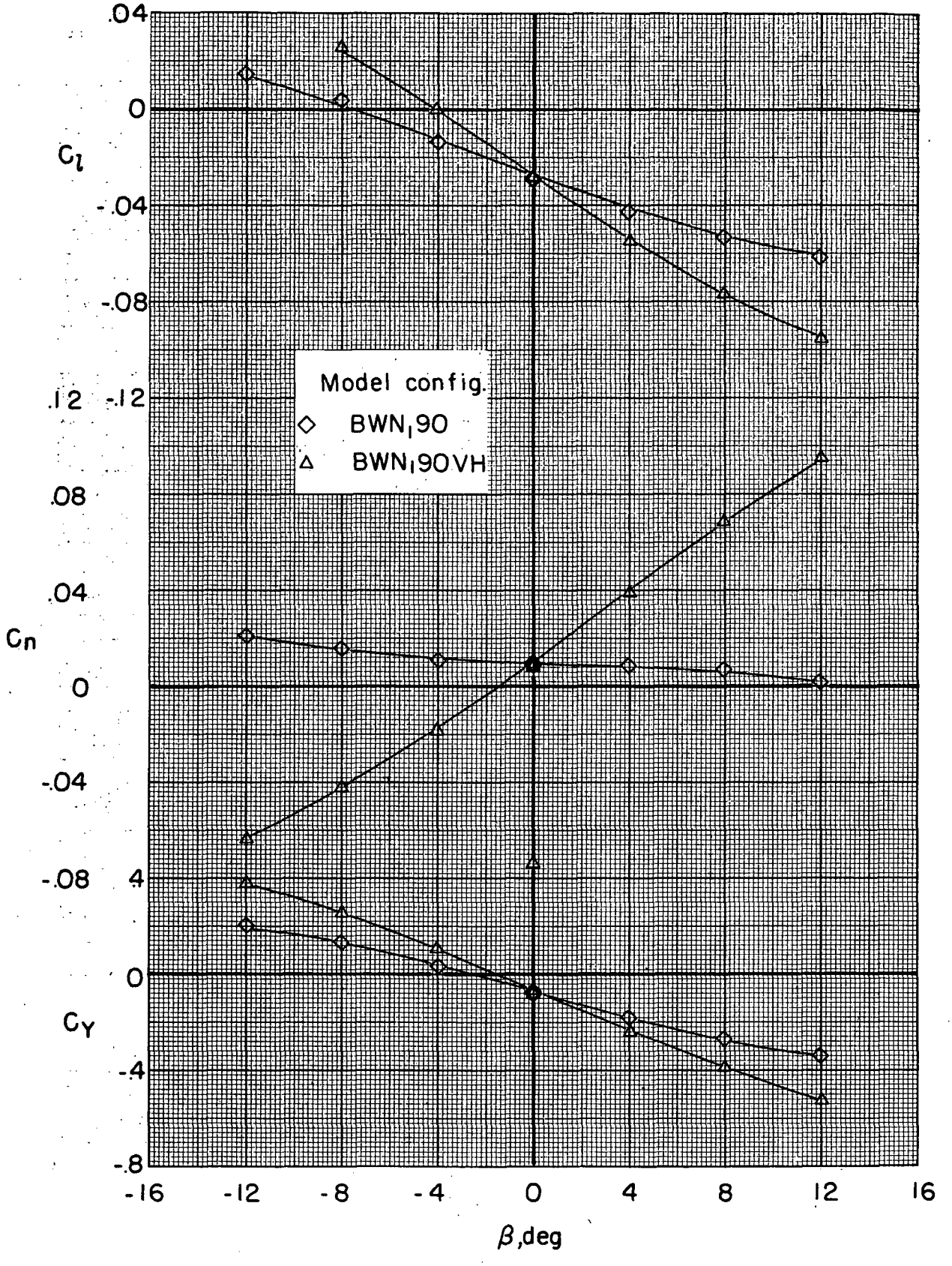
(b) Variation of C_l, C_n, and C_Y with β.

Figure 92.- Concluded.



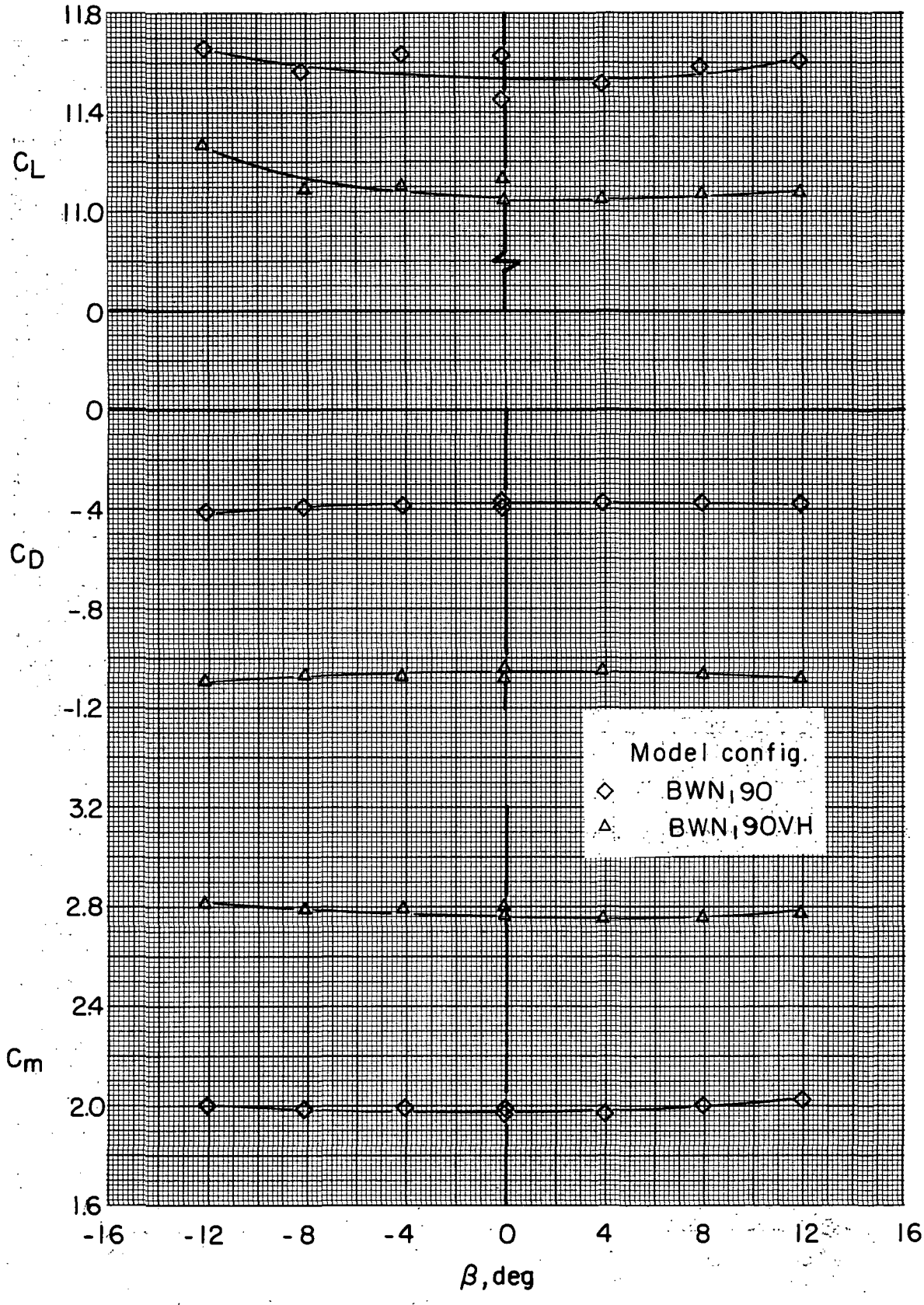
(a) Variation of C_L, C_D, and C_m with β.

Figure 93.- Effect of model components on aerodynamic characteristics in sideslip of front vectored-thrust configuration with power. $\left(V_\infty/V_j\right)_e = 0.2$.



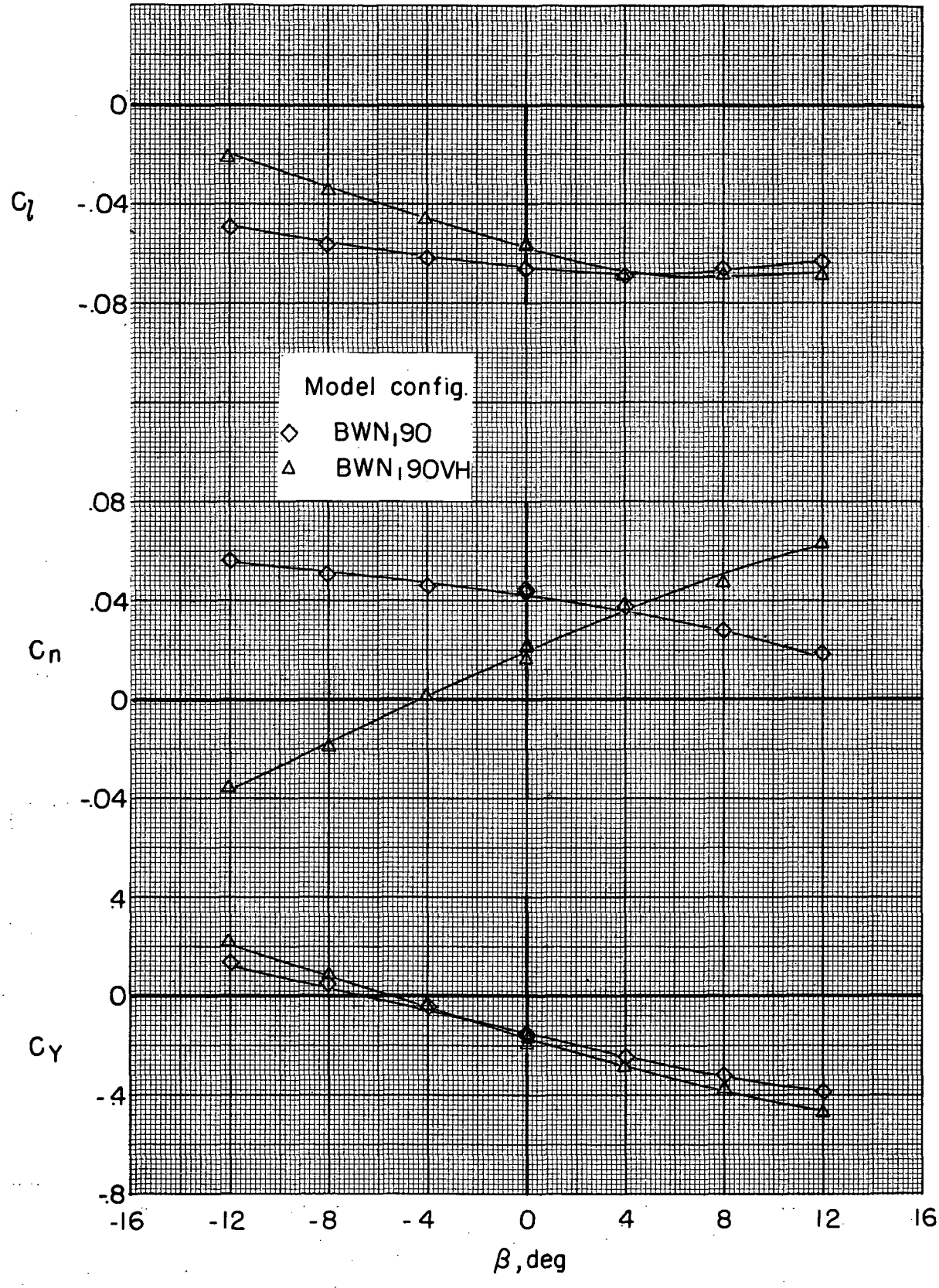
(b) Variation of C_l, C_n, and C_Y with β.

Figure 93.- Concluded.



(a) Variation of C_L, C_D, and C_m with β.

Figure 94.- Effect of model components on stability characteristics of front vectored-thrust configuration with power.



(b) Variation of C_l, C_n, and C_Y with β.

Figure 94.- Concluded.

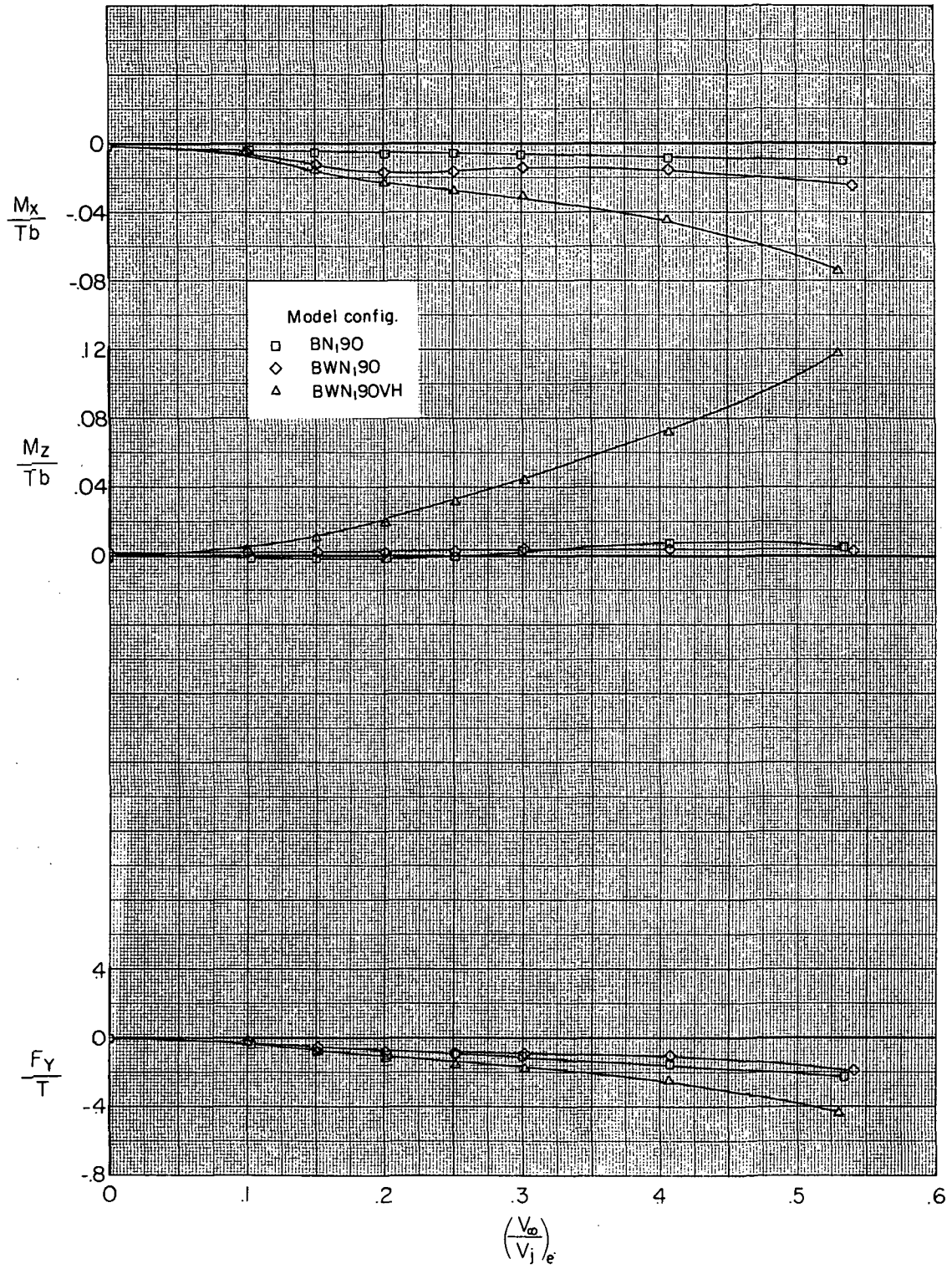


Figure 95.- Effect of model components on aerodynamic characteristics of front vectored-thrust configuration at an angle of sideslip of 8^{o} with power.

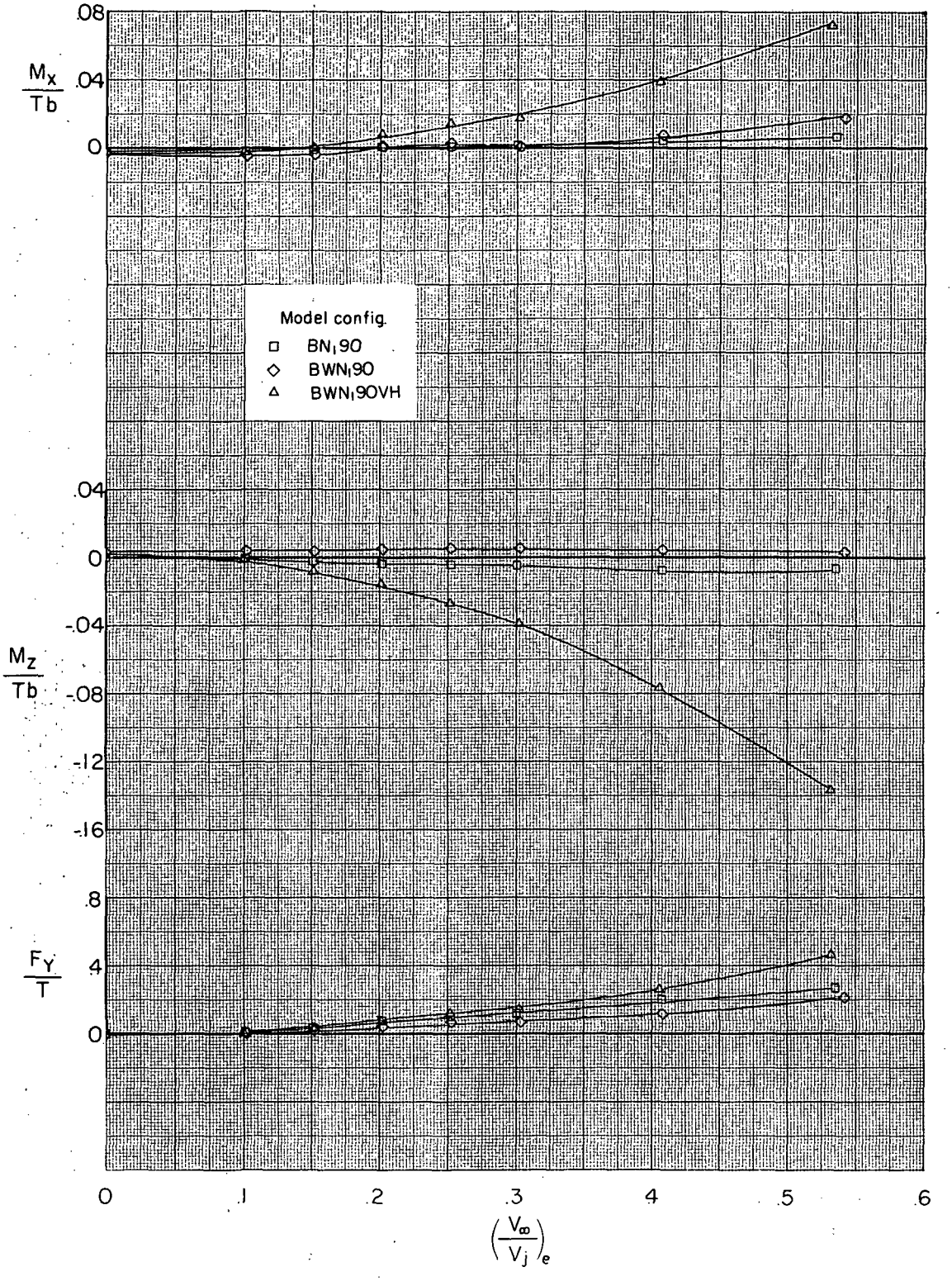
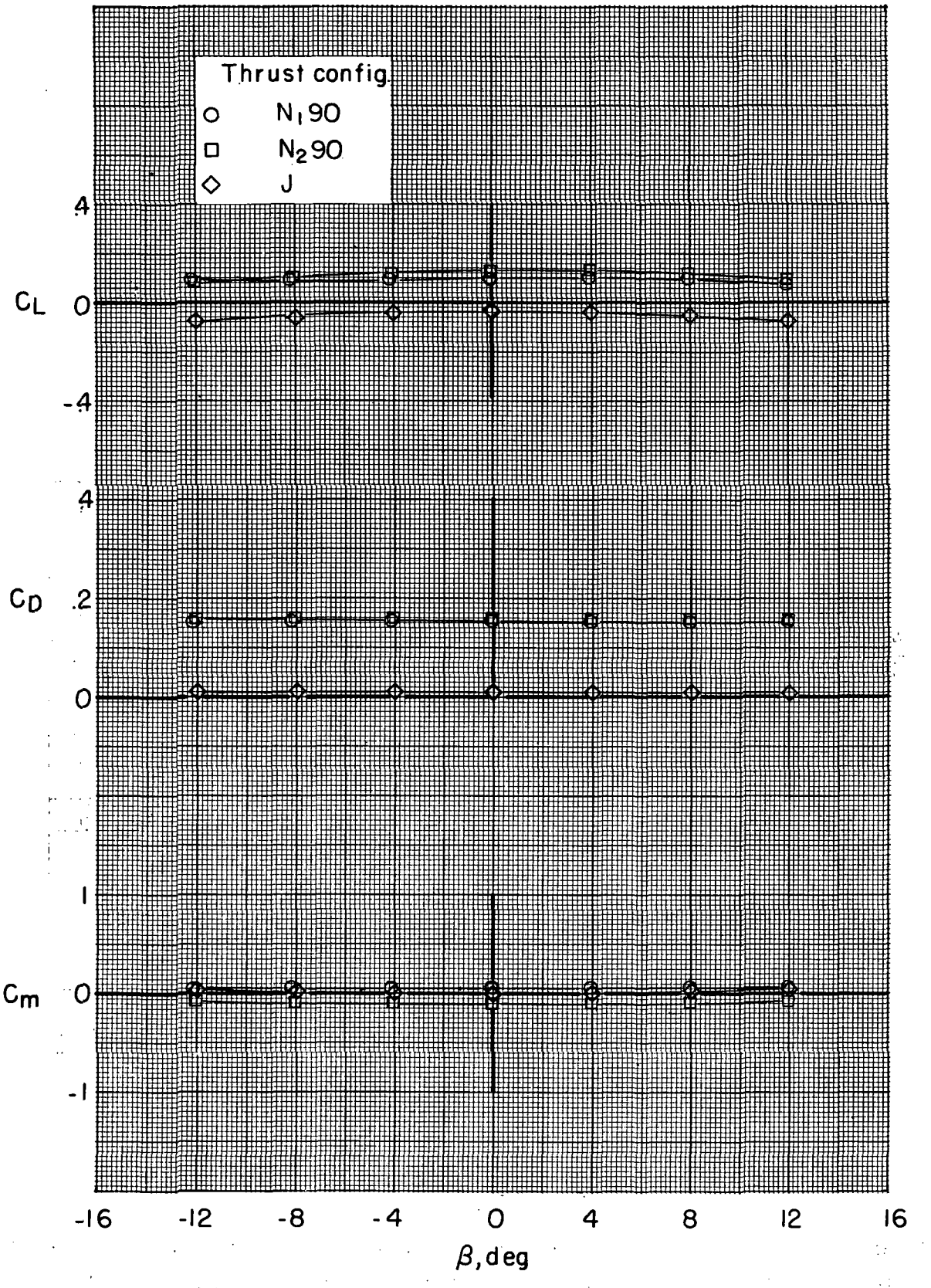
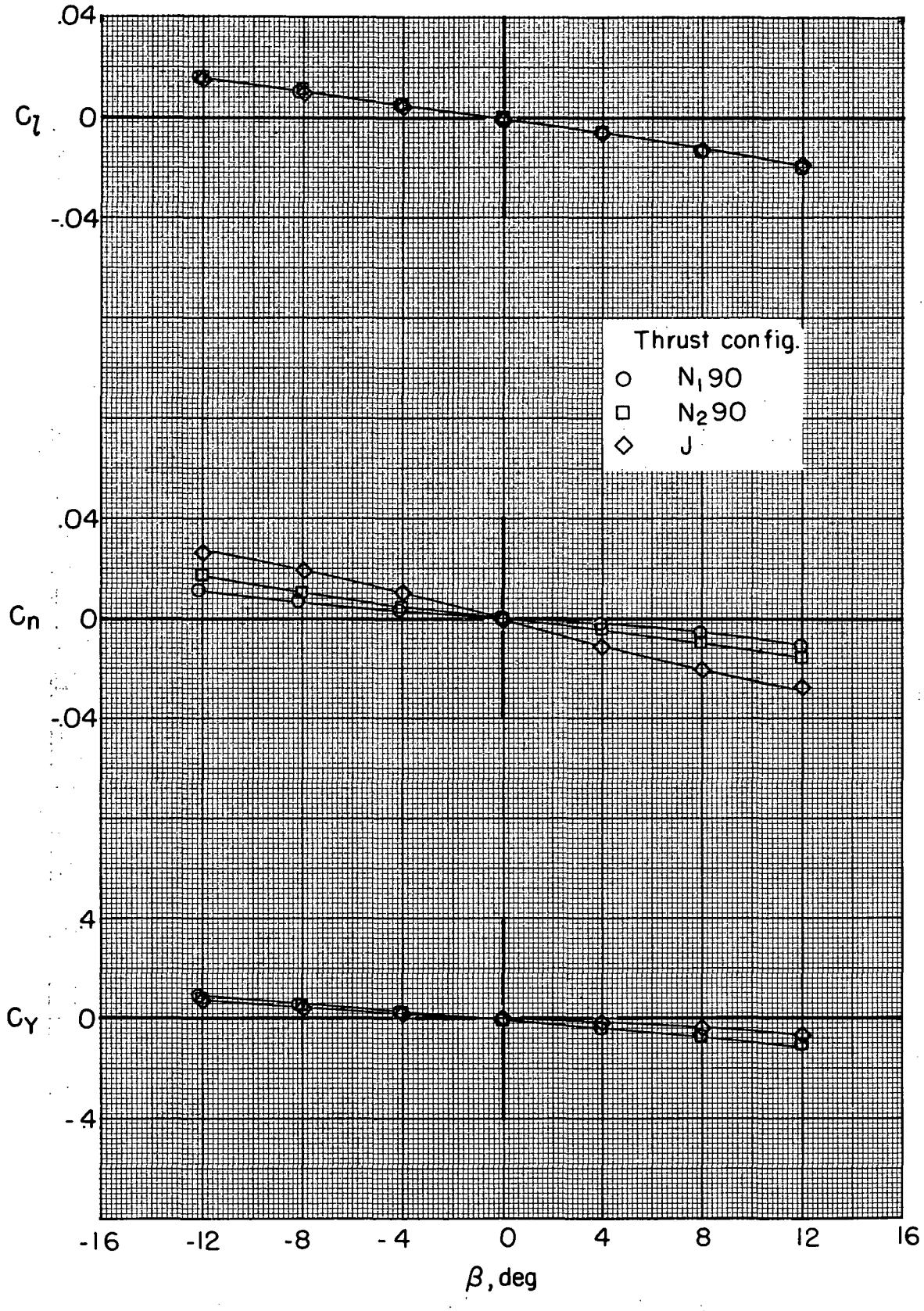


Figure 96.- Effect of model components on aerodynamic characteristics of front vectored-thrust configuration at an angle of sideslip of -8^{o} with power.



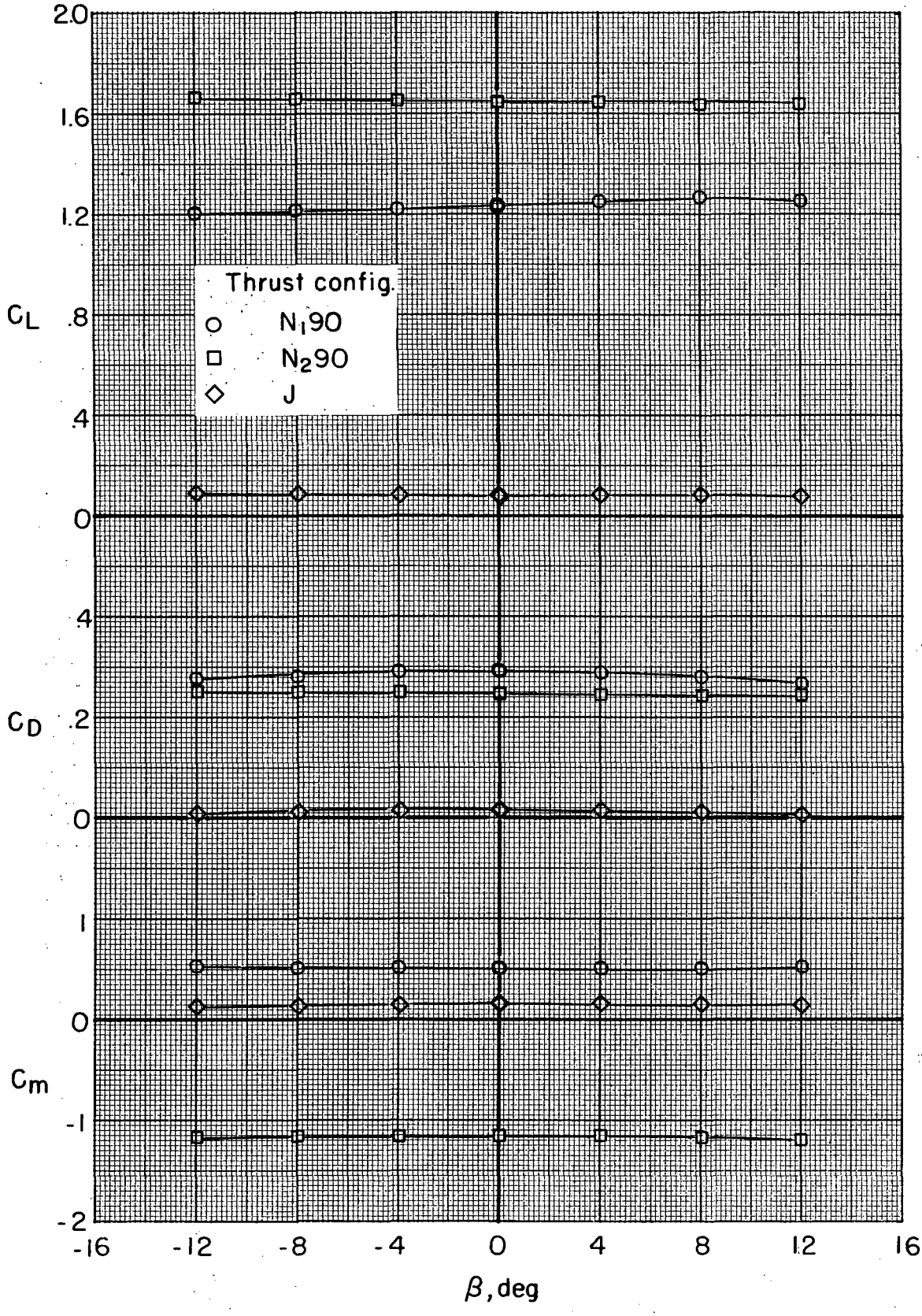
(a) Variation of C_L, C_D, and C_m with β.

Figure 97.- Effect of thrust configuration on aerodynamic characteristics in sideslip without power. $\left(V_\infty/V_j\right)_e = \infty$.



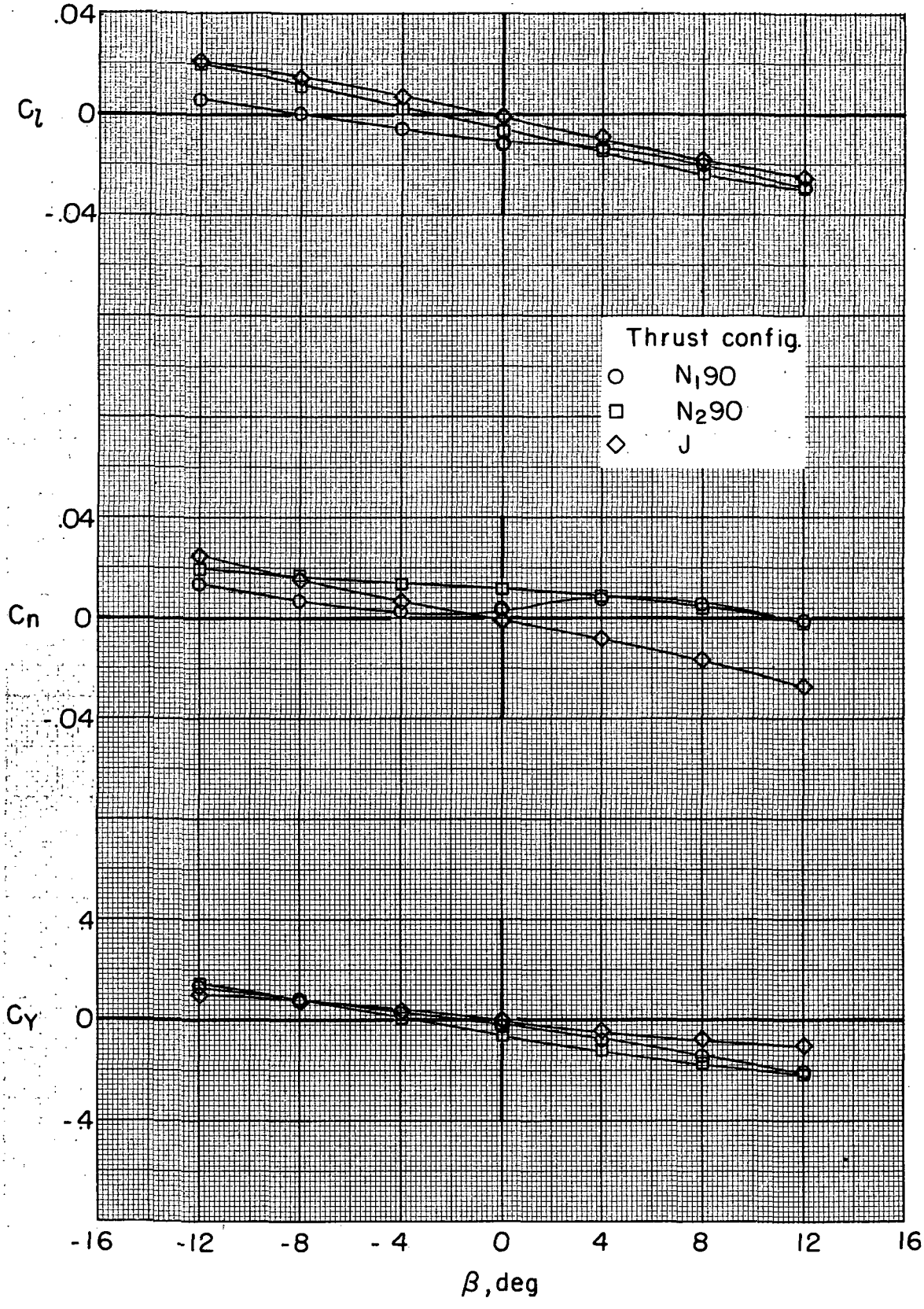
(b) Variation of C_l, C_n, and C_Y with β.

Figure 97.- Concluded.



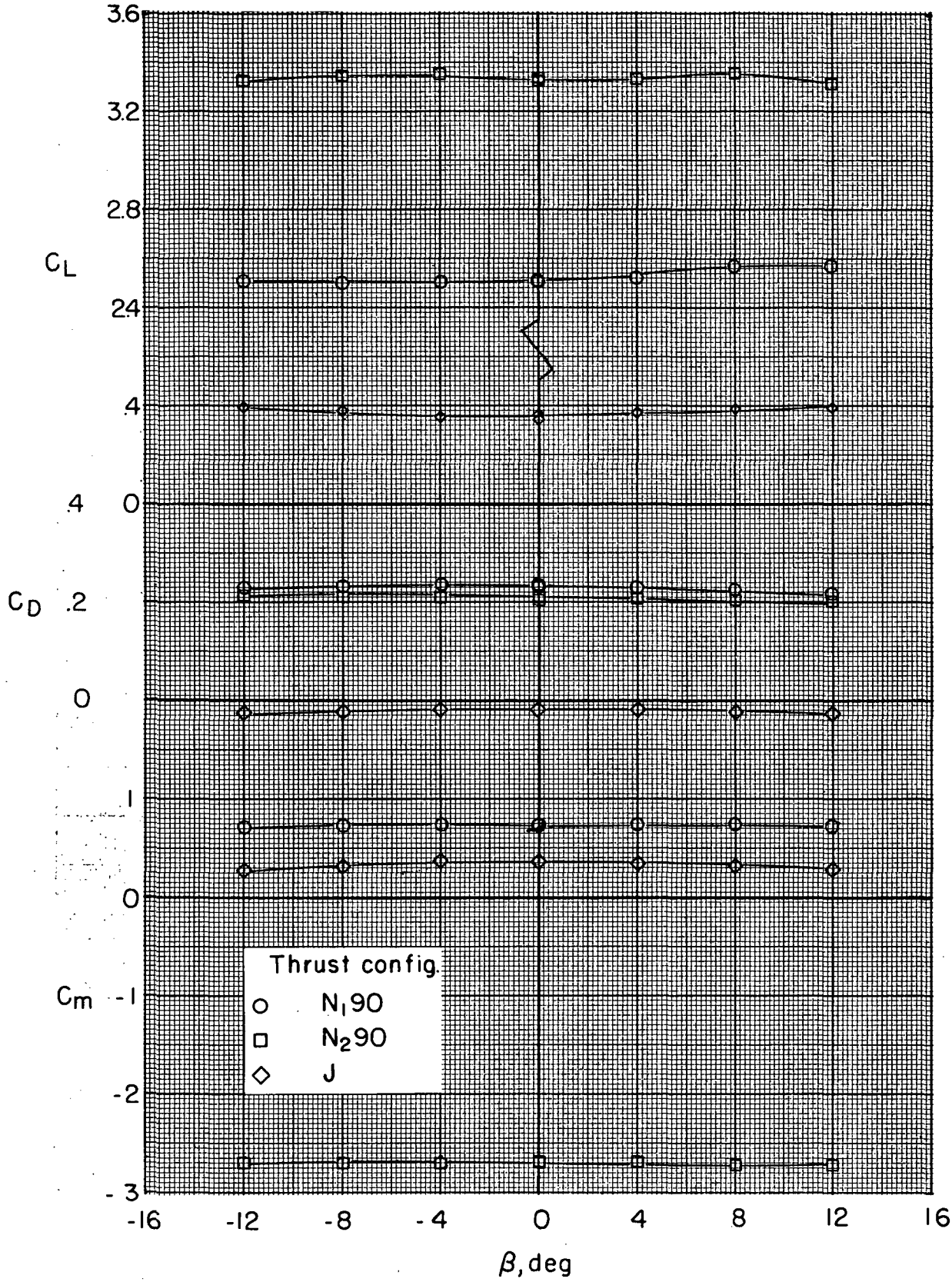
(a) Variation of C_L, C_D, and C_m with β.

Figure 98.- Effect of thrust configuration on aerodynamic characteristics in sideslip with power. $\left(V_\infty/V_j\right)_e = 0.3$.



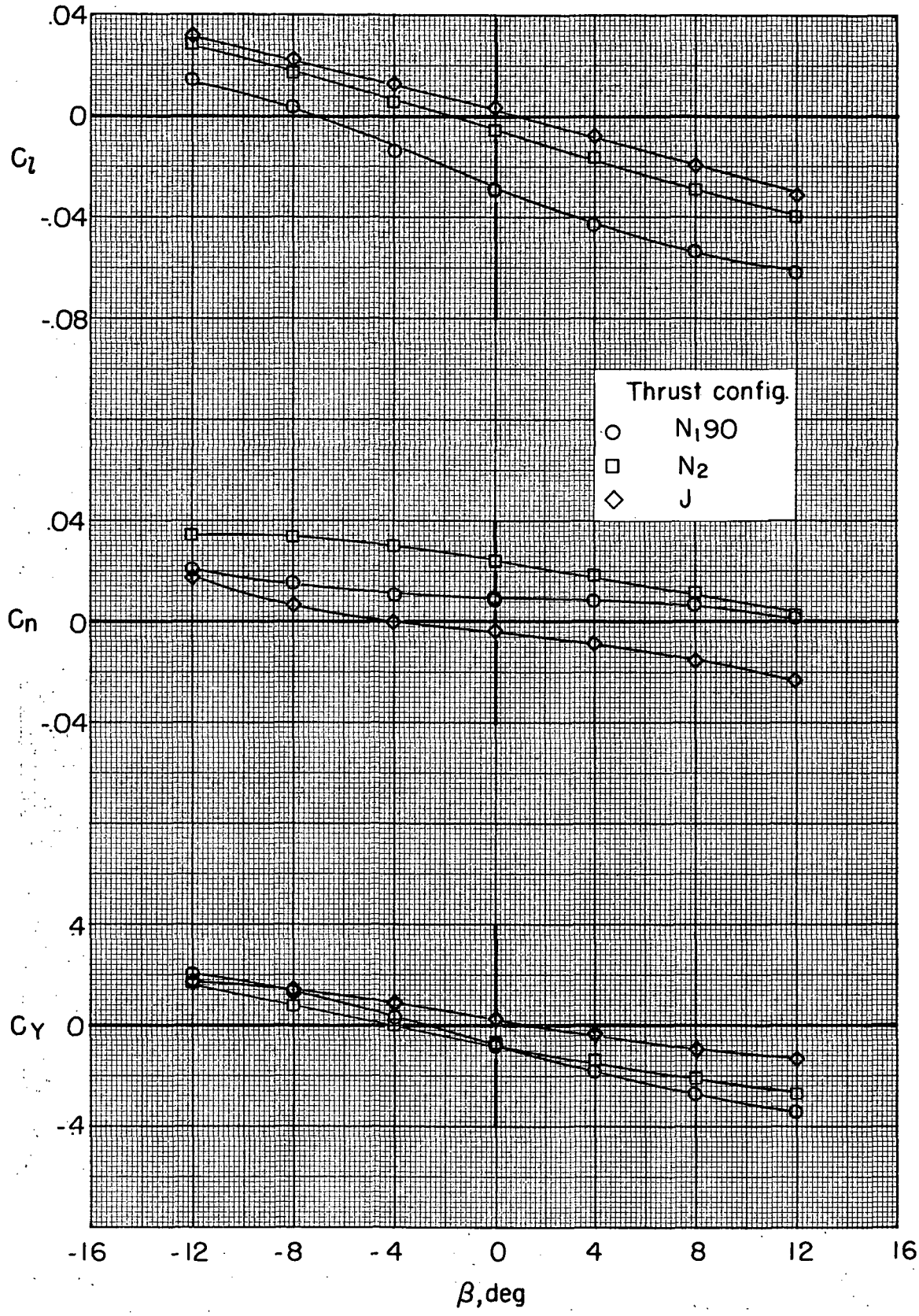
(b) Variation of C_l, C_n, and C_Y with β.

Figure 98.- Concluded.



(a) Variation of C_L, C_D, and C_m with β.

Figure 99.- Effect of thrust configuration on aerodynamic characteristics in sideslip with power. $\left(V_\infty/V_j\right)_e = 0.2$.



(b) Variation of C_l, C_n, and C_Y with β.

Figure 99.- Concluded.

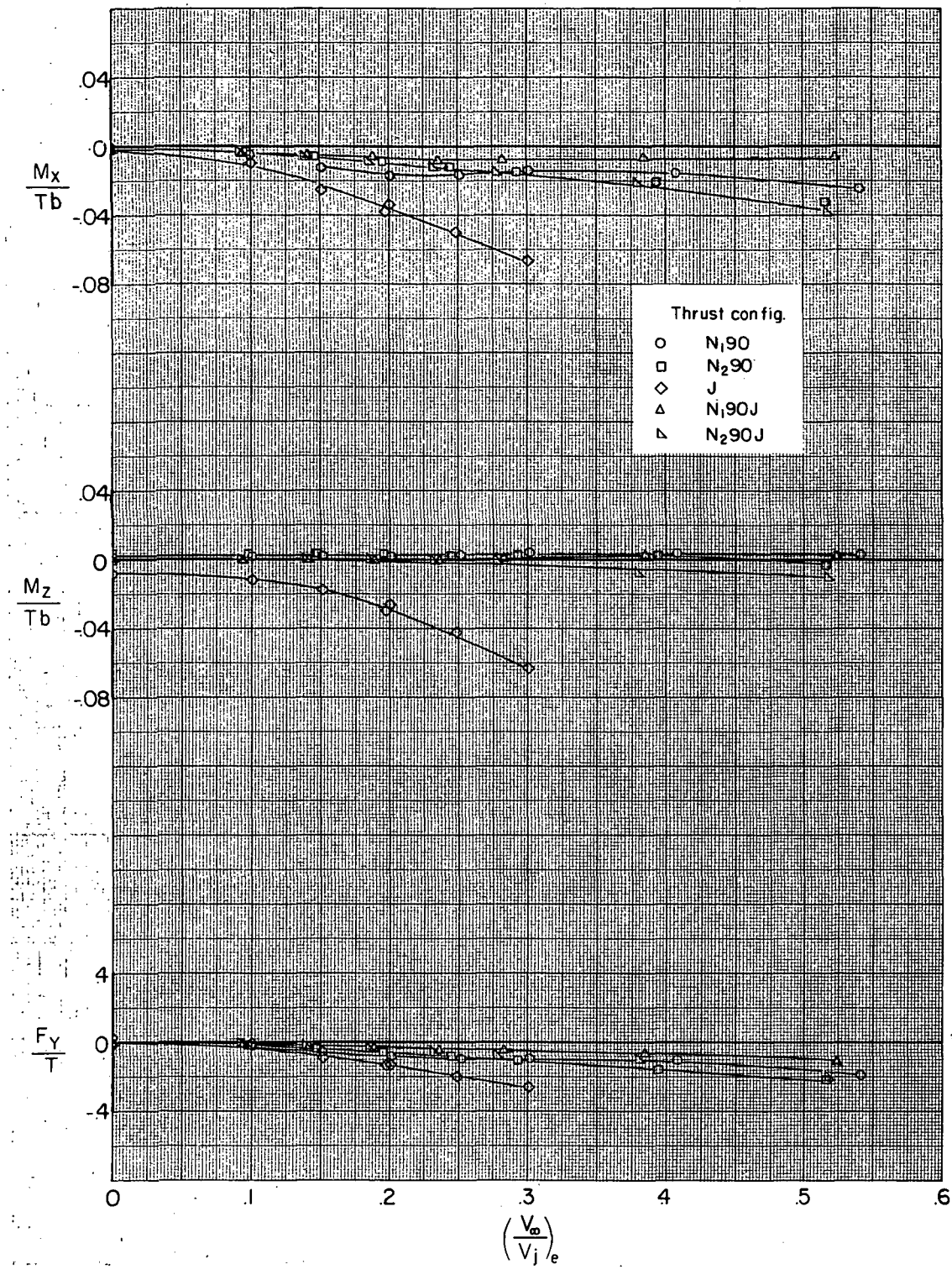


Figure 100.- Effect of thrust configuration on aerodynamic characteristics at an angle of sideslip of 8^o.

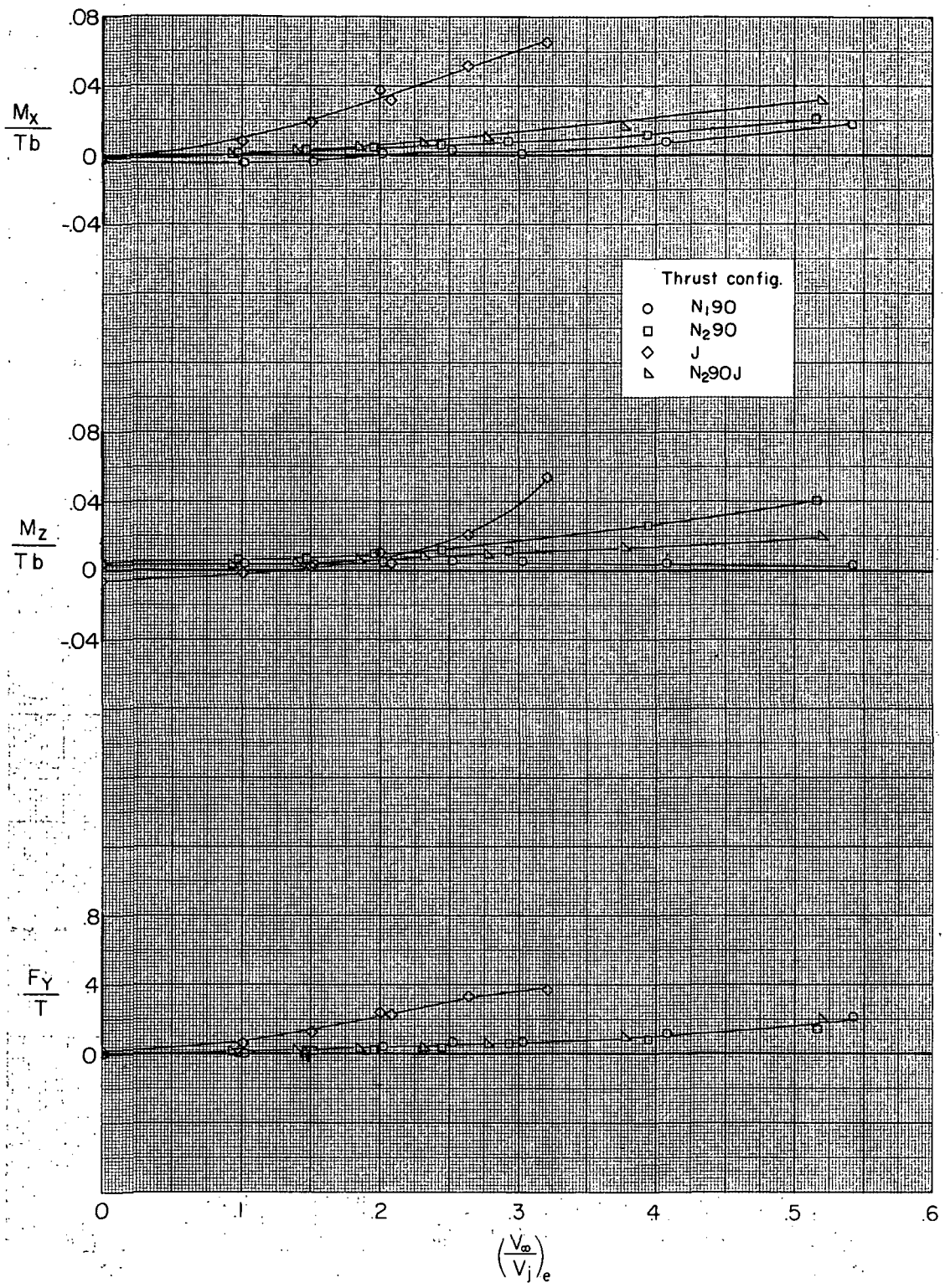
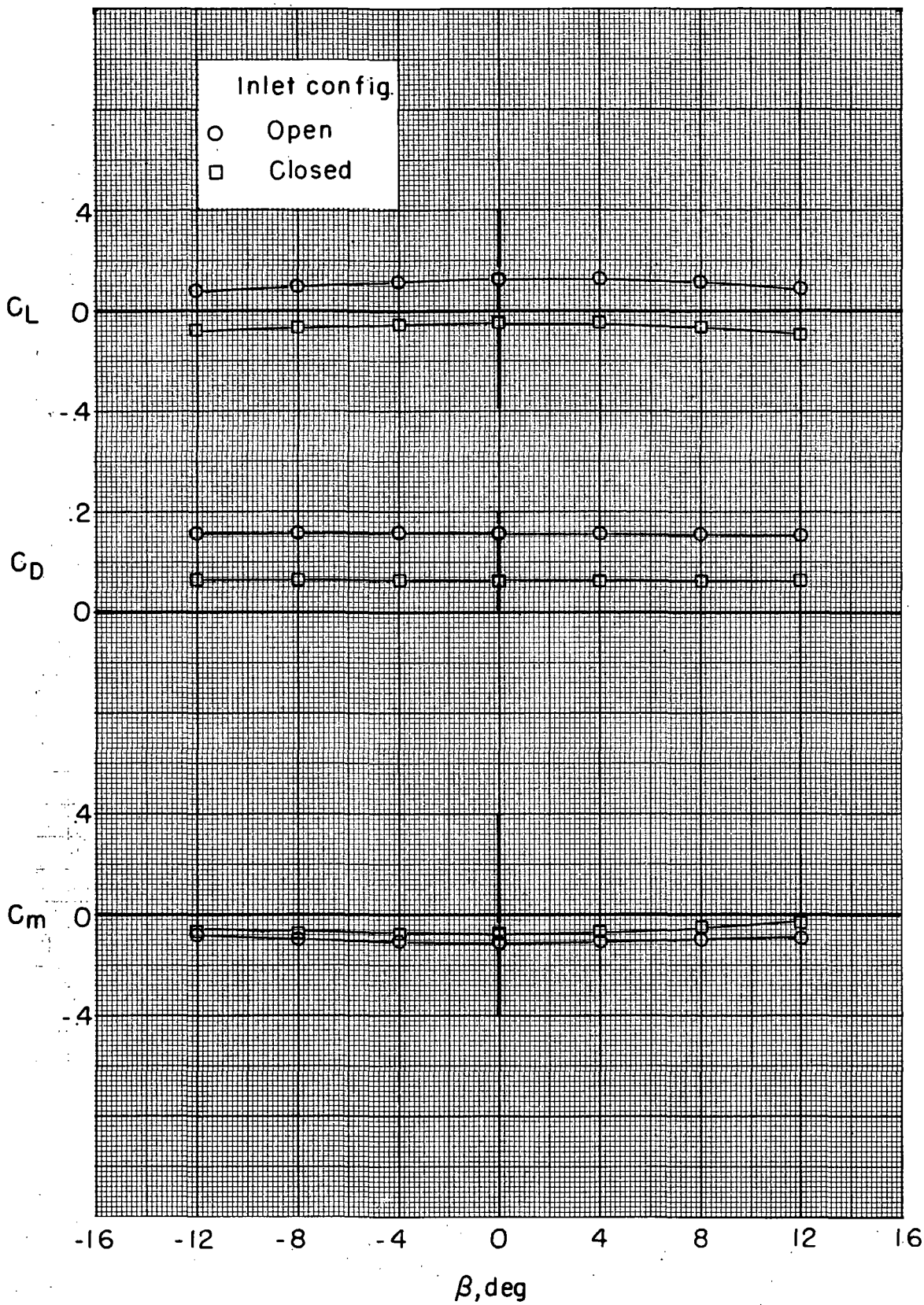
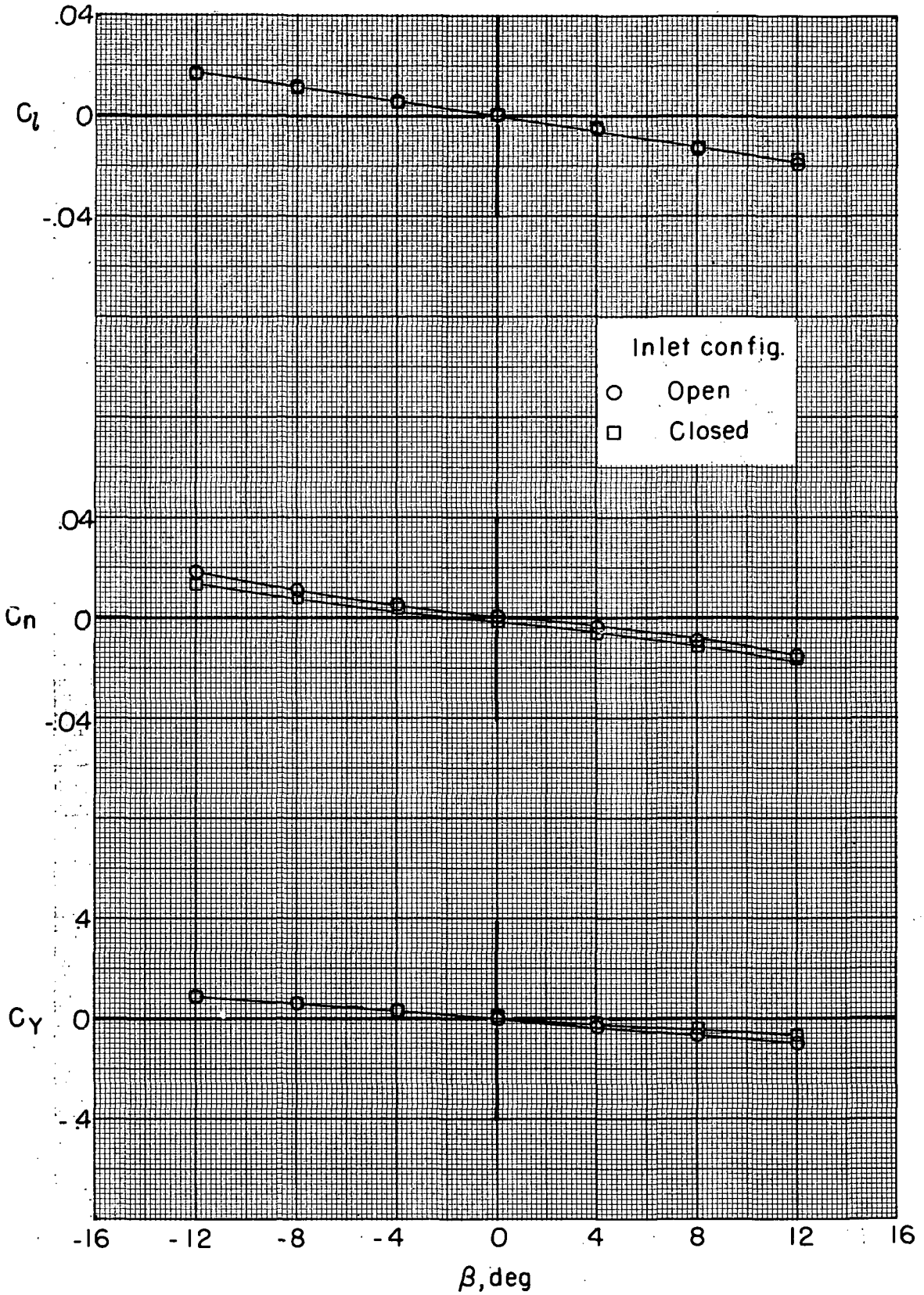


Figure 101.- Effect of thrust configuration on aerodynamic characteristics at an angle of sideslip of -8°.



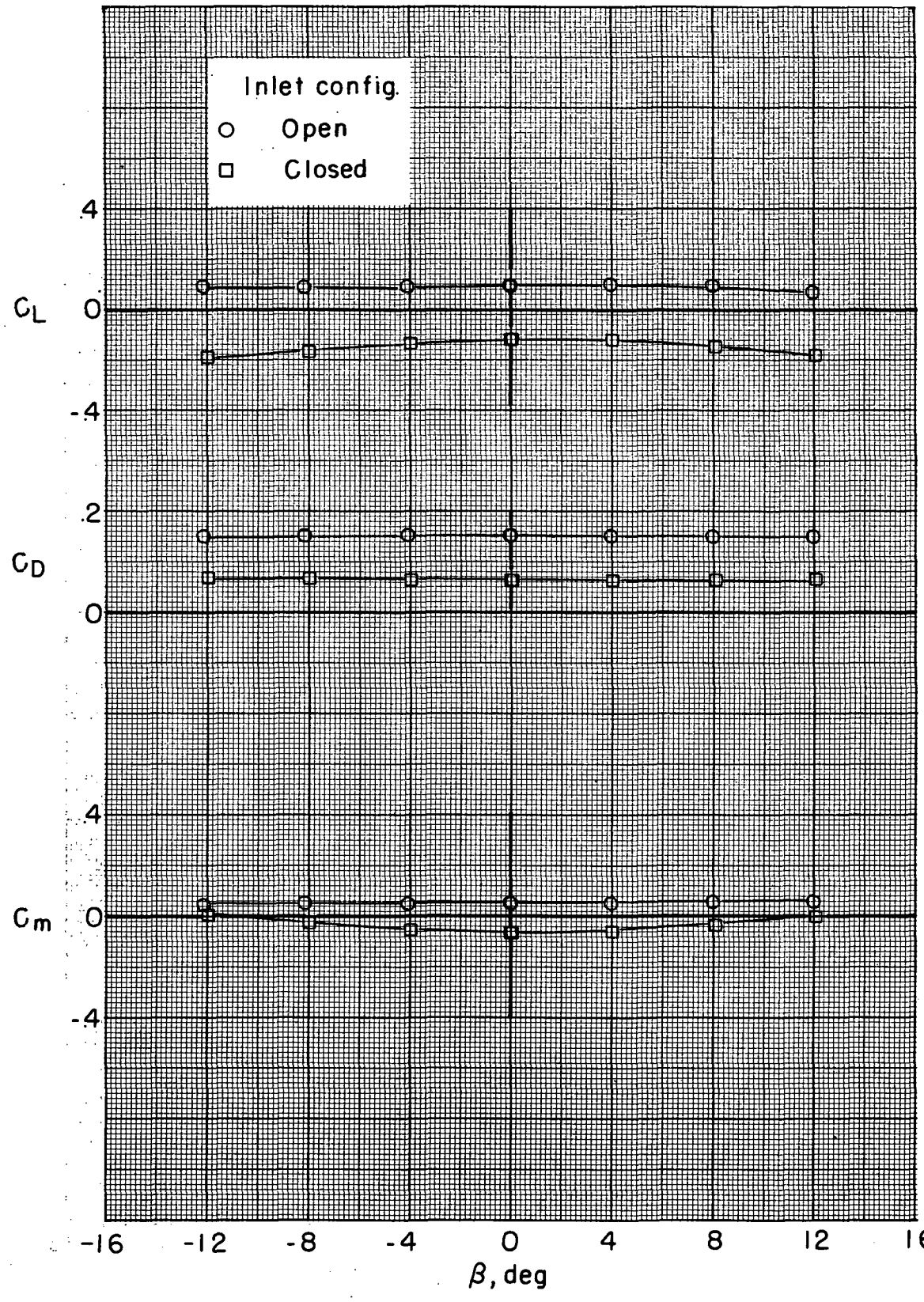
(a) Variation of C_L, C_D, and C_m with β.

Figure 102.- Effect of inlet flow on aerodynamic characteristics in sideslip of $BWN_2 90$ configuration without power. $\left(V_\infty / V_j\right)_e = \infty$.



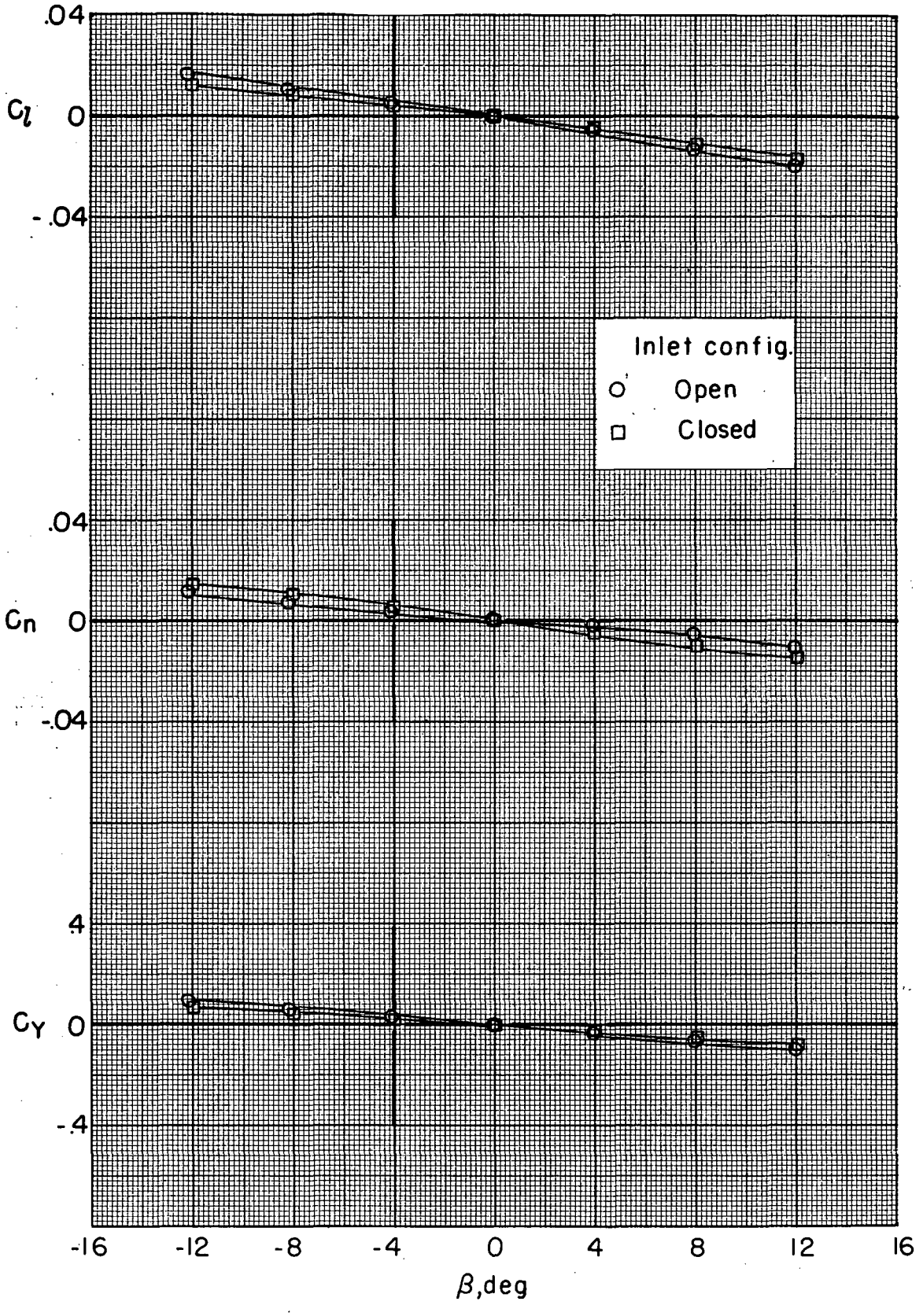
(b) Variation of C_l, C_n, and C_Y with β.

Figure 102. - Concluded.



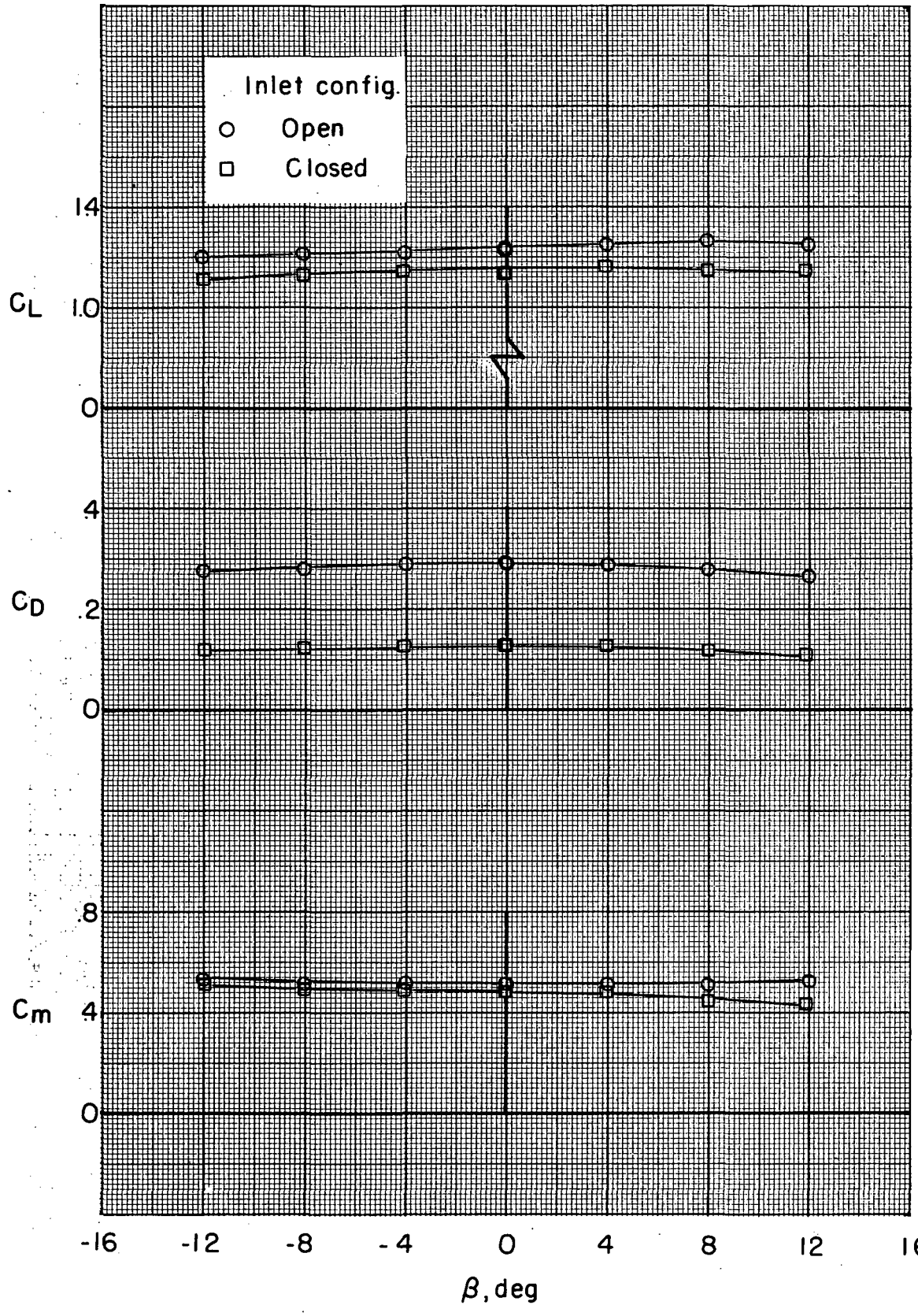
(a) Variation of C_L, C_D, and C_m with β.

Figure 103.- Effect of inlet flow on aerodynamic characteristics in sideslip of BWN$_1$90 configuration without power. $\left(V_\infty/V_j\right)_e = \infty$.



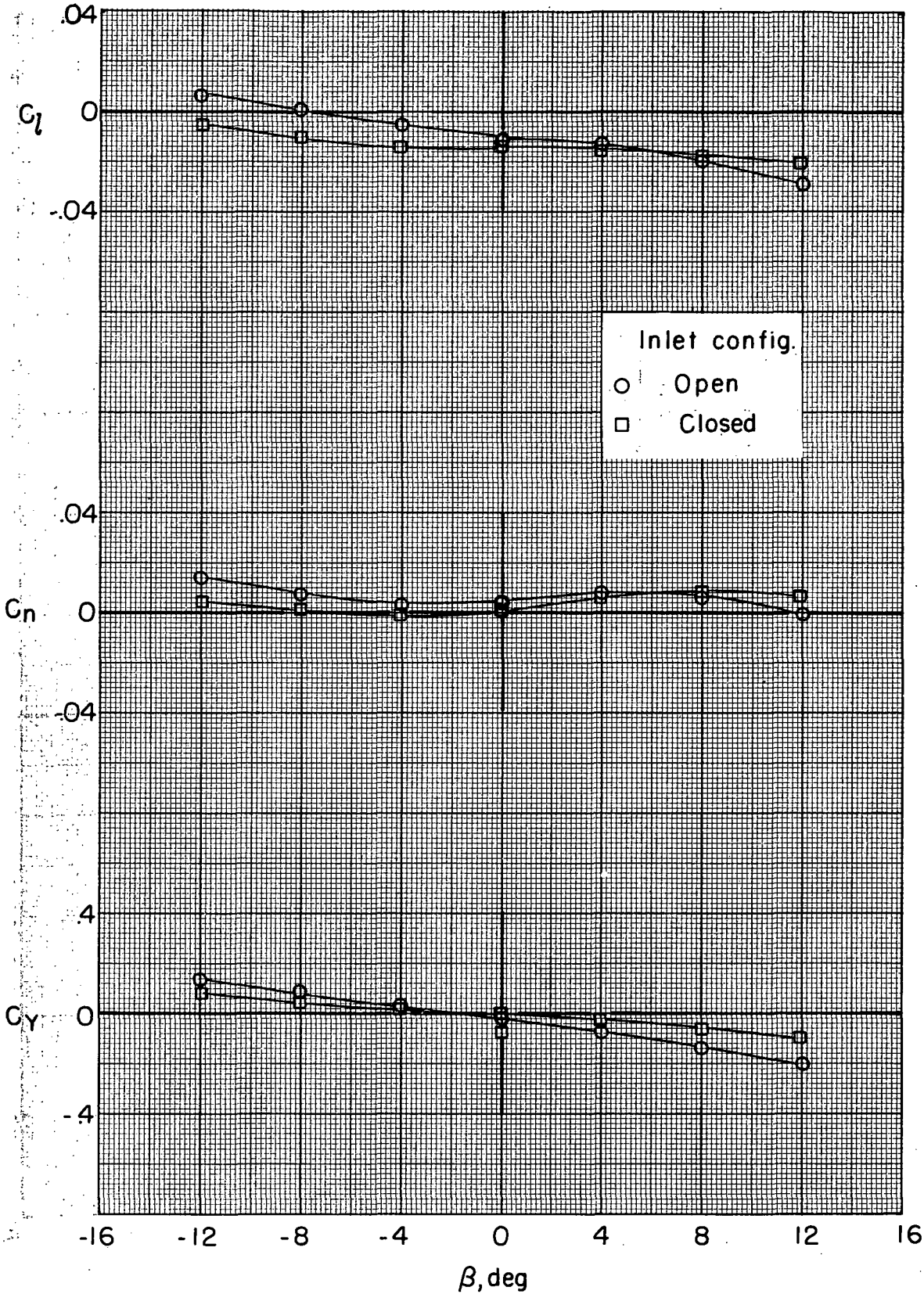
(b) Variation of C_l, C_n, and C_Y with β.

Figure 103.- Concluded.



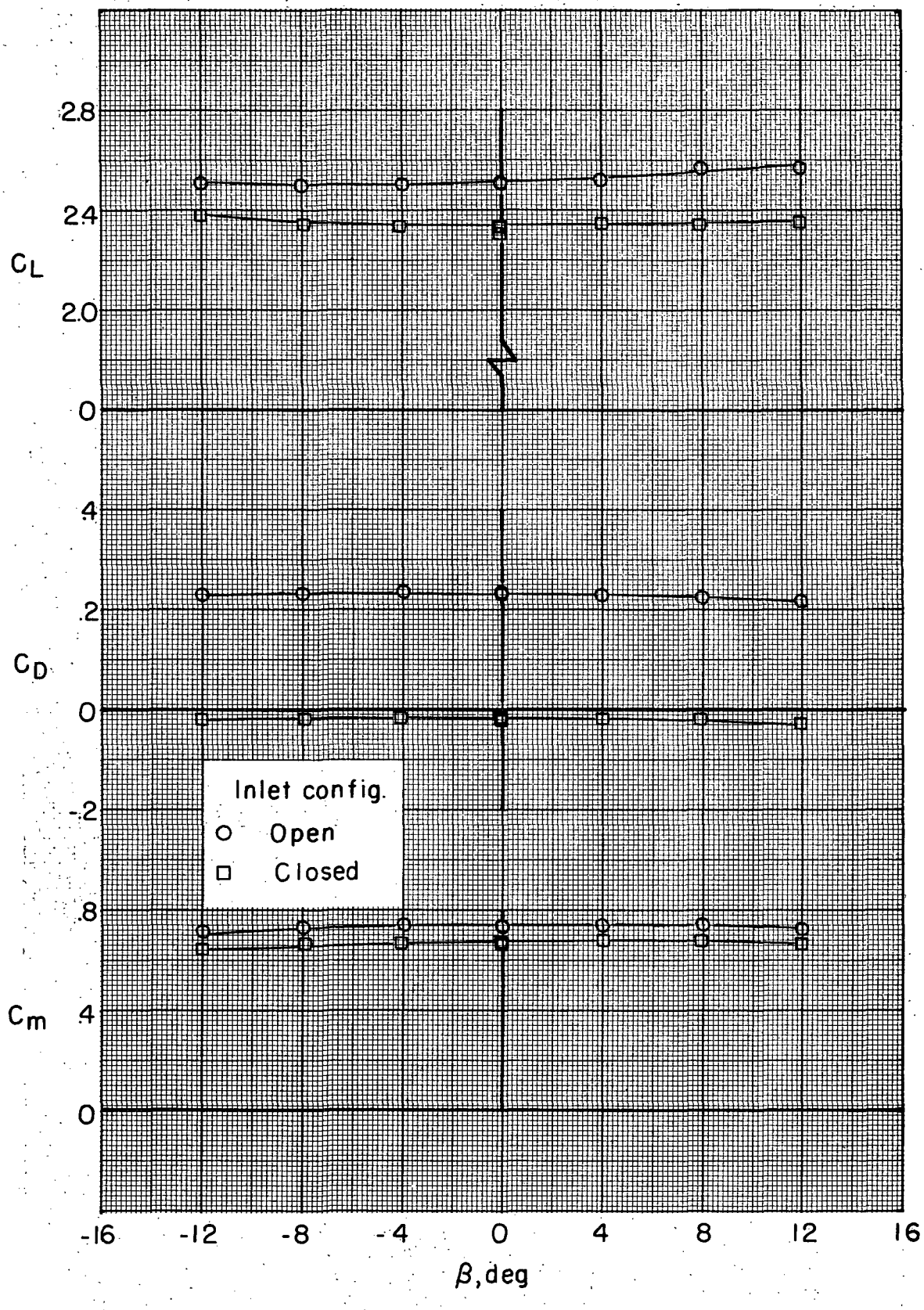
(a) Variation of C_L, C_D, and C_m with β.

Figure 104.- Effect of inlet flow on aerodynamic characteristics in sideslip of $BWN_1 90$ configuration with power. $\left(V_\infty/V_j\right)_e = 0.3$.



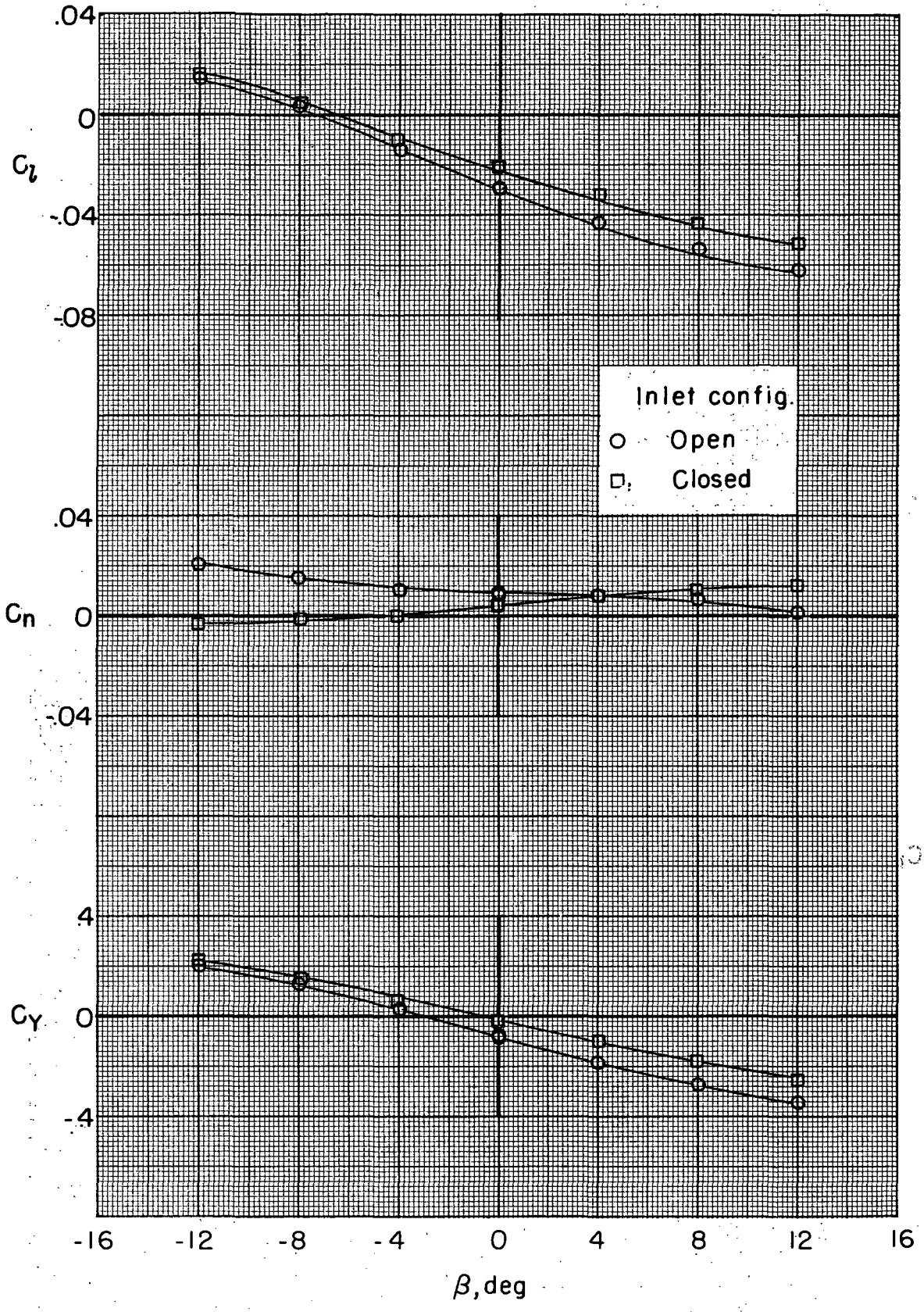
(b) Variation of C_l, C_n, and C_Y with β.

Figure 104.- Concluded.



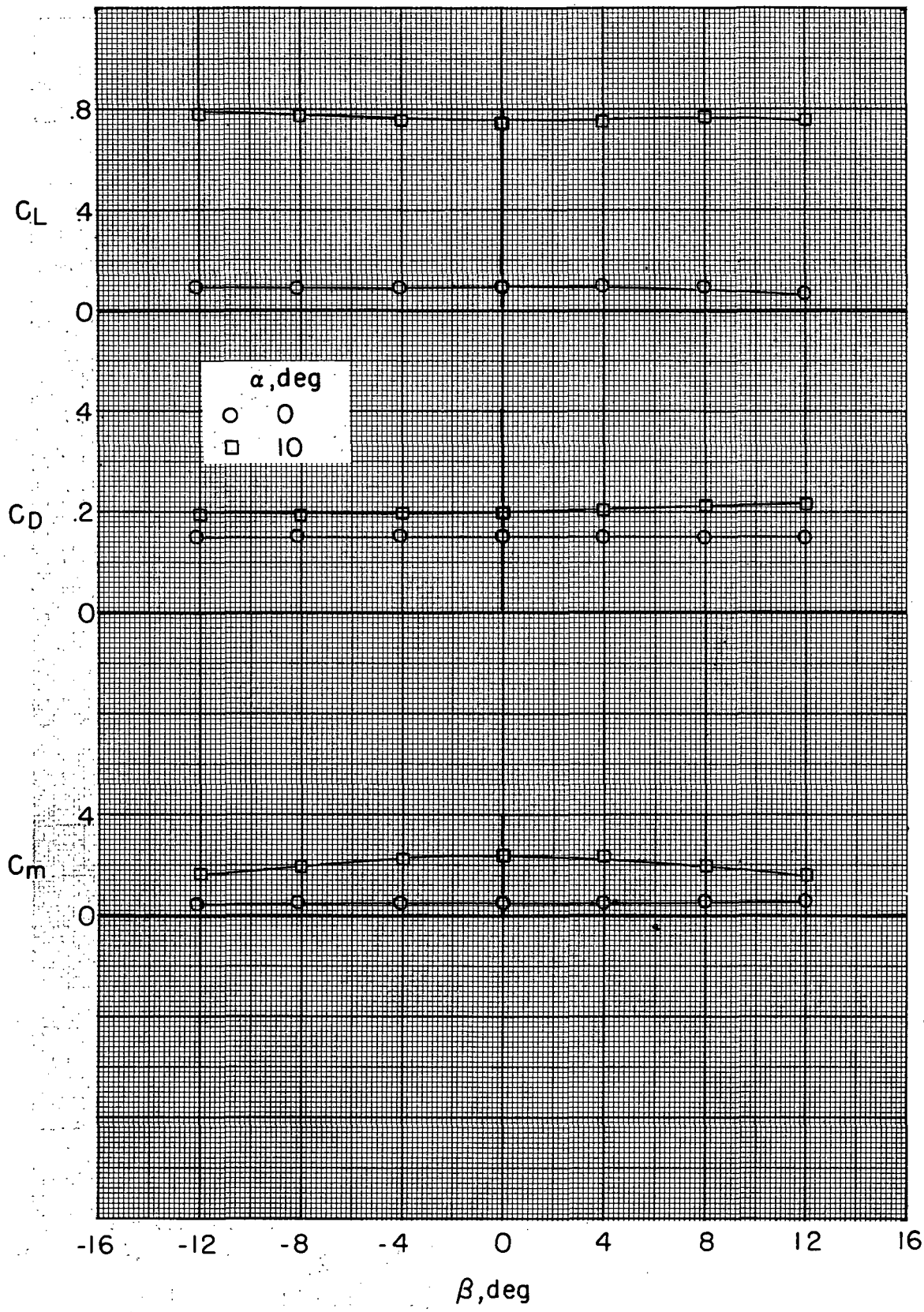
(a) Variation of C_L, C_D, and C_m with β.

Figure 105.- Effect of inlet flow on aerodynamic characteristics in sideslip of $BWN_1 90$ configuration with power. $\left(V_\infty/V_j\right)_e = 0.2$.



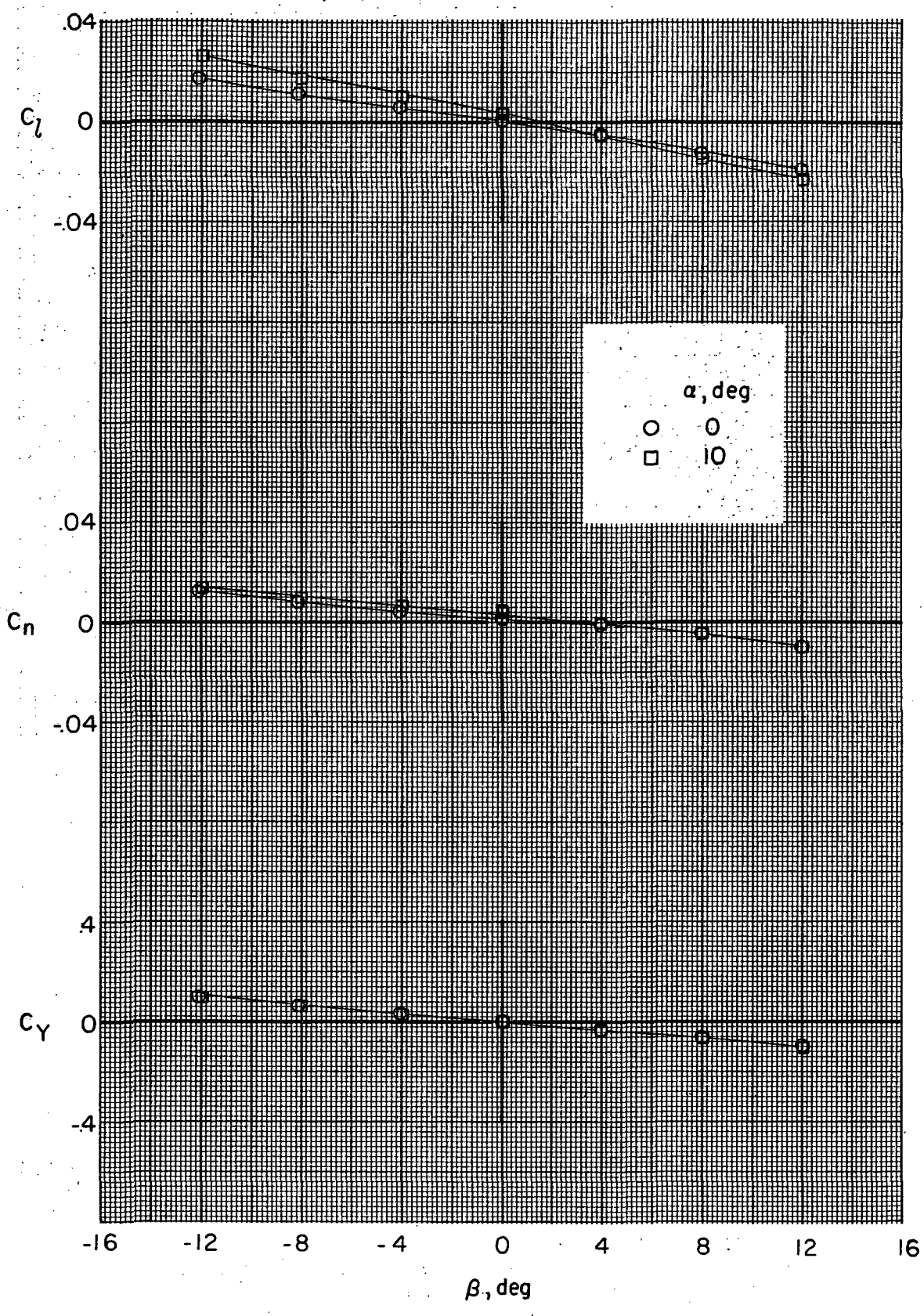
(b) Variation of C_l, C_n, and C_Y with β.

Figure 105.- Concluded.



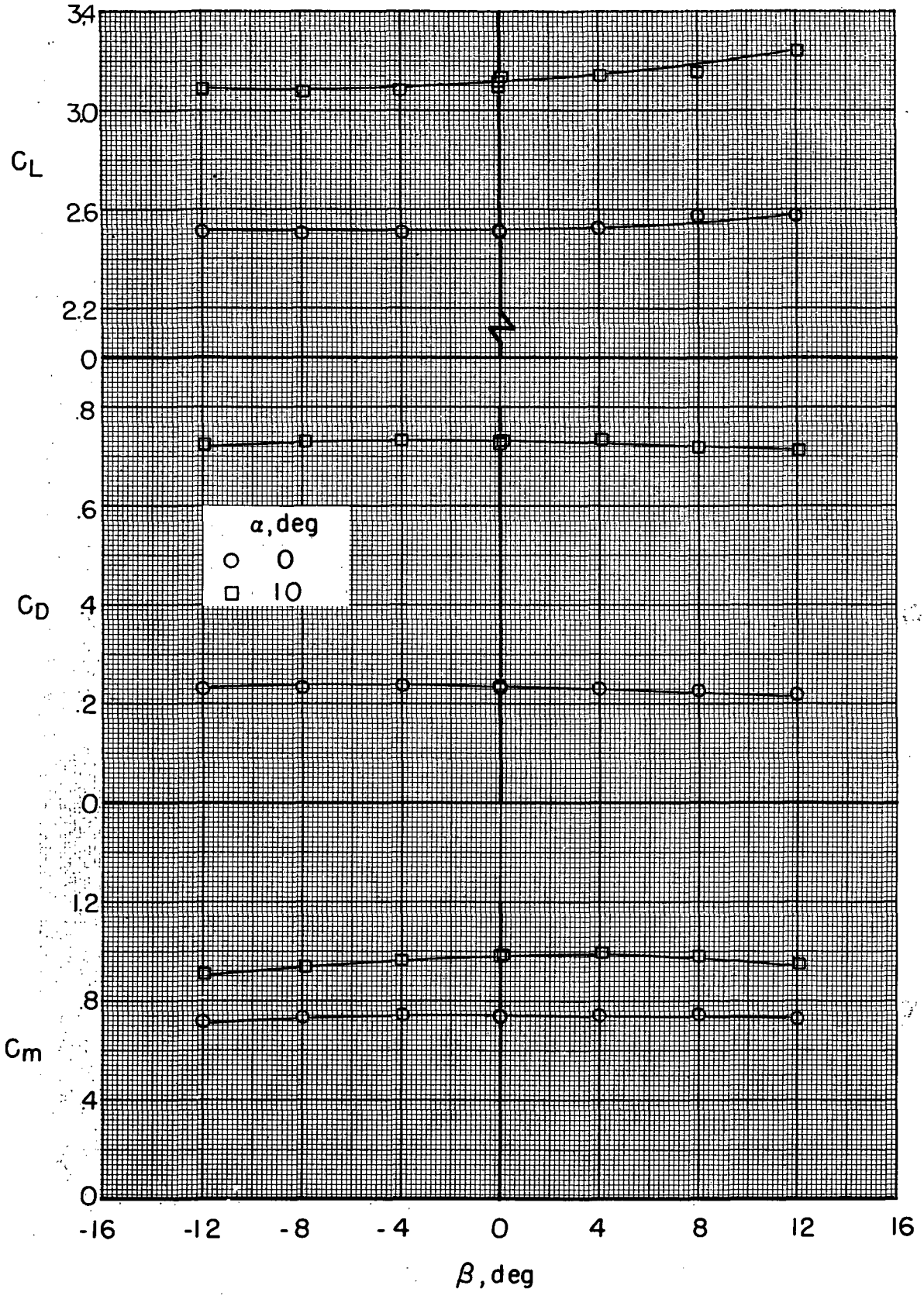
(a) Variation of C_L, C_D, and C_m with β.

Figure 106.- Effect of angle of attack on aerodynamic characteristics in sideslip of $BWN_1 90$ configuration without power. $\left(V_\infty / V_j\right)_e = \infty$.



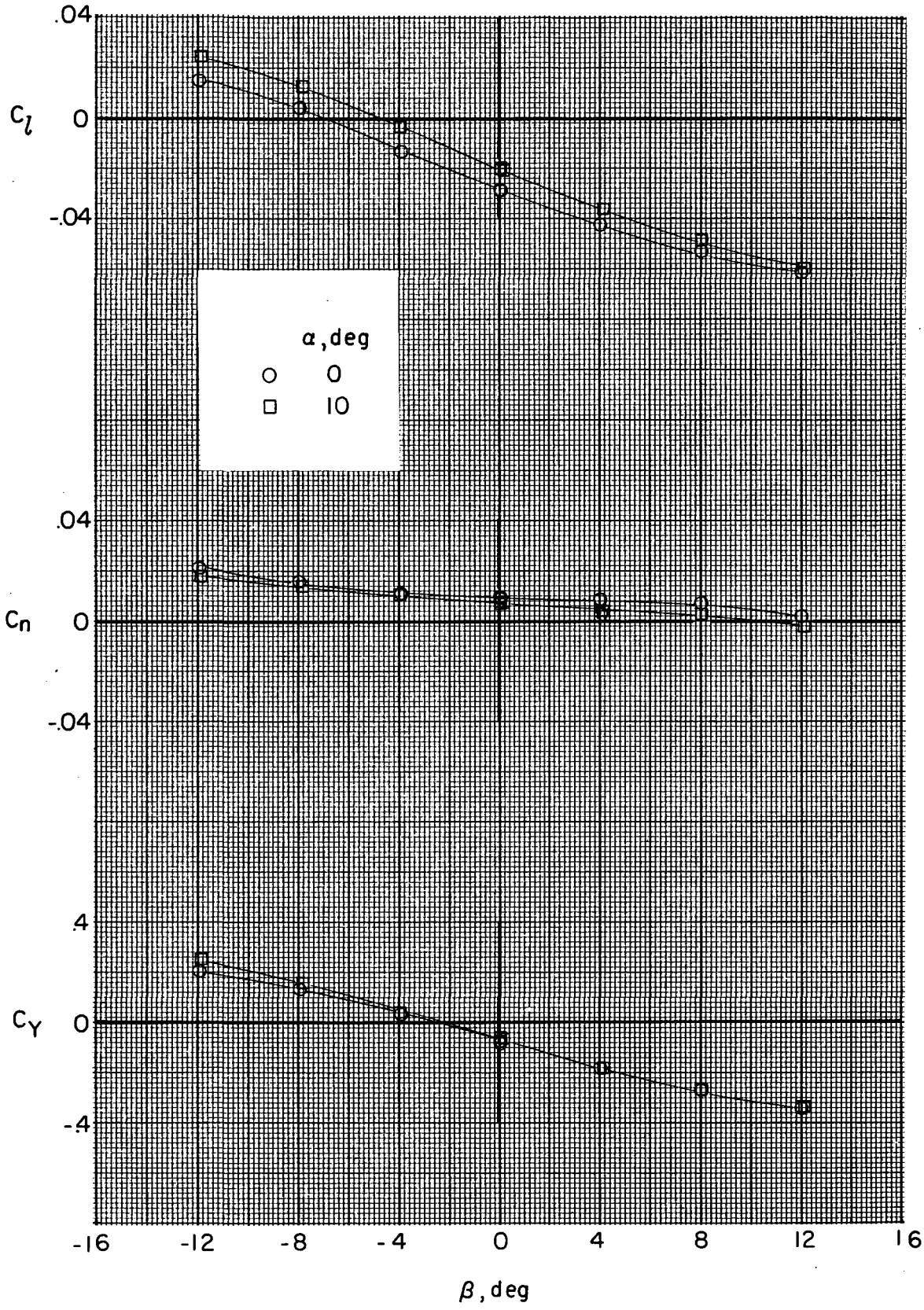
(b) Variation of C_l, C_n, and C_Y with β.

Figure 106.- Concluded.



(a) Variation of C_L, C_D, and C_m with β.

Figure 107.- Effect of angle of attack on aerodynamic characteristics in sideslip of $BWN_1 90$ configuration with power. $\left(V_\infty / V_j\right)_e = 0.2$.



(b) Variation of C_l, C_n, and C_Y with β.

Figure 107.- Concluded.

GOVERNMENT PRINTING OFFICE: 1973-739-027/33

NATIONAL AERONAUTICS AND SPACE ADMINISTRATION
WASHINGTON, D.C. 20546

OFFICIAL BUSINESS
PENALTY FOR PRIVATE USE $300

SPECIAL FOURTH-CLASS RATE BOOK

POSTAGE AND FEES PAID
NATIONAL AERONAUTICS AND SPACE ADMINISTRATION
451

U.S.MAIL

POSTMASTER: If Undeliverable (Section 158 Postal Manual) Do Not Return

"The aeronautical and space activities of the United States shall be conducted so as to contribute . . . to the expansion of human knowledge of phenomena in the atmosphere and space. The Administration shall provide for the widest practicable and appropriate dissemination of information concerning its activities and the results thereof."

—NATIONAL AERONAUTICS AND SPACE ACT OF 1958

NASA SCIENTIFIC AND TECHNICAL PUBLICATIONS

TECHNICAL REPORTS: Scientific and technical information considered important, complete, and a lasting contribution to existing knowledge.

TECHNICAL NOTES: Information less broad in scope but nevertheless of importance as a contribution to existing knowledge.

TECHNICAL MEMORANDUMS: Information receiving limited distribution because of preliminary data, security classification, or other reasons. Also includes conference proceedings with either limited or unlimited distribution.

CONTRACTOR REPORTS: Scientific and technical information generated under a NASA contract or grant and considered an important contribution to existing knowledge.

TECHNICAL TRANSLATIONS: Information published in a foreign language considered to merit NASA distribution in English.

SPECIAL PUBLICATIONS: Information derived from or of value to NASA activities. Publications include final reports of major projects, monographs, data compilations, handbooks, sourcebooks, and special bibliographies.

TECHNOLOGY UTILIZATION PUBLICATIONS: Information on technology used by NASA that may be of particular interest in commercial and other non-aerospace applications. Publications include Tech Briefs, Technology Utilization Reports and Technology Surveys.

Details on the availability of these publications may be obtained from:

SCIENTIFIC AND TECHNICAL INFORMATION OFFICE

NATIONAL AERONAUTICS AND SPACE ADMINISTRATION

Washington, D.C. 20546